UNIVERSITY OF CALIFORNIA

Santa Barbara

VISCOELASTIC EFFECT OF THIN SHELL FIBER REINFORCED COMPOSITES USED FOR DEPLOYABLE SPACE STRUCTURES

A Dissertation submitted in partial satisfaction of the
requirements for the degree of

Doctor of Philosophy

in

Mechanical Engineering

by

Christopher Van Peterson

Committee in charge:

Professor Robert McMeeking, Chair

Professor Glenn Beltz

Professor Frank Zok

Professor Keith Kedward, in memoriam

September 2020

The Dissertation of

Christopher Van Peterson is approved by:

_____

Professor Glenn Beltz

_____

Professor Frank Zok

_____

Professor Robert McMeeking, Committee Chair

July 2020

Viscoelastic Effect of Thin Shell Fiber Reinforced Composites Used for Deployable Space Structures

by

Christopher Van Peterson

In dedication to my father, Edward Peterson. You are the reason I have completed this Ph.D. Your love, support, and encouragement have been invaluable. Thank you for being my sounding board, my research advisor, my biggest cheerleader, my father, and my friend.

ACKNOWLEDGEMENTS

First and foremost, I would like to thank the late, great Professor Keith Kedward, for starting me down the path of higher education. His mentorship and guidance throughout undergrad and graduate school were invaluable. His love for teaching and educating future generations has motivated me through this challenging and rewarding experience during my Ph.D.

I would also like to thank Professor Robert McMeeking for taking over as lead advisor when Professor Kedward became ill. Your mentorship and guidance has been invaluable during this time and has helped me grow as an individual and as a researcher.

I would also like to thank my Ph.D. committee members. Thank you, Professor Glenn Beltz, for being a supportive role throughout my time at UCSB. It has been a rewarding experience to TA many of your courses. Thank you, Professor Frank Zok, for helping develop my technical writing skills. You have all helped to guide me during my Ph.D., and your feedback has helped shape my research during graduate school.

I would like to thank Kirk Field, the lead of UCSB's Mechanical Test Lab, for guiding me through the test campaign critical to my Ph.D. research. Your knowledge and experience in the field of mechanical testing were invaluable. Thank you for always making time to meet.

I would like to thank Julie Dunson and Laura Reynolds in the Mechanical Engineering Office for helping me through the Ph.D. process. You made this difficult journey that much easier. Thank you for always having my back.

I would like to thank the team at Deployable Space Systems for supporting my research in collaboration with a NASA STTR grant. You were the seed that sparked my doctoral research. Thank you for your support and guidance.

Lastly, I want to thank my friends and family. I thank my parents for always encouraging me to be the best that I can be. I thank my brother and sister for being great role models and exemplifying incredible work ethics. I thank my 102-year-old grandmother for instilling the value of education in me as far back as pre-school. I thank my wife for her abundance of patients and love through this journey. Thank you all for always being there with unconditional support and encouragement.

CURRICULUM VITAE

Christopher Van Peterson

EDUCATION

2008-2012: Bachelor of Science in Mechanical Engineering, University of California, Santa Barbara, with honors

2012-Present: Doctor of Philosophy in Mechanical Engineering, University of California, Santa Barbara.

PROFESSIONAL EMPLOYMENT

2012-2014: Graduate Student Researcher for Keith Kedward, Ph.D. and Robert McMeeking, Ph.D. Received a 3-year NASA funded STTR grant in affiliation with Deployable Space Structures' (DSS) to aid in their development of DSS's Mega ROSA deployable array in Goleta, CA.

2013-2019: Teaching Assistant, Department of Mechanical Engineering, University of California, Santa Barbara. Appointed as head TA for most courses. Responsible for managing graders, students, and the development of course material (e.g., exams, homework, teaching material, and design projects).

2018-Current: Principal Mechanical Engineer, Northrop Grumman Inc. Design engineer tasked with the development of unique deployable space structures, including high precision telescoping booms for large flexible antennas, coil-able booms used for x-ray telescopes (most notably ARCUS and IXPE), and compact lite-weight flexible solar arrays (CTA and E-CTA).

VOLUNTEER WORK:

2013-2019: Santa Barbara County Search and Rescue. Responded to hundreds of search and rescue calls in Santa Barbara County, including the Montecito mudslide of 2018.

2016-2017: UCSB Undergraduate Mechanical Engineering Academic Committee. Appointed as the student representative on the committee to aid in the improvement of UCSB's ME curriculum and to help ensure that national and global standards were met (e.g., ABET).

AWARDS AND ACHIEVEMENTS:

- UCSB Swimming Scholar-Athlete of the year award (2008/2009).
- Student spokesperson for the UCSB athletic department and the ME department.

- Full swimming scholarship for 2010/2011 and 2011/2012.
- Participated in the 2010/2011 NCAA DIV I Swimming Championships, 2012, and 2016 Olympic Swimming Trials.
- A three-time champion at the 2015 Master Swimming Nationals.
- College of Engineering Academic Scholastic Award.
- Dean's Honors four times for mechanical engineering.
- 2010/2011 UCSB Golden Eagle award for academic and athletic achievement.
- UCSB Mechanical Engineering Outstanding Teaching Assistant award 2016/2017.
- Community Hero by the American Red Cross Santa Barbara County Chapter.
- Orbital ATK Star Award for outstanding performance.

ABSTRACT

Viscoelastic Effect of Thin Shell Fiber Reinforced Composites Used for Deployable Space Structures

by

Christopher Van Peterson

Composite tape springs, and a related design called a storable tubular extendable member (STEM), are used in aerospace structures as deployment mechanisms for various components on satellites, e.g., solar arrays, antennae, booms. Laminates used in their designs must be thin to prevent micro-buckling when deformed into compact stowed configurations. As a result, they have matrix dominated properties that viscoelastically evolve in time and can result in deployable space structure designs with reduced deployment torque and deployed stiffness. In order to understand how to mitigate the effects of viscoelasticity in STEM designs, this dissertation explores how laminate stacking sequence and fiber orientation affect composite viscoelastic behavior and incorporates this knowledge in a method to model the performance of a particular biaxially stowed and then deployed STEM design.

To explore the effect that stacking sequence and fiber orientation have on viscoelastic behavior, tensile and four-point bend creep tests are performed on neat resin, unidirectional and plain weave lamina, and 3-ply [45PW/0/45PW] and 4-ply [0/45PW/45PW/0] laminate samples, all composed of the same epoxy resin and carbon fiber system. The results of the creep tests indicate that fibers placed in the load path, e.g., surface plies in composites under flexure loads or fibers in the direction of tensile loads, mitigate the viscoelastic creep and relaxation of the composites. The presence of elastic fibers also increases the stiffness of the

laminae and laminates and reduces the degree to which they creep. The proportional viscoelastic change in the transient properties of the neat resin, lamina, and laminate, e.g., percent strain change over time at fixed stress between the initial elastic response and the equilibrium response of the material, are compared to one another. The results from indicate that the viscoelastic behavior of the resin system composing the matrix of the laminae and laminates is unchanged by the presence of fibers.

An analytical model is developed to predict the viscoelastic behavior of a STEM after prolonged deformation in a state of biaxial bending, e.g., the stowed configuration. The model predicts the extent to which biaxial bending moments relax during the period of time a viscoelastic composite STEM is subjected to a state of constant biaxial bending curvature (i.e., stowage) and then predicts the resulting recovery curvature and moments after the stowed STEM is allowed to deploy. The predictions of the model for a one-dimensional beam in bending are shown to compare favorably to the predictions of validated one-dimensional beam models found in the literature.

Knowledge of a STEM's laminate flexural creep and relaxation properties is needed for the model to predict the biaxial bending curvature and moments of a STEM design. Since the available test data provides information on creep performance only, viscoelastic inversion methods are needed to obtain relaxation information. Several approaches are explored for converting the creep compliance and flexure properties that are ascertained by the tensile and four-point bending creep tests. A review of one-dimensional viscoelastic inversion methods such as Gutierrez-Lemini's exact method shows them not to be applicable for inversion of the multidimensional creep properties of the anisotropic laminae and laminates tested for this dissertation. To accomplish the task of inverting the creep data, a Laplace transform based

numerical method is developed for multidimensional viscoelastic materials. The creep properties for the neat resin, unidirectional and plain weave laminae, and 3-ply and 4-ply laminates are inverted using the Laplace transform based numerical inversion method. The flexure properties cannot be inverted because the axial/transverse flexure creep properties could not be measured by the four-point bend test method utilized. To acquire the relevant information, the inverted unidirectional and plain weave tensile creep properties are used as inputs for a viscoelastic version of classical laminate theory to predict the relaxation flexure properties of the unidirectional and plain weave laminae, and 3-ply and 4-ply laminates.

TABLE OF CONTENTS

Chapter 1 Introduction 1

1.1 Composite History 1
1.2 Composite Background 4
1.3 Viscoelasticity Background 11
1.4 Motivation and Outline 16

Chapter 2 Viscoelastic Response of Composites in Tension and Flexure 21

2.1 Introduction: Anisotropic Viscoelasticity of Composites 21
2.2 Background 22
2.3 Test Method 27
2.4 Results 34
2.5 Discussion 39
2.5.1 Unidirectional Laminae 48
2.5.2 Plain Weave Laminae 48
2.5.3 3-ply Laminate 49
2.5.4 4-ply Laminate 51
2.6 Conclusion 53

Chapter 3 Inversion of Anisotropic Viscoelastic Properties 54

3.1 Introduction 54
3.2 Background 56
3.3 Methods 60
3.3.1 Laplace Inversion—Schapery's Technique 60
3.3.2 Numerical Laplace Inversion 63
3.3.3 Numerical Laplace Inversion for Multidimensional Materials 66
3.3.4 Gutierrez-Lemini's Exact Inversion 70
3.4 Results 74
3.5 Discussion 79
3.6 Conclusion 82

Chapter 4 Relaxation Stiffness and Flexure Properties of the Neat Resin, Unidirectional and Plain Weave Laminae, and the 3-ply and 4-ply Laminates Predicted Using the Numerical Laplace Inversion Method and Viscoelastic Classical Laminate Theory 84

4.1 Introduction 84
4.2 Background 85
4.3 Results 87
4.4 Discussion 96
4.5 Conclusion 100

Chapter 5 Viscoelastic Behavior of a Biaxially Bent Composite Storable Tubular Extendable Member 102

5.1 Introduction 102
5.2 Background.....103
5.3 Methods 108
5.4 Results 117
5.5 Discussion.....127
5.6 Conclusion 129

Chapter 6 Concluding Remarks.....131

References 134

Appendix 140

TABLE OF FIGURES

Figure 1.1.1: Three example configurations of storable tubular extendable members (STEMs) [1]: (a) the stowed end of a STEM wrapped around a fixed drum that when rotated deploys the STEM into a long cylinder; (b) the reverse of (a) with the cylindrical end fixed and the stowed end wrapped around a drum unrolling to extend outwards; and (c) helical shaped STEM that extends outward as the stowed end rotates. *2*

Figure 1.1.2: Deployable Space Systems' solar array consists of two STEMs on either side of a blanket of solar cells. The strain energy from stowing the two STEMs is used to unroll and deploy the blanket of cells. As the STEMs unroll, they deploy into their tubular shape providing a stiff structure, supporting the blanket upon deployment. *3*

Figure 1.1.3: A STEM deploying from its stowed configuration (a) to its deployed configuration (d). (a) through (d) the STEM forms into a long cylinder as the stowed end of the STEM unrolls and extends outward. (b) and (c) the STEM transitions through a non-uniform curvature as it deforms from the stowed configuration (a) to the deployed configuration (d). *3*

Figure 1.2.1: A unidirectional reinforced lamina with 1, 2, and 3 axes in the fiber direction (axial), transverse fiber direction, and out-of-plane direction, respectively [14]. *5*

Figure 1.2.2: The coordinate system of a laminate is defined by x as the 0º axis of the laminate, y as the 90º axis of the laminate, and z as the out of plane axis. The origin lies at the midplane or reference plane of the laminate. The laminate consists of n laminae (plies) k = 1 through n each a distance $\bar{z}_k$ *from the laminate reference plane. Each lamina has a specified degree of rotation [14].* *6*

Figure 1.2.3: Cross-sectional view of a laminate with varying degrees of rotation of unidirectional laminae (plies) [14]. *7*

Figure 1.2.4: A laminate comprised of three laminae with varying Young's moduli is deformed by a strain variation as in equation (1.2.5), resulting in discontinuous stress variations in the laminate arising from equation (1.2.6) and consistent with classical lamination theory [15]. *8*

Figure 1.2.5: Laminate force and moment resultants on a single ply [14]. *9*

Figure 1.3.1: The creep compliance C(t) and relaxation stiffness M(t) of a composite viscoelastically changes as a function of time on a log scale. The glassy region defines the material's elastic response. The transient region defines the material's time-dependent deformation response. The equilibrium region defines the material's final stabilized deformation response [18]. *12*

Figure 1.3.2: Creep compliance master curve: (a) master curve formed from (b) short-term creep data measured at different temperatures that are shifted based on time-temperature superposition principles mathematically defined using an Arrhenius law [20]. *14*

Figure 2.2.1: The graph on the left depicts a constant stress applied at $t = 0$*. The graph on the right depicts the creep response of a material due to the applied stress. As* $t \to \infty$ *the material reaches equilibrium.* *26*

Figure 2.3.1: Unidirectional lamina loading configurations *28*

Figure 2.3.2: Plain weave laminate loading configurations. *29*

Figure 2.3.3: 3-Ply Laminate loading configurations. *29*

Figure 2.3.4: 4-Ply laminate loading configurations. *30*

Figure 2.3.5: Four-point bend test setup consisting of a thermal chamber, heater coil, fan, thermal data recorder, and thermal controller. Clamshell thermal chamber is supported around a four-point bend test fixture. *34*

Figure 2.4.1: The neat resin creep compliance test data conducted at four different constant temperatures are shifted on the time axis to create a creep compliance master curve. Creep compliance is normalized by the instantaneous (i.e., glassy) compliance of the initial creep test. A Prony series is fit to the data representing the master curve of the neat resin epoxy. *35*

Figure 2.4.2: The log10 of the shifted time coefficient obtained when generating the neat resin creep master curve from the compliance data measured at four different constant temperature tests are plotted verse the inverse of the corresponding test temperatures. A linear fit depicting the Arrhenius law (equation (1.3.5)) is used to obtain the viscoelastic activation energy. *35*

Figure 2.4.3: Linear viscoelasticity is determined by preforming a series of creep test at vary increments of applied constant stress. The top graph depicts three varying constant applied stresses; middle graphs depict the creep strain results due to the applied stresses; bottom graph depicts the stress/strain results at three different elapsed time intervals. The linearity of the stress/strain results at varying time intervals indicates that the material is linear viscoelastic [16]. *38*

Figure 2.4.4: The creep stress/strain results for neat resin tensile samples due to three different constant applied stresses are plotted. Tests are performed at the maximum constant test temperature (~80°C). The stress/strain results at 1 sec., 10 sec., 100 sec., and 1000 sec. are identified in the graph. Linear fits indicate that the neat resin samples, in the applied stress and temperature range studied, exhibit linear viscoelasticity. *39*

Figure 2.5.1: The normalized Prony series master curve fits to the measured axial creep compliance data for the neat resin, unidirectional, plain weave, 3-ply and 4-ply laminates are complied in a single graph. *42*

Figure 2.5.2: The normalized Prony series master curve fits to the measured axial/transverse creep compliance data for the neat resin, unidirectional, plain weave, 3-ply and 4-ply laminates are complied in a single graph. *42*

Figure 2.5.3: The normalized Prony series master curve fits to the measured transverse creep compliance data for the neat resin, unidirectional, plain weave, 3-ply and 4-ply laminates are complied in a single graph. *43*

Figure 2.5.4: The normalized Prony series master curve fits to the measured axial creep flexure data for the neat resin, unidirectional, plain weave, 3-ply and 4-ply laminates are complied in a single graph. *43*

Figure 2.5.5: The normalized Prony series master curve fits to the measured transverse creep flexure data for the neat resin, unidirectional, plain weave, 3-ply and 4-ply laminates are complied in a single graph. *44*

Figure 2.5.6: The transient proportional response of the measured axial creep compliance data for the neat resin, unidirectional, plain weave, 3-ply and 4-ply laminates are recored in a single graph. *45*

Figure 2.5.7: The transient proportional response of the measured axial/transverse creep compliance data for the neat resin, unidirectional, plain weave, 3-ply and 4-ply laminates are recorded in a single graph. *46*

Figure 2.5.8: The transient proportional response of the measured transverse creep compliance data for the neat resin, unidirectional, plain weave, 3-ply and 4-ply laminates are recorded in a single graph. *46*

Figure 2.5.9: The transient proportional response of the measured axial creep flexure data for the neat resin, unidirectional, plain weave, 3-ply and 4-ply laminates are recorded in a single graph. *47*

Figure 2.5.10: The transient proportional response of the measured transverse creep flexure data for the neat resin, unidirectional, plain weave, 3-ply and 4-ply laminates are recorded in a single graph. *47*

Figure 3.2.1: Left graph depicts a step response in applied stress. The right graph depicts the resulting creep response of a material to the constant stress depicted in the left graph. *57*

Figure 3.2.2: Left graph depicts a step response in applied strain. The right graph depicts the relaxation response of a material to the constant strain depicted in the left graph. *58*

Figure 3.3.1: The graph depicts the linearly inverted Laplace Neat Resin Creep data from (3.3.11) fitted with an assumed relaxation Laplace function (3.3.5b) over the negative frequency domain plotted on a log-log of the absolute value of $M(s)$ *vs. the absolute value of* s. *65*

Figure 3.3.2: The figure is a magnified portion of Figure 3.3.1, spanning one Prony constant inflection point. The upward vertical spike is a result of the limit of the denominator of the linearly inverted Laplace creep data (3.3.14) approaching infinity as s *approaches* $-\alpha^i$. *The downward spike is a result of the numerator of the linearly inverted Laplace creep data (3.3.13) approaching zero as* s *approaches* $-\beta^i$. *The upward spikes can be used to obtain the values of the unknown relaxation Prony time constants* α^i *66*

Figure 3.3.3: The Laplace numerical inversion of the unidirectional carbon fiber lamina creep compliance properties resulting in the relaxation modulus, M_{11}, M_{12}, *and* M_{22} *are plotted over the absolute value of the negative frequency domain on a log-log scale.* *69*

Figure 3.3.4: A magnified view of Figure 3.3.3 spans one of the zero/infinite spikes. The known relaxation properties are defined by a black-dotted line. The fitted relaxation properties are defined by a red-dashed line. *70*

Figure 3.4.1: The relaxation modulus properties, $M(t)$ (equation (3.2.5b)) with Prony series coefficients recorded in Table 3.4.2 which are obtained from inverting the creep compliance properties presented in Table 3.4.1 are plotted on a log10 time scale. The results of Schapery's least square method, the numerical method, and Gutierrez-Lemini's exact method are normalized using their corresponding glassy response, M^g. The exact method and numerical method produce the same solution resulting in both lines in the graph lying on top of one another. *76*

Figure 3.4.2: The log10 scaled time domain of the inverted creep compliance properties with Prony coefficients recorded in Table 3.4.4 are presented for both the numerical method and Schapery's least-squares inversion method. The relaxation modulus properties, $M(t)$ (equation (3.2.5b), are normalized by the glassy response, M^g, of the corresponding modulus component and inversion method. Both methods produce nearly identical solutions resulting in the lines of the graphs lying on top of one another. *78*

Figure 4.2.1: The lamina and laminate samples tested in Chapter 2 are illustrated graphically. The plies composing the laminates are oriented with respect to the x-axis. *87*

Figure 4.3.1: The relaxation axial stiffness master curves, $Q_{xx}(t)$, for the unidirectional and plain weave laminae, and 3-ply and 4-ply laminates are normalized by their respective glassy response, Q_{xx}^g. The relaxation master curves are obtained by inverting the measured creep compliance properties recorded in Chapter 2 using the numerical inversion method developed in Chapter 3. The solid blue line represents the inverted neat resin, the short dashed-dotted green line represents the unidirectional lamina, the long dashed-dotted red line represents the plain weave lamina, the short dashed light blue line represents the 3-ply laminate, and the long dashed orange line represents the 4-ply laminate. *88*

Figure 4.3.2: The relaxation axial/transverse stiffness master curves, $Q_{xy}(t)$, for the unidirectional and plain weave laminae, and 3-ply and 4-ply laminates are normalized by their respective glassy response, Q_{xy}^g. The relaxation master curves are obtained by inverting the measured creep compliance properties recorded in Chapter 2 using the numerical inversion method developed in Chapter 3. The solid blue line represents the inverted neat resin, the short dashed-dotted green line represents the unidirectional lamina, the long dashed-dotted red line represents the plain weave lamina, the short dashed light blue line represents the 3-ply laminate, and the long dashed orange line represents the 4-ply laminate. *88*

Figure 4.3.3: The relaxation transverse stiffness master curves, $Q_{yy}(t)$, for the unidirectional and plain weave laminae, and 3-ply and 4-ply laminates are normalized by their respective glassy response, Q_{yy}^g. The relaxation master curves are obtained by inverting the measured creep compliance properties recorded in Chapter 2 using the numerical inversion method developed in Chapter 3. The solid blue line represents the inverted neat resin, the short dashed-dotted green line represents the unidirectional lamina, the long dashed-dotted red line represents the plain weave lamina, the short dashed light blue line represents the 3-ply laminate, and the long dashed orange line represents the 4-ply laminate. *89*

Figure 4.3.4: The relaxation axial flexure stiffness $D_{xx}(t)$ for the neat resin, unidirectional and plain weave lamina, and 3-ply and 4-ply laminates are normalized by their respective

glassy response, D_{xx}^{g}. The relaxation flexure stiffnesses are predicted by the viscoelastic CLT. The solid blue line represents the inverted neat resin, the short dashed-dotted green line represents the unidirectional lamina, the long dashed-dotted red line represents the plain weave lamina, the short dashed light blue line represents the 3-ply laminate, and the long dashed orange line represents the 4-ply laminate.....90

Figure 1.1.1: The relaxation axial/transverse flexure stiffness $D_{xy}(t)$ for the neat resin, unidirectional and plain weave lamina, and 3-ply and 4-ply laminates are normalized by their respective glassy response, D_{xy}^{g}. The relaxation flexure stiffnesses are predicted by the viscoelastic CLT. The solid blue line represents the inverted neat resin, the short dashed-dotted green line represents the unidirectional lamina, the long dashed-dotted red line represents the plain weave lamina, the short dashed light blue line represents the 3-ply laminate, and the long dashed orange line represents the 4-ply laminate.....91

Figure 4.3.6: The relaxation transverse flexure stiffness $D_{yy}(t)$ for the neat resin, unidirectional and plain weave lamina, and 3-ply and 4-ply laminates are normalized by their respective glassy response, D_{yy}^{g}. The relaxation flexure stiffnesses are predicted by the viscoelastic CLT. The solid blue line represents the inverted neat resin, the short dashed-dotted green line represents the unidirectional lamina, the long dashed-dotted red line represents the plain weave lamina, the short dashed light blue line represents the 3-ply laminate, and the long dashed orange line represents the 4-ply laminate.....91

Figure 4.3.7: The measured and inverted CLT axial creep compliance master curves, $S_{xx}(t)$, for the 3-ply and 4-ply laminates are normalized by their respective properties. The measured axial creep compliance for the 3-ply laminate represented by the dashed light blue line and the predicted creep compliance is represented by the dashed-dotted blue line. The measured axial creep compliance for the 4-ply laminate is represented by the long dashed orange line and the predicted creep compliance is represented by the long dashed-dotted red line. 93

Figure 4.3.8: The measured and inverted CLT axial/transverse creep compliance master curves, $S_{xy}(t)$, for the 3-ply and 4-ply laminates are normalized by their respective glassy properties. The measured axial/transverse creep compliance for the 3-ply laminate represented by the dashed light blue line and the predicted creep compliance is represented by the dashed-dotted blue line. The measured axial/transverse creep compliance for the 4-ply laminate is represented by the long dashed orange line and the predicted creep compliance is represented by the long dashed-dotted red line. 93

Figure 4.3.9: The measured and inverted CLT transverse creep compliance master curves, $S_{yy}(t)$, for the 3-ply and 4-ply laminates are normalized by their respective glassy properties. The measured transverse creep compliance for the 3-ply laminate represented by the dashed light blue line and the predicted creep compliance is represented by the dashed-dotted blue line. The measured transverse creep compliance for the 4-ply laminate is represented by the long dashed orange line and the predicted creep compliance is represented by the long dashed-dotted red line. 94

Figure 4.3.10: The measured and inverted CLT axial creep flexure master curves, $dxxt$, for the 3-ply and 4-ply laminates are normalized by their respective glassy properties. The measured axial creep flexure for the 3-ply laminate represented by the dashed light blue line

and the predicted creep flexure is represented by the dashed-dotted blue line. The measured axial creep flexure for the 4-ply laminate is represented by the long dashed orange line and the predicted creep flexure is represented by the long dashed/dotted red line. 94

Figure 4.3.11: The measured and inverted CLT transverse creep flexure master curves, $d_{yy}(t)$, for the 3-ply and 4-ply laminates are normalized by their respective glassy properties. The measured transverse creep flexure for the 3-ply laminate represented by the dashed light blue line and the predicted creep flexure is represented by the dashed-dotted blue line. The measured transverse creep flexure for the 4-ply laminate is represented by the long dashed orange line and the predicted creep flexure is represented by the long dashed-dotted red line. 95

Figure 5.2.1: The viscoelastic curvature (a) and bending moment (b) for a one-dimensional beam in pure bending. A constant curvature is imposed during $0 \leq t < t_o$, resulting in a bending moment that relaxes. At $t = t_o$ the imposed constant curvature is quickly released and the bending moment reduces to zero. As a result of relaxation, the released curvature is nonzero. However, as time progresses $t > t_o$ the curvature recovers viscoelastically to zero, due to the slow rearranging of the polymer chains of the neat resin matrix to a minimum potential energy state (e.g., the beam's undeformed, unstressed state). 108

Figure 5.3.1: A segment of a STEM in its deployed (a), flattened (c), and biaxial stowed configuration (c). The STEM is longer than shown in the z-direction as only a segment is illustrated. In the stowed configuration, the STEM is rolled up around the x-axis in a coil. The stowed curvature $\Delta K_{zz} = 1/r_2$ (c) is selected such that micro buckling in the laminate does not occur. The other principal curvature $\Delta K_{xx} = 1/r_1$ is determined by the deployed state (a), which must be flattened to stow the STEM. 110

Figure 5.3.2: The biaxial curvature and bending moment histories of a viscoelastic STEM. The curvatures are shown in illustrations (a) and (c) and the bending moments in illustrations (b) and (d). Illustrations (a) and (b) show the axial curvature and bending moment while illustration (c) and (d) show the transverse curvature and bending moment. Biaxial curvatures are applied at $t = 0$ to stow the STEM and are released at $t = t_o$ to deploy the STEM. The STEM recovers during $t > t_o$ to its original undeformed, unstressed, deployed state 112

Figure 5.4.1: The histories of one-dimensional bending moment (a) and bending curvature (b) are shown for a one-dimensional beam in bending composed of a viscoelastic material. The relaxation and creep flexure properties represented by Prony series constants are given in Table 5.4.1 and Table 5.4.2, respectively. The dashed blue line is the solution from the one-dimensional beam bending equations developed in this chapter based on the solutions of the hereditary integrals found in the literature [16], [18], [20], [49]. *The orange solid line presents the numerical solution from the biaxial bend model developed in this chapter but reduced to one-dimensional bending. 119*

Figure 1.1.2: The bending curvature and moment histories obtained using the numerical method developed in Chapter 5 are graphed for a viscoelastic STEM in a state of biaxial bending. (a) illustrates the axial curvature, (b) the axial moment, (c) the transverse curvature, and (d) the transverse moment histories of a STEM composed of a 3-ply composite [45º PW/0º Uni/45º PW] with viscoelastic flexure properties recorded in Table 5.4.4. The

STEM is subjected to biaxial bending during stowage $0 \leq t < t_o$*, then deployed at* $t_o = 100{,}000{,}000\ sec\ (\sim 3.17\ years)$*, and lastly allowed to recover to a zero-stress state over time* $t > t_o$*.* *123*

Figure 1.1.3: A magnified view of Figure 5.4.2 (b) depicts the axial moment in the 3-ply composite STEM due to a nonzero transverse curvature at the onset of deployment at $t = t_o$ *after prolonged stowage during* $0 \leq t < t_o$*. The viscoelastic properties of the 3-ply laminate used to form the STEM are modest, and as a result, the axial moment on deployment is small.* *123*

Figure 5.4.4: The bending curvature and moment histories obtained using the numerical method developed in Chapter 5 are graphed for a viscoelastic STEM in a state of biaxial bending. (a) illustrates the axial curvature, (b) the axial moment, (c) the transverse curvature, and (d) the transverse moment histories of a STEM composed of a 4-ply composite [0º Uni/45º PW/45º PW/0º Uni] with viscoelastic flexure properties recorded in Table (5.4.6). The STEM is subjected to biaxial bending during stowage $0 \leq t < t_o$*, then deployed at* $t_o = 100{,}000{,}000\ sec\ (\sim 3.17\ years)$*, and lastly allowed to recover to a zero-stress state over time* $t > t_o$*.* *125*

Figure 5.4.5: A magnified view of Figure 5.4.4 (b) depicts the axial moment in the 4-ply composite STEM due to a nonzero transverse curvature at the onset of deployment at $t = t_o$ *after prolonged stowage during* $0 \leq t < t_o$*. The viscoelastic properties of the 4-ply laminate used to form the STEM are modest, and as a result, the axial moment on deployment is small.* *125*

Figure A.1: The master curves for the unidirectional laminate axial compliance (top graph), axial/transverse coupling compliance (middle graph), and transverse compliance (bottom graph) obtained from tensile test data. Tests are conducted at four different constant temperature tests for each material property. The axial and axial/transverse coupling compliance are elastic with a mean value that is constant in time. The transverse compliance is viscoelastic. A master curve is formed by shifting the data gathered at the four different temperatures on the time axis to create a creep compliance master curve. The creep compliance properties are normalized by the respective instantaneous (i.e., glassy) compliance of the initial creep test. A Prony series is fitted to the transverse creep compliance data representing the master curve. *142*

Figure A.2: The master curves for the unidirectional laminate axial flexure (top graph) and transverse flexure (bottom graph) obtained from four-point-bend test data. Four different constant temperature tests are conducted for each material property. The laminate behaves elastically in axial flexure. The transverse flexure response is viscoelastic. A master curve is formed by shifting the four temperature data sets along the time axis to create a creep flexure master curve. The creep flexure properties are normalized by the respective instantaneous (i.e., glassy) flexure of the initial creep test. A Prony series is fitted to the transverse creep flexure data representing the master curve. *143*

Figure A.3: The master curves for the plain weave laminate axial compliance (top graph) and axial/transverse coupling compliance (bottom graph) obtained from tensile test data. Tests at four different constant temperatures are conducted for each material property. The axial and axial/transverse coupling compliance are viscoelastic. The master curves of the respective properties are formed by shifting the four temperature data sets on the time axis.

The creep compliance properties are normalized by the respective instantaneous (i.e., glassy) compliance of the initial creep test comprising the master curve. A Prony series is fitted to the creep compliance data representing the master curve axial and axial/transverse coupling properties. *145*

Figure A.4: The master curve for the plain weave laminate axial flexure obtained from four-point-bend test data. Four different constant temperature tests are conducted for each material property. The response in axial flexure is viscoelastic. The master curves of this property are formed by shifting the four temperature data sets along the time axis. The creep flexure property is normalized by the instantaneous (i.e., glassy) flexure of the initial thermal test. A Prony series is fitted to the creep flexure data to form the master curve for the axial property. *146*

Figure A.5: The master curves for the 3-Ply laminate axial compliance (top graph), axial/transverse coupling compliance (middle graph), and transverse compliance (bottom graph) obtained from tensile test data. Tests at four different constant temperatures are conducted for each material property. The axial, axial/transverse coupling, and transverse compliance show some degree of viscoelasticity. The master curves of the respective properties are formed by shifting the four constant temperature data sets along the time axis. The creep compliance properties are normalized by the respective instantaneous (i.e., glassy) compliance of the initial creep test. A Prony series is fitted to the creep compliance data representing the master curve axial, axial/transverse coupling, and transverse properties. *148*

Figure A.6: The master curves for the 3-Ply laminate axial flexure (top graph) and transverse flexure (bottom graph) obtained from four-point-bend test data. Four constant temperature tests are conducted for each material property. The axial and transverse flexure properties are viscoelastic. A master curve is formed by shifting the data from the tests at the four different temperatures on the time axis to create a creep flexure master curve. The creep flexure properties are normalized by the respective instantaneous (i.e., glassy) flexure from the initial creep test. A Prony series is fitted to both the axial and transverse creep flexure data representing the master curve. *149*

Figure A.7: The master curves for the 4-Ply laminate axial compliance (top graph), axial/transverse coupling compliance (middle graph), and transverse compliance (bottom graph) obtained from tensile test data. Tests are conducted at four different constant temperatures for each material property. The axial, axial/transverse coupling, and transverse compliance show some degree of viscoelasticity. The master curves of the respective properties are formed by shifting the four constant temperature data sets along the time axis. The creep compliance properties are normalized by the respective instantaneous (i.e., glassy) compliance of the initial creep test. A Prony series is fitted to the creep compliance data representing the master curve axial, axial/transverse coupling, and transverse properties. *151*

Figure A.8: The master curves for the 4-ply laminate axial flexure (top graph) and transverse flexure (bottom graph) obtained from the four-point-bend test data. Four constant temperature tests are conducted for each material property. The axial and transverse flexure is viscoelastic. A master curve is formed by shifting the four temperature data sets along the time axis to create a creep flexure master curve. The creep flexure properties are nominalized by the respective instantaneous (i.e., glassy) flexure of the initial creep test. A

Prony series is fitted to both the axial and transverse creep flexure data representing the master curve. 152

LIST OF TABLES

Table 3.4.1: The one-dimensional creep compliance properties obtained from a neat resin tensile creep test at 30^0C are recorded in Dirichlet-Prony series form. 75

Table 3.4.2: The neat resin relaxation modulus are obtained by inverting the measured neat resin compliance properties (Table 3.4.1) using Schapery's least squares method, the numerical method, and Gutierrez-Lemini's exact method. Properties are recorded in Dirichlet-Prony series form. Percent differences in the Prony time constants are also presented. 76

Table 3.4.3: Creep compliance Dirichlet-Prony series properties for a unidirectional carbon fiber/epoxy lamina. 77

Table 3.4.4: The unidirectional relaxation modulus are obtained by inverting the measured unidirectional creep compliance properties (Table 3.4.3) using the numerical method and Schapery's least-squares method. 77

Table 4.3.1: The creep compliance and creep flexure glassy properties for the 3-ply laminate obtained from both measured and inverted CLT predicted data. The table records the percent error between the respective measured and predicted properties. The measured and adjusted laminate thicknesses are also recorded. 95

Table 4.3.2: The creep compliance and creep flexure glassy properties for the 4-ply laminate obtained from both measured and invertedd CLT predicted data. The table records the percent error between the respective measured and predicted properties. The measured and adjusted laminate thicknesses are also recorded. 96

Table 5.4.1: The Prony series coefficient are recorded for the relaxation flexure properties $D(t)$ of the isotropic, one-dimensional, neat resin epoxy. The table lists the relaxation flexure properties starting with the equilibrium parameter D^e, followed by thirteen Prony series coefficients D^m and their respective time constants α^m where m = 1 through 13. The Prony coefficients have units of N-mm and the time constants have units of sec^{-1}. 120

Table 5.4.2: The Prony series coefficient are recorded for the creep flexure properties $d(t)$ of the isotropic, one-dimensional, neat resin epoxy. The table lists the creep flexure properties starting with the equilibrium parameter d^e, followed by thirteen Prony series coefficients d^m and their respective time constants β^m where m = 1 through 13. The Prony coefficients have units of N-mm^{-1} and the time constants have units of sec^{-1}. 120

Table 5.4.3: The numerically predicted Prony series coefficients, ΔK^l and λ^l estimating the recovery response $\Delta K(t)$ defined in equation (5.3.16) are recorded for a neat resin, one-dimensional beam in bending. The one-dimensional curvature ΔK^o is initially imposed and then released at $t_o = 100{,}000{,}000\ sec$. A series of thirteen coefficients are listed with l = 1 through 13. All curvature properties have units of mm^{-1} and the Prony series time coefficients have units of sec^{-1}. 121

Table 5.4.4: The 3-ply composite [45° PW/0° Uni/45° PW] relaxation flexure properties recorded in Chapter 4. The Prony series coefficients are used to define the axial $D_{zz}(t)$, transverse/axial $D_{zx}(t)$, and transverse $D_{xx}(t)$ flexure properties in the curvature equations (5.3.1) and (5.3.8), and bending moment equations (5.3.13) and (5.3.15) developed in

Chapter 5 for a STEM in a state of biaxial bending. The table lists the relaxation flexure Prony coefficients starting with the equilibrium parameters D_{ij}^{e} in which i, j = x or z followed by the Prony series coefficients D_{ij}^{m} where m = 1 through 13. The respective Prony series time constants α^{i} are also listed. The Prony coefficients have units of N-mm and the time constants have units of sec^{-1}. 124

Table 5.4.5: The numerically predicted Prony series coefficients, ΔK_{xx}^{l} and λ^{l}, estimating the transverse recovery response $\Delta K_{xx}(t)$ defined in equation (5.3.8) are recorded for the 3-ply composite STEM in biaxial bending. The biaxial curvatures ΔK_{zz}^{o} and ΔK_{xx}^{o} are initially imposed at $t = 0$ on the 3-ply composite STEM and then released at $t_o = 100{,}000{,}000\ sec$. A series of thirteen Prony coefficients listed with l = 1 through 13 are used to define the transverse recovery curvature of the STEM. All curvature properties have units of mm^{-1}. Prony series time coefficients have units of sec^{-1}. 124

Table 5.4.6: The 4-ply composite [0^{o} Uni/45^{o} PW/45^{o} PW/0^{o} Uni] relaxation flexure properties recorded in Chapter 4. The Prony series coefficients are used to define the axial $D_{zz}(t)$, transverse/axial $D_{zx}(t)$, and transverse $D_{xx}(t)$ flexure properties in the curvature equations (5.3.1) and (5.3.8), and bending moment equations (5.3.13) and (5.3.15) developed in Chapter 5 for a STEM in a state of biaxial bending. The table lists the relaxation flexure Prony coefficients starting with the equilibrium parameters D_{ij}^{e} in which i, j = x or z followed by the Prony series coefficients D_{ij}^{m} where m = 1 through 13. The respective Prony series time constants α^{i} are also listed. The Prony coefficients have units of N-mm and the time constants have units of sec^{-1}. 126

Table 5.4.7: The numerically predicted Prony series coefficients, ΔK_{xx}^{l} and λ^{l}, estimating the transverse recovery response $\Delta K_{xx}(t)$ defined in equation (5.3.8) are recorded for the 4-ply composite STEM in biaxial bending. The biaxial curvatures ΔK_{zz}^{o} and ΔK_{xx}^{o} are initially imposed at $t = 0$ on the 4-ply composite STEM and then released at $t_o = 100{,}000{,}000\ sec$. A series of thirteen Prony coefficients listed with l = 1 through 13 are used to define the transverse recovery curvature of the STEM. All curvature properties have units of mm^{-1}. Prony series time coefficients have units of sec^{-1}. 126

Table A.1: Neat resin master curve Prony series constants and Arrhenius law activation energy from measured data. 141

Table A.2: The Prony time constants representing the creep compliance and flexure master curves of the unidirectional laminate. The table also records the Arrhenius law activation energies used to form the master curves from test data at varying constant temperatures. 144

Table A.3: The Prony time constants representing the creep compliance and flexure master curves of the plain weave laminate. The table also records the Arrhenius law activation energies used to form the master curves from test data at varying constant temperatures. 147

Table A.4: The Prony time constant representing the creep compliance and flexure master curves of the 3-ply laminate. The table also records the Arrhenius law activation energies used to form the master curves from test data at varying constant temperatures..... 150

Table A.5: The Prony time constant representing the creep compliance and flexure master curves of the 4-ply laminate. The table also records the Arrhenius law activation energies used to form the master curves from test data at varying constant temperatures..... 153

Table A.6: The neat resin Prony series constants representing the relaxation stiffness master curve properties inverted from measured creep compliance data using the Laplace numerical inversion method developed in Chapter 3. 154

Table A.7: The unidirectional lamina Prony series constants representing the relaxation stiffness master curve properties inverted from measured creep compliance data using the Laplace numerical inversion method developed in Chapter 3. The table also records the relaxation flexure stiffness Prony series constants predicted using viscoelastic classical laminate theory (CLT) with the unidirectional lamina inverted relaxation stiffness as an input. 155

Table A.8: The plain weave lamina Prony series constants representing the relaxation stiffness master curve properties inverted from measured creep compliance data using the Laplace numerical inversion method developed in Chapter 3. The table also records the relaxation flexure stiffness Prony series constants predicted using viscoelastic classical laminate theory (CLT) with the plain weave lamina inverted relaxation stiffness as an input. 156

Table A.9: The 3-ply laminate Prony series constants representing the relaxation stiffness master curve properties inverted from measured creep compliance data using the Laplace numerical inversion method developed in Chapter 3. The table also records the relaxation flexure stiffness Prony series constants predicted using viscoelastic classical laminate theory (CLT) with the unidirectional lamina and plain weave lamina inverted relaxation stiffness as inputs. 157

Table A.10: The 4-ply laminate Prony series constants representing the relaxation stiffness master curve properties inverted from measured creep compliance data using the Laplace numerical inversion method developed in Chapter 3. The table also records the relaxation flexure stiffness Prony series constants predicted using viscoelastic classical laminate theory (CLT) with the unidirectional lamina and plain weave lamina inverted relaxation stiffness as inputs. 158

Chapter 1

Introduction

1.1 Composite History

Composites are versatile materials utilized in a broad range of applications. They are lightweight, strong, and can be molded into an endless variety of shapes and sizes. Storable Tubular Extendable Members (STEMs) are one application where composites are being used. STEMs are long slit cylindrical tubes that are flattened and rolled longitudinally into a compact stowed configuration. They have been used in various applications since the 1960s [1]. These applications range from passive springs, such as hinges, to motor-driven telescoping antennae [2]. The versatility and compact storage configuration of STEMs make them ideal for use as deployable structures. Figure 1.1.1 illustrates a few STEM deployment configurations. Figure 1.1.1(a) shows a STEM with the stowed end wrapped around a fixed drum that rotates to deploy the STEM into a long cylindrical shape. Figure 1.1.1(b) illustrates the reverse of Figure 1.1.1(a) where the long cylindrical end of the STEM is fixed, and the stowed end wrapped around a drum deploys as it is unrolled. Figure 1.1.1(c) shows a long helical shaped STEM deployed outward by the rotation of the rolled base of the STEM.

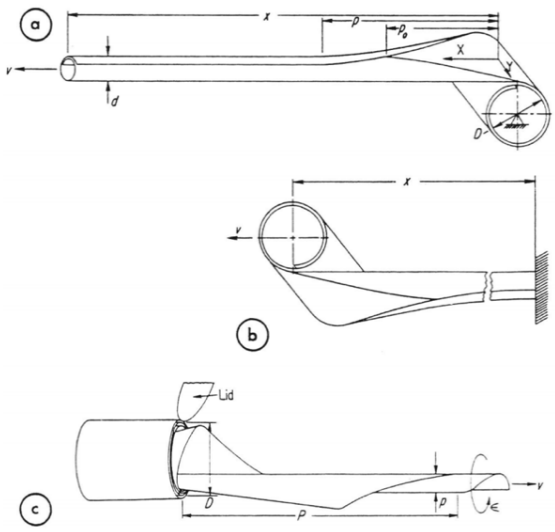

Figure 1.1.1: Three example configurations of storable tubular extendable members (STEMs) [1]: (a) the stowed end of a STEM wrapped around a fixed drum that when rotated deploys the STEM into a long cylinder; (b) the reverse of (a) with the cylindrical end fixed and the stowed end wrapped around a drum unrolling to extend outwards; and (c) helical shaped STEM that extends outward as the stowed end rotates.

Historically, STEMs have been manufactured from metallic materials, but in the past decade, the fabrication of STEMs from composite materials has become more prevalent [3]–[6]. Deployable Space Systems (DSS) is one of many companies implementing composite STEMs to deploy various structures for space applications [7]. DSS's design utilizes the high stowed strain energy and high strength to weight ratio of a pair of composite STEMs to deploy a blanket of solar arrays, as illustrated in Figure 1.1.2. This is a working application of the STEM configuration illustrated in Figure 1.1.1(b). Figure 1.1.3 illustrates the deployment of a STEM in more detail where (a) shows the STEM in a stowed biaxial state of bending. Figure 1.1.3(b) and (c) illustrates the stowed end of the STEM unrolling and deploying outward while the stored strain energy is released as the fixed end springs back into its original cylindrical tubular configuration. During the deployment stage illustrated in Figure 1.1.3(b) and (c), the STEM transitions through a non-uniform curvature as it unrolls from the stowed to the deployed configuration. Figure 1.1.3(d) illustrates the STEM's final deployed configuration, where it forms a stiff, nearly cylindrical-shaped beam.

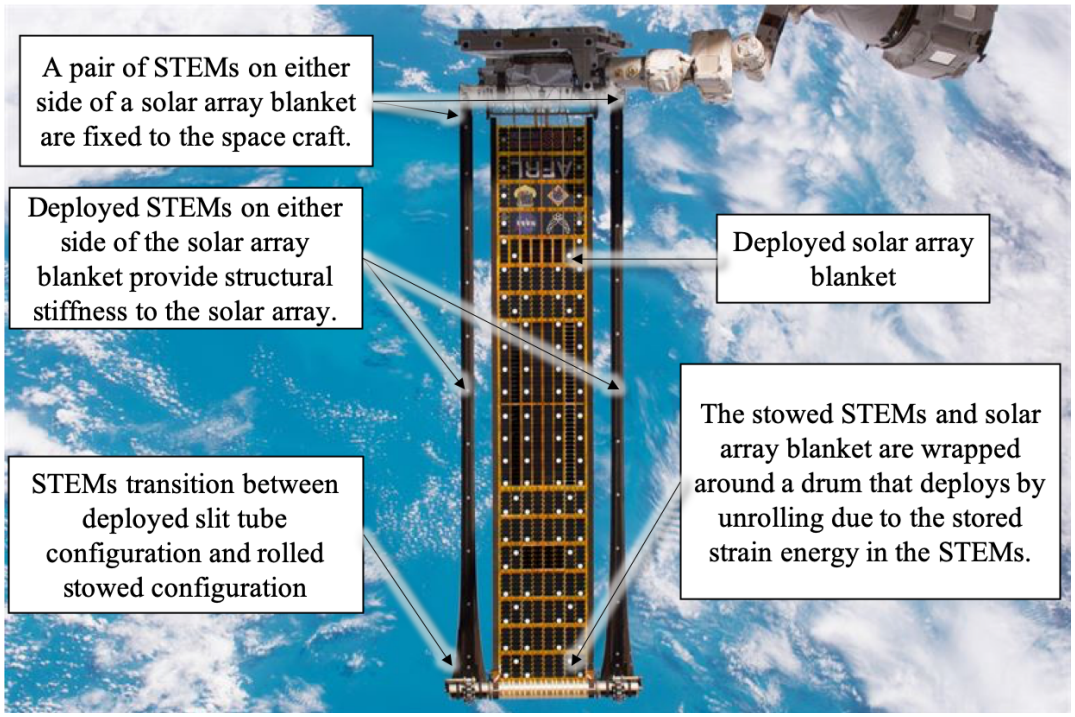

Figure 1.1.2: Deployable Space Systems' solar array consists of two STEMs on either side of a blanket of solar cells. The strain energy from stowing the two STEMs is used to unroll and deploy the blanket of cells. As the STEMs unroll, they deploy into their tubular shape providing a stiff structure, supporting the blanket upon deployment.

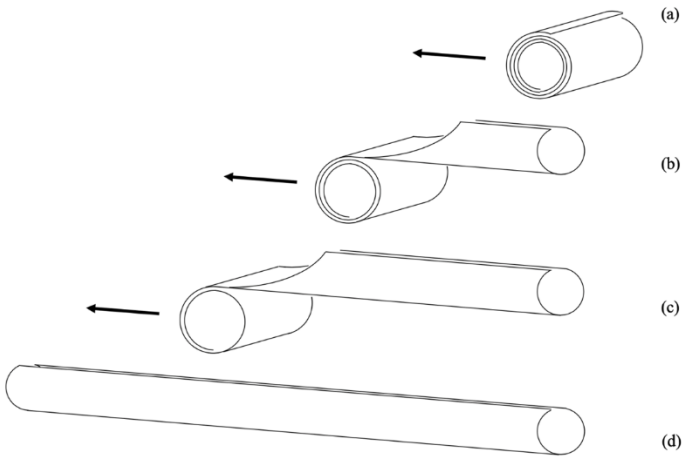

Figure 1.1.3: A STEM deploying from its stowed configuration (a) to its deployed configuration (d). (a) through (d) the STEM forms into a long cylinder as the stowed end of the STEM unrolls and extends outward. (b) and (c) the STEM transitions through a non-uniform curvature as it deforms from the stowed configuration (a) to the deployed configuration (d).

Composite STEMs are commonly composed of continuous carbon fiber laminae with a polymer resin matrix. The fibers of the composite provide stiffness and strength, especially along the orientation of the fibers, while the resin binds the fibers in place, allowing the

composite to be molded into the tubular shape of a STEM. The laminate layups of STEMs are constructed from a stacked set of laminae comprised of either unidirectional continuous fiber strands (Uni) or plain weave continuous fiber mats (PW). High stowed bending strains in STEMs can cause laminates to micro buckle and delaminate [8]. To eliminate high strains, laminate layups must remain thin, limiting the number of plies to as few as two and, typically, to not more than four. As a consequence, the options of ply orientation and stacking sequence for such thin laminates makes it impossible to align elastic fibers in all loading directions. This results in some directions and modes of deformation in the composite being matrix dominated, such as the transverse direction and the shear properties, and, consequently, they often exhibit significant viscoelasticity as the polymer matrix relaxes [9], [10]. In contrast, fiber dominated directions and modes of deformation exhibit limited, transient viscoelasticity. The net viscoelasticity of the system can be detrimental to the deployment states of a STEM. Relaxation in the strain energy of a composite STEM may result in its failure to deploy due to loss in deployment toque. In addition, reduction in the material's modulus due to viscoelastic effects may compromise the STEM's deployed stiffness.

1.2 Composite Background

The viscoelasticity present in composites is a direct result of the neat resin (matrix), which binds the purely elastic fibers in place. In the case of a unidirectionally reinforced lamina, the axial extension properties are fiber dominated and essentially elastic. However, the transverse response– both extension and shear– and the longitudinal shear properties are all matrix dominated and are time-dependent [11], [12]. The fundamental theories and system of equations used to define elastic composites [13] are the stepping off points for discussing

composite viscoelasticity. Figure 1.2.1 depicts a unidirectional reinforced lamina with a coordinate system in which the axial (fiber direction), transverse, and out of plane directions are the 1, 2, and 3 axes respectively. Lamina properties are best represented using classical laminate theory (CLT). The elastic reduced stiffness matrix, Q, represents the elastic plane stress state of a lamina in contracted notation [14]. The relationship between Voigt notation and double subscript notation is

$$\sigma_{11} = \sigma_1; \quad \sigma_{22} = \sigma_2; \quad \sigma_{33} = \sigma_3;$$
$$\sigma_{23} = \tau_4; \quad \sigma_{31} = \tau_5; \quad \sigma_{12} = \tau_6 \tag{1.2.1a}$$
$$\varepsilon_{11} = \varepsilon_1; \quad \varepsilon_{22} = \varepsilon_2; \quad \varepsilon_{33} = \varepsilon_3;$$
$$2\varepsilon_{23} = \gamma_{23} = \gamma_4; \quad 2\varepsilon_{31} = \gamma_{31} = \gamma_5; \quad 2\varepsilon_{12} = \gamma_{12} = \gamma_6 \tag{1.2.1b}$$

$$\sigma_i = Q_{ij}\varepsilon_j \qquad (i,j = 1,2,6) \tag{1.2.2}$$

in which $\sigma_3 = 0$, $\tau_4 = 0$, and $\tau_5 = 0$. The inverse relationship (elastic compliance) of equation (1.2.2) is written as

$$\varepsilon_i = S_{ij}\sigma_j \qquad (i,j = 1,2,6) \tag{1.2.3}$$

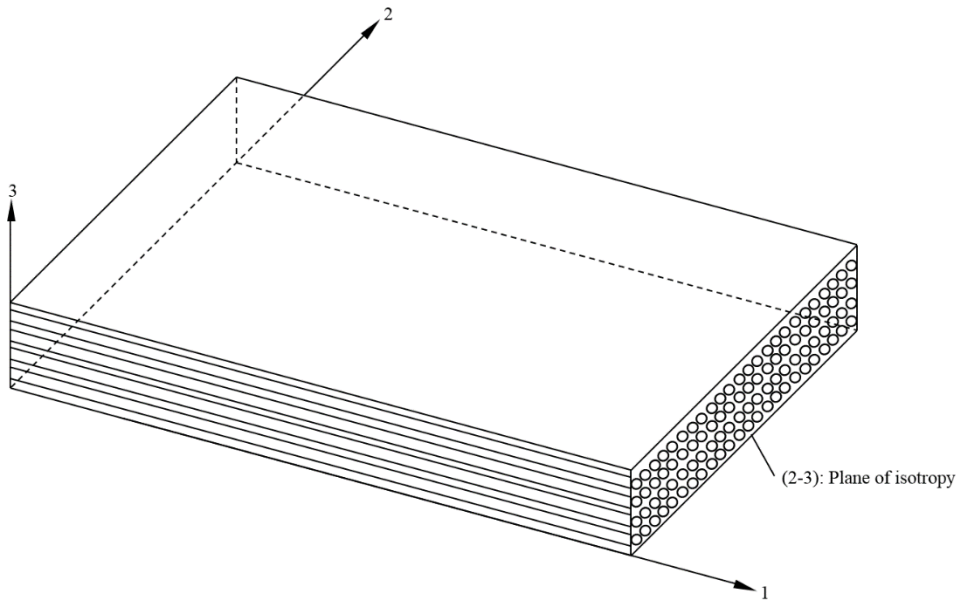

Figure 1.2.1: A unidirectional reinforced lamina with 1, 2, and 3 axes in the fiber direction (axial), transverse fiber direction, and out-of-plane direction, respectively [14].

Unidirectional (continuous fiber) lamina experiences little to no viscoelasticity in the axial (fiber) direction due to the fibers' resistance to creep and their high modulus in comparison to that of the neat resin. The transverse and longitudinal shear lamina properties, however, experience creep the extent of which varies based on fiber modulus and volume fraction. The features of viscoelasticity are also present at the laminate level but are more complex due to interactions and constraints between the variously oriented laminae and their stacking sequence. Figure 1.2.2 represents the coordinate system of a laminate in which *x* is defined as the *0º* axis of the laminate, *y* as the *90º* axis of the laminate, and *z* is the out of plane axis in which the origin lies at the midplane or reference plane of the laminate. The laminate consists of *n* laminae (plies) $k = 1$ through *n*, each a distance $\bar{z}^k$ from the laminate reference plane. Each lamina has a specified degree of rotation. All laminates considered are symmetric about the midplane and are therefore balanced.

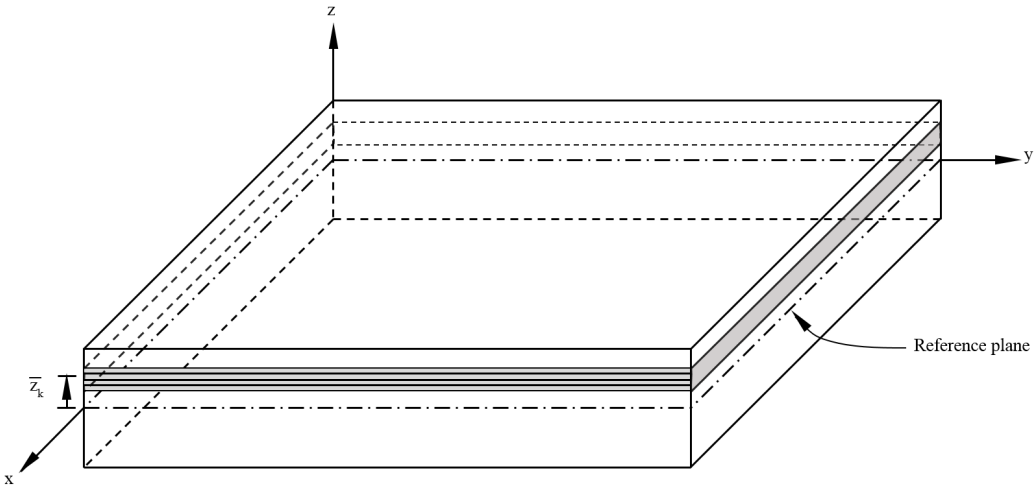

Figure 1.2.2: The coordinate system of a laminate is defined by x as the 0º axis of the laminate, y as the 90º axis of the laminate, and z as the out of plane axis. The origin lies at the midplane or reference plane of the laminate. The laminate consists of n laminae (plies) k = 1 through n each a distance $\bar{z}_k$ *from the laminate reference plane. Each lamina has a specified degree of rotation* [14].

Figure 1.2.3 depicts a cross-sectional view of a laminate with unidirectional laminae at varying degrees of rotation.

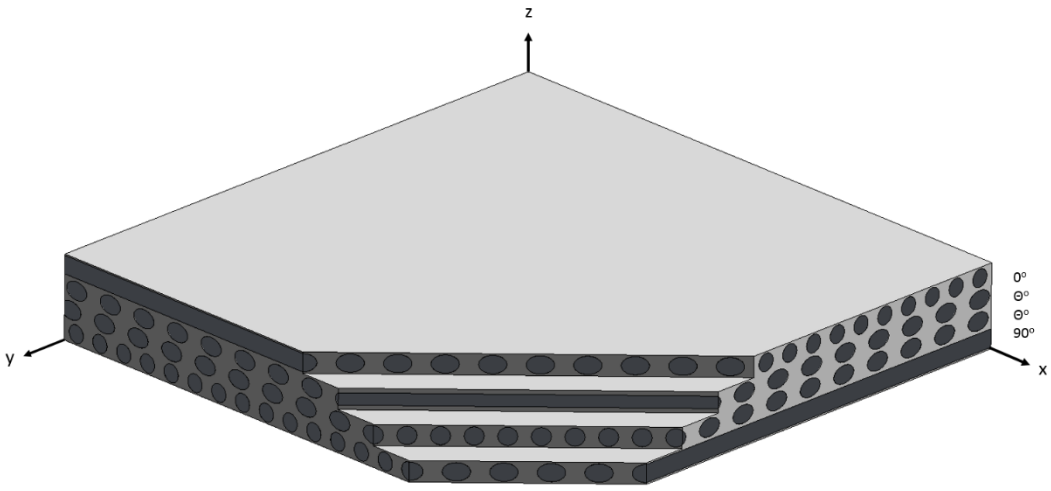

Figure 1.2.3: Cross-sectional view of a laminate with varying degrees of rotation of unidirectional laminae (plies) [14].

Classical laminate theory is used to predict the behavior of a laminate under a set of assumptions [14]:

1. Each layer (lamina) of the laminate is quasi-homogeneous and orthotropic.
2. The laminate is thin with its lateral dimensions much larger than its thickness and is loaded in its plane only, that is, the laminate and its layers (except for their edges) are in a state of plane stress ($\sigma_z = \tau_{xz} = \tau_{yz} = 0$).
3. All displacements are small compared with the thickness of the laminate.
4. Displacements are continuous throughout the laminate.
5. In-plane displacements vary linearly through the thickness of the laminate.
6. Straight lines normal to the middle surface remain straight and normal to the surface after deformation. This implies that the transverse shear strains γ_{xz} and γ_{yz} are zero.
7. Strain-displacement and stress-strain relations are linear.
8. Normal distances from the middle surface are taken to remain constant, that is, the transverse normal strain ε_z is infinitesimal.

The reduced elastic stiffness matrix of the k^{th} lamina in a laminate is represented using the composite x, y, and s notation for stress and strain where s is defined as the in-plane shear stress of the lamina or laminate.

$$\sigma_i^k = Q_{ij}^k \varepsilon_j^k \qquad (i,j = x,y,s) \tag{1.2.4}$$

where σ_i^k is the elastic plane stress of the k^{th} lamina; Q_{ij}^k is the elastic reduced stiffness of the k^{th} lamina; ε_j^k is the elastic strain in the k^{th} lamina. The strain at any point in the laminate is related to the reference plane strain, (ε_x^o, ε_y^o, and γ_s^o) and the laminate curvatures (K_x, K_y, and K_s).

$$\varepsilon_j^k = \varepsilon_j^o + zK_j \qquad (j = x,y,s) \tag{1.2.5}$$

Equation (1.2.4) is rewritten by substituting the expression for the strain in equation (1.2.5).

$$\sigma_i^k = Q_{ij}^k \varepsilon_j^o + zQ_{ij}^k K_j \qquad (j = x,y,s) \tag{1.2.6}$$

Figure 1.2.4 represents the discontinuous stress variation throughout a laminate due to an applied strain and varying lamina stiffness (E represents the Young's modulus of the lamina).

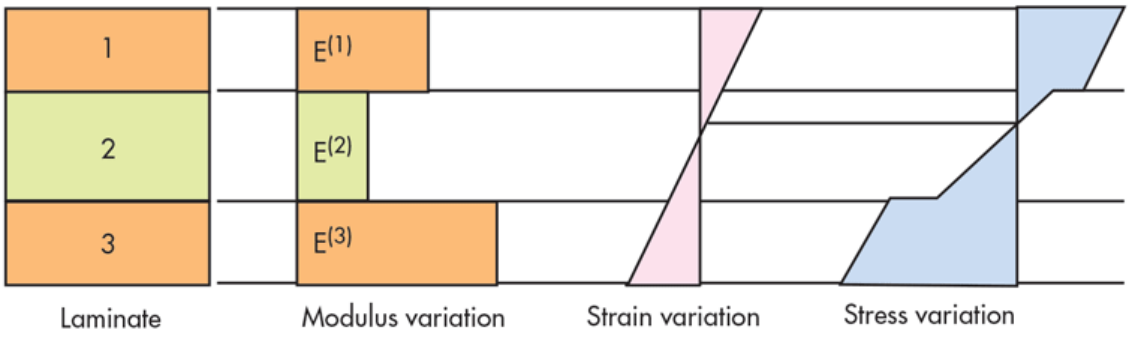

Figure 1.2.4: A laminate comprised of three laminae with varying Young's moduli is deformed by a strain variation as in equation (1.2.5), resulting in discontinuous stress variations in the laminate arising from equation (1.2.6) and consistent with classical lamination theory [15].

Laminate forces and moments are a more useful expression when evaluating the laminate's response to deformations. Figure 1.2.5 shows the force and moment resultants on a single layer of a laminate.

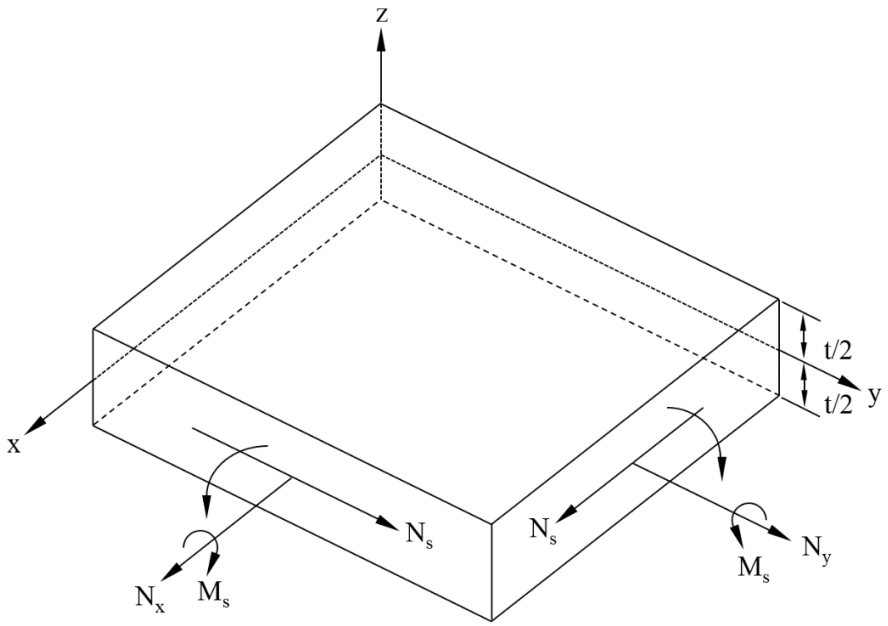

Figure 1.2.5: Laminate force and moment resultants on a single ply [14].

The sum of the lamina stresses over its thickness t results in the resultant forces.

$$N_i^k = \int_{-t/2}^{t/2} \sigma_i dz \quad (i = x, y, s) \tag{1.2.7a}$$

N_x and N_y are the elastic normal forces per unit length and N_s is the elastic shear force per unit length. The resultant moment is a sum of the moments due to stresses a distance z from the midplane (reference plane) of the lamina, as depicted in Figure 1.2.2.

$$M_i^k = \int_{-t/2}^{t/2} \sigma_i z dz \qquad (i = x, y, s) \tag{1.2.7b}$$

M_x and M_y are the elastic bending moments per unit length and M_s the elastic twisting moment or torque per unit length. Summing the stresses in each lamina over the thickness of a laminate results in the laminate force and moment resultants.

$$N_i = \sum_{k=1}^{n} \int_{z_{k-1}}^{z_k} \sigma_i^k dz \qquad (i = x, y, s) \tag{1.2.8a}$$

$$M_i = \sum_{k=1}^{n} \int_{z_{k-1}}^{z_k} \sigma_i^k z dz \qquad (i = x, y, s) \tag{1.2.8b}$$

z_k and z_{k-1} are the upper and lower in-plane surface distances from the midplane of the laminate. Replacing the lamina stress σ_i^k in the equations (1.2.8a) and (1.2.8b) with the expression in equation (1.2.6) yields the following results

$$N_i = \sum_{k=1}^{n} \int_{z_{k-1}}^{z_k} Q_{ij}^k \varepsilon_j^o dz + \sum_{k=1}^{n} \int_{z_{k-1}}^{z_k} z Q_{ij}^k K_j dz \qquad (i,j = x,y,s) \qquad (1.2.9a)$$

$$M_i = \sum_{k=1}^{n} \int_{z_{k-1}}^{z_k} z Q_{ij}^k \varepsilon_j^o dz + \sum_{k=1}^{n} \int_{z_{k-1}}^{z_k} z^2 Q_{ij}^k K_j dz \qquad (i,j = x,y,s) \qquad (1.2.9b)$$

The integral expression of equations (1.2.9a) and (1.2.9b) are represented by three commonly defined symmetric matrices discussed in detail by Daniel and Ishai [14]:

- The in-plane moduli, or extensional stiffness matrix, A_{ij}, relates in-plane loads to in-plane strains.
- The coupling stiffness matrix, B_{ij}, relates in-plane curvatures and moments to in-plane strains. A non-zero B_{ij} matrix results in flexural and twisting due to in-plane forces. Moments produce a similar response with the addition of extensional and shear deformations of the middle surface.
- The bending and flexural laminate stiffness matrix, D_{ij}, relates moments to curvatures.

$$N_i = A_{ij}\varepsilon_j^o + B_{ij}K_j \qquad (1.2.10a)$$

$$M_i = B_{ij}\varepsilon_j^o + D_{ij}K_j \qquad (1.2.10b)$$

It is common to refer to the laminate moduli, A_{ij}, B_{ij}, and D_{ij}, as the ABD matrix. The laminate compliance is the inverse of the ABD matrix expressing the strains and curvatures as a function of the applied loads and moments.

$$\varepsilon_i^o = a_{ij}N_j + b_{ij}M_j \qquad (1.2.11a)$$

$$K_i = c_{ij}N_j + d_{ij}M_j \qquad (1.2.11b)$$

The laminate compliance is referred to as the $abcd$ matrix.

$$\begin{bmatrix} a_{ij} & b_{ij} \\ c_{ij} & d_{ij} \end{bmatrix} = inv \begin{bmatrix} A_{ij} & B_{ij} \\ B_{ij} & D_{ij} \end{bmatrix} \tag{1.2.12}$$

1.3 Viscoelasticity Background

A material that exhibits both elastic and time-dependent properties is defined as viscoelastic. Most polymers are viscoelastic as a result of weak Van der Waals forces between polymer chains that can shift over time based on the applied loads and thermal energy [16], [17]. Viscoelasticity can be defined by two main loading categories, either relaxation or creep. Relaxation is a result of the polymer chains thermally rearranging to a minimum potential energy state due to the presence of an applied fixed displacement. As time progresses, the stress in the polymers due to the applied displacement decreases. Creep is a result of the polymer chains also thermally rearranging to a minimum potential energy state but as a result of a fixed load, which produces a change in displacement. Polymers are categorized into two main groups. One category is thermoplastics, which have no cross-linking between polymer chains, resulting in an unbonded viscoelastic response leading to failure over long loading durations. The other category is thermosets, which have crosslinked polymers that limit the extent polymer chains can rearrange, preventing the material from straining viscoelastically after long durations. It is common practice to use tough, heavily crosslinked polymer resin systems for composites, *i.e.,* thermosets. This disertation will focus on the behavior of thermoset resin systems.

A thermoset's viscoelastic response is broken down into three main behaviors: elastic glassy response, transient response, and long-time equilibrium response, often referred to as

an infinite equilibrium response. These features are depicted in Figure 1.3.1 for both the relaxation modulus and creep compliance. The relaxation modulus gives the stress as a function of time for a unit strain applied suddenly at time zero, whereas the creep compliance gives the strain as a function of time for a unit stress suddenly applied at time zero. The transient response of relaxation and creep differ due to the loading mechanisms that drive viscoelastic change. As a result, the interchange between the two properties requires special inversion methods, which are discussed in detail in Chapter 3.

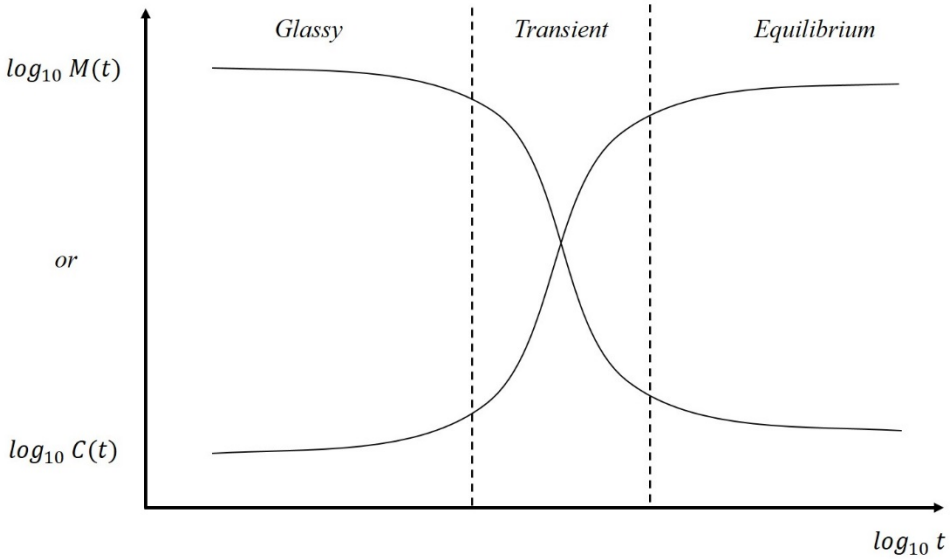

Figure 1.3.1: The creep compliance C(t) and relaxation stiffness M(t) of a composite viscoelastically changes as a function of time on a log scale. The glassy region defines the material's elastic response. The transient region defines the material's time-dependent deformation response. The equilibrium region defines the material's final stabilized deformation response [18].

A Prony series is commonly used to define the viscoelastic behavior of polymers [16]. The relaxation modulus $M(t)$ and creep compliance $C(t)$ are defined as follows

$$M(t) = M^g - \sum_{i=1}^{k} M^i \left(1 - e^{-\alpha^i t}\right) \tag{1.3.1a}$$

$$C(t) = C^g + \sum_{i=1}^{k} C^i \left(1 - e^{-\beta^i t}\right) \tag{1.3.1b}$$

where M^i and C^i are the Prony modulus and creep constants; α_i and β_i are the Prony modulus and compliance time constants; M^g and C^g are the initial glassy modulus and

compliance and thus are $M(t=0)$ and $C(t=0)$, respectively. The equilibrium region can be defined mathematically by the limit of equation (1.3.1a) and (1.3.1b) as t approaches infinity. The parameter k is the number of Prony series terms needed to fully define a material's transient behavior between the initial glassy response and the equilibrium response.

$$\lim_{t\to\infty} M(t) = M^e \tag{1.3.2a}$$

$$\lim_{t\to\infty} C(t) = C^e \tag{1.3.2b}$$

The equilibrium response is also related to the initial modulus and compliance by the following expressions

$$M^e = M^g - \sum_{i=1}^{k} M^i \tag{1.3.3a}$$

$$C^e = C^g + \sum_{i=1}^{k} C^i \tag{1.3.3b}$$

Equations (1.3.1a) and (1.3.1b) can also be written using the equilibrium response as defined in equations (1.3.2a) and (1.3.2b), respectively.

$$M(t) = M^e + \sum_{i=1}^{k} M^i e^{-\alpha^i t} \tag{1.3.4a}$$

$$C(t) = C^e - \sum_{i=1}^{k} C^i e^{-\beta^i t} \tag{1.3.4b}$$

The rate at which a material relaxes or creeps is dependent on temperature. The higher the temperature, the faster the material reaches equilibrium. A master curve defining the viscoelastic behavior of a material over its entire lifetime (glassy to equilibrium) can take more than a year to measure at room or similar modest temperatures. Fortunately, most polymers are thermorheologically simple [19], and obey an Arrhenius law for time-temperature superposition. Experimental results from tests carried out over short periods of time at various levels of higher temperatures can be shifted along the time axis to form a

master curve, which is illustrated in Figure 1.3.2. The mathematical representation of the Arrhenius data shift is

$$\log(a_T) = \frac{E_a}{R}\left(\frac{1}{T} - \frac{1}{T_o}\right) \tag{1.3.5}$$

in which T_o is the reference temperature for a material master curve. The shift coefficient, a_T, is the required time axis shift to move the reference master curve to a new desired temperature T. R is the gas constant (J/(mol °K)), and E_a is the viscoelastic activation energy of the material (J/mol).

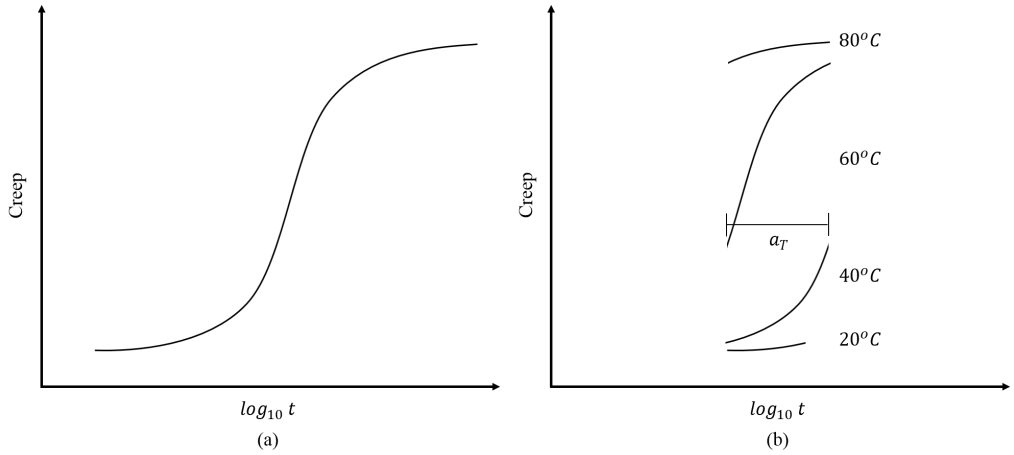

Figure 1.3.2: Creep compliance master curve: (a) master curve formed from (b) short-term creep data measured at different temperatures that are shifted based on time-temperature superposition principles mathematically defined using an Arrhenius law [20].

A mathematical representation of the master curve is created by fitting a Prony series to the master curve data. The Prony series functions (1.3.1a) and (1.3.1b) defining the viscoelastic master curve of a material can be modified to include the time/temperature effects expressed by the Arrhenius law, equation (1.3.5). This is accomplished by dividing the Prony time constants for both the relaxation modulus and creep compliance by the shift coefficient.

$$\alpha^{i,T} = \frac{\alpha^{i,T_o}}{\alpha^T} \tag{1.3.6a}$$

$$\beta^{i,T} = \frac{\beta^{i,T_o}}{\beta^T} \tag{1.3.6b}$$

Where $\alpha^{i,T}$ and $\beta^{i,T}$ are the relaxation modulus and creep compliance Prony time constants at the desired temperature, and α^{i,T_o} and β^{i,T_o} are the relaxation modulus and creep compliance Prony time constants at the reference temperature.

The elastic laminate theory discussed earlier can be redefined using the viscoelastic theory just established [21]. The lamina reduced stiffness and compliance for elastic materials defined in equations (1.2.2) and (1.2.3), respectively, are presented below in viscoelastic form using the Prony series defined in equation (1.3.1a) for relaxation and equation (1.3.1b) for creep.

$$Q_{ij}(t) = Q_{ij}^g - \sum_{l=1}^{k} Q_{ij}^l \left(1 - e^{-\alpha_Q^l t}\right) \tag{1.3.7a}$$

$$S_{ij}(t) = S_{ij}^g + \sum_{l=1}^{k} S_{ij}^l \left(1 - e^{-\beta_S^l t}\right) \tag{1.3.7b}$$

α_Q^l and β_S^l are the Prony time constants for the relaxation reduced stiffness and creep compliance, respectively; Q_{ij}^g and S_{ij}^g are the lamina relaxation reduced stiffness and creep compliance glassy response; Q_{ij}^l and S_{ij}^l are the Prony constants for the lamina relaxation reduced stiffness and creep compliance, respectively. The laminate stiffness ABD and compliance $abcd$ matrices defined in equations (1.2.10) and (1.2.11) are presented below in viscoelastic form using Prony series.

$$A_{ij}(t) = A_{ij}^g - \sum_{l=1}^{k} A_{ij}^l \left(1 - e^{-\alpha_A^l t}\right) \tag{1.3.8a}$$

$$B_{ij}(t) = B_{ij}^g - \sum_{l=1}^{k} B_{ij}^l \left(1 - e^{-\alpha_B^l t}\right) \tag{1.3.8b}$$

$$D_{ij}(t) = D_{ij}^g - \sum_{l=1}^{k} D_{ij}^l \left(1 - e^{-\alpha_D^l t}\right) \tag{1.3.8c}$$

$$a_{ij}(t) = a_{ij}^{g} + \sum_{l=1}^{k} a_{ij}^{l}\left(1 - e^{-\beta_a^l t}\right) \tag{1.3.9a}$$

$$b_{ij}(t) = b_{ij}^{g} + \sum_{l=1}^{k} b_{ij}^{l}\left(1 - e^{-\beta_b^l t}\right) \tag{1.3.9b}$$

$$c_{ij}(t) = c_{ij}^{g} + \sum_{l=1}^{k} c_{ij}^{l}\left(1 - e^{-\beta_c^l t}\right) \tag{1.3.9c}$$

$$d_{ij}(t) = d_{ij}^{g} + \sum_{l=1}^{k} d_{ij}^{l}\left(1 - e^{-\beta_d^l t}\right) \tag{1.3.9d}$$

α_A^l, α_B^l, α_D^l, and β_a^l, β_b^l, β_c^l, β_d^l are the Prony time constants for the laminate relaxation modulus and creep compliance; A_{ij}^g, B_{ij}^g, D_{ij}^g, and a_{ij}^g, b_{ij}^g, c_{ij}^g, d_{ij}^g are the laminate relaxation modulus and creep compliance glassy response; A_{ij}^l, B_{ij}^l, C_{ij}^l, and a_{ij}^l, b_{ij}^l, c_{ij}^l, d_{ij}^l are the Prony constants for the laminate relaxation modulus and creep compliance.

1.4 Motivation and Outline

My Ph.D. advisor, the late Dr. Keith Kedward, and I were awarded a NASA STTR grant in collaboration with Deployable Space Systems, tasked with understanding the underlying cause of viscoelasticity present in its deployable solar array. The program initially started as a year-long Phase I program at the end of which a Phase II and Phase II extension was awarded. It is common practice for most aerospace design applications to rely on experimental data at the system level to validate the reliability of deployments [22]. This approach, while valid, is costly and fails to elicit the underlying cause of viscoelasticity in structures, a necessity for the development of accurate and reliable predictive models. The goal of this research is to identify the presence of viscoelasticity in composites and how various laminate layups, orientations, and stacking sequences influence their viscoelastic properties. Furthermore, it also aims to develop a model to predict the behavior of viscoelastic STEMs used in structural applications such as DSS' MEGA ROSA solar array.

Each chapter of this dissertation addresses a different aspect of viscoelasticity in composites. Chapter 2 discusses the results of creep tests conducted on various laminae and laminates. Chapter 3 develops a viscoelastic inversion method for predicting relaxation and creep properties from measured creep and relaxation properties, respectively. Chapter 4 presents the results of inverting the creep properties recorded in Chapter 2 using the inversion method developed in Chapter 3. Chapter 4 also presents predictions of relaxation flexural properties using a viscoelastic variant of classical laminate theory. Lastly, Chapter 5 derives a mathematical model to predict the viscoelastic behavior of composite STEMs when stowed for varying durations before being deployed using the measured and inverted relaxation data recorded in Chapter 2 and 4.

Chapter 2 discusses the results of tensile and four-point bend tests performed on anisotropic viscoelastic composites and their neat resin matrix in order to determine the effect that fiber integration, lamina orientation, and laminate stacking sequence have on the viscoelastic behavior of composites. Four constant temperature tests are conducted below the glass transition temperature on all samples and laminate types. The results are combined to form master curves that model up to 3 years of the viscoelastic history of the samples. Normalization of the master curve equation allows for a comparison between the compliance and flexure properties obtained by the tensile and four-point bend tests, respectively. Similarities in the results between compliance and flexure properties validate the quality of the tests and confirm the absence of artifacts particular to a specific test method. The proportional transient response of the compliance and flexure master curves provides a means of comparing the rate of viscous change of these different properties. The evaluation of the tested materials using this method shows that the proportional transient response in all

laminate directions and variant properties (flexure and tension) matches that of the matrix neat resin system. This indicates that the neat resin time-dependent properties are unaffected by the integration of fibers and are independent of orientation and stacking sequence of the fiber dominant directions. The degree of creep and stiffness that the materials possess, however, is affected by orientation and stacking sequence. The results indicate that the placement of fibers in the highest strain/stress directions mitigate the viscoelastic response of the material. In the case of flexure, the surfaces of lamina/laminate experience the largest loads. With the utilization of these findings, composite laminates that mitigate creep can be predicted and used in deployable space applications. Furthermore, measuring the viscoelastic response of the resin system can provide the time-dependent proportional transient response of composites without the need to perform complex system-level tests. This significantly improves design development time and reduces development costs.

Chapter 3 explores inversion techniques between creep and relaxation for anisotropic viscoelastic materials like the lamina and laminates tested in Chapter 2. An accurate constitutive law inversion for anisotropic viscoelastic materials, such as those used in thin shell composites, between relaxation and creep, is required to produce reliable structural models and to enable their practical utilization. Since most materials are tested for either relaxation stiffness or creep compliance properties, viscoelastic inversion is needed to obtain both sets of properties. The development of a Laplace numerical inversion method using a Dirichlet-Prony series for anisotropic viscoelastic materials is presented in this chapter. The Laplace numerical method is compared to Schapery's least squares method and Gutierrez-Lemini's exact matrix inversion techniques found in the literature. The Laplace numerical

method best models the critical characteristics required for robust inversion of anisotropic viscoelastic materials.

Chapter 4 presents the inverted measured compliance data recorded in Chapter 2 using the numerical Laplace method developed in Chapter 3 and records the relaxation stiffness results using Prony series. It is not possible to invert the creep flexure data recorded in Chapter 2 due to the inability to measure the axial/transverse properties. Instead, a viscoelastic model of classical laminate theory is used to predict the relaxation flexure properties of the laminae and laminates measured in Chapter 2. The relaxation stiffness properties for the unidirectional and plain weave laminae are used as inputs into a viscoelastic version of the classical laminate theory. Ply orientation and ply thickness consistent with the measured samples are also used as inputs. The resulting relaxation flexure properties are presented in this chapter and recorded using Prony series. The results are compared to the measured creep flexure data by inverting the relaxation flexure properties using the numerical Laplace inversion method. The relaxation compliance properties from direct inversion and the relaxation flexure properties predicted from viscoelastic classical laminate theory produce properties that mimic the expected behavior as exemplified by the measured creep data. The results presented in this chapter demonstrate the viability of the numerically solved Laplace inversion method in combination with a viscoelastic version of classical laminate theory for obtaining relaxation and creep data required to predict the viscoelastic behavior of structures composed of viscoelastic materials.

Chapter 5 develops a means for modeling the anisotropic viscoelastic behavior of STEMs through the use of hereditary integrals and classical laminate theory. The model predicts the bending curvature and moment histories of STEMs stowed in a state of biaxial bending for

varying duration and then deployed. Test data is not available to validate the model. However, confidence in the model's prediction of viscoelastic composite STEMs in biaxial bending is established by comparing the results from the model for a one-dimensional beam in bending to solutions derived based on hereditary expressions found in the literature. The model is also used to evaluate composite STEMs composed of the 3-ply laminate [45^{o} PW/0^{o} Uni/45^{o} PW] and 4-ply laminate [0^{o} Uni /45^{o} PW/45^{o} PW/0^{o} Uni] with creep properties from measured data recorded in Chapter 2 and relaxation properties predicted using the inversion method discussed in Chapter 3. The bending moment and curvature histories behave as expected for the modeled stowed configuration, stowed duration, and deployed configuration. The model can help in the design development of composite STEMs for use in deployable structures.

Chapter 6 provides some concluding remarks as an assessment of the research discussed in Chapters 2 through Chapter 5.

Chapter 2

Viscoelastic Response of Composites in Tension and Flexure

2.1 Introduction: Anisotropic Viscoelasticity of Composites

It is common for aerospace design applications to rely on experimental data for a deployable structure to anticipate the reliability of composite design deployments [22]. This approach, while valid, is costly and fails to account for the root cause of viscoelasticity, which is necessary for the development of accurate and reliable predictive models. A review of the literature shows the primary research approach is to experimentally measure the viscoelasticity of unidirectional laminae under tensile loading conditions [12], [23]–[26]. While lamina properties of a specific material system are useful, these tests fail to provide insight into the effects elastic fibers have on a resin system resulting in anisotropic viscoelastic laminae. Flexure tests on both unidirectional and plain weave laminae are found in the literature [27]–[29]. However, an understanding of how various loading conditions affect the viscoelastic properties of laminae by comparing the response in bending and tension has yet to be published. Furthermore, little has been explored in the realm of more sophisticated composites and how laminate layup and stacking sequence affect the

viscoelastic properties of composites. As a result, there is an incomplete picture in the literature on this subject. Pellegrino and Kwok [30] have done the most work on creating a comprehensive picture of viscoelasticity in composites. They have explored the root cause of viscoelasticity by measuring the properties of the resin system and developing a lamina prediction method through the use of FEA microfiber modeling in Abaqus. Their research has focused on a plain weave lamina in bending [20]. However, their research does not characterize the effects elastic fibers have on the viscoelastic resin system at the lamina and laminate level. Instead, they use measured properties of a specific composite system for structural applications, e.g., a plain weave lamina. This chapter aims to characterize the viscoelastic behavior of composites by observing the various viscoelastic responses of a resin system at the neat resin, lamina, and laminate level under both tensile and four-point bend loading conditions in order to produce a generalized theory applicable to all continuous fiber lamina/laminate systems.

2.2 Background

The variation in viscoelastic behavior among laminae and laminate materials of various stiffnesses can best be assessed using the normalized form of the data. The anisotropic relaxation and creep properties of a composite presented in equations (1.3.1a) and (1.3.1b) are normalized by their respective material glassy property M^g and C^g.

$$\frac{M(t)}{M^g} = 1 - \sum_{i=1}^{k} \left(\frac{M^i}{M^g} \left(1 - e^{-\alpha^i t} \right) \right) \tag{2.2.1a}$$

$$\frac{C(t)}{C^g} = 1 + \sum_{i=1}^{k} \left(\frac{C^i}{C^g} \left(1 - e^{-\beta^i t} \right) \right) \tag{2.2.1b}$$

The lamina and laminate relaxation and creep equations (1.3.8a) through (1.3.9d) are presented in normalized form in the appendix (equation (A.1a) through (A.2d)). The

normalized relaxation modulus defining the viscoelastic response is 1 at t = 0, and 0 if full relaxation is possible before fracture occurs as $t \to \infty$. In the case of a heavily cross-linked polymer, e.g., a thermoset, the material will relax to an equilibrium state (a non-zero normalized value for the relaxation modulus less than one) as $t \to \infty$. The normalized creep, on the other hand, increases in value from unity until the material fractures or, in the case of a thermoset polymer, reaches some equilibrium state.

While the normalized forms of relaxation and creep are useful in comparing viscoelastic materials with various stiffnesses, a means of studying the effects of fiber layup and laminate orientation on the transient response is also needed. For this purpose, Equations 2.2.1a and 2.2.1b can be written in the following form.

$$\frac{M(t)}{M^g} = 1 - b * \widetilde{M}(t) \tag{2.2.2a}$$

$$\frac{C(t)}{C^g} = 1 - B * \tilde{C}(t) \tag{2.2.2b}$$

$\widetilde{M}(t)$ and $\tilde{C}(t)$ are the time-dependent (transient) portions of equations (2.2.2a) and (2.2.2b), which will be referred to in this dissertation as the transient proportional response function.

$$\widetilde{M}(t) = \sum_{i=1}^{k} \left(\frac{M^i}{\sum_{i=1}^{n} M^i} (1 - e^{-\alpha^i t}) \right) \tag{2.2.3a}$$

$$\tilde{C}(t) = \sum_{i=1}^{k} \left(\frac{C^i}{\sum_{i=1}^{n} C^i} (1 - e^{-\beta^i t}) \right) \tag{2.2.3b}$$

The transient relaxation modulus and creep compliance coefficients are normalized by the sum of all the series coefficients, which represents the extent the modulus and compliance change over the lifetime of an applied material load. The transient proportional response function ranges from zero (no transient response) to one (maximum transient response). This function is used to evaluate the neat resin's influence on the transient behavior of different laminae and laminates, as presented in the appendix. The extent that the modulus and

compliance change over the lifetime of an applied material load is also equivalent to the difference between the glassy and the equilibrium response of a material, $M^g - M^e$ for relaxation and $C^g - C^e$ for creep. Dividing $M^g - M^e$ by M^g yields b in equation (2.2.2a), which will be referred to as the degree of relaxation. Dividing $C^e - C^g$ by C^g yields B in equation (2.2.2b), which will be referred to as the degree of creep.

$$b = \left(\frac{M^g - M^e}{M^g}\right) \tag{2.2.4a}$$

$$B = \left(\frac{C^e - C^g}{C^g}\right) \tag{2.2.4b}$$

These expressions are useful for understanding the influence continuous fibers and their orientation have on the viscoelastic nature of laminae and laminates. The degree of relaxation can have values from -1 for a material that completely relaxes to a value greater than zero for a material that stiffens. The degree of creep can have values greater than or equal to zero. When the degree of relaxation or creep is zero, the material is elastic.

Hereditary integrals are used to define the viscoelastic stress and strain histories of a material [31]. The elastic constitutive expressions representing the stress and strain of laminae and laminates defined in equations (1.2.2) and (1.2.3), and equations (1.2.10a) through (1.2.11b) are expressed below for viscoelasticity using hereditary integrals.

$$\sigma_i(t) = \int_{0^-}^{t} Q_{ij}(t-\tau)\frac{d}{d\tau}\varepsilon_j(\tau)d\tau \tag{2.2.5}$$

$$\varepsilon_i(t) = \int_{0^-}^{t} S_{ij}(t-\tau)\frac{d}{d\tau}\sigma_j(\tau)d\tau \tag{2.2.6}$$

$$N_i(t) = \int_{0^-}^{t} A_{ij}(t-\tau)\frac{d}{d\tau}\varepsilon_j^o(\tau)d\tau + \int_{0^-}^{t} B_{ij}(t-\tau)\frac{d}{d\tau}K_j(\tau)d\tau \tag{2.2.7a}$$

$$M_i(t) = \int_{0^-}^{t} B_{ij}(t-\tau)\frac{d}{d\tau}\varepsilon_j^o(\tau)d\tau + \int_{0^-}^{t} D_{ij}(t-\tau)\frac{d}{d\tau}K_j(\tau)d\tau \tag{2.2.7b}$$

$$\varepsilon_i^o(t) = \int_{0^-}^{t} a_{ij}(t-\tau)\frac{d}{d\tau}N_j(\tau)d\tau + \int_{0^-}^{t} b_{ij}(t-\tau)\frac{d}{d\tau}M_j(\tau)d\tau \tag{2.2.8a}$$

$$K_i(t) = \int_{0^-}^{t} c_{ij}(t-\tau)\frac{d}{d\tau}N_j(\tau)d\tau + \int_{0^-}^{t} d_{ij}(t-\tau)\frac{d}{d\tau}M_j(\tau)d\tau \quad (2.2.8b)$$

The viscoelastic form of the viscoelastic constitutive equations can be rewritten for more specific loading conditions. The lamina and laminate properties measured in this chapter are obtained through a classic creep test in which a stress is quickly imposed at $t = 0$, thereafter held constant, and the corresponding strain response is measured over time. Figure 2.2.1 depicts the general stress input and response of a creep test. The Heaviside step function is used to define the step response of the applied stress.

$$H(t) = \begin{cases} 0, & t < 0 \\ 1, & t > 0 \end{cases} \quad (2.2.9)$$

This assumption is valid for viscoelastic material systems with sufficiently fast ramped deformations, preventing viscoelasticity from occurring during loading. The graph on the left of Figure 2.2.1 depicts the applied stress.

$$\sigma(t) = H(t)\sigma_j = \begin{cases} 0, & t < 0 \\ \sigma_j, & t > 0 \end{cases} \quad (2.2.10)$$

Equations (2.2.10) can be input into the reduced lamina strain equation (2.2.6). The hereditary integration of a Heaviside step response is well defined in the literature. The equation for the viscoelastic creep response of a lamina due to the applied stress reduces to a simple expression.

$$\varepsilon_i(t) = S_{ij}(t)H(t)\sigma_j \quad (2.2.11)$$

The graph on the right of Figure 2.2.1 depicts the creep response of the applied stress.

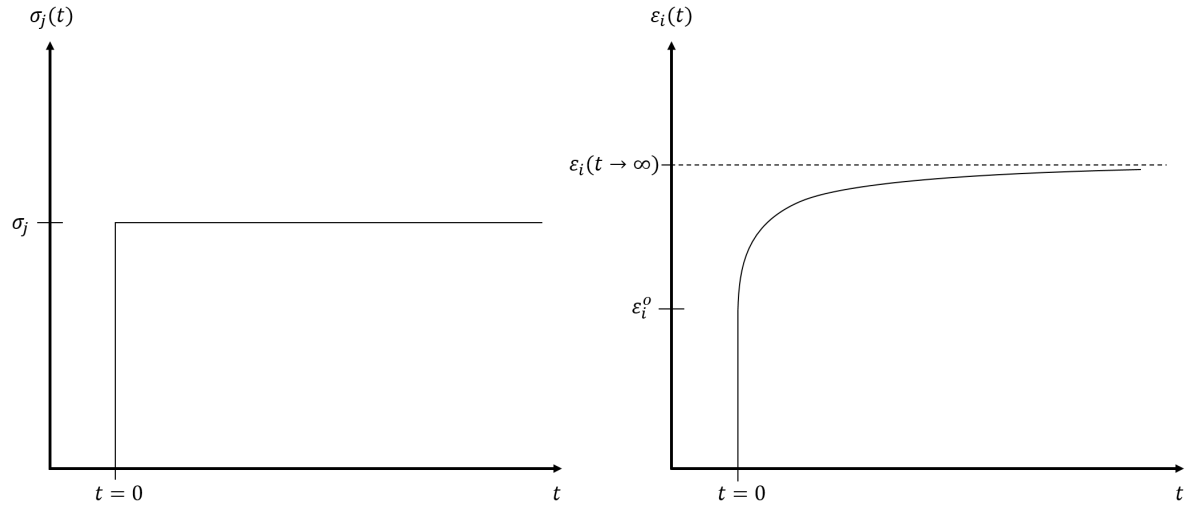

Figure 2.2.1: The graph on the left depicts a constant stress applied at $t = 0$. The graph on the right depicts the creep response of a material due to the applied stress. As $t \to \infty$ the material reaches equilibrium.

The above steps can be applied to the laminate equations (2.2.8a) and (2.2.8b). The rapidly applied stress and bending moments that are thereafter held constant are represented using the Heaviside step function for axial and flexure composite creep tests.

$$N_i(t) = H(t)N_j = \begin{cases} 0, & t < 0 \\ N_j, & t > 0 \end{cases} \tag{2.2.12}$$

$$M_i(t) = H(t)M_j = \begin{cases} 0, & t < 0 \\ M_j, & t > 0 \end{cases} \tag{2.2.13}$$

The composite creep strain response to the applied stress and moment is mathematically defined by inserting equation (2.2.12) and (2.2.13) into equation (2.2.8a).

$$\varepsilon_i^o(t) = a_{ij}(t)H(t)N_j + b_{ij}(t)H(t)M_j \tag{2.2.14}$$

The composite creep curvature response to the applied stress and moment is mathematically defined by inserting equations (2.2.12) and (2.2.13) into equation (2.2.8b).

$$K_i(t) = c_{ij}(t)H(t)N_j + d_{ij}(t)H(t)M_j \tag{2.2.15}$$

2.3 Test Method

Creep tests are performed on a series of sample laminae and laminates composed of the same resin and fiber system. Both tensile and four-point bend tests are used to obtain the anisotropic compliance and bending stiffness of the samples. Creep tests are favored over relaxation tests due to the complex loading conditions required by relaxation tests to obtain the necessary anisotropic viscoelastic properties. The lamina and laminate test samples are comprised of IM7 carbon fibers and a proprietary epoxy resin system similar to 977-3. Cuboidal samples, of planform 152.4 mm x 25.4 mm of neat resin, 24 ply unidirectionally reinforced laminate (Figure 2.3.1), 12 ply plain weave (PW) laminate (Figure 2.3.2), 3-ply laminate [45PW/0/45PW] (Figure 2.3.3), and 4-Ply laminate [0/45PW/45PW/0] (Figure 2.3.4) are tested. The thickness of the resin specimen is 2.250 mm, while that of the unidirectionally reinforced laminate specimen consisting of 24 plies is 2.701 mm. The volume fraction of fibers in this specimen is 52%. The thickness of the specimen consisting of a 12 ply, plain weave laminate is 2.17 mm, while the volume fraction of fibers within it is 54%. In the designation [45PW/0/45PW], the 3-ply laminate consists of a central, unidirectionally reinforced lamina with fibers parallel to the x-axis sandwiched between two plain weave laminae with fibers at 45^{o} to those in the central lamina. The thickness of the 3-ply laminate is 0.55 mm, and it is comprised of a unidirectional lamina ~0.115 mm thick and two plain weave lamina ~ 0.218 mm thick. The volume fraction of fibers in the unidirectionally reinforced lamina is 52% and in the plain weave lamina is 54%. In the designation [0/45PW/45PW/0], the 4-ply laminate consists of two outer, unidirectionally reinforced laminae with fibers identically aligned parallel to the x-axis, while the two inner laminae are plain weaves with their fibers at 45^{o} to those in the unidirectionally reinforced

laminae. The 4-ply laminate thickness is 0.65 mm, consisting of two unidirectional laminae each ~0.115 mm and two plain weave lamina each ~0.210 mm. The volume fraction of fibers in the unidirectionally reinforced lamina is 52% and in the plain weave laminae it is 54%.

All laminates being tested are symmetric and balanced due to the layup and stacking sequence of the laminae. The plain weave lamina is also intrinsically balanced and symmetric with an even number of fibers along both the positive and negative 45° axis that are an equal distance from the reference plane or mid-plane of the laminate. Due to their symmetry, the in-plane/flexure coupling laminate moduli, B_{ij}, relating in-plane loads to curvatures and moments to in-plane strains, are zero. Also, in-plane shear/flexure coupling laminate moduli, D_{xs} and D_{ys}, and in-plane shear/axial coupling laminate moduli A_{xs} and A_{ys}, are zero.

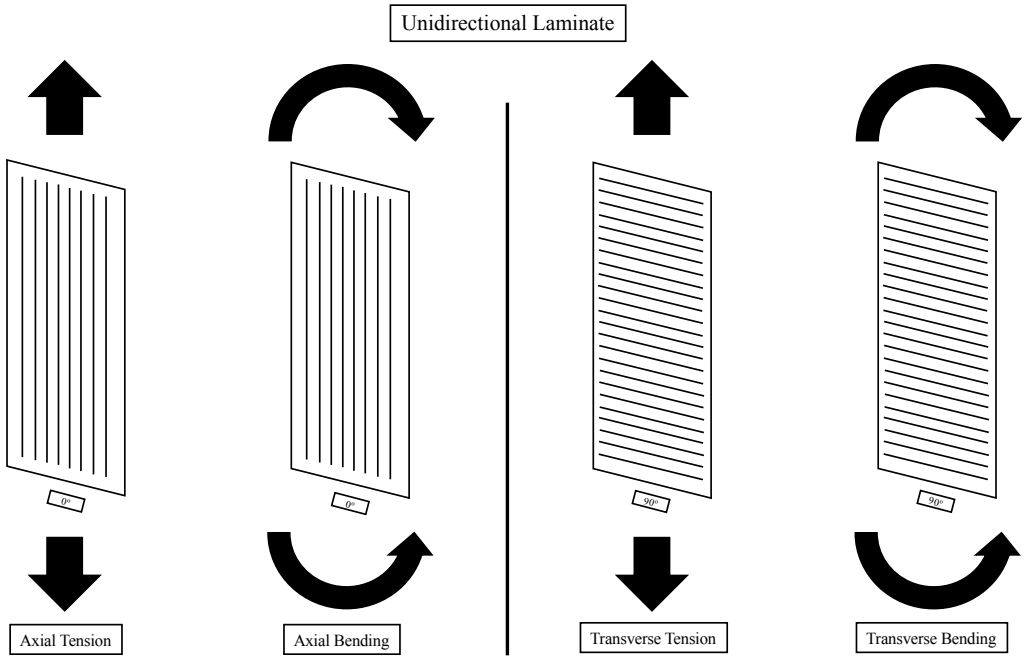

Figure 2.3.1: Unidirectional lamina loading configurations

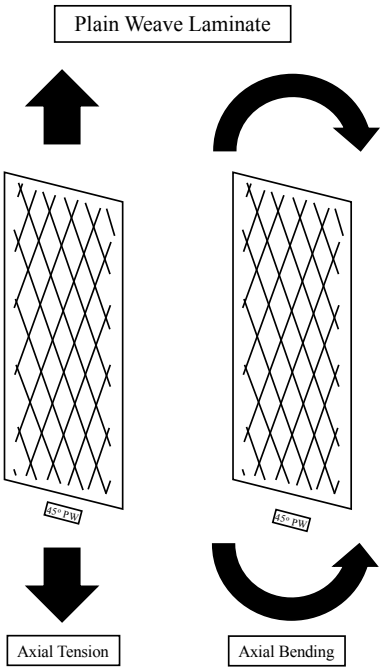

Figure 2.3.2: Plain weave laminate loading configurations.

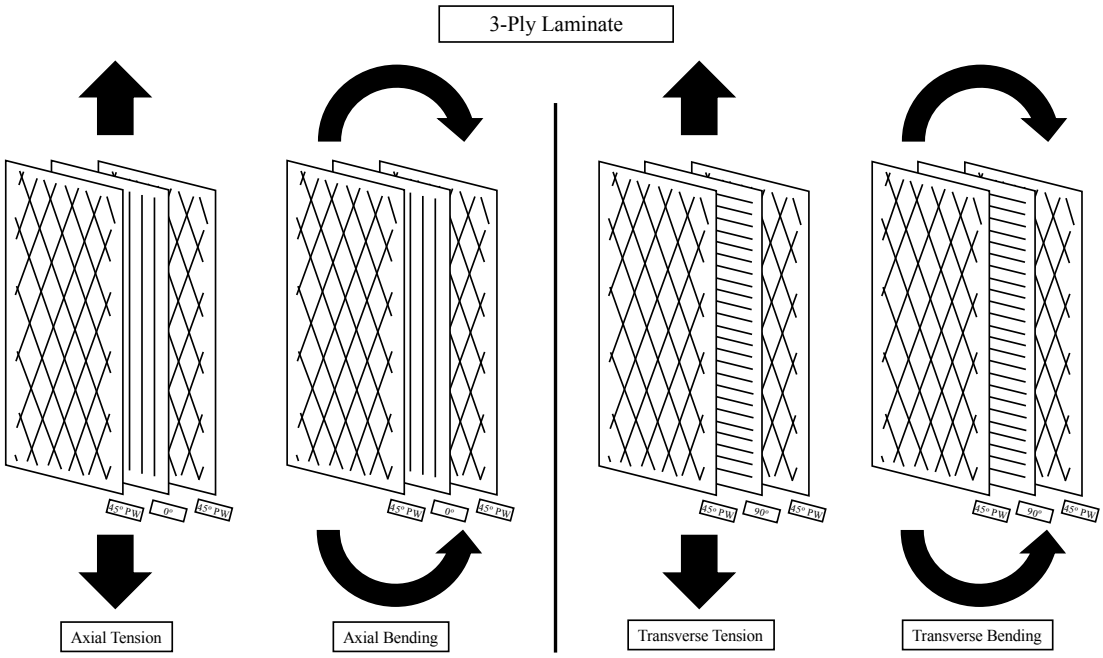

Figure 2.3.3: 3-Ply Laminate loading configurations.

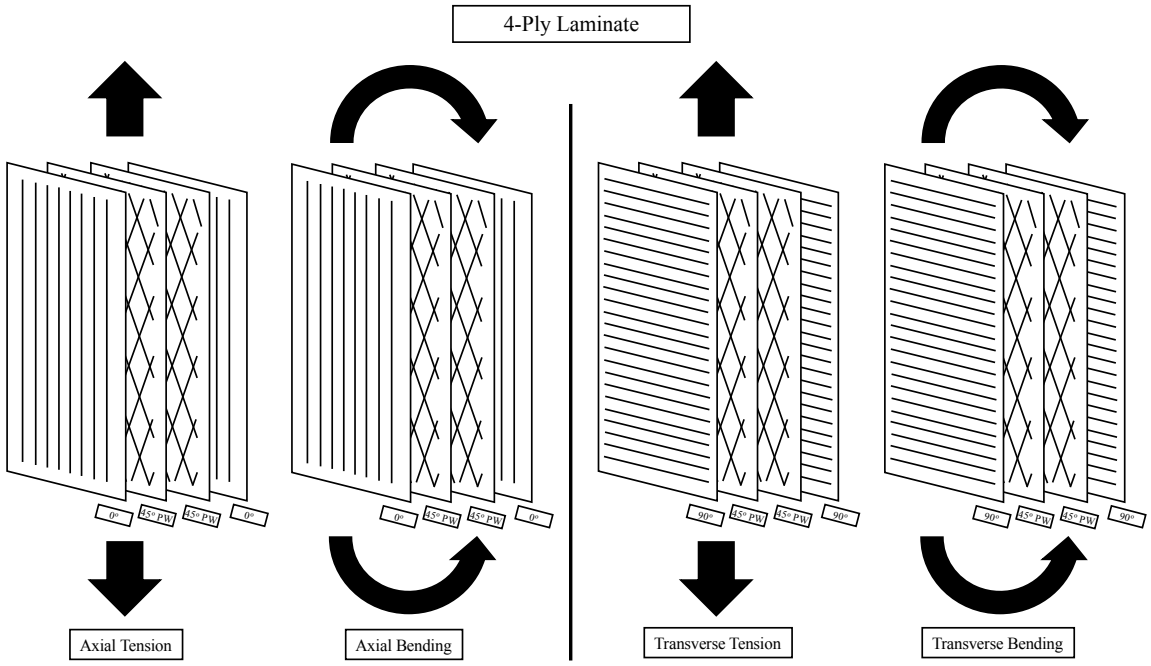

Figure 2.3.4: 4-Ply laminate loading configurations.

An Instron machine is used to apply a constant load for the tensile creep test. A 4-point bend fixture loaded by dead weights is used for the flexure tests, also at constant load. In the tensile tests, each layup is tested as follows; (1) with the load applied parallel to the fibers of their unidirectionally reinforced laminae (0° case, laminate x-axis) and; (2) with the load applied orthogonal to the fibers of their unidirectionally reinforced laminae (90° case, laminate y-axis). The specimen consisting of 12 plain weave laminae had the load applied at 45° to the fibers in the tensile tests and the axial bending strain was applied at 45° to the fiber directions for the flexure tests. The general applied stress function defined in equation (2.2.10) and (2.2.12) for lamina and laminate, respectively, can be rewritten for the two tensile creep test loading conditions. The x-axis lamina and laminate applied stress are presented below. Note that the in-plane/flexure coupling, $b_{ij}(t)$ and $c_{ij}(t)$, are zero for the laminates studied.

$$\sigma_i(t) = \begin{cases} \sigma_x H(t) \\ \sigma_y, \sigma_s = 0 \end{cases} \tag{2.3.1}$$

$$N_i(t) = \begin{cases} N_x H(t) \\ N_y, N_s = 0 \end{cases} \qquad M_i(t) = M_x, M_y, M_s = 0 \tag{2.3.2}$$

The lamina axial and transverse/axial creep compliance properties, S_{xx} and S_{yx}, respectively, can be calculated from the measured creep strain expressed in equation (2.2.11).

$$S_{xx}(t) = \frac{\varepsilon_x(t)}{\sigma_x} \tag{2.3.3}$$

$$S_{yx}(t) = \frac{\varepsilon_y(t)}{\sigma_x} \tag{2.3.4}$$

The laminate axial and transverse/axial creep compliance properties, a_{xx} and a_{yx}, respectively, can be calculated from the measured creep strain expressed in equation (2.2.14).

$$a_{xx}(t) = \frac{\varepsilon_x^o(t)}{N_x} \tag{2.3.5}$$

$$a_{yx}(t) = \frac{\varepsilon_y^o(t)}{N_x} \tag{2.3.6}$$

The lamina transverse/axial and transverse creep compliance properties, S_{xy} and S_{yy}, respectively, can be calculated from the measured creep strain due to an applied transverse stress, σ_y.

$$S_{xy}(t) = \frac{\varepsilon_x(t)}{\sigma_y} \tag{2.3.7}$$

$$S_{yy}(t) = \frac{\varepsilon_y(t)}{\sigma_y} \tag{2.3.8}$$

Similarly, the laminate transverse/axial and transverse creep compliance properties, a_{xy} and a_{yy}, respectively, can be calculated from the measured creep strain due to an applied stress, N_y.

$$a_{xy}(t) = \frac{\varepsilon_x^o(t)}{N_y} \tag{2.3.9}$$

$$a_{yy}(t) = \frac{\varepsilon_y^o(t)}{N_y} \tag{2.3.10}$$

In the flexure tests, each layup is tested as follows; (1) with the axial bending strains applied parallel to the fibers of their unidirectional reinforced laminae (0^o case, bending about the laminate y-axis) and; (2) with the axial bending strains applied orthogonal to the fibers of their unidirectional reinforced laminae (90^o case, bending about the laminate x-axis). Similar to the axial loaded condition, the general applied bending moment function defined in equation (2.2.13) for a laminate can be rewritten for the two flexure conditions. The x-axis applied moment is defined below.

$$M_i(t) = \begin{cases} M_x H(t) \\ M_y, M_s = 0 \end{cases} \qquad N_i(t) = N_x, N_y, N_s = 0 \tag{2.3.11}$$

The lamina and laminate axial creep flexure compliance property, d_{xx}, can be calculated from the measured creep curvature expressed in equation (2.2.15).

$$d_{xx}(t) = \frac{K_x(t)}{M_x} \tag{2.3.12}$$

The lamina and laminate transverse creep flexure compliance property, d_{yy}, can be calculated from the measured creep curvature due to an applied transverse moment, M_y.

$$d_{yy}(t) = \frac{K_y(t)}{M_y} \tag{2.3.13}$$

For the tensile tests, each specimen has two single-axis strain gauges, each a quarter inch in length, adhered to the mid-span section of the composite sample in both the transverse and axial directions. A Wheatstone bridge is used to increase the gain on the strain gauge signal as well as balance the strain gauges for each test temperature. The gauges are then used to measure the axial and transverse strains in the specimen throughout the test. The through-thickness strain is not measured. For the flexure tests, a laser extensometer is used to measure the midspan deflection. The anticlastic curvature, if any, is not measured.

A clamshell thermal chamber encloses the sample for both test configurations (Figure 2.3.5). A window in the front allows for visual inspection of the test sample as well as a means for the four-point bend test laser extensometer measurements. Calibration of the laser through the glass ensures that there is no noticeable refraction affecting the measurements. K-type thermo-couples are used to measure the surface temperature of the sample as well as the internal and external chamber temperature. A thermal controller maintains the sample surface temperature to +/- 1^{o}C. Each sample is subjected to a random order of four temperature conditions, 25^{o}C, 40^{o}C, 60^{o}C, and 80^{o}C. For the tensile tests, the temperature of the chamber is allowed to equilibrate (~30 min soak time) before the strain gauges are balanced, and the tensile creep tests are carried out. The same temperature profile is applied for the four-point bend tests before the datum for the laser extensometer is established, and the flexural creep tests are carried out. The load in each test is set such that the largest principal glassy strain is under 0.5%. Creep can occur during load ramp-up and is detectable if the resulting measured strain during ramp-up is a non-linear function of time. A fast ramp-up rate for the load is used to prevent this from occurring. An elapsed time of 60 sec. or less for the ramp-up of the load is found to be suitable for avoiding creep during ramp-up at all temperatures for all specimen types. The specimens are allowed to creep for roughly ten minutes. The material is allowed to then fully recover at the test temperature before a new temperature condition is set. The above procedure is repeated for all four test temperatures.

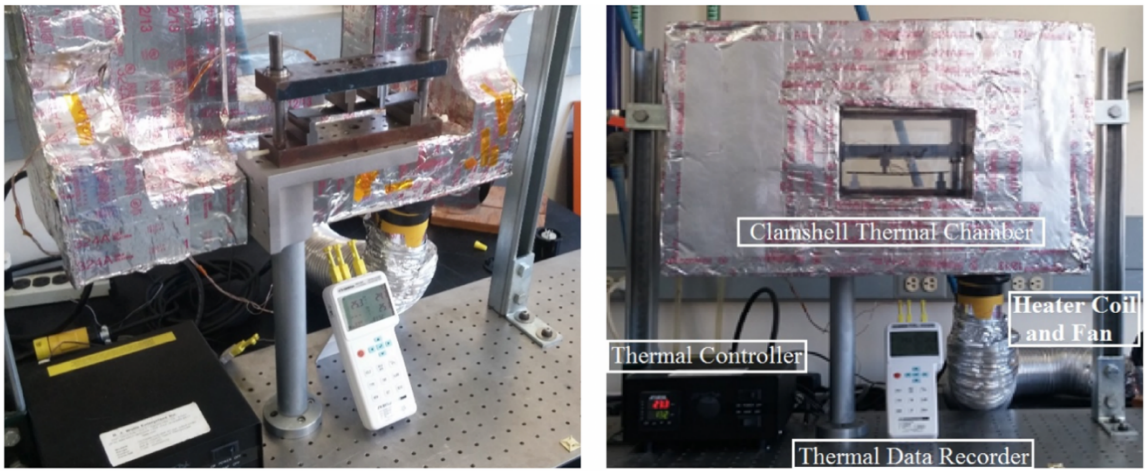

Figure 2.3.5: Four-point bend test setup consisting of a thermal chamber, heater coil, fan, thermal data recorder, and thermal controller. Clamshell thermal chamber is supported around a four-point bend test fixture.

2.4 Results

The axial creep compliance properties (equation (2.3.3)) of a neat resin sample measured from axial tensile creep tests (applied stress defined by equation (2.3.1)) at various temperatures are plotted in Figure 2.4.1 in normalized form (equation (2.2.1b)). A series of four creep tests at constant stress, but different constant temperatures are shifted such that a master curve is formed with the reference temperature equaling that for the first creep test in the curve. The creep compliance master curve is normalized by dividing all the master curve data by the compliance for the glassy response determined from the initial loading of the specimen. A logarithmic (base 10) time axis is used to better view the test data, which spans several orders of magnitude. A MATLAB [32] fitting algorithm uses time-temperature superposition to align the creep compliance data from the four different constant temperature tests into a master curve by shifting the data sets along the time axis. As discussed in Chapter 1, section 3, an Arrhenius law (equation (1.3.5)) [19] is used to mathematically define the time-temperature superposition behavior of the neat resin master curve. The viscoelastic

activation energy and reference temperature of the master curve is obtained from linearly fitting the logarithm (base 10) of the shift coefficients versus the inverse of the test temperatures graphed in Figure 2.4.2. The Prony series (equation (1.3.7b)) fit to the master curve is depicted by the dashed black line.

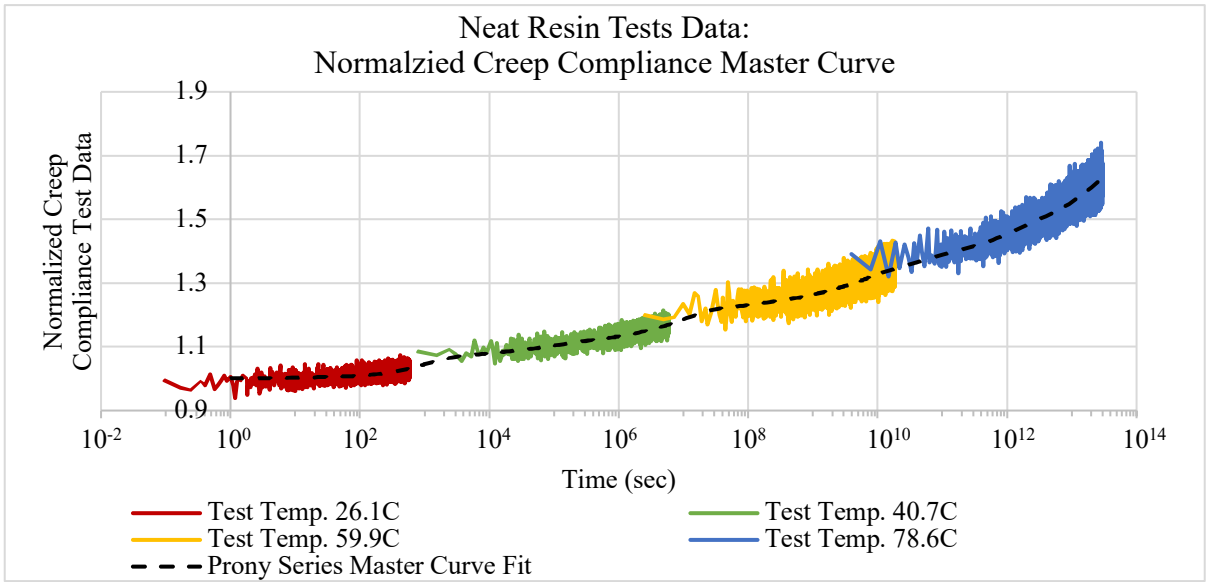

Figure 2.4.1: The neat resin creep compliance test data conducted at four different constant temperatures are shifted on the time axis to create a creep compliance master curve. Creep compliance is normalized by the instantaneous (i.e., glassy) compliance of the initial creep test. A Prony series is fit to the data representing the master curve of the neat resin epoxy.

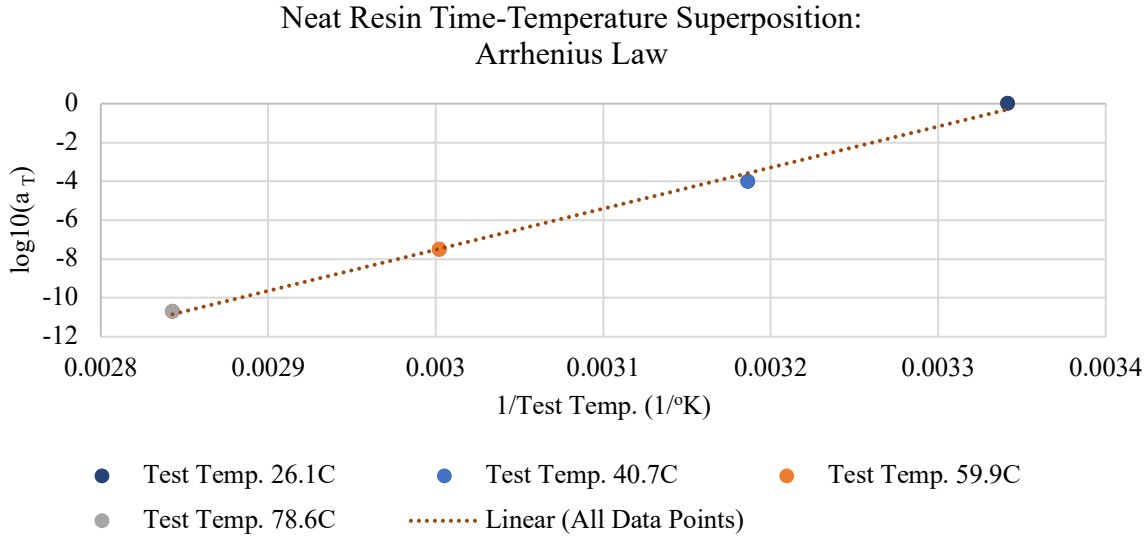

Figure 2.4.2: The log10 of the shifted time coefficient obtained when generating the neat resin creep master curve from the compliance data measured at four different constant temperature tests are plotted verse the inverse of the corresponding test temperatures. A linear fit depicting the Arrhenius law (equation (1.3.5)) is used to obtain the viscoelastic activation energy.

The same steps describing the formation of the neat resin master curve are applied to the measured unidirectional, plain weave, 3-ply, and 4-ply laminate material properties in order to generate their respective master curves. The measured unidirectional, plain weave, 3-ply, and 4-ply laminate master curve properties are presented in Figure A.9 through Figure A.16 in the appendix. Each laminate sample, except that of the plain weave, requires a series of three graphs to depict the tensile creep normalized master curve axial (equation (2.3.3)), transverse/axial (equation (2.3.4)), and transverse (equation (2.3.8)) properties. The PW only requires two graphs because the axial and transverse properties are equivalent due to the laminate's symmetry. Two graphs for each laminate sample are needed to depict the axial (equation (2.3.12)), and transverse (equation (2.3.13)) creep flexure master curves in normalized form. The Prony coefficients of the compliance master curve fits are presented in Table A.11 through Table A.15 in the appendix along with the Arrhenius viscoelastic activation energy and the master curve reference temperature. The measured unidirectional laminate axial creep compliance and axial creep flexure master curves reveal that these laminate properties are elastic, not viscoelastic. As a result, the raw data in Figure A.9 and Figure A.10 are presented without a Prony series fit or an Arrhenius viscoelastic activation energy. The axial creep compliance and axial creep flexure properties of the 4-ply laminate presented in Figure A.15 and Figure A.16 can also be treated elastically due to the small degree of creep measured. Further evidence for treating the 4-ply laminate as an elastic material in the axial direction is the time-temperature superposition shift of its flexure creep compliance master curve test data (Figure A.16) not aligning sequentially. The lowest constant temperature test, at 24.0^{o}C, should be the initial data set when forming the axial

flexure master curve. Instead, the 39.7°C and 60.1°C test data align more favorably, superseding the 24.0°C data set.

A viscoelastic material is defined as linear viscoelastic when the stress/strain response is a linear superposition of the effects of multiple individual loads. Figure 2.4.3 depicts a series of creep tests with different constant stresses. The linear stress and strain relationship from the creep tests at a given moment in time are plotted in the bottom graph. The same method depicted in Figure 2.4.3 is performed on all tensile creep samples to check the linearity of the response. Similar to elastic materials, the stress/strain behavior is dependent on the applied load and temperature. However, the stress/strain response tends to become nonlinear as the applied load increases and as the test temperature approaches the glass transition temperature [16], [33]. To avoid the non-linear behavior near the glass transition temperature, a maximum temperature (~80°C) is used for all linear viscoelastic validation tests. Figure 2.4.4 plots the stress/strain results for neat resin samples at three different constant stresses. The stress/strain results at 1 sec., 10 sec., 100 sec., and 1000 sec. are identified in the graph. Linear fits indicate that the neat resin samples in the applied stress and temperature range studied exhibit linear viscoelasticity. Linear viscoelastic stress/strain tests in both bending and tension were conducted on all of the material samples. Results indicate that all materials in the experimental stress/strain and temperature ranges behave linearly viscoelastic.

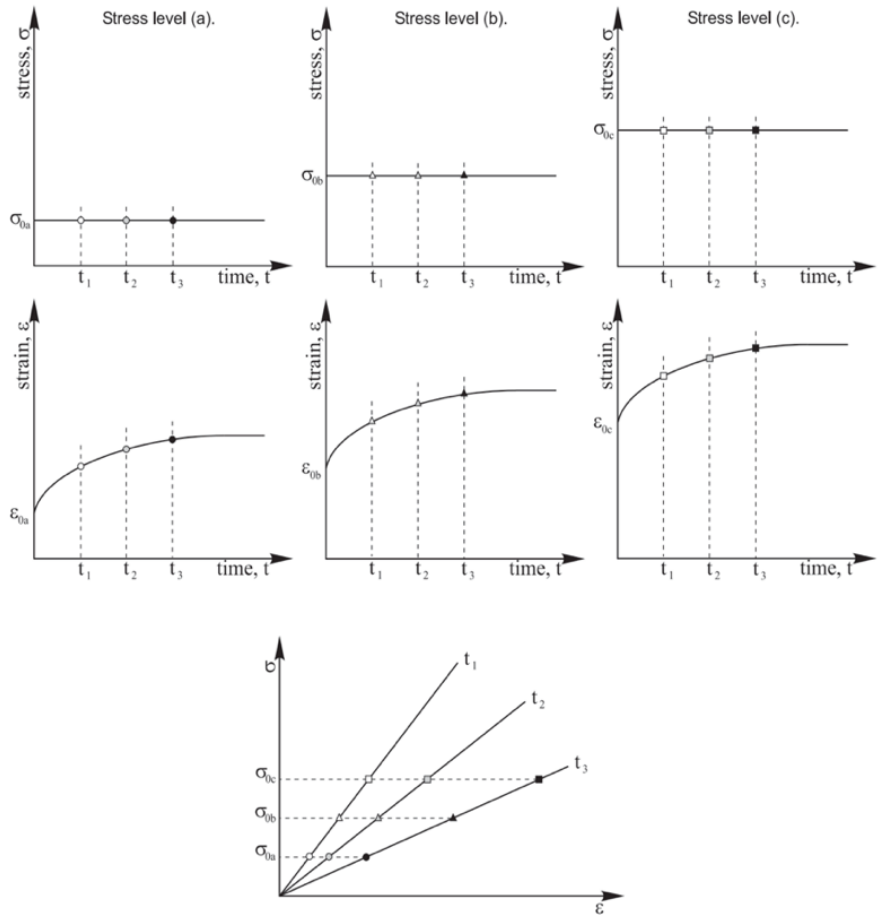

Figure 2.4.3: Linear viscoelasticity is determined by preforming a series of creep test at vary increments of applied constant stress. The top graph depicts three varying constant applied stresses; middle graphs depict the creep strain results due to the applied stresses; bottom graph depicts the stress/strain results at three different elapsed time intervals. The linearity of the stress/strain results at varying time intervals indicates that the material is linear viscoelastic. [16]

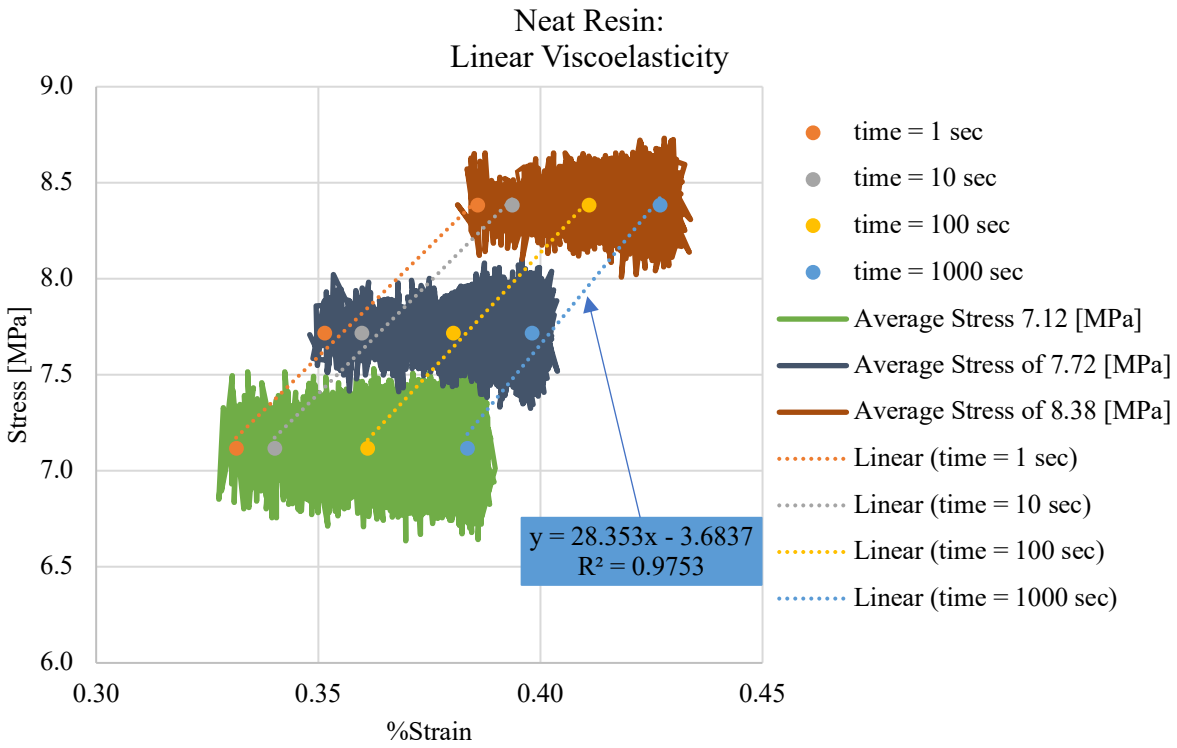

Figure 2.4.4: The creep stress/strain results for neat resin tensile samples due to three different constant applied stresses are plotted. Tests are performed at the maximum constant test temperature (~80°C). The stress/strain results at 1 sec., 10 sec., 100 sec., and 1000 sec. are identified in the graph. Linear fits indicate that the neat resin samples, in the applied stress and temperature range studied, exhibit linear viscoelasticity.

2.5 Discussion

The viscoelastic response of neat resin, unidirectional, 45° plain weave, 3-Ply [45PW/0/45PW] and 4-Ply [0/45PW/45PW/0] samples tested in this dissertation under both tension and bending loading conditions provide deeper insight into the viscoelastic characteristics of composites than if only one test method or one type of laminate had been measured. The effects of stacking sequence and orientation of laminae on the viscoelastic properties of composites are more accurately quantified as a result of using the two loading conditions and a variety of laminates. The experimental results for each laminate type from the tests at the four constant levels of temperature spanned a time duration that was sufficient

to provide a continuous material master curve using time-temperature superposition. The master curve properties, however, are incomplete since they do not completely measure a sample's glassy ($t = 0$) to equilibrium ($t \to \infty$) properties. Even at the maximum elevated temperature (~80°C), the experimental time durations are not sufficient to determine the equilibrium properties.

A test temperature greater than 80°C was attempted for the neat resin sample, but this resulted in noticeable discoloration in the sample indicating damage to the polymer chains. Furthermore, the properties of a sample approaching the glass transition temperature are known to be non-linear. The experimental measurements of each sample in the selected thermal range, 25°C to 80°C, are within the linear viscoelastic regime, exemplified in the neat resin results presented in Figure 2.4.4. Time did not permit experiments to be conducted that captured the material equilibrium properties of the samples tested. As a result, a comparison of the equilibrium properties of each laminate type to assess the effects that elastic fiber stacking sequence and orientation have on the viscoelastic properties of composites are not quantified in this chapter. However, the transient viscoelastic properties of the tested material can be compared and analyzed without the equilibrium properties being known. The transient properties that are quantified in this chapter are arguably the most important characteristic to understand. Most design applications rarely involve materials reaching equilibrium even at increased temperatures due to the long transient times (years) characteristic of the heavily crosslinked polymers. The effective transient time of the materials tested in our experiments spanned a time frame of at least three years, exceeding the typical storage cycle of most deployables.

The measured data discussed in the results section (including Figure A.9 through Figure A.16 in the appendix) records the tensile and flexure tests used to observe the viscoelastic behavior of various composites. A comparison of the data is best achieved by comparing the neat resin, unidirectional, plain weave, 3-ply, and 4-ply laminates equivalent master curve properties (e.g., all laminates' axial creep compliance properties) on the same graph in normalized Prony series form. The laminate master curve properties, axial creep compliance (equation (2.3.3)), axial/transverse creep compliance (equation (2.3.4)), transverse creep compliance (equation (2.3.8)), axial creep flexure (equation (2.3.12)), and transverse creep flexure (equation (2.3.13)), are presented for all measured laminate samples in Figure 2.5.1 through Figure 2.5.5, respectively. As noted in the results section, the axial creep compliance, axial/transverse creep compliance, and axial creep flexure properties of the unidirectional laminate result in an elastic response due to the presences of the purely elastic carbon fibers aligned in the axial direction (0^o). Similarly, the 4-ply laminate axial creep compliance and axial creep flexure properties are elastic due to the two axially aligned unidirectional surface ply laminae. A straight horizontal line equal to unity represents the elastic behavior of the unidirectional laminate in Figure 2.5.1, Figure 2.5.2, and Figure 2.5.4. The normalized Prony series master curves presented in Figure 2.5.1 to Figure 2.5.5 are shifted to a common temperature of 25^oC using the respective laminate material Arrhenius law. Additional thermal corrective shifts to the time axis using the respective laminate master curve Arrhenius laws are required to best align the unidirectional transverse creep compliance and flexure, 3-ply axial, axial/transverse, and transverse creep compliance, and 4-ply axial/transverse and transverse creep compliance, as well as the axial flexural creep

properties. A thermal shift of $+5^0$C, -2^0C, $+5^0$C, $+5^0$C, $+8^0$C, $+10^0$C, $+10^0$C, and -5^0C are applied to the respective laminate master curves.

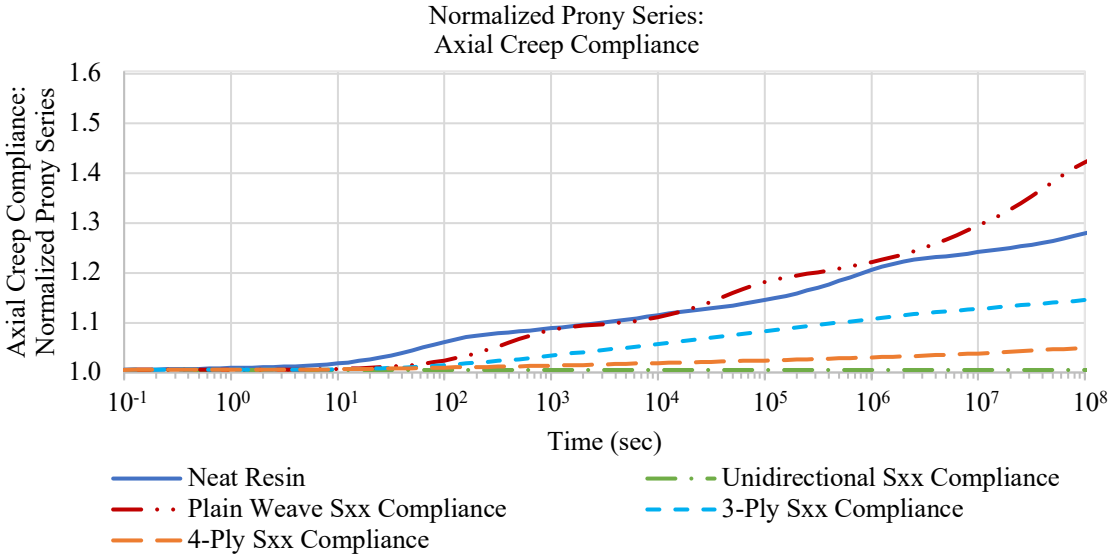

Figure 2.5.1: The normalized Prony series master curve fits to the measured axial creep compliance data for the neat resin, unidirectional, plain weave, 3-ply and 4-ply laminates are complied in a single graph.

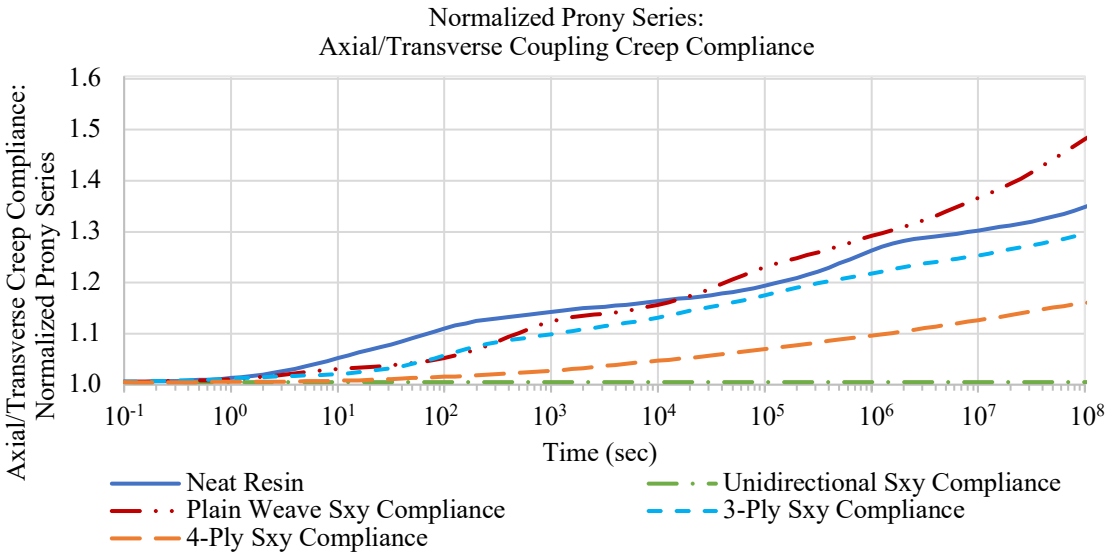

Figure 2.5.2: The normalized Prony series master curve fits to the measured axial/transverse creep compliance data for the neat resin, unidirectional, plain weave, 3-ply and 4-ply laminates are complied in a single graph.

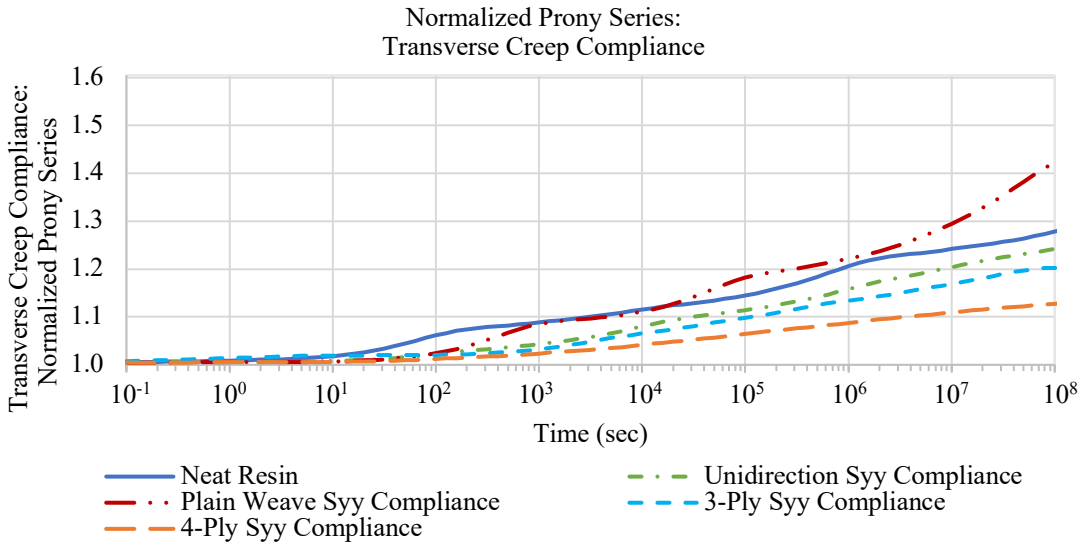

Figure 2.5.3: The normalized Prony series master curve fits to the measured transverse creep compliance data for the neat resin, unidirectional, plain weave, 3-ply and 4-ply laminates are complied in a single graph.

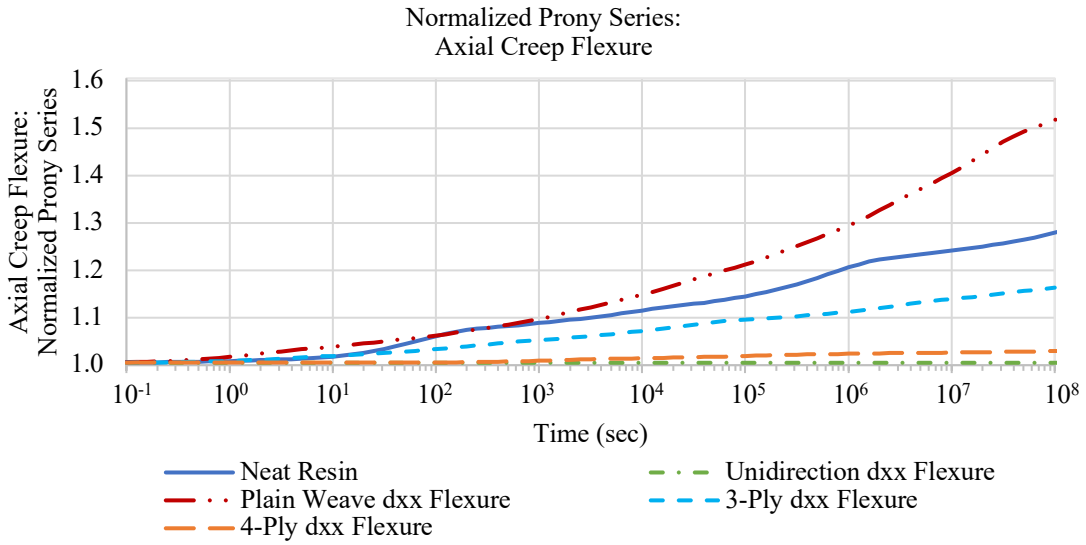

Figure 2.5.4: The normalized Prony series master curve fits to the measured axial creep flexure data for the neat resin, unidirectional, plain weave, 3-ply and 4-ply laminates are complied in a single graph.

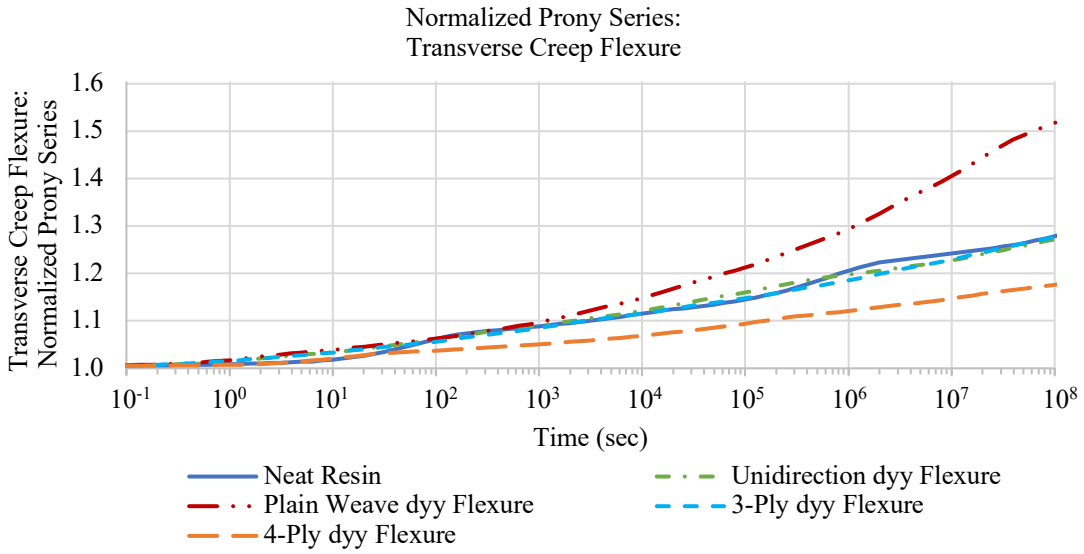

Figure 2.5.5: The normalized Prony series master curve fits to the measured transverse creep flexure data for the neat resin, unidirectional, plain weave, 3-ply and 4-ply laminates are compiled in a single graph.

In addition to the normalized Prony series representation of the data, the time-dependent transient contribution to viscoelasticity represented by the transient proportional response function defined in equation (2.2.3b) for creep can give further insight to the effects fiber integration, laminate stacking sequence, and laminate orientation have on the viscoelastic response of composites. Similar to the normalized Prony series master curves presented above, the transient proportional response functions of the neat resin, unidirectional, plain weave, 3-ply, and 4-ply laminates for a particular material property are compared on the same graph. Figure 2.5.6 to Figure 2.5.10 present the respective axial creep compliance, axial/transverse creep compliance, transverse creep compliance, axial creep flexure, and transverse creep flexure for all tested laminates. The transient proportional response ranges from zero, i.e., no viscoelastic change at $t = 0$ (glassy response), to one, i.e., maximum viscoelastic change at $t \to \infty$ (equilibrium response). In the case of the materials measured in this chapter, the tests were unable to access the equilibrium properties of the laminate samples. The transient proportional response represented by equation (2.2.3b) can be

redefined for data sets that do not reach equilibrium. C^e is replaced by $C^{t_{end}}$ in which t_{end} is the time interval of the last measured data point of a viscoelastic master curve.

$$\tilde{C}(t) = \sum_{i=1}^{n} \left(\frac{C^i}{C^{t_{end}} - C^i} \left(1 - e^{-\beta^i t} \right) \right) \tag{2.5.1}$$

The measured master curve properties all have varying test durations; as a result, a comparison of the viscous contribution of various laminates must be evaluated based on the master curve data set with the shortest time duration, $t = 10^8 sec$.

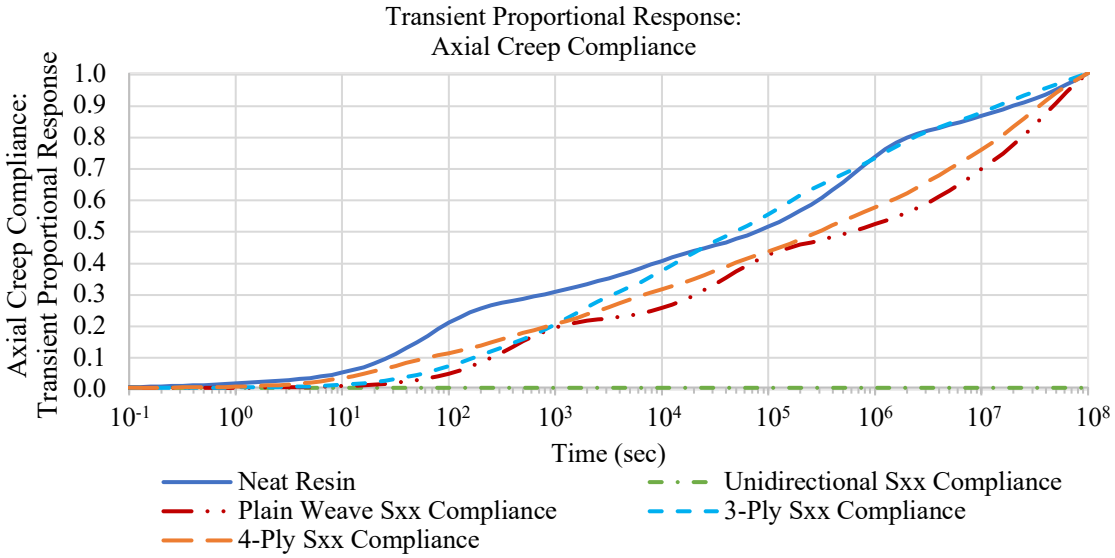

Figure 2.5.6: The transient proportional response of the measured axial creep compliance data for the neat resin, unidirectional, plain weave, 3-ply and 4-ply laminates are recorded in a single graph.

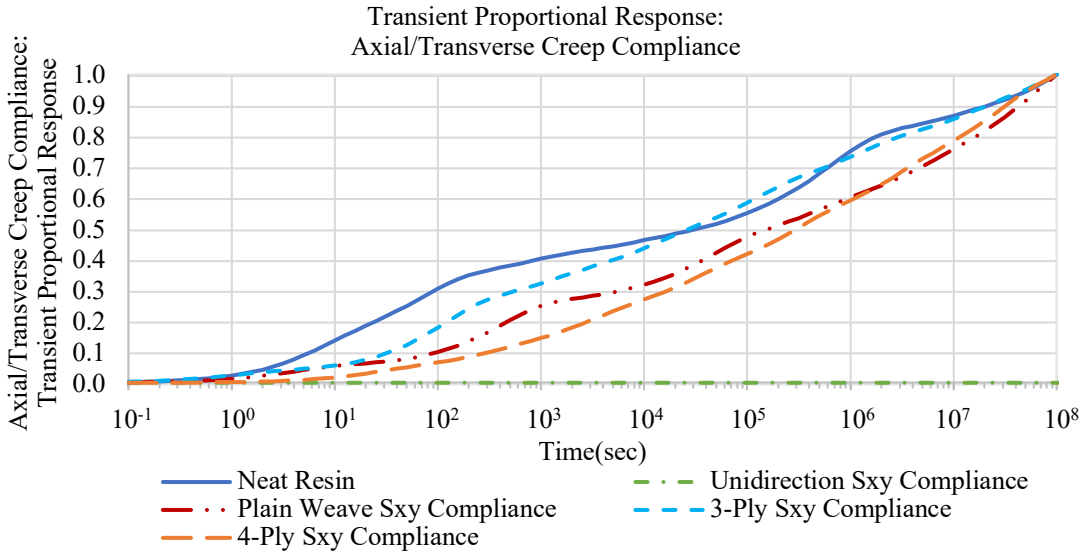

Figure 2.5.7: The transient proportional response of the measured axial/transverse creep compliance data for the neat resin, unidirectional, plain weave, 3-ply and 4-ply laminates are recorded in a single graph.

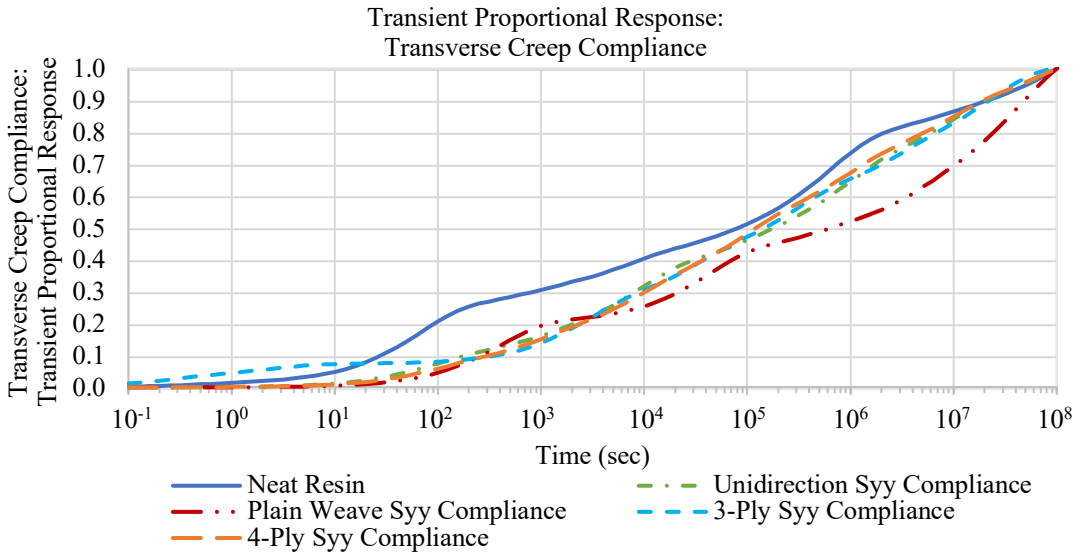

Figure 2.5.8: The transient proportional response of the measured transverse creep compliance data for the neat resin, unidirectional, plain weave, 3-ply and 4-ply laminates are recorded in a single graph.

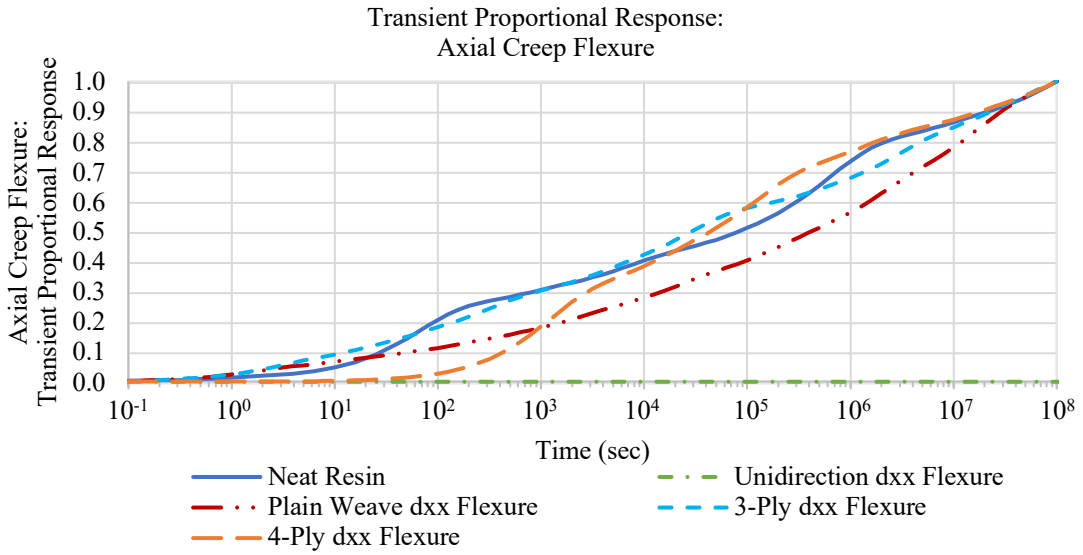

Figure 2.5.9: The transient proportional response of the measured axial creep flexure data for the neat resin, unidirectional, plain weave, 3-ply and 4-ply laminates are recorded in a single graph.

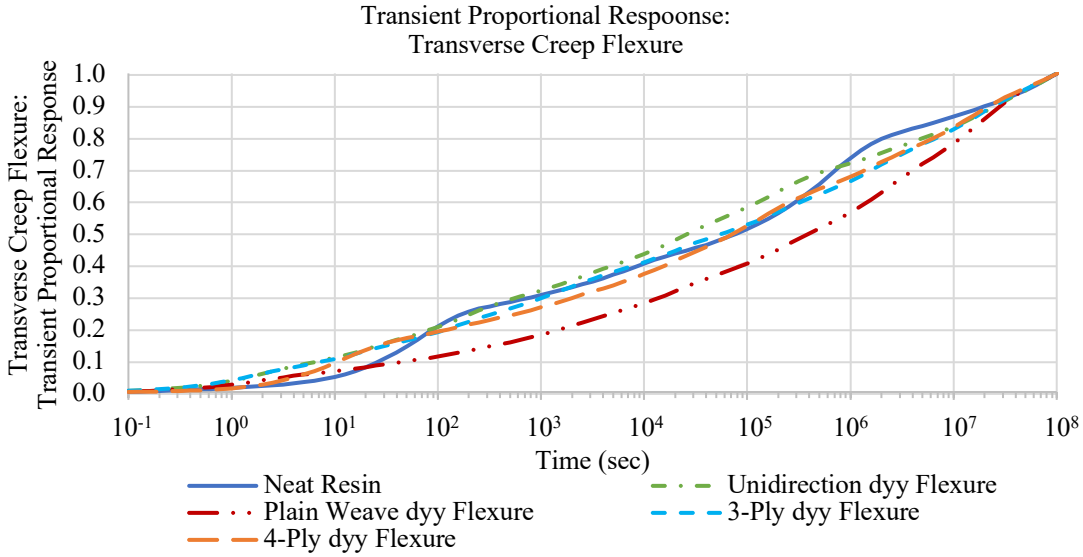

Figure 2.5.10: The transient proportional response of the measured transverse creep flexure data for the neat resin, unidirectional, plain weave, 3-ply and 4-ply laminates are recorded in a single graph.

The laminate material properties derived from the creep test performed on the unidirectional, plain weave, 3-ply and 4-ply laminates are compared to the viscoelastic properties of the neat resin, the source of the viscoelastic behavior in the tested laminates, in order to understand how the integration of purely elastic continuous carbon fibers constrain the neat resin viscous properties through either direct integration in the case of the

unidirectional and plain weave laminae or by variation in stacking sequence and orientation of such laminates in the case of the 3-ply and 4-ply laminates.

2.5.1 Unidirectional Laminae

In the case of the unidirectional lamina, the introduction of continuous elastic fibers results in axial compliance and flexure properties that are purely elastic (Figure 2.5.1 and Figure 2.5.4, respectively). The transverse tensile creep compliance (Figure 2.5.3) and creep flexure (Figure 2.5.5) properties are matrix dominated (viscoelastic) due to the absence of fibers oriented in the transverse direction. More notably, however, the viscoelastic transverse properties presented in normalized form and transient proportional response form (Figure 2.5.3 and Figure 2.5.8 for transverse creep compliance, respectively, and Figure 2.5.5 and Figure 2.5.10 for creep flexure, respectively) match that of the neat resin. The stiffness is greater in the transverse property than the neat resin due to the integration of the fibers. However, when compared using the transient proportional response over the span of 10^8 seconds, they are equivalent. The transverse/axial creep compliance, unlike the neat resin, is elastic due to the presence of the elastic fibers. The integration of elastic fibers in the neat resin that form the unidirectional lamina result in a composite with elastic properties in the direction of the fibers and viscoelastic properties in the matrix dominant directions that directly match that of the neat resin except with increased stiffness.

2.5.2 Plain Weave Laminae

The woven elastic continuous fiber tows of the plain weave laminae oriented 45^o to the x-axis do not prevent viscoelasticity. In fact, the measured plain weave lamina axial properties (tensile creep compliance and creep flexure) are more viscoelastic than the neat resin system as depicted in the normalized Prony series plot presented in Figure 2.5.1 and Figure 2.5.4,

respectively. The compliance and flexure properties from the two different loading systems, however, match favorably when compared using the normalized Prony series plots. The transient proportional response between flexure and creep are also similar, but the transient proportional response is greater than that of the neat resin. This is more noticeable when comparing the transient proportional response of the plain weave's axial/transverse creep compliance to that of the neat resin (Figure 2.5.7). It is believed that the material's transient proportional response is great than the neat resin properties due to the fiber weave elongating over time. Traditionally, it has been suspected that the fibers in the plain weave lamina would mitigate the transient response of the matrix to some degree, regardless of fiber orientation. On the contrary, the test data indicate that the laminate with plain weave laminae exhibits a more pronounced transient response. Publications indicate that the stress response behavior of plain weave laminae differs from that of unidirectional laminae due to the kinked tows of the plain weave [28], [34], [35]. Our results suggest that further testing of plain weave laminae in different orientations along with further stress analysis is required to better understand the effects of woven fibers on the transient response behavior of a plain weave laminate.

2.5.3 3-ply Laminate

The unidirectional lamina at the center of the 3-ply laminate does not mitigate creep in the tensile axial compliance property. This is surprising, considering that the measured unidirectional lamina presented in Figure 2.5.1 exhibits no viscoelasticity in the fiber direction. The axial bending stiffness, however, as expected, crept due to the majority of the bending stresses being applied to the viscoelastic 45^{o} plain weave laminae on both surfaces of the 3-ply laminate. The clamping method used to hold the samples may account for the

transient proportional response in the axial direction as a result of shear loading in the viscoelastic 45^{o} plain weave laminae on both surfaces of the composite. The plain weave laminae shear out-of-plane while the fiber direction of the unidirectional lamina in the center remains fixed. This is different than slipping in which the grips would lose their hold on the samples. Continuous clamping is monitored by observing the Instron machine's displacement behavior, which indicates continuous viscoelastic evolution without sudden jumps (skips) that would occur when static frictional grip is lost. The load path of the axial tensile test is through the viscous plain weave ply, which may explain why the normalized axial tensile creep compliance and creep flexure are so similar.

The transient proportional response of the transverse compliance and flexure properties presented in Figure 2.5.8 and Figure 2.5.10, respectively, are nearly equivalent and almost match the behavior of the neat resin. This is interesting since the majority of the laminate is comprised of the plain weave laminae, which were found to exhibit a degree of viscoelasticity greater than that of the resin system. The elastic fibers of the unidirectional lamina at the midplane of the 3-ply laminate in the axial direction may be preventing the plain weave laminae from elongating due to constrained Poisson's interactions. As mentioned earlier, further investigation into the plain weave laminate behavior is required before a more robust conclusion can be drawn. The 3-ply laminate's normalized axial/transverse compliance presented in Figure 2.5.2 exhibits less viscoelastic change than that of the neat resin, indicating the unidirectional lamina at the midplane of the 3-ply laminate does mitigate creep to some degree.

While the normalized axial creep compliance and creep flexure curves (Figure 2.5.1 and Figure 2.5.4, respectively) differ from the normalized neat resin, the corresponding transient

proportional response (Figure 2.5.6 and Figure 2.5.9, respectively) match that of the neat resin. This indicates that the viscous contribution of the neat resin, the root of viscoelasticity in composites, is unchanged by the integration of elastic fibers. This behavior is also present in the transverse creep compliance and creep flexure properties, as well as the axial/transverse creep compliance.

2.5.4 4-ply Laminate

The orientation and stacking sequence of the 4-ply laminate prevent creep from occurring in the axial direction. For example, the plain weave lamina at the neutral axis of the 4-ply laminate experiences little to no stress in bending. On the other hand, the unidirectional laminae located at the surface of the laminate react to applied bending stresses. As a result, the axial flexure properties (Figure 2.5.4) are essentially elastic. Similarly, the tensile axial creep compliance (Figure 2.5.1) is also nearly elastic, with the majority of the applied stress carried by the much stiffer unidirectional plies. It was assumed that the 3-ply laminate would behave similarly, but as previously stated, the clamping method used to apply a constant load to the samples is believed to apply an out-of-plane shear load (matrix dominant load condition) to the plain weave surface plies. This may also indicate why the tensile axial creep compliance has a small degree of creep over the duration of the normalized compliance curve. The transverse compliance and flexure properties of the 4-Ply laminate presented in Figure 2.5.3 and Figure 2.5.5, respectively, are nearly identical, with both properties exhibiting a degree of creep that is less than that of the neat resin. The slight difference between the results from the tensile and flexure loading conditions is a consequence of stress distribution throughout the laminate. In the case of the tensile test, which distributed the stress across each ply of the 4-ply laminate, the normalized compliance is slightly stiffer and

is believed to be a result of the fiber contribution from the two innermost 45^{o} plain weave plies. The bending test, which primarily loads the viscoelastic unidirectional transverse laminae at the surface of the laminate, is affected less by the plain weave laminae due to the plies' close proximity to the neutral axis. This behavior is contrary to the results of the plain weave test in which the laminate exhibits more viscoelasticity than the neat resin. As with the 3-ply laminate, it appears the introduction of the unidirectional fibers resists the Poisson contraction of the laminate, which may contribute to a reduction in the creep compliance of the plain weave response in the 4-ply laminate. The axial/transverse creep compliance presented in Figure 2.5.2 in normalized Prony series form is viscoelastic. The unidirectional plies at the surface of the 4-Ply laminate do not behave like the tested unidirectional laminate in which the axial/transverse coupling compliance properties are elastic. This is believed to be the result of the axial properties having only a slight viscoelastic response.

The creep master curves obtained by the experimental measurements of the neat resin, unidirectional, plain weave, 3-ply and 4-ply laminates in both tension and bending provide a means of quantifying the drivers of viscoelasticity in composites. By observing the transient proportional response of the test sample properties measured, it is clear that the source of viscoelasticity is the neat resin, and this response is unchanged by the integration, orientation, or stacking layup of elastic carbon fibers. The neat resin normalized compliance is mitigated in composites when plies with viscoelastic resistant properties in specific directions are oriented and stacked such that they resist creep in the direction of applied loads. Ideal laminate layups that reduce viscoelastic response can better be determined by understanding the effects of fiber placement, which does not always guarantee non-viscoelastic composites as exemplified in the 3-Ply and 4-Ply axial properties. The integration of the fibers and,

orientation and stacking sequence of the laminae affect the degree of creep and stiffness of the composite materials. However, the transient proportional response of the resin system comprising the matrix of the laminates is unaffected. It is shown that viscoelasticity of thin shell composites commonly used in aerospace hinge and deployable applications is a result of the resin system. Prediction methods built on the framework of resin driven creep can be validated and improved based on these findings.

2.6 Conclusion

Tensile and flexure creep tests performed on neat resin, unidirectional, plain weave, 3-ply, and 4-ply laminate samples proved that fiber integration, stacking sequence, and orientation play a crucial role in the viscoelastic properties of laminates. Comparison of the two loading conditions not only validates the quality of the tests and confirm the absence of artifacts particular to a specific test method but, more importantly, show how load distribution affects the viscoelastic properties of laminates. The degree of creep is affected by the integration of fibers and the orientation and stacking sequence of plies with viscoelastic resistant properties. In general, the placement of viscoelastic resistant plies in the direction of loads reduces the composite's viscoelastic response. In other words, as the degree of creep decreases, the stiffness increases. However, observation of the transient proportional response of the measured data reveals that the neat resin transient proportional response is unchanged in laminates regardless of fiber integration, laminate orientation, or stacking sequence. Based on these findings, viscoelastic laminate prediction methods can be established based on the neat resin properties alone.

Chapter 3

Inversion of Anisotropic Viscoelastic Properties

3.1 Introduction

The mathematical analysis and prediction of the behavior of viscoelastic materials are dependent on accurate models of their relaxation modulus and creep compliance properties. Unlike elastic materials, where conversion from moduli to compliances and *vice versa* is a simple linear matrix inversion, interchange between such properties of a viscoelastic material due to time dependence requires direct measurements or special inversion methods. Direct experimental tests for both relaxation and creep properties are often difficult and time-consuming. The ability to convert between these properties by mathematical inversion methods only requires the measurement of one set of viscoelastic properties.

Almost all available inversion methods for viscoelasticity utilize the Laplace transform domain to convert time-dependent problems to equivalent elasticity techniques. This was first introduced by Schapery [36], [37] and has set the framework for most viscoelastic Laplace transform inversion methods. In his approach, the inverted viscoelastic properties, in the form of a Dirichlet-Prony series (equations 1.3.4a and 1.3.4b), are approximated through the

use of least-squares. Given the limitation of computational capacity in the 1960s, Schapery's method was a system that aimed to make linear equations solvable by conventional mathematics. Several disadvantages, however, result from this outcome. 1) The unknown function's Prony time constants (α^i and β^r) must be assumed empirically and are often set equal to those of the known function's Prony time constants. The validity of such an assumption will be elaborated on later in this chapter. The predicted inverted Prony constants that should represent creep or relaxation curves can result in a function that does not satisfy energy principles, e.g., the relaxation Prony constants M^i are not all positive or the creep Prony constants C^r are not all negative. As a consequence, Schapery's method may poorly represent viscoelastic materials. Gutierrez-Lemini [38] defines a better means for achieving the ideal approach for 1-D materials. His method, while approximate in the sense that measured data is required to be fitted with a Dirichlet-Prony series, is defined by him as being exact because it remains in the time domain, using the hereditary integral form of the viscoelastic stress and strain equation to invert the material properties. There is no need for the method to use approximate transformations or inverse transformations between the time domain and Laplace domain. Furthermore, this inversion process does not require the time-dependent properties of the inverse function to be known and results in consistent, appropriate signs for all Prony constants (e.g., negative for creep and positive for relaxation).

The complexity of inverting creep and relaxation is dramatically increased for anisotropic materials. The material's directional properties may vary in the degree of viscoelasticity. In the case of a unidirectional carbon fiber lamina, matrix dominated directions such as shear and transverse properties will experience viscoelastic evolution while the fiber direction will remain elastic. Few inversion methods are found in the literature to model such materials and

they make assumptions in general that limit the application and accuracy of solutions. One method of handling 2- and 3-dimensional viscoelastic constitutive behavior is to treat it as 1-dimensional by breaking it into the deviatoric and isotropic contributions [39], [40], an approach that proves less useful for anisotropic materials. Other approaches attempt to predict the time-dependent Poisson's ratio [41], [42], so that anisotropic materials can be handled. Due to the high precision required to measure viscoelastic Poisson's ratios, comparisons between predictions and experimental data often result in unacceptable error. The ideal method, however, forgoes predicting Poisson's ratios and directly computes the inversion of the anisotropic creep compliance and relaxation moduli [43]–[45]. This chapter shows how the principles of Schapery's Laplace inversion for 1-dimensional problems can be developed into a robust anisotropic viscoelastic (multidimensional) method that maintains consistency with fundamental energy principles and provides the means of solving for the unknown Prony time constant, (α^i and β^r). Furthermore, Gutierrez-Lemini's [18] exact method while useful for 1-D materials and treatments is shown to be unusable as a means of inverting the multiaxial response of anisotropic viscoelastic materials.

3.2 Background

The Stieltjes convolution integral (3.2.3b), which describes the relationship between known creep and unknown relaxation properties, is derived below. Figure 3.2.1 shows the results of a creep test in which viscoelastic strain is measured as a result of an applied steady-state, uniaxial stress, σ_o, (e.g., all other components of the array are zero) which is represented mathematically by equations (3.2.1) and (3.2.2b) respectively.

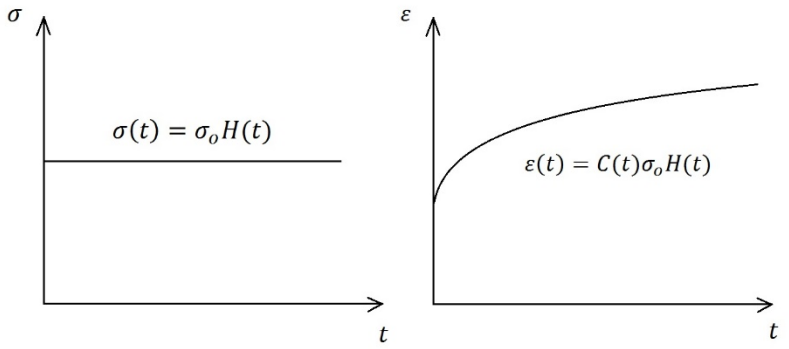

Figure 3.2.1: Left graph depicts a step response in applied stress. The right graph depicts the resulting creep response of a material to the constant stress depicted in the left graph.

$$\sigma_l(t) = H(t)\sigma_l$$
$$\sigma_l = \begin{cases} \sigma_o & for\ l = v \\ 0 & for\ l \neq v \end{cases} \tag{3.2.1}$$

The applied stress (3.2.1) is input into the strain hereditary integral (2.2.6). The derivative of the Heaviside step function results in the Dirac delta function $\delta(t)$.

$$\varepsilon_k(t) = \int_{0^-}^{t} C_{kl}(t-\tau)\delta(\tau)\sigma_l d\tau \tag{3.2.2a}$$

The creep compliance becomes a vertical array with column v due to the uniaxial stress state.

$$\varepsilon_k(t) = C_{kl}(t)\sigma_l = C_{kv}(t)\sigma_o \tag{3.2.2b}$$

The creep strain due to an applied stress step function (3.2.2b) is then placed into stress hereditary integral (2.2.5) and set equal to stress input (3.2.1).

$$H(t)\sigma_m = \int_{0^-}^{t} M_{mk}(t-\tau)\frac{d}{d\tau}C_{kv}(t)\sigma_o d\tau \tag{3.2.3a}$$

The stress tensor is factored out and inverted to the left side of equation (3.2.3a), resulting in the Kronecker delta in which all values are zero except at the uniaxial stress state $m = v$.

$$H(t)\delta_{mv} = \int_{0^-}^{t} M_{mk}(t-\tau)\frac{d}{d\tau}C_{kv}(\tau)d\tau \tag{3.2.3b}$$

The above method is repeated to obtain the Stieltjes convolution integral relating unknown creep to known relaxation properties. Figure 3.2.2 depicts the applied strain and

relaxation stress response represented mathematically by equations (3.2.4) and (3.2.5), respectively.

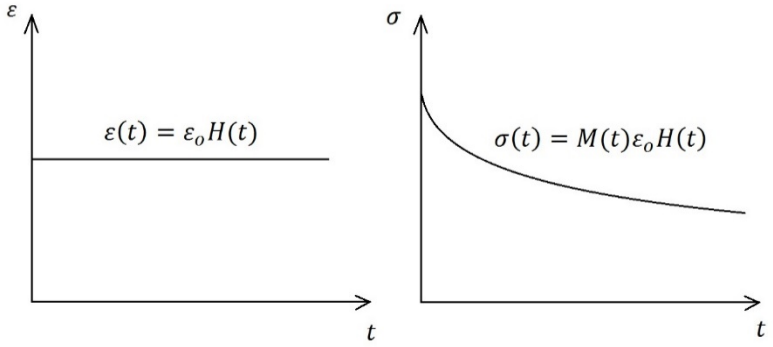

Figure 3.2.2: Left graph depicts a step response in applied strain. The right graph depicts the relaxation response of a material to the constant strain depicted in the left graph.

$$\varepsilon_m(t) = H(t)\varepsilon_m$$
$$\varepsilon_m = \begin{cases} \varepsilon_o & for\ m = v \\ 0 & for\ m \neq v \end{cases} \tag{3.2.4}$$

The applied strain (3.2.4) is input into the hereditary stress integral (2.2.5).

$$\sigma_n(t) = \int_{0^-}^{t} M_{nm}(t-\tau)\delta(\tau)\varepsilon_m d\tau \tag{3.2.5a}$$

The relaxation modulus becomes a vertical array with column v due to the uniaxial strain state.

$$\sigma_n(t) = M_{nm}(t)\varepsilon_m = M_{nv}(t)\varepsilon_o \tag{3.2.5b}$$

Inserting (3.2.5b) into strain hereditary integral (2.2.6) and setting it equal to equation (3.2.4) results in the following.

$$H(t)\varepsilon_k = \int_{0^-}^{t} C_{kn}(t-\tau)\frac{d}{d\tau}M_{nv}(\tau)\varepsilon_o d\tau \tag{3.2.6a}$$

The strain tensor is factored out and inverted to the left side of equation (3.2.6a), resulting in the Kronecker delta in which all values are zero except at the uniaxial strain state $k = v$.

$$H(t)\delta_{kv} = \int_{0^-}^{t} C_{kn}(t-\tau)\frac{d}{d\tau}M_{nv}(\tau)d\tau \tag{3.2.6b}$$

The Laplace transform of equations (3.2.3b) and (3.2.6b), derived below, prove that either equation can be used for inverting between relaxation and creep regardless of which viscoelastic properties are known. Starting with the right side of equation (3.2.3b), the Laplace transform of the hereditary integral is expressed below.

$$\mathcal{L}\left[\int_{0^-}^{t} M_{mk}(t-\tau)\frac{d}{d\tau}C_{kv}(\tau)d\tau\right] = \mathcal{L}[M_{mk}(t)]\,\mathcal{L}\left[\frac{d}{dt}C_{kv}(t)\right] = s\bar{M}_{mk}(s)\bar{C}_{kv}(s) \qquad (3.2.7a)$$

The Laplace transform of equation (3.2.6b) results in the same form as the Laplace transform of equation (3.2.3b), proving that both Stieltjes convolution integrals are independent of inversion direction.

$$\mathcal{L}\left[\int_{0^-}^{t} C_{kn}(t-\tau)\frac{d}{d\tau}M_{nv}(\tau)d\tau\right] = \mathcal{L}[C_{kn}(t)]\,\mathcal{L}\left[\frac{d}{dt}M_{nv}(t)\right] = s\bar{C}_{kn}(s)\bar{M}_{nv}(s) \qquad (3.2.7b)$$

The Laplace inversion of a Heaviside step function acting at $t = 0$ is $\frac{1}{s}$, where s is the frequency domain. The Laplace transforms of equations (3.2.3b) and (3.2.6b) produces the equation below.

$$\frac{\delta_{kv}}{s^2} = \bar{C}_{kn}(s)\bar{M}_{nv}(s) \qquad (3.2.8)$$

The Laplace transforms of equations (2.2.5) and (2.2.6)

$$\bar{\sigma}_l(s) = s\bar{M}_{lk}(s)\bar{\varepsilon}_k(s) \qquad (3.2.9)$$

$$\bar{\varepsilon}_k(s) = s\bar{C}_{kl}(s)\bar{\sigma}_l(s) \qquad (3.2.10)$$

can also be used to derive equation (3.2.8) by insetting equation (3.2.9) into equation (3.2.10) and factoring like terms.

3.3 Methods

3.3.1 Laplace Inversion—Schapery's Technique

Schapery's least-squares Laplace inversion method uses the one-dimensional case of equation (3.2.8) to invert creep and relaxation. This chapter will show how Schapery's method can be used for multidimensional materials. In the Laplace domain, the creep compliance and relaxation modulus can be linearly inverted. The exponential decay and growth of relaxation and creep, which is represented by Dirichlet-Prony series equations (1.3.4a) and (1.3.4b), make the transformation into the Laplace domain easy and accurate.

$$\bar{M}_{mk}(s) = \frac{M^e_{mk}}{s} + \sum_{i=1}^{n} \frac{M^i_{mk}}{s+\alpha^i_{mk}} \tag{3.3.1}$$

$$\bar{C}_{kl}(s) = \frac{C^e_{kl}}{s} - \sum_{r=1}^{n} \frac{C^r_{kl}}{s+\beta^r_{kl}} \tag{3.3.2}$$

Schapery's approximate Laplace inversion method [43] takes $f(t)$ to be the unknown viscoelastic response being sought with an assumed known behavior of either creep or relaxation depending on the direction of inversion. Dirichlet-Prony series (2.2.5) or (2.2.6) are used as an estimate function of the unknown viscoelastic response of the desired material. The total squared error between the approximate function, $f(t)$, and known function, $f_A(t)$, can be minimized by changing the Prony constants of the unknown function, M^i_{mk} or C^r_{kl}.

$$e(f, f_A) \equiv \int_0^\infty \big(f(t) - f_A(t)\big)^2 dt \tag{3.3.3}$$

The Laplace transform of the total squared error, assuming that both functions are represented by a Dirichlet-Prony series, results in the following expression.

$$\bar{f}_A(s)|_{s=\tau^j} = \bar{f}(s)|_{s=\tau^j} \tag{3.3.4}$$

$s = \tau^j$ is equal to the Prony time constants of the unknown function, which are assumed equal to the known function's Prony time constants (e.g., $\beta_{ml}^j = \alpha_{ml}^j$ regardless of inverting from relaxation to creep or creep to relaxation). The α_{ml}^j and β_{ml}^j Prony time constants must be equal for all components of the relaxation modulus and creep compliance, e.g., $\alpha^j = \beta^j$ for all values of m and l. The assumption that the Prony time constants are equal for both creep and relaxation limits the robustness and accuracy of the inversion method.

The following forms of equation (3.2.8) can be used to invert relaxation to creep

$$\bar{C}_{kl}(s) = \frac{\delta_{ml}}{s^2}\left(\bar{M}_{mk}(s)\right)^{-1} \tag{3.3.5a}$$

and creep to relaxation.

$$\bar{M}_{mk}(s) = \frac{\delta_{ml}}{s^2}\left(\bar{C}_{kl}(s)\right)^{-1} \tag{3.3.5b}$$

The inversion from creep to relaxation (3.3.5b) will be used for the following inversion derivation.

$$\bar{f}(s)|_{s=\beta^j} = \bar{M}_{mk}(s)|_{s=\beta^j} = \frac{M_{mk}^e}{\beta^j} + \sum_{r=1}^{n} \frac{M_{mk}^r}{\beta^j+\beta^r} \tag{3.3.6}$$

$$\bar{f}_A(s)|_{s=\beta^j} = \frac{1}{s^2}\left(\bar{C}_{ml}(s)\right)^{-1}|_{s=\beta^j} = \frac{1}{(\beta^j)^2}\left(\frac{C_{ml}^e}{\beta^j} - \sum_{i=1}^{n} \frac{C_{ml}^i}{\beta^j+\beta^i}\right)^{-1} \tag{3.3.7}$$

Equation (3.3.4) with $\bar{f}(s)|_{s=\beta^j}$ and $\bar{f}_A(s)|_{s=\beta^j}$ expressed by (3.3.6) and (3.3.7), respectively, can be represented as a system of linear equations with unknown Prony constants M_{ml}^r and equilibrium constants M_{ml}^e for every component of the relaxation modulus m and l.

$$F^{jr}A_{ml}^r = B_{ml}^j - F_{ml}^e \tag{3.3.8}$$

F^{jr} is a symmetric $n\ x\ n$ matrix where n is equal to the number of Prony series and is the same for all components of the relaxation modulus.

$$F^{jr} = \frac{1}{\beta^j + \beta^r} \qquad j = 1, n \text{ and } r = 1, n; \tag{3.3.8a}$$

A_{ml}^r is a series of vectors containing the unknown relaxation Prony constants for a particular component of the modulus matrix, e.g., $A_{11}^r = M_{11}^r$ for $r = 1, n$.

$$A_{ml}^r = M_{ml}^r \qquad r = 1, n; \tag{3.3.8b}$$

B_{ml}^j is a series of known vectors comprised of Laplace creep properties that have been linearly inverted, e.g., B_{11}^j corresponds to the 11 component of the linearly inverted creep matrix with length $j = n$, the number of Prony series.

$$B_{ml}^j = \frac{1}{(\beta j)^2}\left(\frac{C_{ml}^e}{\beta^j} - \sum_{i=1}^{n} \frac{C_{ml}^i}{\beta^j + \beta^i}\right)^{-1} \qquad j = 1, n \text{ and } i = 1, n; \tag{3.3.8c}$$

F_{ml}^e is a vector, n Prony series in length, containing the equilibrium properties for each component of the unknown viscoelastic matrix response, in this case, relaxation, e.g., $F_{11}^e = M_{11}^e$ for $m = l = 1$. The equilibrium constants of the unknown viscoelastic properties are found from linearly inverting the known viscoelastic equilibrium constants, e.g., $M_{ml}^e = [C_{ml}^e]^{-1}$.

$$F_{ml}^e = \frac{M_{ml}^e}{\beta^j} \tag{3.3.8d}$$

F^{jr} in equation (3.3.8) can be inverted and the unknown relaxation modulus values represented by A_{ml}^r can be solved.

$$A_{ml}^r = \left(F^{jr}\right)^{-1}\left(B_{ml}^j - F_{ml}^e\right) \tag{3.3.9}$$

In order to fully define the unknown relaxation modulus, equation (3.3.9) must be repeated for each component of the matrix, e.g., all values of m and l. For a 9 by 9 orthotropic material, there would be 9 unknown relaxation modulus components resulting in 9 variants of equation (3.3.9).

3.3.2 Numerical Laplace Inversion

A numerical Laplace method for inverting anisotropic materials can be used to provide a more exact means of interchanging between relaxation and creep properties. Based on similar principles used by Schapery's least-squares inversion, the numerical Laplace inversion directly solves equation (3.2.8) by numerical means. Assuming that the creep compliance is known, the relaxation modulus can be solved based on equation (3.3.5b). Unlike Schapery's method, which uses the Laplace inversion of least squares to minimize the error between the known and unknown viscoelastic functions when $s = \tau^j$ (τ^j equals either α^j or β^j), the numerical method instead inverts the data over all of *s* and allows for α^j and β^j to be arbitrary, e.g., $\alpha^j \neq \beta^j$. The unknown viscoelastic function must be fit by an assumed function, either equation (3.3.1) or (3.3.2), in order to be easily inverted back to the time domain. For the case of inverting from creep to relaxation, equation (3.3.1) is used as the assumed function.

In order to obtain an idealized numerical fit between the known linearly inverted Laplace creep function (3.3.5b) and the relaxation fitting function (3.3.1), the span over the frequency domain s must be sufficiently large. An ideal range for s is one magnitude smaller and one magnitude greater than the smallest and largest Prony time constant β^i, respectively. The fit is carried out for all components of the relaxation matrix being sought. The relaxation Prony constants M_{nk}^i of the assumed function are shifted until the error between the inverted data and the relaxation fitting function over the positive frequency domain is sufficiently small. The equilibrium ($t \to \infty$) and glassy ($t = 0$) properties of the desired inverted data are solved by linearly inverting the respective properties that are known from measured data.

$$[C^e] = [M^e]^{-1} \qquad [M^e] = [C^e]^{-1} \qquad (t \to \infty) \tag{3.3.10a}$$

$$[C^g] = [M^g]^{-1} \qquad [M^g] = [C^g]^{-1} \qquad (t = 0) \tag{3.3.10b}$$

Once the resulting relaxation Prony constants M_{nk}^i are solved, the fitting function can be inverted back to the time domain. It is important to note that the data is fit to the assumed function over the positive frequency domain. Data fit to the negative frequency domain results in asymptotic spikes in the Laplace inverted viscoelastic response, making it difficult to obtain ideal fits as compared to the results of the positive frequency domain. The negative frequency domain, however, can be useful in obtaining the unknown Prony time constants, which further improves the data fit.

The assumption made by Schapery's least-squares Laplace method that the Prony time constants are equivalent is valid when there is a small difference between the relaxation and creep time constants (α^i and β^i). However, Schapery discusses a method for obtaining the unknown time constants [46] for one-dimensional materials. Equation (3.3.5) used to obtain relaxation modulus properties from known creep compliance can be expressed for the one-dimensional case as shown by

$$\bar{M}(s) = \frac{\frac{1}{s^2}}{\frac{C^e}{s} - \sum_{i=1}^{n} \frac{C^i}{s+\beta^i}} \tag{3.3.11}$$

This equation can further be rewritten into polynomial form.

$$\bar{M}(s) = \frac{\prod_{i=1}^{n}(s+\beta^i)}{s\left(C^e \prod_{i=1}^{n}(s+\beta^i) - s\sum_{r=1}^{n} C^r \prod_{i=1}^{n} !\delta^{ri}(s+\beta^i)\right)} \tag{3.3.12}$$

where $!\,\delta^{ri} = (1 - \delta^{ri})$ which results in $!\,\delta^{ri}$ equal to zero when $r = i$ and $!\,\delta^{ri}$ equal to one when $r \neq i$.

Using the negative frequency domain s the polynomial in the numerator of equation (3.3.12) goes to zero as s goes to $-\beta^i$.

$$\lim_{s\to-\beta^i} \prod_{i=1}^{n}(s+\beta^i) = 0 \tag{3.3.13}$$

The polynomial in the denominator goes to zero as s approaches $-\alpha^i$ resulting in equation (3.3.12) equaling negative infinity.

$$\lim_{s\to-\alpha^i} \prod_{i=1}^{n}\left(\frac{\prod_{i=1}^{n}(s+\beta^i)}{s(C^e\ \prod_{i=1}^{n}(s+\beta^i)-s\sum_{r=1}^{n}C^r\ \prod_{i=1}^{n}!\delta^{ri}\ (s+\beta^i))}\right) = -\infty \tag{3.3.14}$$

This can be observed graphically by plotting the absolute value of equation (3.3.12) against the absolute value of s on a log-log scale. Estimated relaxation Prony time constants α^i can be obtained where the inverted relaxation data goes to infinity. Figure 3.3.1 and Figure 3.3.2 display the linearly inverted Laplace creep equation (3.3.11) fitted with the assumed Laplace relaxation equation (3.3.5b) for neat resin test data using the numerical method. The Prony time constants α^i of the fitting function are equal to the frequencies s that result in the inverted data equaling infinity. Figure 3.3.2 is a magnified section of Figure 3.3.1 where the inverted data goes to zero and infinity as s approaches $-\beta^i$ and $-\alpha^i$, respectively.

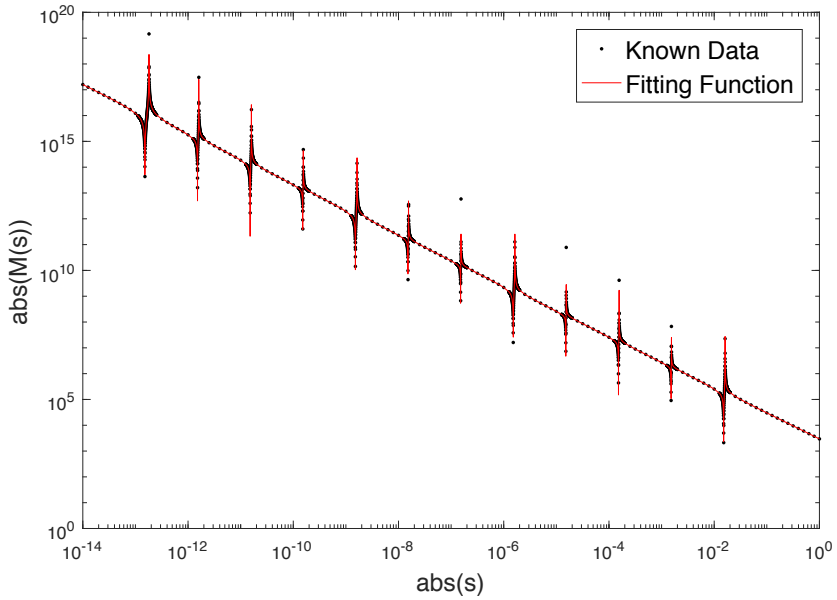

Figure 3.3.1: The graph depicts the linearly inverted Laplace Neat Resin Creep data from (3.3.11) fitted with an assumed relaxation Laplace function (3.3.5b) over the negative frequency domain plotted on a loglog of the absolute value of $M(s)$ vs. the absolute value of s.

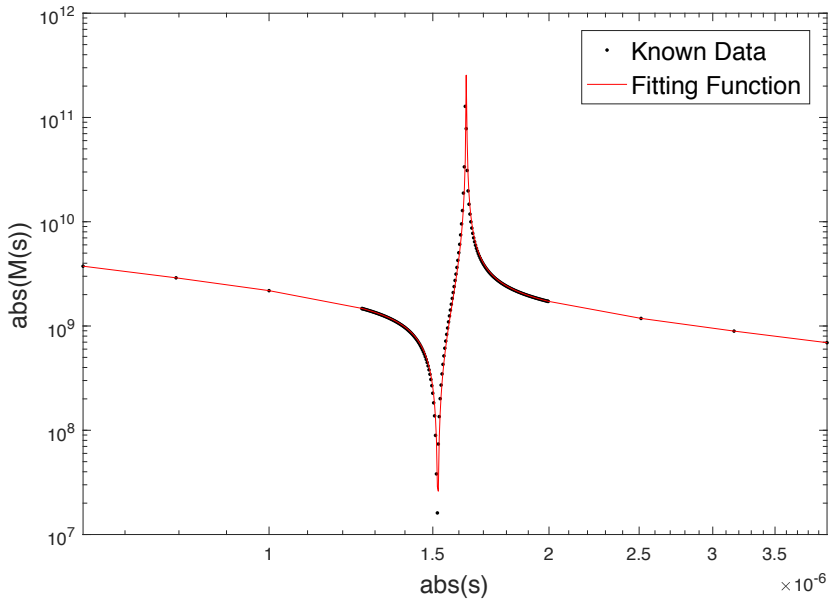

Figure 3.3.2: The figure is a magnified portion of Figure 3.3.1 spanning one Prony constant inflection point. The upward vertical spike is a result of the limit of the denominator of the linearly inverted Laplace creep data (3.3.14) approaching infinity as s approaches $-\alpha^i$. The downward spike is a result of the numerator of the linearly inverted Laplace creep data (3.3.13) approaching zero as s approaches $-\beta^i$. The upward spikes can be used to obtain the values of the unknown relaxation Prony time constants, α^i.

3.3.3 Numerical Laplace Inversion for Multidimensional Materials

The numerical Laplace inversion of multidimensional materials is applied in the same way as the method described above for one-dimension. However, there are unique characteristics of inverting multidimensional materials that become apparent when observing the Laplace inversion over the negative frequency domain. Similar to the one-dimensional case, the inversion of creep to relaxation will be used to discuss the following characteristics. The addition of coupled stresses and strains due to Poisson's contractions and anisotropic properties makes it much more difficult to simplify the inversion expression (3.3.5b) into a polynomial form such as that used for the one-dimensional case (3.3.12). While the specific equations are not as easily solvable, generalized forms of the limit of equation (3.3.5b) can be

useful to study. For a two-dimensional creep compliance matrix, equation (3.3.5b) can be written into a polynomial form.

$$\bar{M}_{kl}(s) = \frac{\tilde{C}_{vm}(s)\prod_{i=1}^{n}(s+\beta^i)}{s\left(\tilde{C}_{11}(s)\tilde{C}_{22}(s)-\left(\tilde{C}_{12}(s)\right)^2\right)} \tag{3.3.15}$$

$$\tilde{C}_{vm}(s) = C_{vm}^{e}\prod_{i=1}^{n}\left(s+\beta^i\right) - s\sum_{r=1}^{n} C_{vm}^{r}\prod_{i=1}^{n}!\,\delta^{ri}\left(s+\beta^i\right) \tag{3.3.16}$$

To simplify equation (3.3.15) the function $\tilde{C}_{vm}(s)$ in the numerator is represented by equation (3.3.16). The behavior of equation (3.3.15) is similar to that of the one-dimensional case (3.3.12) except for the addition of the expression (3.3.16). As a result, the limit of the numerator equals zero at more values of s than those equal to $-\beta^i$. Similarly, the limit of equation (3.3.15) equal to negative infinity can result at more values of s than $-\alpha^i$. A graphical representation of the data is best used to understand how the inverted data behaves as s approaches the Prony time constants $-\beta^i$ and $-\alpha^i$. Figure 3.3.3 displays the inversion of the Laplace creep compliance matrix (3.3.5b) of a unidirectional lamina comprised of the same resin system used in Figure 3.3.1 plotted over the negative frequency domain on an absolute log-log scale. The general form of the inverted data appears similar to the one-dimensional case depicted in Figure 3.3.1. A magnified view, Figure 3.3.4, spanning one of the infinite and zero spikes, however, shows the additional s values that result in the limit of (3.3.15) equaling zero or infinity. Unlike the one-dimensional case, no single frequency value for the relaxation Prony time constants, α^i, can be used to perfectly match the viscoelastic response of the inverted data. As a result, the inversion between creep and relaxation is, at best, an estimate and idealized by the fitting function. The relaxation Prony time constants that provide the best fit for the assumed relaxation function (3.3.1) are found where the limit of (3.3.15) is infinite for all components of the linearly inverted creep compliance matrix. In Figure 3.3.4 this occurs in the farthest right s value. Using the assumed Prony time constants,

the estimated Laplace relaxation function (3.3.1) fitted to the inverted creep compliance function (3.3.15) by solving for the Prony relaxation constants is displayed in Figure 3.4.1. To improve the result of the numerical Laplace inversion method, the predicted relaxation modulus is simultaneously inverted back to the creep compliance and compared directly to the measured creep compliance that is being inverted. Relaxation Prony constants M_{mk}^{i} are selected by the numerical model that minimizes the error between both the inverted predicted relaxation modulus and the originally measured creep compliance. The fit fails to take into account the added infinite and zero spikes present in the inverted data; however, it does provide an accurate estimate for the inverted data.

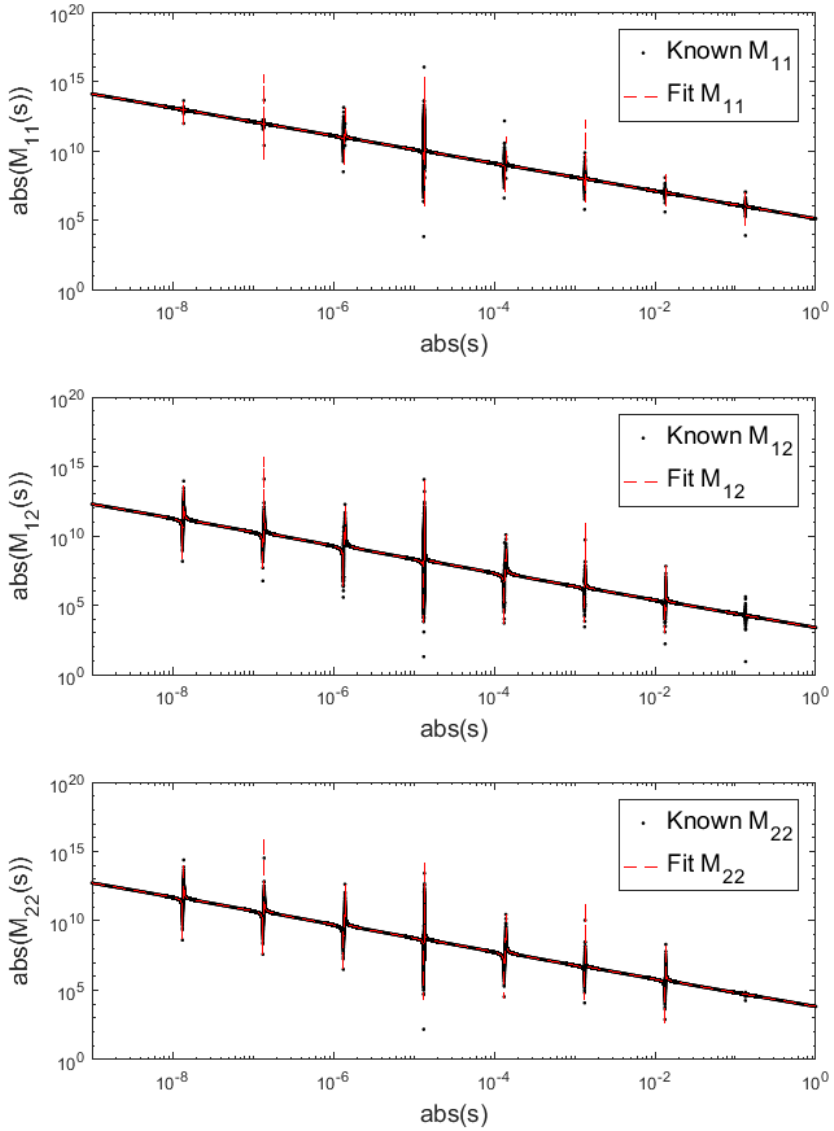

Figure 3.3.3: The Laplace numerical inversion of the unidirectional carbon fiber lamina creep compliance properties resulting in the relaxation modulus, M_{11}, M_{12}, and M_{22} are plotted over the absolute value of the negative frequency domain on a log-log scale.

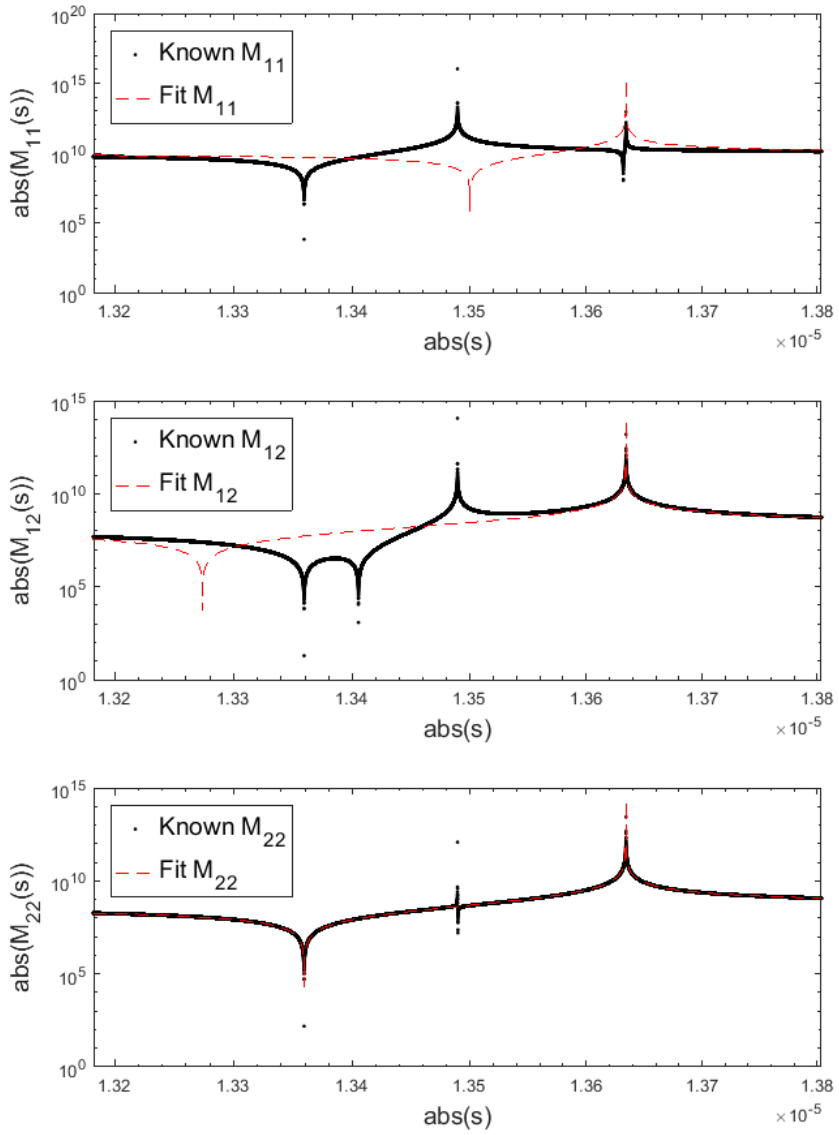

Figure 3.3.4: A magnified view of Figure 3.3.3 spans one of the zero/infinite spikes. The known relaxation properties are defined by a black-dotted line. The fitted relaxation properties are defined by a red-dashed line.

3.3.4 Gutierrez-Lemini's Exact Inversion

Gutierrez-Lemini's exact inversion method has been proven to be a reliable technique for inverting one-dimensional materials. The use of the hereditary integral form of stress and strain (2.2.5) and (2.2.6) allows for a direct inversion between creep and relaxation properties without the use of estimated inversion methods. The method provides a means of solving for

the unknown Prony constants (M^i or C^r) as well as the unknown Prony time constants (α^i or β^r) without any assumed behavior of the sought inverted properties. The robustness of the exact method for the one-dimensional case, however, does not translate for inverting multidimensional materials. The following will discuss the limitations of the exact method for use in inverting viscoelastic multidimensional materials.

The Stieltjes convolution integral (3.2.3b) and (3.2.6b) are interchangeable. Equation (3.2.3b) is expanded for the following derivation of the exact method into two parts. The first part represents where the initial step load is applied between 0^- and 0^+, and the second part represents the viscoelastic response between 0^+ and t.

$$H(t)\delta_{mv} = \int_{0^-}^{0^+} M_{mk}(t-\tau)\frac{d}{d\tau}C_{kv}(\tau)d\tau + \int_{0^+}^{t} M_{mk}(t-\tau)\frac{d}{d\tau}C_{kv}(\tau)d\tau \tag{3.3.17a}$$

$$H(t)\delta_{mv} = M_{mk}(t)C_{kv}(0^+) + \int_{0^+}^{t} M_{mk}(t-\tau)\frac{d}{d\tau}C_{kv}(\tau)d\tau \tag{3.3.17b}$$

Inserting the Prony series expression for relaxation (1.3.4a) and creep (1.3.4b) into equation (3.3.17b) gives the following.

$$\left(M_{mk}^e + \sum_{i=1}^{n} M_{mk}^i e^{-\alpha_{mk}^i t}\right)\left(C_{kv}^e - \sum_{r=1}^{n} C_{kv}^r e^{-\beta_{kv}^r(0^+)}\right)$$

$$+ \int_{0^+}^{t}\left(M_{mk}^e + \sum_{i=1}^{n} M_{mk}^i e^{-\alpha_{mk}^i (t-\tau)}\right)\frac{d}{d\tau}\left(-\sum_{r=1}^{n} C_{kv}^r e^{-\beta_{kv}^r(\tau)}\right)d\tau = H(t)\delta_{mv} \tag{3.3.18a}$$

Equation (3.3.18a) is expanded and reduced.

$$M_{mk}^e C_{kv}^e + \left(\sum_{i=1}^{n} M_{mk}^i e^{-\alpha_{mk}^i t}\right) C_{kv}^e$$

$$- \left(\sum_{i=1}^{n} M_{mk}^i e^{-\alpha_{mk}^i t}\right)\left(\sum_{r=1}^{n} C_{kv}^r e^{-\beta_{kv}^r(0^+)}\right) - M_{mk}^e\left(\sum_{r=1}^{n} C_{kv}^r e^{-\beta_{kv}^r t}\right)$$

$$- \int_{0^+}^{t}\left(\sum_{i=1}^{n} M_{mk}^i e^{-\alpha_{mk}^i (t-\tau)}\right)\frac{d}{d\tau}\left(\sum_{r=1}^{n} C_{kv}^r e^{-\beta_{kv}^r \tau}\right)d\tau = H(t)\delta_{mv} \tag{3.3.18b}$$

The expansion of the integral in equation (3.3.18b), with the sum of the Prony constants M_{mk}^{i}, C_{kv}^{r}, and the exponential $e^{-\alpha_{mk}^{i}t}$ factored out of the integral, is expressed by the following equation.

$$\int_{0^+}^{t}\left(\sum_{i=1}^{n} M_{mk}^{i} e^{-\alpha_{mk}^{i}(t-\tau)}\right)\frac{d}{d\tau}\left(\sum_{r=1}^{n} C_{kv}^{r} e^{-\beta_{kv}^{r}\tau}\right)d\tau$$

$$= \sum_{r=1}^{n}\sum_{i=1}^{n}\left(C_{kv}^{r} M_{mk}^{i} e^{-\alpha_{mk}^{i}t}\int_{0^+}^{t} e^{\alpha_{mk}^{i}\tau}\frac{d}{d\tau}\left(e^{-\beta_{kv}^{r}\tau}\right)d\tau\right) \tag{3.3.19}$$

Equation (3.3.19) can be evaluated through integration by parts.

$$\int[\int g(x)dx]f'(x)dx = f(x)\int g(x)dx - \int f(x)g(x)dx \tag{3.3.20a}$$

The derivative of $e^{-\beta_{kv}^{r}\tau}$ is defined as $f'(x)$.

$$f'(x) = \frac{d}{d\tau}\left(e^{-\beta_{kv}^{r}\tau}\right) \qquad f(x) = \left(e^{-\beta_{kv}^{r}\tau}\right) \tag{3.3.20b}$$

$e^{\alpha_{mk}^{i}\tau}$ is the integral of $g(x)$

$$\int g(x)dx = e^{\alpha_{mk}^{i}\tau} \qquad g(x) = \alpha_{mk}^{i} e^{\alpha_{mk}^{i}\tau} \tag{3.3.20c}$$

Evaluating the integral by parts results in the following expression.

$$\sum_{r=1}^{n}\sum_{i=1}^{n} C_{kv}^{r} M_{mk}^{i}\left(e^{\alpha_{mk}^{i}t} e^{-\beta_{kv}^{r}t} - 1 - \int_{0^+}^{t} \alpha_{mk}^{i} e^{\alpha_{mk}^{i}\tau} e^{-\beta_{kv}^{r}\tau} d\tau\right) \tag{3.3.20d}$$

The integral in (3.3.20d) is rearranged so that the product of exponentials is the sum of their exponents.

$$\sum_{r=1}^{n}\sum_{i=1}^{n} C_{kv}^{r} M_{mk}^{i}\left(e^{\alpha_{mk}^{i}t} e^{-\beta_{kv}^{r}t} - 1 - \int_{0^+}^{t} \alpha_{mk}^{i} e^{\left(\alpha_{mk}^{i}-\beta_{kv}^{r}\right)\tau} d\tau\right) \tag{3.3.20e}$$

The following expression is derived from the integration of (3.3.20e).

$$\sum_{r=1}^{n}\sum_{i=1}^{n}\left(C_{kv}^{r} M_{mk}^{i} e^{-\alpha_{mk}^{i}t}\left(e^{\alpha_{mk}^{i}t} e^{-\beta_{kv}^{r}t}\right.\right.$$

$$\left.\left. -1 - \frac{\alpha_{mk}^{i}}{\left(\alpha_{mk}^{i}-\beta_{kv}^{r}\right)} e^{\left(\alpha_{mk}^{i}-\beta_{kv}^{r}\right)t} + \frac{\alpha_{mk}^{i}}{\left(\alpha_{mk}^{i}-\beta_{kv}^{r}\right)}\right)\right) \tag{3.3.21a}$$

By distributing the expression, $\sum_{r=1}^{n}\sum_{i=1}^{n} C_{kv}^{r} M_{mk}^{i} e^{-\alpha_{mk}^{i} t}$, over the integrated equation and canceling exponentials with like terms, (3.3.21a) becomes:

$$\sum_{i=1}^{n}\sum_{r=1}^{n} M_{mk}^{i} C_{kv}^{r} e^{-\beta_{kv}^{r} t} - \sum_{i=1}^{n}\sum_{r=1}^{n} M_{mk}^{i} C_{kv}^{r} e^{-\alpha_{mk}^{i} t}$$

$$- \sum_{i=1}^{n}\sum_{r=1}^{n} \frac{\alpha_{mk}^{i} M_{mk}^{i} C_{kv}^{r}}{(\alpha_{mk}^{i} - \beta_{kv}^{r})} e^{-\beta_{kv}^{r} t} + \sum_{i=1}^{n}\sum_{r=1}^{n} \frac{\alpha_{mk}^{i} M_{mk}^{i} C_{kv}^{r}}{(\alpha_{mk}^{i} - \beta_{kv}^{r})} e^{-\alpha_{mk}^{i} t} \tag{3.3.21b}$$

Inserting (3.3.21b) into (3.3.18b) produces

$$M_{mk}^{e} C_{kv}^{e} + \left(\sum_{i=1}^{n} M_{mk}^{i} e^{-\alpha_{mk}^{i} t}\right) C_{kv}^{e} - \left(\sum_{i=1}^{n} M_{mk}^{i} e^{-\alpha_{mk}^{i} t}\right)\left(\sum_{r=1}^{n} C_{kv}^{r}\right)$$

$$+ \sum_{i=1}^{n}\sum_{r=1}^{n} \frac{\alpha_{mk}^{i} M_{mk}^{i} C_{kv}^{r}}{(\alpha_{mk}^{i} \beta_{kv}^{r})} e^{-\beta_{kv}^{r} t} - \sum_{i=1}^{n}\sum_{r=1}^{n} \frac{\alpha_{mk}^{i} M_{mk}^{i} C_{kv}^{r}}{(\alpha_{mk}^{i} - \beta_{kv}^{r})} e^{-\alpha_{mk}^{i} t} = H(t)\delta_{mv} \tag{3.3.22a}$$

Applying the Dirichlet-Prony series equation (1.3.3a) and rearranging the terms in (3.3.22a) produces

$$M_{mk}^{e} C_{kv}^{e} + \sum_{i=1}^{n} M_{mk}^{i} e^{-\alpha_{mk}^{i} t}\left(C_{kv}^{e} - \sum_{r=1}^{n} \frac{\alpha_{mk}^{i} C_{kv}^{r}}{(\alpha_{mk}^{i} - \beta_{kv}^{r})}\right)$$

$$- \sum_{r=1}^{n} C_{kv}^{r} e^{-\beta_{kv}^{r} t}\left(M_{mk}^{g} - \sum_{i=1}^{n} \frac{\alpha_{mk}^{i} M_{mk}^{i}}{(\alpha_{mk}^{i} - \beta_{kv}^{r})}\right) = H(t)\delta_{mv} \tag{3.3.22b}$$

Equation (3.3.22b) results in a homogenous equation.

$$\sum_{i=1}^{n} M_{mk}^{i} e^{-\alpha_{mk}^{i} t}\left(C_{kv}^{e} - \sum_{r=1}^{n} \frac{\alpha_{mk}^{i} C_{kv}^{r}}{(\alpha_{mk}^{i} - \beta_{kv}^{r})}\right)$$

$$- \sum_{r=1}^{n} C_{kv}^{r} e^{-\beta_{kv}^{r} t}\left(M_{mk}^{g} - \sum_{i=1}^{n} \frac{\alpha_{mk}^{i} M_{mk}^{i}}{(\alpha_{mk}^{i} - \beta_{kv}^{r})}\right) = 0 \tag{3.3.22c}$$

This is a result of the glassy relaxation modulus and creep compliance on the left side of (3.3.22b) equaling the identity matrix, which cancels the Kronecker delta. Equation (3.3.22c) results in a system of dependent equations. For the one-dimensional case ($v = m = 1$), the exponential functions $e^{-\alpha^{i} t}$ and $e^{-\beta^{r} t}$ in equation (3.3.22c) are linearly independent. The expressions in the brackets in equation (3.3.22c) must be independently equal to zero for the equation to satisfy all choices of the original function. This results in the following:

$$M^g - \sum_{r=1}^{n} \sum_{i=1}^{n} \frac{\alpha^i M^i}{(\alpha^i - \beta^r)} = 0 \tag{3.3.23}$$

$$C^e - \sum_{i=1}^{n} \sum_{r=1}^{n} \frac{\alpha^i C^r}{(\alpha^i - \beta^r)} = 0 \tag{3.3.24}$$

where β^r, C^r, C^g, and C^e are known and $M^e = C^{e^{-1}}$ and $M^g = C^{g^{-1}}$. The unknown Prony time constantans, α^i, can be solved using equation (3.3.24) and the unknown Prony constants, M^i, can be solved using equation (3.3.23).

For multidimensional materials, however, the expressions in brackets in equation (3.3.22c) cannot be independently equal to zero. Equation (3.3.22c) is a system of dependent nonlinear homogenous equations. As a result, a means of rearranging the system into linear equations or the use of numerical solvers are required. The number of unknown variables makes finding reliable inverted viscoelastic properties through numerical means undesirable. The simplification used in Schapery's method ($\alpha^i = \beta^i$) is not feasible using the exact method since the values in the denominator of equation (3.3.22c) would result in indeterminate solutions.

3.4 Results

The inversion methods developed for one-dimensional materials can be evaluated using isotropic materials. The creep compliance properties of epoxy neat resin used as the matrix of a unidirectional carbon/epoxy lamina are obtained from tensile creep tests. Strain gauges are used to measure the creep strain as the load is held constant. A thermal chamber is used to maintain the desired 30^0C temperature by $\pm 1^0$C. A Dirichlet-Prony series is fit to the test data. Table 3.4.1 records the one-dimensional creep compliance of the neat resin. The

relaxation modulus, $M(t)$, is obtained by inverting the measured compliance using Schapery's least squares, the numerical Laplace, and Gutierrez-Lemini's exact method.

$C^e\ (MPa^{-1})$ = 6.21E-4	$C^r\ (MPa^{-1})$	$\beta^r\ (s^{-1})$
$r = 1$	6.21E-4	1.52
2	1.18E-6	1.52E-2
3	5.07E-6	1.52E-3
4	1.03E-5	1.52E-4
5	6.27E-6	1.52E-5
6	2.76E-5	1.52E-6
7	6.88E-6	1.52E-7
8	1.03E-5	1.52E-8
9	3.13E-5	1.52E-9
10	1.12E-5	1.52E-10
11	2.64E-5	1.52E-11
12	2.77E-5	1.52E-12
13	1.02E-4	1.52E-13

Table 3.4.1: The one-dimensional creep compliance properties obtained from a neat resin tensile creep test at 30^0C are recorded in Dirichlet-Prony series form.

Table 3.4.2 provides the relaxation properties inverted using all three methods. The percent difference between the Prony time constants assumed by Schapery or solved for using Gutierrez-Lemini's exact and using the numerical inversion methods are listed. The percent difference between alpha and beta was derived using the average of the alpha properties obtained by the numerical and Gutierrez-Lemini's exact methods. Figure 3.4.1 displays the resulting relaxation response for all three methods in the time domain. The results are normalized by the respective inversion method's glassy response (M^g).

	Schapery (MPa)	Numerical (MPa)	Gutierrez-Lemini (MPa)	$\beta^r\ (s^{-1})$	Numerical $\alpha^i\ (s^{-1})$	Gutierrez-Lemini $\alpha^i\ (s^{-1})$	%Dif. in α^i Numerical & Gutierrez-Lemini	%Dif. Avg. α^i & β^r
M^g	1.61E+3	1.61E+3	1.61E+3					
$i\ or\ r = 1$	-2.13E+1	1.06E+1	1.06E+1	1.52	1.52	1.52	0.01	0.35
2	2.24E+2	1.77E+2	1.77E+2	1.52E-2	1.61E-2	1.61E-2	0.01	6.1
3	-2.26E+1	3.92E+1	3.92E+1	1.52E-3	1.54E-3	1.54E-3	0.04	1.39
4	1.40E+2	7.68E+1	7.69E+1	1.52E-4	1.56E-4	1.56E-4	0.03	2.8
5	-1.70E+1	4.52E+1	4.51E+1	1.52E-5	1.54E-5	1.54E-5	0.02	1.69
6	2.49E+2	1.80E+2	1.80E+2	1.52E-6	1.63E-6	1.63E-6	0.02	7.05
7	-3.59E+1	4.07E+1	4.08E+1	1.52E-7	1.54E-7	1.54E-7	0.00	1.67
8	1.37E+2	5.99E+1	5.99E+1	1.52E-8	1.55E-8	1.55E-8	0.03	2.5
9	9.18E+1	1.63E+2	1.63E+2	1.52E-9	1.63E-9	1.63E-9	0.01	7.13
10	1.18E+2	5.31E+1	5.30E+1	1.52E-10	1.55E-10	1.55E-10	0.05	2.46
11	5.35E+1	1.16E+2	1.17E+2	1.52E-11	1.60E-11	1.60E-11	0.01	5.55
12	1.81E+2	1.12E+2	1.12E+2	1.52E-12	1.60E-12	1.60E-12	0.03	5.58
13	2.71E+2	3.11E+2	3.11E+2	1.52E-13	1.81E-13	1.81E-13	0.02	17.75

Table 3.4.2: The neat resin relaxation modulus are obtained by inverting the measured neat resin compliance properties (Table 3.4.1) using Schapery's least squares method, the numerical method, and Gutierrez-Lemini's exact method. Properties are recorded in Dirichlet-Prony series form. Percent differences in the Prony time constants are also presented.

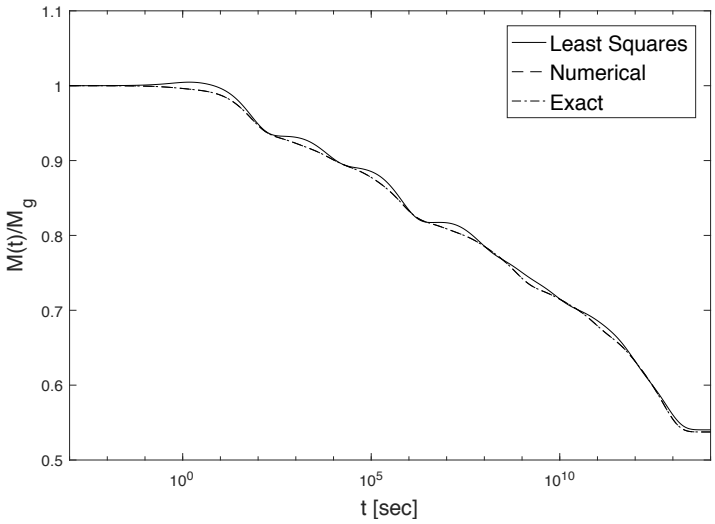

Figure 3.4.1: The relaxation modulus properties, $M(t)$ (equation (3.2.5b)) with Prony series coefficients recorded in Table 3.4.2 which are obtained from inverting the creep compliance properties presented in Table 3.4.1 are plotted on a log10 time scale. The results of Schapery's least square method, the numerical method, and Gutierrez-Lemini's exact method are normalized using their corresponding glassy response, M^g. The exact method and numerical method produce the same solution resulting in both lines in the graph lying on top of one another.

The Laplace numerical method and Schapery's least-squares method are compared by inverting the creep compliance properties of the unidirectional carbon lamina recorded in Table 3.4.3. The unidirectional lamina matrix consists of the same neat resin epoxy used in the one-dimensional viscoelastic inversion. The creep compliance properties are obtained

using the same method as described above, but with modifications to obtain all properties of the anisotropic material.

	$C_{11}^r(MPa^{-1})$	$C_{12}^r\ (MPa^{-1})$	$C_{22}^r\ (MPa^{-1})$	$\beta^r\ (s^{-1})$
$r=e$	8.24E-06	-2.92E-06	1.86E-04	
$r=1$	1.00E-08	-1.00E-08	1.00E-09	1.34E-1
2	7.28E-09	-1.00E-08	3.28E-06	1.34E-02
3	4.51E-08	-1.00E-08	2.10E-06	1.34E-03
4	6.73E-08	-1.00E-08	7.55E-06	1.34E-04
5	7.91E-08	-1.00E-08	3.30E-06	1.34E-05
6	8.64E-08	-1.00E-08	8.06E-06	1.34E-06
7	1.00E-09	0	6.55E-06	1.34E-07
8	0	0	6.25E-06	1.33E-08

Table 3.4.3: Creep compliance Dirichlet-Prony series properties for a unidirectional carbon fiber/epoxy lamina.

The inverted relaxation properties are presented in Table 3.4.4 using Dirichlet-Prony series. The percent variance (3.4.1) in the numerical fit and the percent difference in the beta and numerically estimated alpha Prony time constants are recorded in Table 3.4.4.

$$\%Variance = \frac{\sum abs\left(\frac{Known\ data(s) - Fitting\ function(s)}{Known\ data(s)}\right)}{n};\quad \text{n=number of data point} \tag{3.4.1}$$

	$M_{11}^i\ (MPa)$		$M_{12}^i\ (MPa)$		$M_{22}^i\ (MPa)$		$\alpha^i\ (s^{-1})$		
	Schapery	Num.	Schapery	Num.	Schapery	Num.	Schapery	Num.	%Dif. in α^i
%Var.	2.80E-4		6.21E-2		1.32E-1				
$i=e$	1.22E+5	1.22E+5	1.92E+3	1.92E+3	5.41E+3	5.41E+3			
$i=1$	1.63E+2	1.53E+2	3.27	0	2.25E+1	0	1.34E-1	1.34E-1	0.13
2	1.20E+2	1.32E+2	3.70E+1	4.22E+1	1.22E+2	1.47E+2	1.34E-2	1.37E-2	2.2
3	7.38E+2	7.10E+2	4.90E+1	4.06E+1	1.18E+2	9.16E+1	1.34E-3	1.35E-3	1.38
4	1.08E+3	1.09E+3	1.15E+2	1.22E+2	2.89E+2	3.08E+2	1.34E-4	1.40E-4	4.82
5	1.24E+3	1.22E+3	6.40E+1	5.92E+1	1.38E+2	1.26E+2	1.34E-5	1.36E-5	2.04
6	1.32E+3	1.33E+3	1.14E+2	1.17E+2	2.81E+2	2.87E+2	1.34E-6	1.40E-6	4.81
7	4.05E+1	5.60E+1	7.66E+1	7.56E+1	2.16E+2	2.13E+2	1.34E-7	1.39E-7	3.73
8	2.31E+1	2.14E+1	6.48E+1	6.66E+1	1.83E+2	1.88E+2	1.34E-8	1.38E-8	3.43

Table 3.4.4 contains the relaxation modulus properties in Dirichlet-Prony series form obtained from inverting the creep compliance properties of an unidirectional carbon fiber/epoxy lamina (Table 3.4.3) using the numerical method and using Schapery's least squares method.

Figure 3.4.2 plots the relaxation modulus properties (Table 3.4.4) over the time domain. The properties are normalized by the glassy response M^g for the corresponding inversion method

and modulus components. The results are plotted with the time axis using a logarithm base 10 scale.

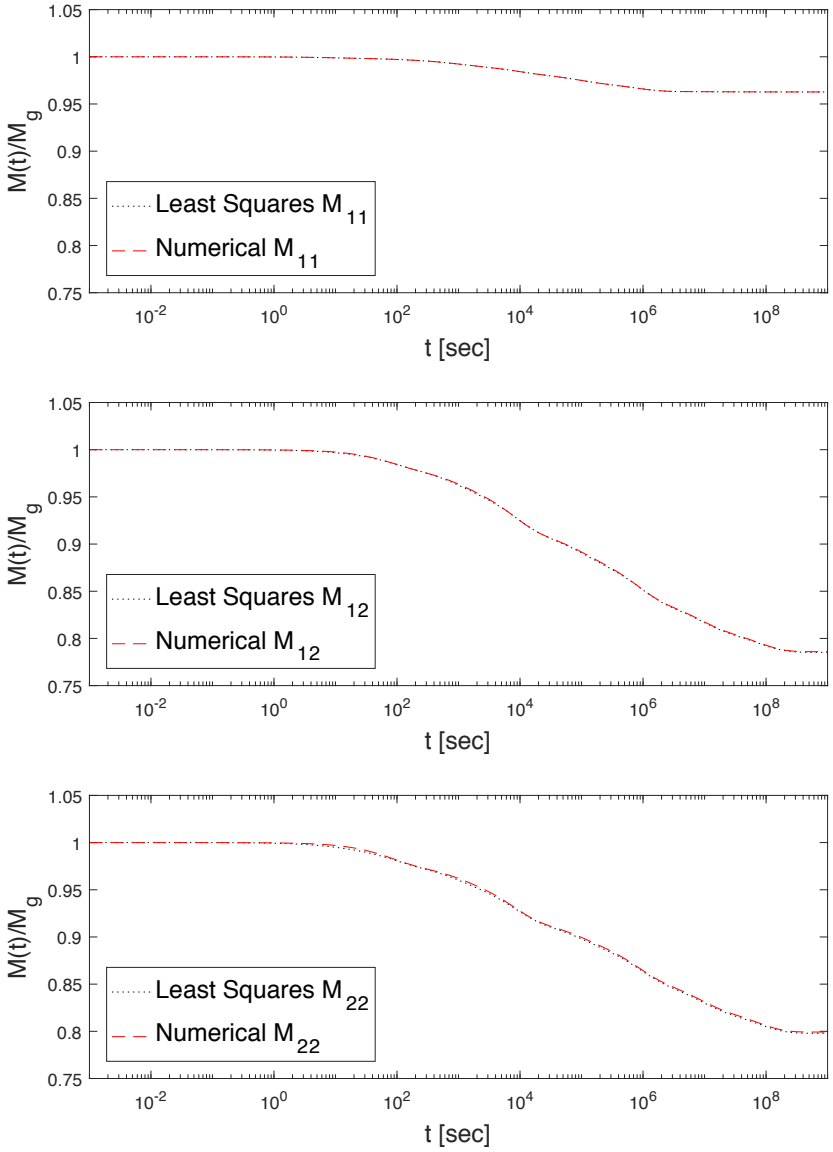

Figure 3.4.2: The log10 scaled time domain of the inverted creep compliance properties with Prony coefficients recorded in Table 3.4.4 are presented for both the numerical method and Schapery's least-squares inversion method. The relaxation modulus properties, $M(t)$ (equation (3.2.5b), are normalized by the glassy response, M^g, of the corresponding modulus component and inversion method. Both methods produce nearly identical solutions resulting in the lines of the graphs lying on top of one another.

3.5 Discussion

Accurate, robust viscoelastic inversion methods are needed to obtain reliable creep and relaxation properties from the corresponding relaxation and creep tests. The ability to invert between material properties eliminates the need for redundant, time-consuming tests. Furthermore, many structural models require both viscoelastic compliance and modulus properties to predict stress/strain time-dependent behavior. The numerical viscoelastic method developed in this chapter used to invert multidimensional material data aims to meet these requirements. Validation of the numerical method is not compared to measured relaxation data due to the difficulty of producing accurate relaxation tests. Instead, the method is compared to Schapery's least squares method and Gutierrez-Lemini's exact method for one-dimensional materials.

Measured creep compliance properties of an isotropic neat resin epoxy presented in Table 3.4.1 in Dirichlet Prony series form is inverted using the three methods. Table 3.4.2 contains the relaxation properties resulting from the three inversion methods. It can be observed that Schapery's least-squares inversion method fails to satisfy basic energy principles and results in several negative relaxation Prony constants M^i. This is not always true for all materials. The oscillatory behavior resulting from such sign changes in the Prony constants can be seen in Figure 3.4.1. Furthermore, the Prony time constants for the inverted relaxation properties have to be assumed equal to the creep compliance Prony time constants for Schapery's least-squares method. The percent difference between α^i found by Gutierrez-Lemini's exact method to that of the measured β^i properties are presented in Table 3.4.2. For some Prony time constants, the difference is as high as 18%. The assumption made by Schapery's least-squares inversion that alpha and beta are equivalent may not be valid for all materials. The

relaxation Prony time constants α^i, however, can be solved using Gutierrez-Lemini's exact method and the numerical method. The exact method solves for α^i by factoring the roots of the polynomial expressed by equation (3.3.12). The numerical method sets α^i equal to the frequencies *s* that result in the limit of equation (3.3.14) equaling negative infinity. The absolute value of equation (3.3.14) is graphically depicted in Figure 3.3.1 and Figure 3.3.2. The one-dimensional creep data inverted by the numerical method and the exact method result in similar solutions. This is graphically observed in Figure 3.4.1 in which the plot of both data sets align identically. The Prony constants, α^i and M^i, calculated by the numerical method, match the exact method with minimum error (Table 3.4.2). It is important to note that, unlike Gutierrez-Lemini's exact method, which directly solves the hereditary integral relating creep compliance and relaxation modulus, the numerical method will always be an idealized solution due to the use of Laplace transforms and the need for numerical fitting. The level of accuracy and reliability in the method is improved when accurate Prony time constants and large spans of the frequency domain are used to fit the assumed fitting function. Furthermore, the method will always satisfy the energy principles by maintaining the fundamental relaxation decay or creep growth known throughout literature.

Inversion of viscoelastic data with anisotropic viscoelastic properties is required for analyzing and predicting the viscoelastic behavior of materials such as anisotropic composites used in tape spring applications. In this setting, the development of the numerical, exact, and least-squares methods for inverting multidimensional materials are estimates, at best. The reliable exact method developed by Gutierrez-Lemini for one-dimensional materials results in a series of dependent nonlinear homogeneous equations when applied to multidimensional materials. As a result, the exact method requires numerical solvers to

obtain all Prony constants and no longer produces an exact solution by directly solving the hereditary integrals (3.2.3b) and (3.2.6b). The level of complexity required to solve the "exact" method makes it an unreliable and cumbersome inversion method. The numerical method and Schapery's least squares method, however, can be developed for multiaxial anisotropic materials. The creep compliance properties of a unidirectional carbon fiber/epoxy lamina recorded in Table 3.4.3 are inverted using the numerical and least-squares methods. The resulting Dirichlet-Prony series relaxation modulus properties are presented in Table 3.4.4. Unlike in the one-dimensional example just discussed, Schapery's least-squares inversion satisfies energy constraints when applied to the multiaxial response of this specific anisotropic material. All relaxation Prony constants M^i maintain positive values. Similar to the one-dimensional case, the multiaxial least-squares method assumes that the Prony time constants are equivalent ($\alpha^i = \beta^i$), which simplifies the inversion into a system of linear equations (3.3.8). The method which uses numerical inversion, while much more computationally taxing, produces reliable estimates for the Prony time constants α^i by observing where each component of the linearly inverted Laplace creep compliance matrix approaches negative infinity. Discerning the ideal alpha terms for the multidimensional case is much more difficult than in the one-dimensional case due to the added infinite and zero spikes which result from anisotropic coupling terms. Figure 3.3.4 depicts a magnified view of the inverted creep compliance data and the ideal relaxation fit. It can be observed that the alpha terms (infinite spike in the fitted relaxation function) align with the infinite spikes for all components of the inverted creep compliance data. The fitted curve, however, fails to predict the added infinite and zero spikes present in the inverted creep data. The numerical method, while an estimated solution of the inverted viscoelastic properties, nevertheless

results in an accurate solution. The variances (equation (3.4.1)) between the inverted creep compliance using Shapery's least-squares method and the numerical method for all components of the modulus matrix, e.g., M_{11}, M_{12}, and M_{22} are recorded in Table 3.4.4. The variance over the positive frequency domain is small (<0.13%). Figure 3.4.2 presents results for the relaxation modulus as a function of time from the numerical method and from Schapery's least-squares method. Both methods appear to give identical results, and we also assume that both are accurate. The percent differences in the numerically estimated relaxation Prony time constants α^i and the measured creep Prony time constants β^i presented in Table 3.4.4 are small (<5%), significantly smaller in some cases than was found for the discrepancies when data was inverted for the neat resin. The assumption made by Schapery's least-squares method that α^i and β^i are equivalent proves to be valid for the unidirectional carbon/epoxy lamina. However, Schapery's least squares method, while computationally easy to solve, sometimes provides unreliable results that are not accurate or fail to satisfy fundamental energy constraints. In contrast, the numerical method used to invert viscoelastic data provides accurate, reliable, and robust means of estimating the inverted viscoelastic properties without violation of energy constraints.

3.6 Conclusion

The numerical inversion method developed in this chapter for viscoelastic materials, when used to invert creep compliance data to generate the relaxation modulus, is more accurate and more reliable than other methods. When applied to uniaxial data for neat resin, the numerical method provides results that differ little from Gutierrez-Lemini's [18] exact method, whereas Schapery's least squares method [36], [37] is both less accurate and has

energetic inconsistencies in its results. Gutierrez-Lemini's method cannot be applied reliably to multiaxial data for anisotropic materials. When applied to multiaxial data for anisotropic carbon fiber reinforced composite materials, the numerical method provides results little different from Schapery's least squares method [36], [37], and, in this case, we presume them to be both accurate. Furthermore, the numerical method requires no foreknowledge of the inverted time-dependent Prony constant values. The numerical method maintains consistent signs (all positive or all negative) across the Prony constants in the series, which satisfies fundamental relaxation and creep characteristics. Schapery's method cannot, in general, be relied upon to stay energetically consistent and, as a result, introduces the possibility of error.

Chapter 4

Relaxation Stiffness and Flexure Properties of the Neat Resin, Unidirectional and Plain Weave Laminae, and the 3-ply and 4-ply Laminates Predicted Using the Numerical Laplace Inversion Method and Viscoelastic Classical Laminate Theory

4.1 Introduction

Most prediction methods for modeling the behavior of viscoelastic structures require the use of both the relaxation stiffness and creep compliance properties. However, relaxation properties are difficult to measure. Therefore, it is common to determine a material's creep compliance properties because they are relatively easy to measure and then invert the data to acquire a material's relaxation stiffness properties. As discussed in the previous chapter (Chapter 3), methods for inverting viscoelastic composite properties are not simple and require complex inversion methods which commonly utilize Laplace transforms. To the best

of our knowledge, the application of viscoelastic inversion methods for multidimensional materials such as the carbon fiber lamina and laminate test results published in Chapter 2 are not described in the literature. Therefore, this chapter will describe the application of the multidimensional viscoelastic inversion methods developed in Chapter 3 to the viscoelastic creep compliance properties of the neat resin, unidirectional and plain weave laminae, and the 3-ply [±45PW/0/±45PW] and 4-ply [0/±45PW/±45PW/0] laminates measured in Chapter 2. Since the axial/transverse flexure properties $d_{xy}(t)$ could not be recorded using the four-point bend test setup discussed in detail in Chapter 2, there is insufficient data to invert the measured creep flexure properties. To overcome this difficulty, the use of viscoelastic classical laminate theory (CLT) to estimate the relaxation flexure stiffness of the samples tested in Chapter 2 from the relaxation stiffness properties of the unidirectional and plain weave lamina is discussed.

4.2 Background

It is not possible to use the numerical Laplace inversion method developed in Chapter 3 to determine the relaxation flexure properties $D_{ij}(t)$ from the measured creep flexure properties $d_{ij}(t)$ recorded in Chapter 2 due to the missing axial/transverse flexure compliance properties $d_{xy}(t)$. However, the relaxation flexure stiffness properties can be predicted using classical laminate theory [47] adapted for viscoelastic composites. Classical laminate theory (CLT) is well established in the literature [14] to reliably predict the elastic flexure properties D_{ij} of a lamina or laminate based the orientation, stacking sequence, thickness, and reduced stiffness properties of the plies composing the lamina or laminate.

Figure 1.2.3 illustrates a cross-sectional view of a laminate with unidirectional plies oriented at varying degrees from the x-axis of the laminate. The viscoelastic variant of classical laminate theory uses the equivalent inputs as the CLT; however, the reduced stiffness properties of the plies composing the lamina or laminate are represented using the relaxation reduced stiffness properties $Q_{ij}(t)$ defined by equation (1.3.7a). The composite relaxation flexure stiffness properties $D_{ij}(t)$ are predicted by the viscoelastic classical laminate theory using the following

$$D_{ij}(t) = \sum_{p=1}^{n} Q_{ij}^{p}(t) \int_{\bar{z}_{p-1}}^{\bar{z}_p} z^2 dz \qquad i,j = x,y,s \tag{4.2.1}$$

The individual plies comprising the lamina or laminate are represented by p ranging from 1, bottom ply of the composite, to n, the total number of plies in the composite, e.g., topmost ply. $Q_{ij}^{p}(t)$ are the relaxation reduced stiffness properties for the individual plies that comprise the laminate. The reduced stiffness properties are oriented according to the laminate's coordinate system illustrated in Figure 4.2.1 with the zero ply angle along the x-axis of the laminate. z represents the through-thickness position of the laminate from its reference plane or midplane. $\bar{z}_p$ and $\bar{z}_{p-1}$ represents the distance between the plies surface from the reference plane of the laminate as depicted in Figure 1.2.2. The predicted lamina and laminate relaxation flexure properties can be compared to the measured creep flexure by inverting the predicted laminate relaxation flexure properties using the numerical inversion method developed in Chapter 3.

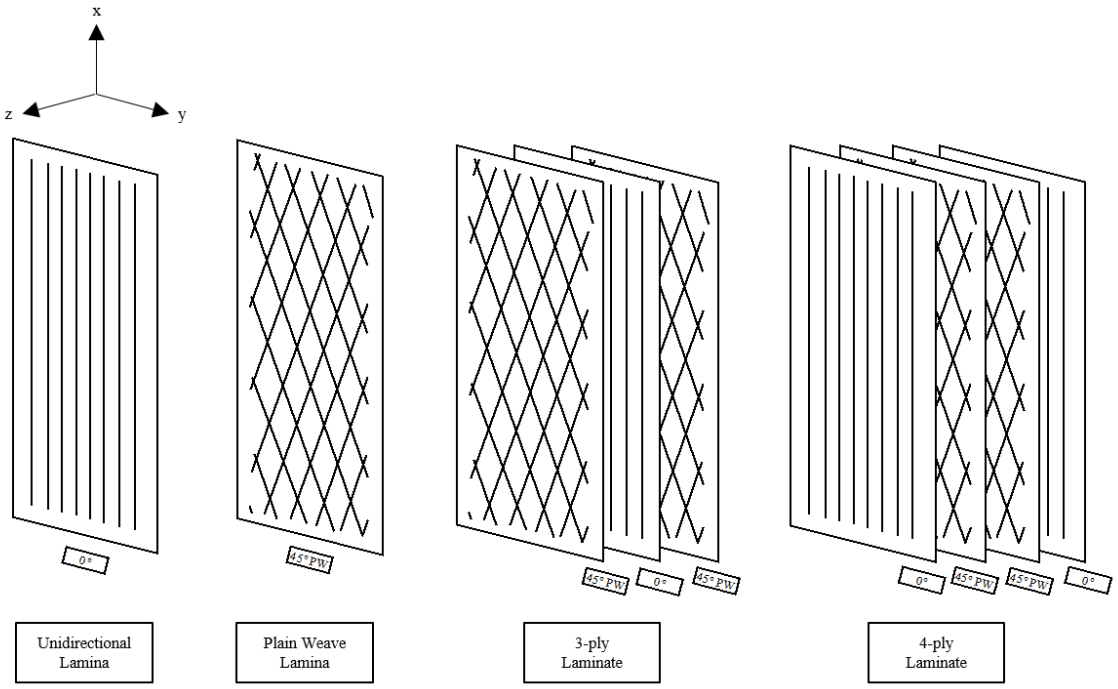

Figure 4.2.1: The lamina and laminate samples tested in Chapter 2 are illustrated graphically. The plies composing the laminates are oriented with respect to the x-axis.

4.3 Results

The Prony series coefficients defining the predicted relaxation stiffness properties for the neat resin, unidirectional and plain weave laminae, and the 3-ply and 4-ply laminates are recorded in Table A.16 through Table A.20 in the appendix, respectively. The predicted axial relaxation stiffness $Q_{xx}(t)$ for these laminae and laminates normalized by their respective glassy properties Q_{xx}^{g} are illustrated in Figure 4.3.1. The solid blue line represents the inverted neat resin, the short dashed-dotted green line represents the unidirectional lamina, the long dashed-dotted red line represents the plain weave lamina, the short dashed light blue line represents the 3-ply laminate, and the long dashed orange line represents the 4-ply laminate. Similarly, the normalized axial/transverse relaxation stiffness $Q_{xy}(t)/Q_{xy}^{g}$ and normalized transverse relaxation stiffness $Q_{yy}(t)/Q_{yy}^{g}$ for the listed laminae and laminates

are illustrated in Figure 4.3.2 and Figure 4.3.3, respectively. The relaxation data is plotted and predicted up to 10^8 sec. This duration corresponds to the shortest master curves measured by the creep tests performed in Chapter 2.

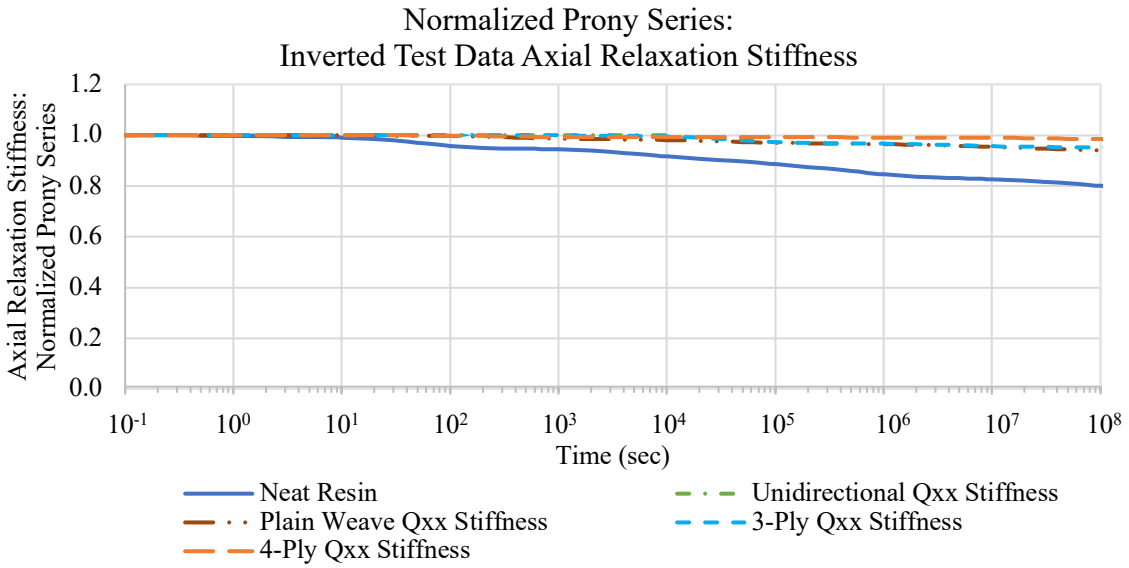

Figure 4.3.1: The relaxation axial stiffness master curves, $Q_{xx}(t)$, for the unidirectional and plain weave laminae, and 3-ply and 4-ply laminates are normalized by their respective glassy response, Q_{xx}^g. The relaxation master curves are obtained by inverting the measured creep compliance properties recorded in Chapter 2 using the numerical inversion method developed in Chapter 3. The solid blue line represents the inverted neat resin, the short dashed-dotted green line represents the unidirectional lamina, the long dashed-dotted red line represents the plain weave lamina, the short dashed light blue line represents the 3-ply laminate, and the long dashed orange line represents the 4-ply laminate.

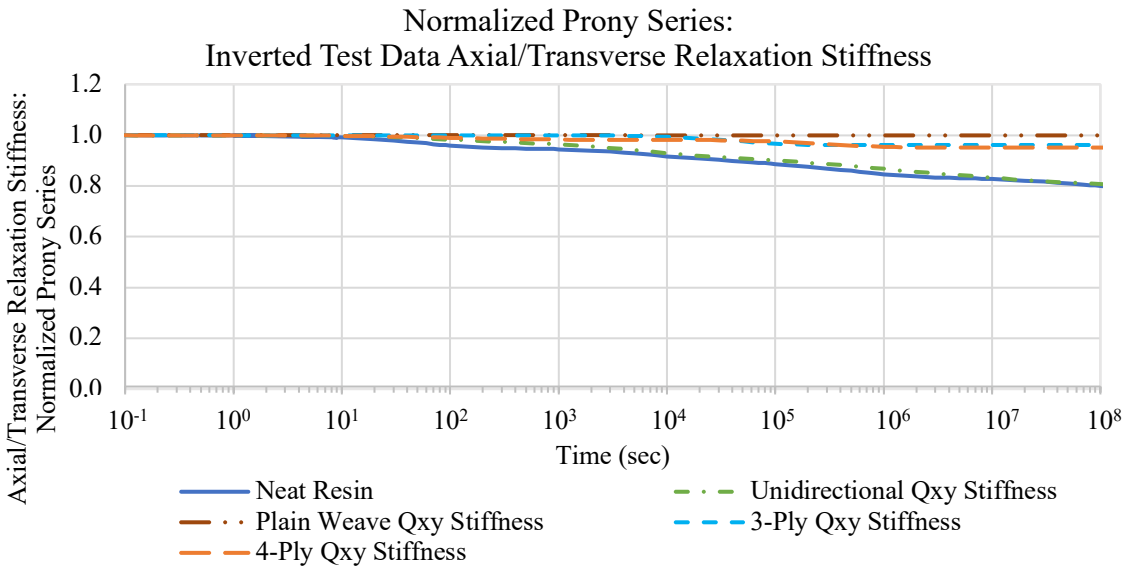

Figure 4.3.2: The relaxation axial/transverse stiffness master curves, $Q_{xy}(t)$, for the unidirectional and plain weave laminae, and 3-ply and 4-ply laminates are normalized by their respective glassy response, Q_{xy}^g. The relaxation master curves are obtained by inverting the measured creep compliance properties recorded in

Chapter 2 using the numerical inversion method developed in Chapter 3. The solid blue line represents the inverted neat resin, the short dashed-dotted green line represents the unidirectional lamina, the long dashed-dotted red line represents the plain weave lamina, the short dashed light blue line represents the 3-ply laminate, and the long dashed orange line represents the 4-ply laminate.

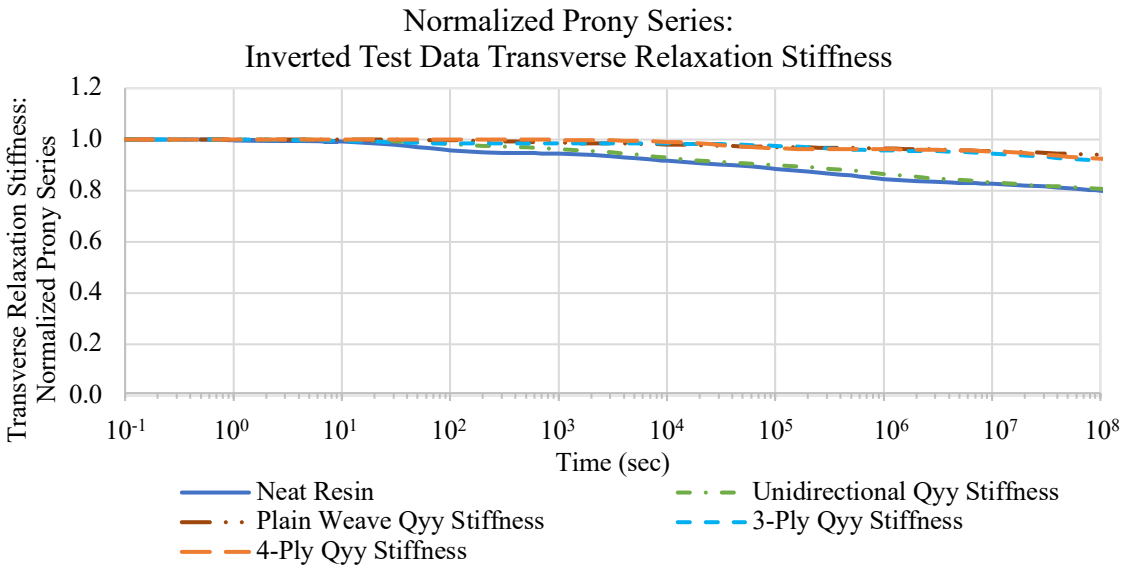

Figure 4.3.3: The relaxation transverse stiffness master curves, $Q_{yy}(t)$, for the unidirectional and plain weave laminae, and 3-ply and 4-ply laminates are normalized by their respective glassy response, Q_{yy}^{g}. The relaxation master curves are obtained by inverting the measured creep compliance properties recorded in Chapter 2 using the numerical inversion method developed in Chapter 3. The solid blue line represents the inverted neat resin, the short dashed-dotted green line represents the unidirectional lamina, the long dashed-dotted red line represents the plain weave lamina, the short dashed light blue line represents the 3-ply laminate, and the long dashed orange line represents the 4-ply laminate.

The relaxation flexure properties for the neat resin, unidirectional and plain weave laminae, and the 3-ply and 4-ply laminates are predicted using the viscoelastic classical laminate theory defined by equation (4.2.1). The predicted relaxation Prony coefficients for the unidirectional and plain weave laminae recorded in Table A.17 through Table A.18, respectively, are used as inputs in the viscoelastic classical laminate theory to predict the relaxation flexure properties of the laminae and laminates. Figure 4.3.4 plots the relaxation axial flexure stiffness $D_{xx}(t)$ normalized by the glassy property D_{xx}^{g} for the respective laminae and laminates. The solid blue line represents the inverted neat resin, the short dashed-dotted green line represents the unidirectional lamina, the long dashed-dotted red line represents the plain weave lamina, the short dashed light blue line represents the 3-ply

laminate, and the long dashed orange line represents the 4-ply laminate. Figure 4.3.5 plots the relaxation axial/transverse flexure stiffness $D_{xy}(t)$ normalized by the glassy property D_{xy}^{g} and Figure 4.3.6 plots the relaxation transverse flexure stiffness $D_{yy}(t)$ in normalized form for these same laminae and laminates. Table A.17 through Table A.20 in the appendix, record the Prony coefficients of the relaxation flexure properties predicted by the viscoelastic classical laminate theory for the neat resin, unidirectional and plain weave laminae, and the 3-ply and 4-ply laminates, respectively.

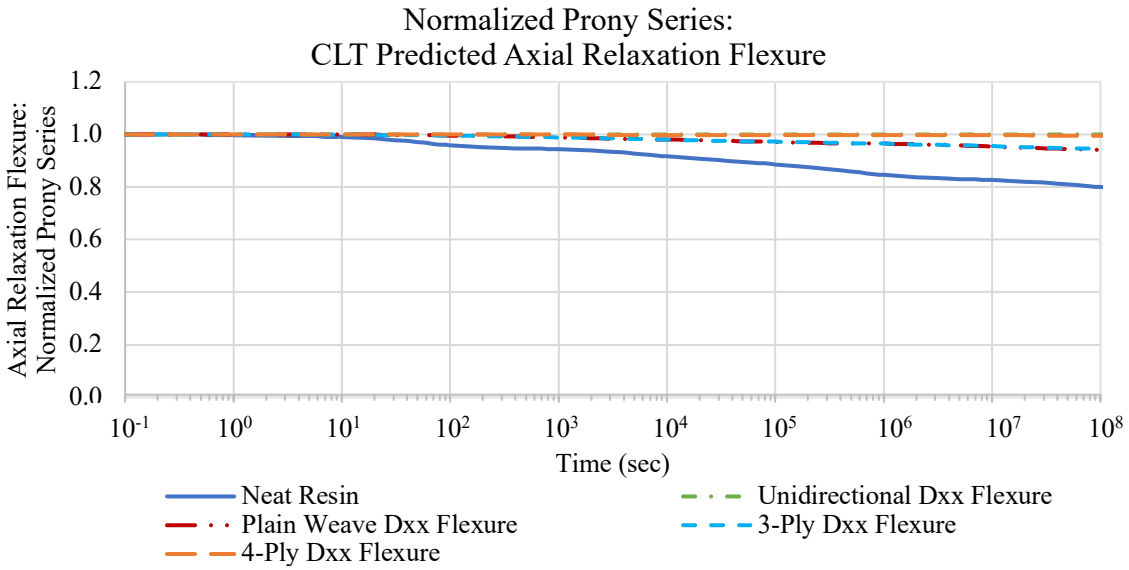

Figure 4.3.4: The relaxation axial flexure stiffness $D_{xx}(t)$ for the neat resin, unidirectional and plain weave lamina, and 3-ply and 4-ply laminates are normalized by their respective glassy response, D_{xx}^{g}. The relaxation flexure stiffnesses are predicted by the viscoelastic CLT. The solid blue line represents the inverted neat resin, the short dashed-dotted green line represents the unidirectional lamina, the long dashed dotted red line represents the plain weave lamina, the short dashed light blue line represents the 3-ply laminate, and the long dashed orange line represents the 4-ply laminate.

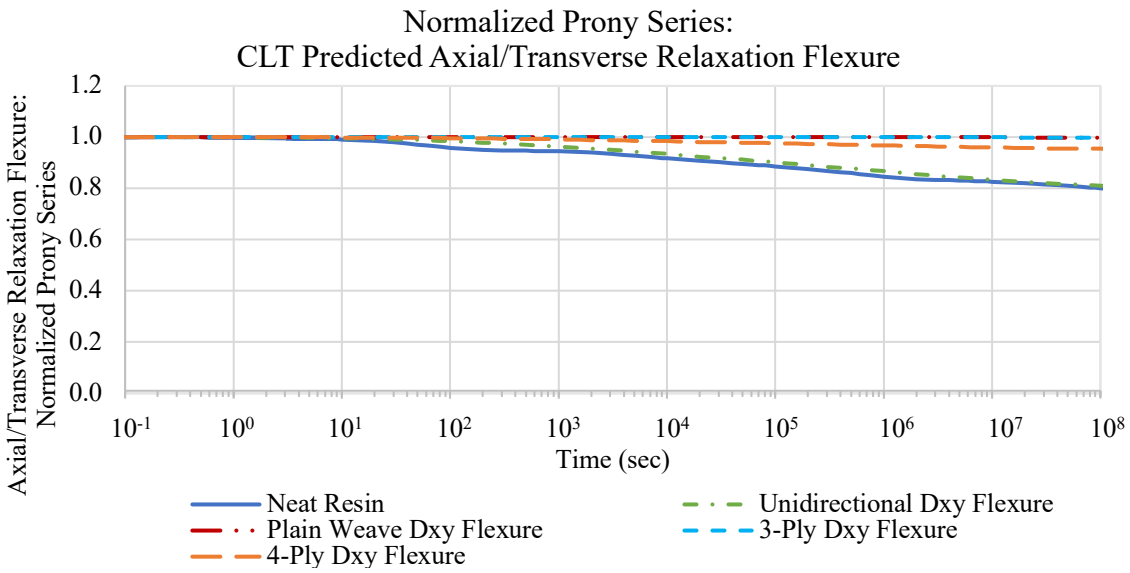

Figure 4.3.5: The relaxation axial/transverse flexure stiffness $D_{xy}(t)$ for the neat resin, unidirectional and plain weave lamina, and 3-ply and 4-ply laminates are normalized by their respective glassy response, D_{xy}^{g}. The relaxation flexure stiffnesses are predicted by the viscoelastic CLT. The solid blue line represents the inverted neat resin, the short dashed-dotted green line represents the unidirectional lamina, the long dashed-dotted red line represents the plain weave lamina, the short dashed light blue line represents the 3-ply laminate, and the long dashed orange line represents the 4-ply laminate.

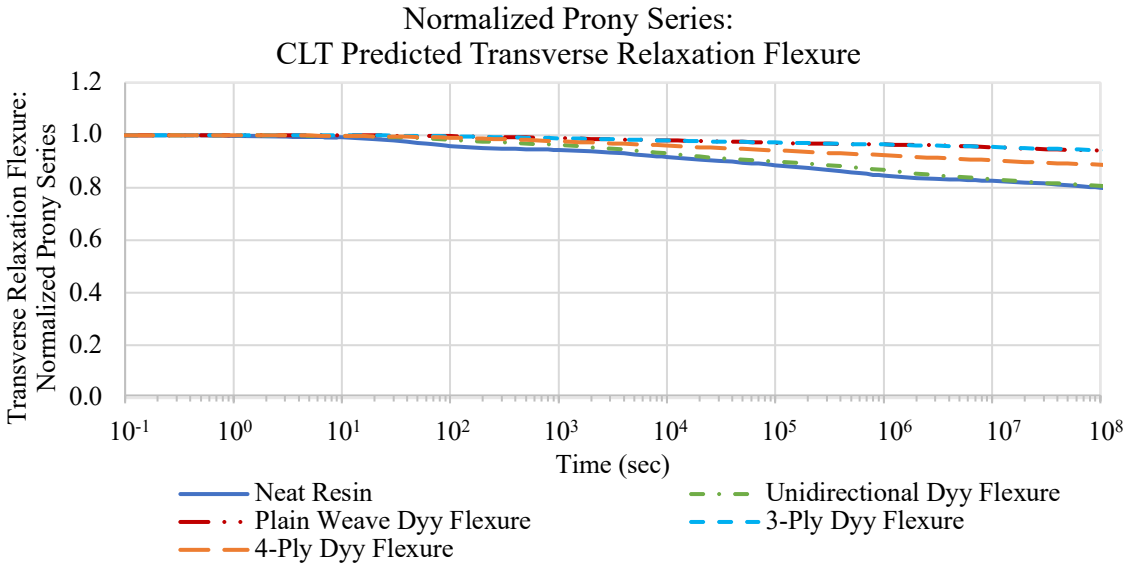

Figure 4.3.6: The relaxation transverse flexure stiffness $D_{yy}(t)$ for the neat resin, unidirectional and plain weave lamina, and 3-ply and 4-ply laminates are normalized by their respective glassy response, D_{yy}^{g}. The relaxation flexure stiffnesses are predicted by the viscoelastic CLT. The solid blue line represents the inverted neat resin, the short dashed-dotted green line represents the unidirectional lamina, the long dashed-dotted red line represents the plain weave lamina, the short dashed light blue line represents the 3-ply laminate, and the long dashed orange line represents the 4-ply laminate.

The relaxation stiffness properties $Q_{ij}(t)$ and flexure stiffness properties $D_{ij}(t)$ predicted by the viscoelastic CLT are compared to the measured creep compliance $S_{ij}(t)$ and flexure

stiffness $d_{ij}(t)$ recorded in Chapter 2 by inverting the predicted relaxation results for the 3-ply and 4-ply laminates listed in Table A.19 through Table A.20, respectively, using the numerical Laplace inversion method developed in Chapter 3. Figure 4.3.7 through Figure 4.3.9 illustrate the predicted compliance properties $S_{ij}(t)$ for the 3-ply and 4-ply laminates compared to the measured compliance properties. Figure 4.3.7 compares the normalized axial properties $S_{xx}(t)/S_{xx}^{g}$, Figure 4.3.8 the normalized axial/transverse properties, $S_{xy}(t)/S_{xy}^{g}$, and Figure 4.3.9 the normalized transverse properties $S_{yy}(t)/S_{yy}^{g}$. In a similar format, the normalized creep flexure stiffness for the 3-ply and 4-ply laminates are illustrated in Figure 4.3.10 and Figure 4.3.11 comparing measured and predicted axial stiffness $d_{xx}(t)/d_{xx}^{g}$ and transverse $d_{yy}(t)/d_{yy}^{g}$ stiffness, respectively. The 3-ply laminate's measured properties are represented by the dashed light blue line and the predicted properties are represented by the dashed-dotted blue line in Figure 4.3.7 through Figure 4.3.11. The 4-ply laminate's measured properties are represented by the long dashed orange line and the predicted properties by the long dashed-dotted red line. The flexure stiffness $D_{ij}(t)$ predicted by the viscoelastic CLT is sensitive to slight variations in the laminate thickness as a result of cubing the thickness in equation (4.2.1). The input thickness of the unidirectional and plain weave plies composing the 3-ply and 4-ply laminates were estimated based on the lamina and laminate thicknesses of the samples tested in Chapter 2. The input ply thicknesses were adjusted to produce laminate thicknesses that match closely to the measured 3-ply and 4-ply laminates as well as produce glassy flexure stiffnesses $d_{ij}^{g}(t)$ predicted by inverting the viscoelastic CLT flexure stiffness to within <10% of the measured data. Table 4.3.1 and Table 4.3.2 record the measured and predicted glassy compliance, glassy flexure, and laminate thicknesses for the 3-ply and 4-ply

laminates, respectively. The percent error between the measured and predicted properties are also listed.

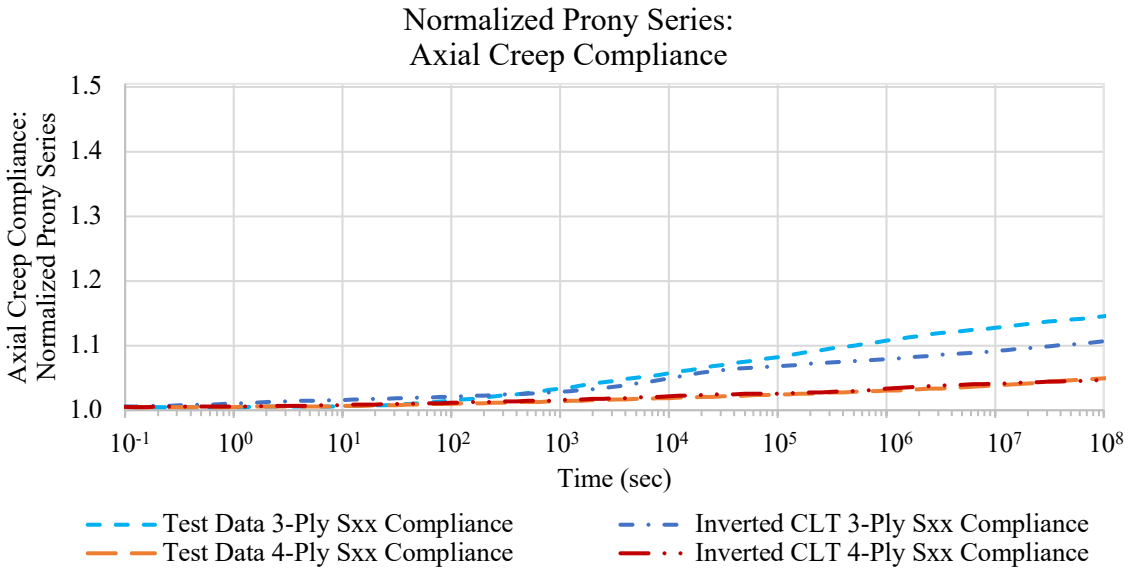

Figure 4.3.7: The measured and inverted CLT axial creep compliance master curves, $S_{xx}(t)$, for the 3-ply and 4-ply laminates are normalized by their respecrtive glassy propeties. The measured axial creep compliance for the 3-ply laminate represented by the dashed light blue line and the predicted creep compliance is represented by the dashed-dotted blue line. The measured axial creep compliance for the 4-ply laminate is represented by the long dashed orange line and the predicted creep compliance is represented by the long dashed-dotted red line.

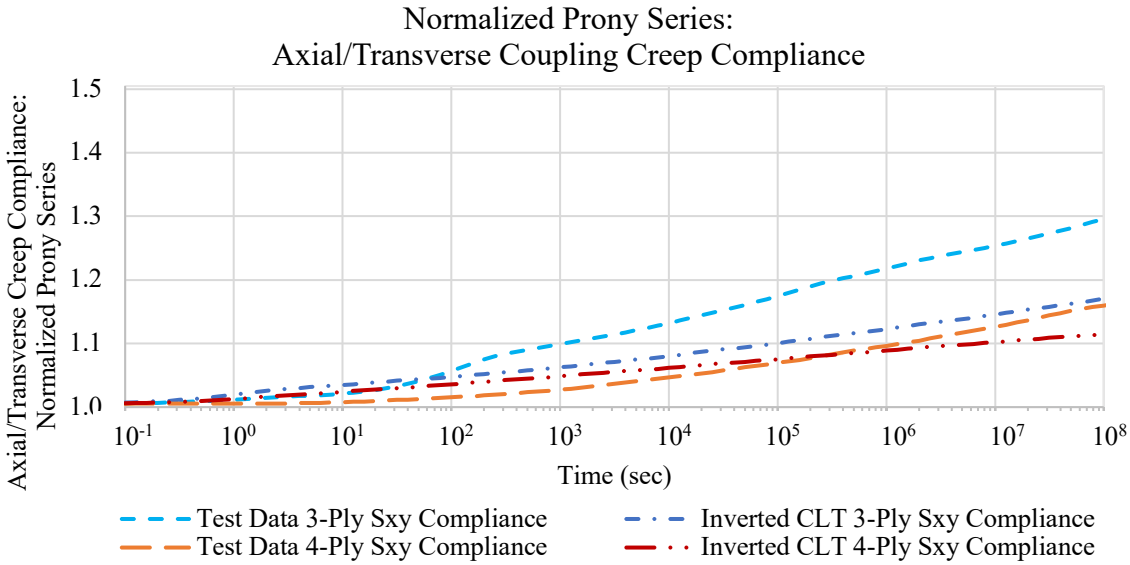

Figure 4.3.8: The measured and inverted CLT axial/transverse creep compliance master curves, $S_{xy}(t)$, for the 3-ply and 4-ply laminates are normalized by their respecrtive glassy properties. The measured axial/transverse creep compliance for the 3-ply laminate represented by the dashed light blue line and the predicted creep compliance is represented by the dashed-dotted blue line. The measured axial/transverse creep compliance for the 4-ply laminate is represented by the long dashed orange line and the predicted creep compliance is represented by the long dashed-dotted red line.

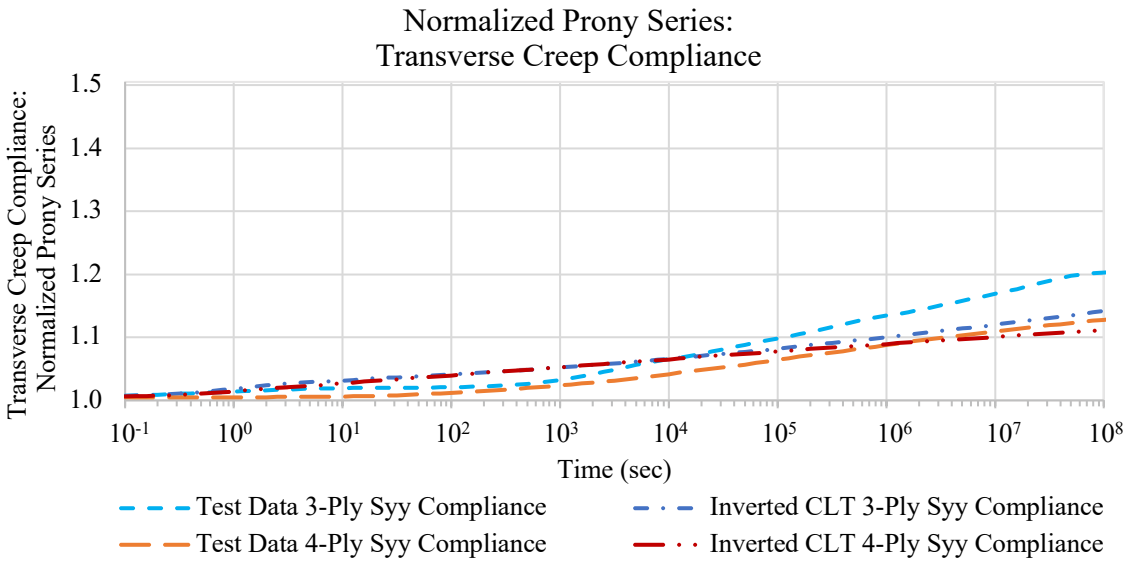

Figure 4.3.9: The measured and inverted CLT transverse creep compliance master curves, $S_{yy}(t)$, for the 3-ply and 4-ply laminates are normalized by their respective glassy properties.The measured transverse creep compliance for the 3-ply laminate represented by the dashed light blue line and the predicted creep compliance is represented by the dashed-dotted blue line. The measured transverse creep compliance for the 4-ply laminate is represented by the long dashed orange line and the predicted creep compliance is represented by the long dashed-dotted red line.

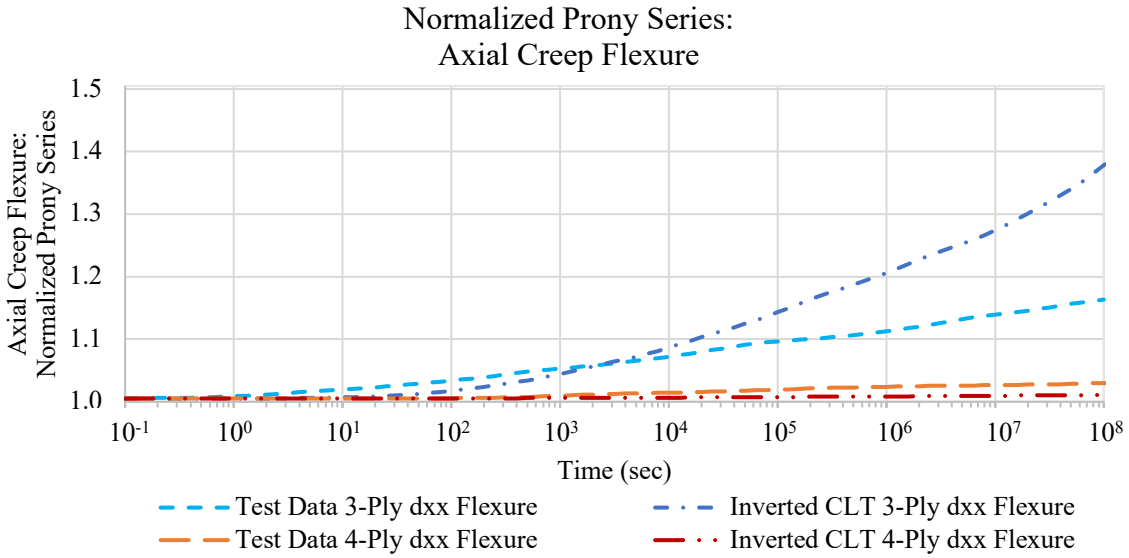

Figure 4.3.10: The measured and inverted CLT axial creep flexure master curves, $d_{xx}(t)$, for the 3-ply and 4-ply laminates are normalized by their repsective glassy properties.The measured axial creep flexure for the 3-ply laminate represented by the dashed light blue line and the predicted creep flexure is represented by the dashed-dotted blue line. The measured axial creep flexure for the 4-ply laminate is represented by the long dashed orange line and the predicted creep flexure is represented by the long dashed/dotted red line.

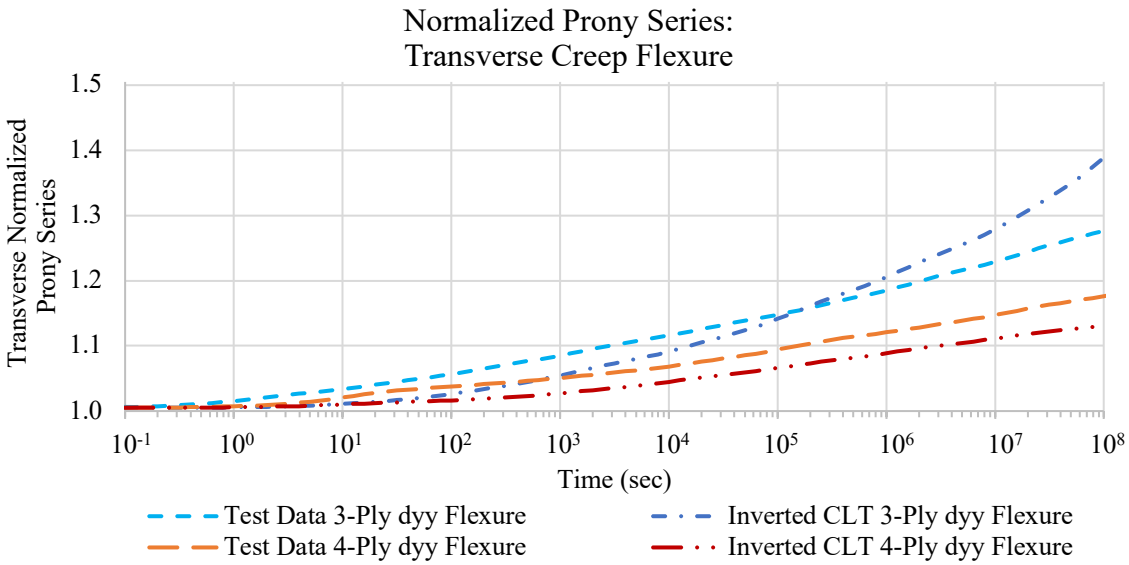

Figure 4.3.11: The measured and inverted CLT transverse creep flexure master curves, $d_{yy}(t)$, for the 3-ply and 4-ply laminates are normalized by their respective glassy properties. The measured transverse creep flexure for the 3-ply laminate represented by the dashed light blue line and the predicted creep flexure is represented by the dashed-dotted blue line. The measured transverse creep flexure for the 4-ply laminate is represented by the long dashed orange line and the predicted creep flexure is represented by the long dashed-dotted red line.

	Measured 3-ply S^g_{xx}	Predicted 3-ply S^g_{xx}	Measured 3-ply S^g_{xy}	Predicted 3-ply S^g_{xy}	Measured 3-ply S^g_{yy}	Predicted 3-ply S^g_{yy}	Measured 3-ply d^g_{xx}	Predicted 3-ply d^g_{xx}	Measured 3-ply d^g_{yy}	Predicted 3-ply d^g_{yy}
Uni Ply Thickness (mm)	-	.1	-	.1	-	.1	-	.1	-	.1
PW Ply Thickness (mm)	-	.2475	-	.2475	-	.2475	-	.2475	-	.2475
Laminate Thickness (mm)	.55	.595	.55	.595	.61	.595	.5	.595	.5	.595
Units	MPa^{-1}		MPa^{-1}		MPa^{-1}		Nmm^{-1}		Nmm^{-1}	
S^g or d^g	2.82E-5	2.97E-5	-2.01E-5	-2.38E-5	6.24E-5	4.55E-5	3.82	3.72	3.19	3.77
Error (%)	5.22		18.54		26.99		2.61		18.08	

Table 4.3.1 records the creep compliance and creep flexure glassy properties for the 3-ply laminate obtained from both measured and inverted CLT predicted data. In addition, the table records the percent error between the respective measured and predicted properties. The measured and adjusted laminate thickness are also recorded.

	Measured 4-ply S_{xx}^{g}	Predicted 4-ply S_{xx}^{g}	Measured 4-ply S_{xy}^{g}	Predicted 4-ply S_{xy}^{g}	Measured 4-ply S_{yy}^{g}	Predicted 4-ply S_{yy}^{g}	Measured 4-ply d_{xx}^{g}	Predicted 4-ply d_{xx}^{g}	Measured 4-ply d_{yy}^{g}	Predicted 4-ply d_{yy}^{g}
Uni Ply Thickness (mm)	-	.14	-	.14	-	.14	-	.14	-	.14
PW Ply Thickness (mm)	-	.18	-	.18	-	.18	-	.18	-	.18
Laminate Thickness (mm)	.62	.64	.62	.64	.65	.64	.60	.64	.63	.64
Units	MPa^{-1}		MPa^{-1}		MPa^{-1}		$N\ mm^{-1}$		$N\ mm^{-1}$	
S^{g} or d^{g}	1.68E-5	1.56E-5	-1.09E-5	-1.20E-5	5.07E-5	4.52E-5	0.416	0.429	3.74	3.58
Error (%)	6.88		9.73		10.89		3.09		4.30	

Table 4.3.2 records the creep compliance and creep flexure glassy properties for the 4-ply laminate obtained from both measured and CLT predicted data. In addition, the table records the percent error between the respective measured and predicted properties. The measured and adjusted laminate thickness are also recorded.

4.4 Discussion

The effects of fiber placement, ply orientation, and stacking sequence on the viscoelastic behavior of the composites were described in Chapter 2 by plotting the normalized axial, axial/transverse, and transverse creep master curves on respective graphs and comparing the viscoelastic behavior of the tested laminae and laminates with each other. Similarly, the normalized relaxation master curves predicted from the application of the numerical Laplace inversion method developed in Chapter 3 are presented in Figure 4.3.1 through Figure 4.3.3. As expected, the unidirectional lamina illustrated in Figure 4.3.1 exhibits elastic behavior in the axial direction due to the axially placed carbon fibers while its matrix dominated axial/transverse and transverse normalized properties illustrated in Figure 4.3.2 and Figure 4.3.3, respectively, match that of the neat resin. The plain weave lamina relaxes in both the axial and transverse directions but has a nearly elastic axial/transverse property. It is observed that the 3-ply laminate [±45PW/0/±45PW] composed of two surface plain weave plies and a unidirectional ply at its neutral axis has a normalized modulus in the axial

direction that behaves similarly to the plain weave lamina. The effect of the elastic fibers from the unidirectional ply in the 3-ply laminate has little influence on the laminate's axial relaxation modulus. In contrast, the 4-ply laminate [0/±45PW/±45PW/0] composed of two unidirectional surface plies and two plain weave plies at its midplane has a nearly elastic axial modulus that mimics the behavior of the normalized unidirectional lamina master curve. The normalized axial/transverse and transverse relaxation master curves for both the 3-ply and 4-ply laminates are nearly identical. The additional unidirectional ply in the 4-ply laminate layup makes the laminate's normalized axial/transverse properties relax slightly more than the 3-ply laminate. The relaxation properties of the unidirectional and plain weave laminae, and the 3-ply and 4-ply laminates behave as expected, having similar viscoelastic tendencies that align with the observations of the measured creep properties presented in Chapter 2.

Using the same format discussed above, the relaxation behavior of the flexure master curves predicted by the viscoelastic classical laminate theory for the neat resin, unidirectional and plain weave laminae, and the 3-ply and 4-ply laminates are compared in Figure 4.3.4 through Figure 4.3.6 using plots of the normalized axial, axial/transverse, and transverse flexure properties, respectively. The unidirectional lamina's normalized flexure in the axial direction is observed in Figure 4.3.4 to have nearly elastic behavior. In contrast, the matrix dominated relaxation properties of the unidirectional lamina's axial/transverse and transverse flexure properties illustrated in Figure 4.3.5 and Figure 4.3.6, respectively, behave similarly to the neat resin when comparing their normalized master curves. The plain weave lamina's axial and transverse normalized flexure properties relax but are less than the neat resin. This behavior is attributed to the carbon fiber woven tows aligned ±45^{o} to the axial direction of

the lamina mitigating some of the viscoelasticity of the matrix. This is notably a different response than what was observed in the creep tests. As mentioned in Chapter 2, more experimental testing of the plain weave lamina is required to better understand how kinks in the continuous fiber tows due to the weave affect the viscoelastic response of the material. The relaxation behaviors observed in the unidirectional and plain weave laminae are much more pronounced in the relaxation flexure response of the 3-ply and 4-ply laminates compared to their relaxation modulus properties discussed earlier. The plies at the surface of the laminate make a greater contribution to the flexure properties than the plies located closer to the midplane (bending neutral axis). The unidirectional ply at the neutral axis of the 3-ply laminate does little to mitigate relaxation. As a result, the surface plain weave plies of the 3-ply laminate primarily influence its relaxation flexure properties. Similar behavior is observed with the 4-ply laminate's flexure properties where the unidirectional surface plies of the laminate dominate the relaxation flexure stiffness in the axial direction resulting in an elastic behavior that matches the normalized master curve of the unidirectional lamina. The 4-ply laminate's axial/transverse and transverse relaxation flexure properties, on the other hand, are a combination of the relaxation behavior of the unidirectional plies on either side of the laminate's neutral axis and the laminates plain weave surface plies. The 4-ply laminate's normalized axial/transverse and transverse master curves lie between the more viscoelastic unidirectional lamina and the less viscoelastic plain weave lamina.

The measured creep compliance and flexure test data for the 3-ply and 4-ply laminates is directly compared to relaxation properties predicted by the viscoelastic CLT by inverting the relaxation stiffness and flexure properties using the numerical Laplace inversion method developed in Chapter 3. Figure 4.3.7 through Figure 4.3.11 present the originally measured

3-ply and 4-ply data alongside the inverted CLT master curves for the individual material properties normalized by their respective glassy properties, e.g., axial creep compliance $S_{xx}(t)/S_{xx}^{g}$, axial/transverse creep compliance $S_{xy}(t)/S_{xy}^{g}$, transverse creep compliance $S_{yy}(t)/S_{yy}^{g}$, axial creep flexure $d_{xx}(t)/d_{xx}^{g}$, and transverse creep flexure $d_{yy}(t)/d_{yy}^{g}$, respectively. The inverted CLT 4-ply creep compliance properties illustrated in Figure 4.3.7 through Figure 4.3.9 using normalized master curves, match well with the measured data. The inverted CLT creep compliance properties for the 3-ply laminate, however, tends to creep less than the measured data. This may be a further indication of the observations discussed in Chapter 2, which noted that the grips used in the tensile creep tests may have been applying shear loading to the more viscoelastic plain weave surface plies of the 3-ply laminate resulting in test results exhibiting a greater degree of viscous response. However, the CLT model appears to over predict the creep flexure properties illustrated in Figure 4.3.10 and Figure 4.3.11 in which the plain weave surface plies of the 3-ply laminate dominate the creep normalized master curves resulting in more creep than illustrated by the measured data. The flexure master curves predicted by the CLT for the 4-ply laminate match more favorably to measured data with predictions creeping slightly less. The variation between the measured and predicted normalized master curves appears to be primarily the result of discrepancies in the laminate's ply thickness. This is evident when comparing the measured and predicted glassy properties of the 3-ply and 4-ply laminates listed in Table 4.3.1 and Table 4.3.2. The 4-ply laminates glassy properties (compliance and flexure) fall within a 10% error. The 3-ply laminates glassy properties, however, vary more with a maximum transverse compliance error of 26%. The laminate thicknesses of the predicted and measured samples are quite similar, but the unidirectional and plain weave ply thicknesses

vary more between laminates. As discussed in Chapter 2, samples were water-jet cut from a single sheet of the respective unidirectional and plain weave laminae, and the 3-ply and 4-ply laminates. Slight variations in the lamina or laminate's sheet thickness, resin concentration, and ply orientations could contribute to the variability observed in the material properties. Tighter quality control and greater statistical test profiles could provide more accurate test data reducing the variability between the measured and predicted glassy values for the axial, axial/transverse, and transverse properties. Overall, the viscoelastic CLT and inversion method predictions trend towards the expected creep response of the 3-ply and 4-ply laminate and provide the relaxation modulus and flexure properties required for the development of structural models.

4.5 Conclusion

Creep compliance and flexure properties are often experimentally obtained in lieu of the more difficult to measure relaxation properties. The Laplace numerical inversion method developed in Chapter 3 provides a means of predicting the relaxation properties from measured creep data. The numerical Laplace inversion of the measured creep compliance properties of the neat resin, unidirectional and plain weave laminae, and the 3-ply and 4-ply laminates from Chapter 2 are recorded in this chapter. Inversion of the creep flexure properties is not possible due to the lack of measured axial/transverse creep flexure properties. As a result, the viscoelastic classical laminate theory is used to predict the lamina and laminate relaxation flexure properties using measured inverted unidirectional and plain weave compliance data as inputs. The numerical Laplace inversion method and the viscoelastic classical laminate theory discussed in this chapter provide a means of obtaining

relaxation properties without the need for complex relaxation tests. The relaxation properties predicted by the two methods can be used in structural models.

Chapter 5

Viscoelastic Behavior of a Biaxially Bent Composite Storable Tubular Extendable Member

5.1 Introduction

An analytical model is needed to define how laminate composition (plies composed of either unidirectional fibers or plain weave mats), ply orientation, and stacking sequence impact the viscoelastic performance of a composite STEM. The viscoelastic behavior of tape springs, which are very similar to STEMs, has been studied in the literature [3], [9], [10], [48]–[50]. Tapes spring have a more open U-shaped cross-section and are less tubular than STEMs. Nonetheless, the stowage configuration of STEMs and their unfolding action is comparable to the behavior of a tape spring, in which imposed biaxial bending curvatures result in moments that can relax, impeding the tape springs deployment. Similarly, the deformation in the tape spring's deployed curvature due to viscoelasticity, like that of the STEM, can affect the stiffness of the structure. In an attempt to understand viscoelastic effects in tape springs, Kwok and Pellegrino [30] modified elastic finite element analysis (FEA) methods to model a tape spring made from a plain weave composite. The stowed

configuration of their tape spring varies slightly from the STEMs shown in Figure 1.1.1. Kwok and Pellegrino's tape spring are severely bent in half rather than rolled, resulting in a biaxial bend state in a localized section of the tape spring as opposed to the entire length of a STEM as illustrated in Figure 1.1.3. Once bent, their tape spring is held in this position for some time and allowed to relax. It is then deployed and allowed to return to its original configuration. The resulting advanced FEA model is useful for predicting complex transitional shapes of deployable tape spring structures. However, the approach is computationally time-consuming and does not provide a quick and straightforward method for modeling various STEMs composed of differing laminate layups, and geometric configurations (e.g., stowed and deployed geometries). In contrast, a mathematical model is developed in this chapter that can quickly predict the relaxation moments and recovery curvature of composite STEMs in biaxial bending. The model builds upon analytical solutions for one-dimensional simple beam structures [20], [49], and uses hereditary integral expressions, found in the literature [18], [51], to model the viscoelastic behavior of STEMs. Through the use of classical laminate theory, the model provides a tool to aid in the design evaluation of composite STEMs for various applications based on structural composition (e.g., number of plies, laminae type and ply orientation), geometrical configurations (e.g., deployed and stowed curvatures), and stowed durations.

5.2 Background

Hereditary integrals were developed by Boltzmann and Volterra as part of their work on hereditary mechanics to account for time-dependent stress-strain relationships, also known as the memory effect [52]. Deformation or creep processes in viscoelastic solids with memory

have been modeled using hereditary integrals [18], [51]. Time-dependent beam bending equations of the hereditary integral type are found in the literature representing beam deflection and moment response [20], [49], [53]. A one-dimensional, viscoelastic, isotropic beam in bending provides the foundation for the anisotropic biaxial bending equations developed in this chapter. The general form of the beam bending equations represented in the literature is derived using time-dependent laminate convolution integrals in the form

$$K(t) = \int_{-\infty}^{t} d(t-\tau)\frac{d}{d\tau}M(\tau)d\tau \tag{5.2.1a}$$

$$M(t) = \int_{-\infty}^{t} D(t-\tau)\frac{d}{d\tau}K(\tau)d\tau \tag{5.2.1b}$$

where $K(t)$ is the curvature, t is time, $d(t)$ is the creep flexural compliance, $M(t)$ is the bending moment and $D(t)$ is the relaxation flexure modulus. The hereditary integral spans the entire load history from time $-\infty$ to the current time t, but the material is assumed to be unchanged until just before the deformation is applied at time 0. As a result, the integration from $-\infty$ to t can be rewritten from 0^- to t,

$$K(t) = \int_{0^-}^{t} d(t-\tau)\frac{d}{d\tau}M(\tau)d\tau \tag{5.2.2a}$$

$$M(t) = \int_{0^-}^{t} D(t-\tau)\frac{d}{d\tau}K(\tau)d\tau \tag{5.2.2b}$$

What follows is the development of the equations that represent the relaxation form of the general hereditary equations, in which the resulting bending moment is deduced from the curvature that the beam experiences. The same methods applied to relaxation can be applied to creep, in which the curvature is deduced from the applied bending moment.

Figure 5.2.1 represents the bending curvature and moment histories of a one-dimensional beam in bending, (a) and (b), respectively. An imposed constant change in curvature ΔK^o is quickly applied at $t = 0$ and the resulting moment relaxes while the change in curvature is

held fixed. At time $t = t_o$ the constant change in curvature is released, and the bending moment is reduced to zero. Due to the preceding viscoelastic response (e.g., relaxation of the material), the change in curvature at $t = t_o$ is initially nonzero, but over time $t > t_o$, the beam's curvature will recover to its original undeformed state. This phenomenon occurs because the polymer chains of the resin matrix slowly rearrange to a minimum potential energy state (e.g., the beam's undeformed, unstressed state). All imposed changes in the moment and curvature of the beam are assumed to occur instantaneously and are represented by a Heaviside step function, $H(t)$. This is a valid representation for viscoelastic materials when imposed deformation rates and the rate of change of imposed curvatures are sufficiently fast to render viscoelasticity negligible during such transitions. The Heaviside function is such that.

$$H(t) = \begin{cases} 0, & t < 0 \\ 1, & t \geq 0 \end{cases} \tag{5.2.3}$$

As shown in Figure 5.2.1a, a constant change in curvature ΔK^o is imposed on the beam from $0 < t \leq t_o$. The beam equations (5.2.2a) and (5.2.2b) are broken into two stages, relaxation ($0 < t \leq t_o$), and recovery ($t_o < t < \infty$). The initial applied constant change in curvature ΔK^o is represented using the Heaviside step function as given in equation (5.2.3).

$$\Delta K(t) = H(t)\Delta K^o = \begin{cases} 0, & t < 0 \\ \Delta K^o, & t \geq 0 \end{cases} \tag{5.2.4}$$

The resulting relaxation moment is obtained by inserting equation (5.2.4) into the general hereditary beam bending equation (5.2.2b).

$$M(t) = \int_{0^-}^{t} D(t-\tau)\frac{d}{d\tau}H(\tau)\Delta K^o d\tau \tag{5.2.5a}$$

The derivative of the Heaviside step function is the Dirac delta function $\delta(t)$.

$$M(t) = \int_{0-}^{t} D(t-\tau)\delta(\tau)\Delta K^o d\tau \tag{5.2.5b}$$

The integration of equation (5.2.5b) results in the final expression of the moment equation for an applied constant change in curvature.

$$M(t) = D(t)\Delta K^o \tag{5.2.5c}$$

At time $t = t_o$ the constant curvature is quickly released, and the resulting moment is reduced to zero. Equation (5.2.5c) is modified with the use of the Heaviside step function to represent the zero moment for $t \geq t_o$.

$$M(t) = D(t)\Delta K^o - H(t-t_o)D(t)\Delta K^o = \begin{cases} D(t)\Delta K^o, & 0 \leq t < t_o \\ 0, & t \geq 0 \end{cases} \tag{5.2.6}$$

Inserting equation (5.2.6) into the general form of the curvature equation (5.2.2a) results in the curvature equation for a relaxing beam in pure bending.

$$\Delta K(t) = \int_{0-}^{t} d(t-\tau)\frac{d}{d\tau}(D(\tau)\Delta K^o - H(\tau-t_o)D(\tau)\Delta K^o)d\tau \tag{5.2.7a}$$

The result in equation (5.2.7a) can be formed into two integrals.

$$\Delta K(t) = \int_{0-}^{t} d(t-\tau)\frac{d}{d\tau}(D(\tau)\Delta K^o)d\tau$$

$$-\int_{0-}^{t} d(t-\tau)\frac{d}{d\tau}(H(\tau-t_o)D(\tau)\Delta K^o)d\tau \tag{5.2.7b}$$

Note that

$$\int_{0-}^{t} d(t-\tau)\frac{d}{d\tau}D(\tau)d\tau = \int_{0-}^{t} D(t-\tau)\frac{d}{d\tau}d(\tau)d\tau = H(t) \tag{5.2.8}$$

Replacing the first integral in (5.2.7b) by the result from equation (5.2.8) and deriving the products in the second integrand we obtain

$$\Delta K(t) = H(t)\Delta K^o - \int_{0-}^{t}[d(t-\tau)\delta(\tau-t_o)D(\tau)\Delta K^o$$

$$+H(\tau-t_o)d(t-\tau)\frac{d}{d\tau}D(\tau)\Delta K^o]d\tau \tag{5.2.7c}$$

The integral in equation (5.2.7c) containing the Dirac delta function becomes

$$\int_{0^-}^{t} d(t-\tau)\delta(\tau-t_o)D(\tau)\Delta K^o d\tau = d(t-t_o)D(t_o)\Delta K^o \tag{5.2.9}$$

The other integral in equation (5.2.7c) can be rearranged to provide

$$\int_{0^-}^{t} H(\tau-t_o)d(t-\tau)\frac{d}{d\tau}D(\tau)\Delta K^o d\tau$$

$$= H(t-t_o)\int_{t_o}^{t} d(t-\tau)\frac{d}{d\tau}D(\tau)\Delta K^o d\tau \tag{5.2.10}$$

As a result, the change in curvature from equation (5.2.7c) can be simplified by the use of equations (5.2.9) and (5.2.10) to give

$$\Delta K(t) = H(t)\Delta K^o - d(t-t_o)D(t_o)\Delta K^o$$

$$-H(t-t_o)\int_{t_o}^{t} d(t-\tau)\frac{d}{d\tau}D(\tau)\Delta K^o d\tau \tag{5.2.7d}$$

where it is to be understood that $D(t) = 0$ for $t < 0$. The curvature equation (5.2.7d) can be expressed for the different time intervals involving constant curvature, $0 \le t < t_o$, elastic recovery at time $t = t_o$, and viscoelastic recovery thereafter for $t > t_o$.

$$\Delta K(t) = \begin{cases} \Delta K^o, & 0 \le t < t_o \\ \Delta K^o - d(0)D(t_o)\Delta K^o, & t = t_o^+ \\ \Delta K^o - d(t-t_o)D(t_o)\Delta K^o - \int_{t_o}^{t} d(t-\tau)\frac{d}{d\tau}D(\tau)\Delta K^o d\tau\,, & t > t_o \end{cases} \tag{5.2.7e}$$

In the next section, equations (5.2.6) and (5.2.7d), representing the moment and curvature history of a beam in pure bending, will be used as the foundations to develop expressions for the biaxially bent condition of the composite material.

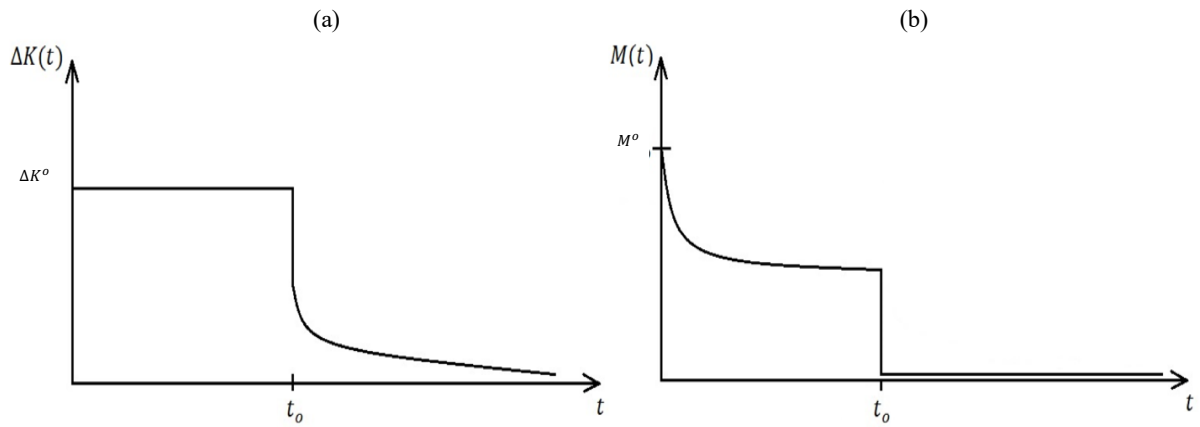

Figure 5.2.1: The viscoelastic curvature (a) and bending moment (b) for a one-dimensional beam in pure bending. A constant curvature is imposed during $0 \leq t < t_o$*, resulting in a bending moment that relaxes. At* $t = t_o$ *the imposed constant curvature is quickly released and the bending moment reduces to zero. As a result of relaxation, the released curvature is nonzero. However, as time progresses* $t > t_o$ *the curvature recovers viscoelastically to zero, due to the slow rearranging of the polymer chains of the neat resin matrix to a minimum potential energy state (e.g., the beam's undeformed, unstressed state).*

5.3 Methods

Biaxial bending of a viscoelastic composite is characterized by the use of time-dependent applied bending moments and curvatures consistent with classical laminate theory. All composites are assumed to be balanced/symmetric laminates in which no torsional/shear coupling occurs in tension and bending. Hereditary integrals are used to define the viscoelastic response of a STEM (e.g., tape spring) deformed by two axial curvatures defined as a biaxial state of bending. Figure 5.3.1 illustrates a section of the STEM presented in Figure 1.1.3 in which the z-direction extends along the length of the undeformed tubular portion of the STEM (a). The STEM in this configuration prior to deformation is assumed to be free of stress. A biaxial state of bending is imposed at $t = 0$ by first flattening the STEM as shown going from illustration (a) to (b) in Figure 5.3.1 by imposing a bending curvature ΔK_{zz}. The STEM is then rolled up about the x-axis into a uniform stowed curvature ΔK_{xx}, as shown going from illustration (b) to (c). Illustration (c) shows the STEM reverse rolled in its

undeployed, stowed configuration with both principal curvatures defined to be positive. This state of bending results in a biaxial compression of the STEM's outer surface and a biaxial tension of the inner surface. In order to prevent the STEM from microbuckling in the compressed state, the laminates must be thin- 2 to 4 plies thick- and the undeformed STEM radius and reversed roll radius must be sufficiently large to reduce compressive strains. The stowed configuration curvature is defined to be $\Delta K_{zz} = 1/r_2$, and is selected to prevent micro buckling. The bending curvature that arises due to flattening the STEM (Figure 5.3.1 (b)) is defined to be ΔK_{xx}, and is equivalent to its undeformed curvature, $K_{xx} = 1/r_1$. The biaxial state of bending imposed to stow the STEM is maintained for a period of time $0 < t \leq t_o$, typically the storage duration of the STEM after production, during which the resulting axial and transverse bending moments, $M_{zz}(t)$ and $M_{xx}(t)$, respectively, relax due to the material's viscoelastic properties. During deployment at $t = t_o$, the STEM unrolls from being coiled around the x-axis and extends in the z-direction. The imposed biaxial bending curvatures, ΔK_{zz} and ΔK_{xx}, are released. Due to the tubular shape of the deployed STEM (nonzero transverse curvature), the axial curvature ΔK_{zz} immediately goes to zero on deployment, which produces a negative axial moment $M_{zz}(t)$ as a result of the viscoelastically changed material. The transverse moment $M_{xx}(t)$ on deployment is zero resulting in a nonzero transverse curvature $\Delta K_{xx}(t)$. As time progresses, i.e., $t > t_o$, both the negative axial moment $M_{zz}(t)$ and nonzero transverse curvature $\Delta K_{xx}(t)$ will slowly return to zero as the STEM recovers to its original stress-free deployed configuration, Figure 5.3.1 (a).

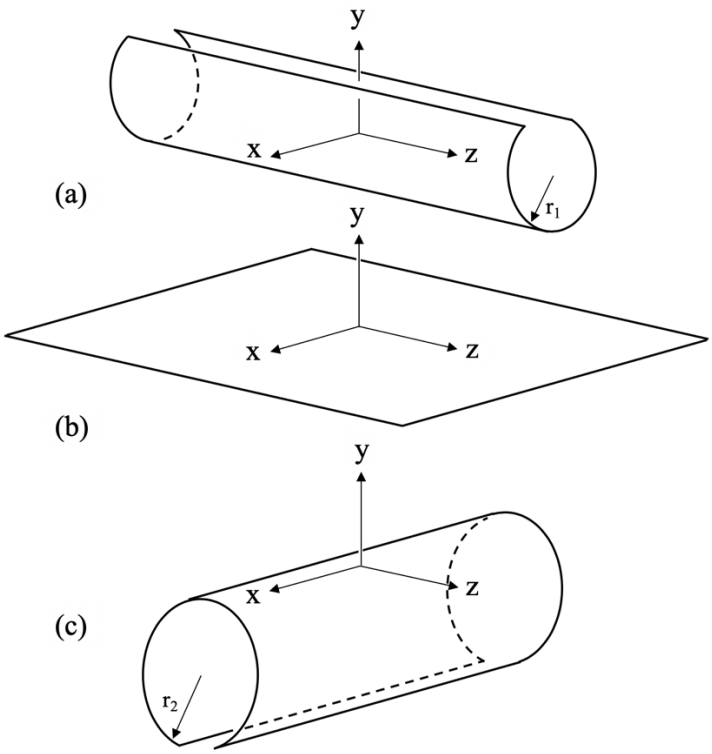

Figure 5.3.1: A segment of a STEM in its deployed (a), flattened (c), and biaxial stowed configuration (c). The STEM is longer than shown in the z-direction as only a segment is illustrated. In the stowed configuration, the STEM is rolled up around the x-axis in a coil. The stowed curvature $\Delta K_{zz} = 1/r_2$ (c) is selected such that micro buckling in the laminate does not occur. The other principal curvature $\Delta K_{xx} = 1/r_1$ is determined by the deployed state (a), which must be flattened to stow the STEM.

In order to simplify the following derivations, it is assumed that at time $t = 0$ both principal curvatures are simultaneously and rapidly imposed to deform the STEM into the biaxially bent stowed configuration and that at time $t = t_o$ both of the principal curvatures are simultaneously and rapidly modified. In reality, during both stowage and deployment, the STEM must be flattened first, inducing the change of one principal curvature, before the other principal curvature change can occur. However, if the duration required to stow and deploy the boom are sufficiently short in comparison to the characteristic time for the material's viscoelastic response, the assumption of simultaneous and rapid biaxial bending deformation is valid for the solutions derived in this chapter. Furthermore, Figure 5.3.1 illustrates the stowed and deployed transitions assumed by the model developed in this

chapter, which ignores the complex transition zones that arise as the boom unrolls from the biaxial stowed configuration to the deployed configuration as illustrated in Figure 1.1.3.

Figure 5.3.2 illustrates a STEM's bending moment and curvature histories in both principal directions resulting from the stowed and deployed configurations illustrated in Figure 5.3.1. The curvatures are shown in Figure 5.3.2 (a) and (c) and the bending moments in Figure 5.3.2 (b) and (d). Figure 5.3.2 (a) and (b) show the axial curvature and bending moment while Figure 5.3.2 (c) and (d) show the transverse curvature and bending moment. The bending moments in the stowed state ($0 < t \leq t_o$) experience relaxation due to constant biaxial curvature. The degree to which the moments relax is dependent on the material. In the case of a composite, stacking sequence and orientation play a significant role in the material's viscoelastic response. At $t = t_o$ the curvatures are released, and the STEM responds elastically and then commences to recover viscoelastically. The material, at this time, has lost some memory of its original undeformed shape, resulting in the retention of a nonzero transverse curvature (Figure 5.3.2 (c)). The transverse moment of the STEM immediately returns to zero (Figure 5.3.2 (d)). As noted above, the axial curvature is forced to zero (illustrated in Figure 5.3.2 (a)) due to the geometric configuration of the STEM even though the material seeks a nonzero curvature similar to that developed for the transverse curvature. As a result, during $t > t_o$, the material experiences an induced bending moment in the axial direction, as shown in Figure 5.3.2 (b). During this phase, the axial bending moment is negative, and the transverse curvature is positive, but both recover towards zero over time as the STEM returns to its original undeformed, unstressed, deployed state.

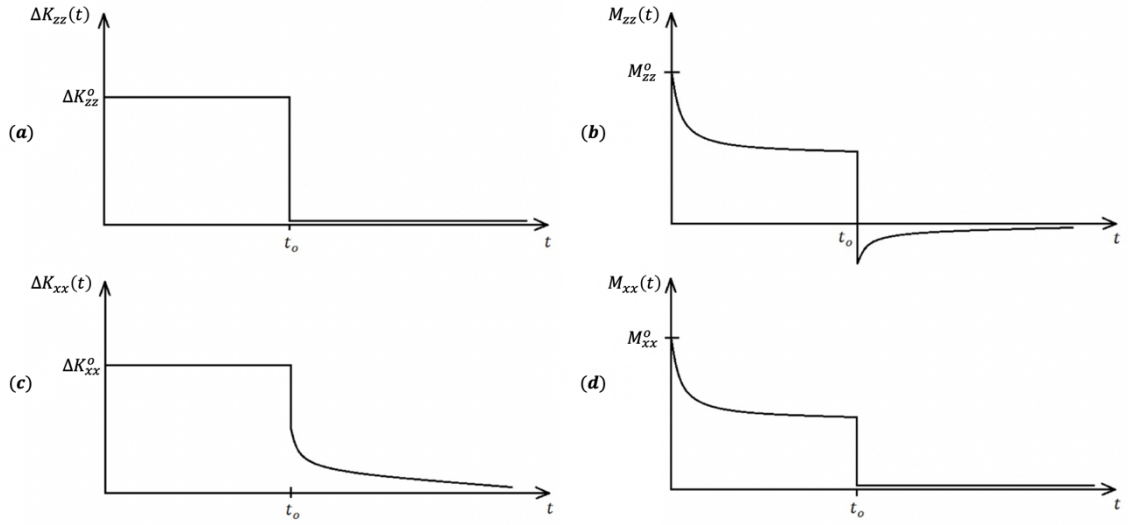

Figure 5.3.2: The biaxial curvature and bending moment histories of a viscoelastic STEM. The curvatures are shown in illustrations (a) and (c) and the bending moments in illustrations (b) and (d). Illustrations (a) and (b) show the axial curvature and bending moment while illustration (c) and (d) show the transverse curvature and bending moment. Biaxial curvatures are applied at $t = 0$ to stow the STEM and are released at $t = t_o$ to deploy the STEM. The STEM recovers during $t > t_o$ to its original undeformed, unstressed, deployed state.

As mentioned earlier, all materials are assumed to be anisotropic and viscoelastic with balanced symmetric properties that eliminate any torsional/shear coupling properties. The flexural relaxation properties of classical laminate theory (CLT), i.e., those contained in D of the ABD matrix, are used. The history of the axial curvature changes is given by

$$\Delta K_{zz}(t) = \big(H(t) - H(t - t_o)\big)\Delta K_{zz}^o \tag{5.3.1}$$

where, at $t = 0$, a curvature change of magnitude ΔK_{zz}^o is rapidly imposed, and then, at $t = t_o$, a second rapid curvature change completely eliminates the initial deformation, with the latter condition persisting for $t > t_o$. The history of the transverse curvature changes is given by

$$\Delta K_{xx}(t) = H(t)\Delta K_{xx}^o - H(t - t_o)\Delta \overline{K}_{xx}(t) \tag{5.3.2}$$

where, at $t = 0$, a curvature change of magnitude ΔK_{xx}^o is rapidly imposed, and then, at $t = t_o$, a second rapid curvature change occurs to eliminate the bending moment, M_{xx}, with the latter quantity remaining zero for $t > t_o$. However, the change of curvature at time $t = t_o$,

and the history of the curvature for $t > t_o$ is, as yet, undetermined and so its negative is represented by an as yet unknown function $\Delta\overline{K}_{xx}(t)$.

A hereditary integral form of the classical laminate theory flexure equation is used for the relationship between the bending moments and the curvature changes in the form

$$M_{zz}(t) = \int_{0^-}^{t} D_{zz}(t-\tau)\frac{d}{d\tau}\Delta K_{zz}(\tau)d\tau + \int_{0^-}^{t} D_{zx}(t-\tau)\frac{d}{d\tau}\Delta K_{xx}(\tau)d\tau \tag{5.3.3a}$$

$$M_{xx}(t) = \int_{0^-}^{t} D_{xz}(t-\tau)\frac{d}{d\tau}\Delta K_{zz}(\tau)d\tau + \int_{0^-}^{t} D_{xx}(t-\tau)\frac{d}{d\tau}\Delta K_{xx}(\tau)d\tau \tag{5.3.4a}$$

Insertion of equations (5.3.1) and (5.3.2) into equations (5.3.3a) and (5.3.4a) then provides

$$\begin{aligned} M_{zz}(t) &= \int_{0^-}^{t} D_{zz}(t-\tau)\frac{d}{d\tau}\Big(\big(H(\tau) - H(\tau-t_o)\big)\Delta K_{zz}^{o}\Big)\,d\tau \\ &+ \int_{0^-}^{t} D_{zx}(t-\tau)\frac{d}{d\tau}\big(H(\tau)\Delta K_{xx}^{o} - H(\tau-t_o)\Delta\overline{K}_{xx}(\tau)\big)d\tau \end{aligned} \tag{5.3.3b}$$

$$\begin{aligned} M_{xx}(t) &= \int_{0^-}^{t} D_{xz}(t-\tau)\frac{d}{d\tau}\Big(\big(H(\tau) - H(\tau-t_o)\big)\Delta K_{zz}^{o}\Big)\,d\tau \\ &+ \int_{0^-}^{t} D_{xx}(t-\tau)\frac{d}{d\tau}\big(H(\tau)\Delta K_{xx}^{o} - H(\tau-t_o)\Delta\overline{K}_{xx}(\tau)\big)d\tau \end{aligned} \tag{5.3.4b}$$

For $t < t_o$ the bending moments from equations (5.3.3) and (5.3.4) are

$$M_{zz}(t) = D_{zz}(t)\Delta K_{zz}^{o} + D_{zx}(t)\Delta K_{xx}^{o} \tag{5.3.5a}$$

$$M_{xx}(t) = D_{xz}(t)\Delta K_{zz}^{o} + D_{xx}(t)\Delta K_{xx}^{o} \tag{5.3.5b}$$

For $t \geq t_o$ they are

$$\begin{aligned} M_{zz}(t) &= \big(D_{zz}(t) - D_{zz}(t-t_o)\big)\Delta K_{zz}^{o} + D_{zx}(t)\Delta K_{xx}^{o} \\ &- D_{zx}(t-t_o)\Delta\overline{K}_{xx}(t_o) - \int_{t_o}^{t} D_{zx}(t-\tau)\frac{d}{d\tau}\Delta\overline{K}_{xx}(\tau)d\tau \end{aligned} \tag{5.3.6a}$$

$$\begin{aligned} M_{xx}(t) &= \big(D_{xz}(t) - D_{xz}(t-t_o)\big)\Delta K_{zz}^{o} + D_{xx}(t)\Delta K_{xx}^{o} \\ &- D_{xx}(t-t_o)\Delta\overline{K}_{xx}(t_o) - \int_{t_o}^{t} D_{xx}(t-\tau)\frac{d}{d\tau}\Delta\overline{K}_{xx}(\tau)d\tau = 0 \end{aligned} \tag{5.3.6b}$$

where the fact that $M_{xx} = 0$ for $t \geq t_o$ is identified in equation (5.3.6b).

To obtain a solution for the curvatures and moments, a numerical method is used utilizing a Prony series to estimate the recovery response for the transverse recovery curvature.

$$\Delta\overline{K}_{xx}(t) = \Delta K^o_{xx} - \sum_{l=1}^{n} \Delta K^l_{xx} e^{-\lambda^l (t-t_o)} \tag{5.3.7}$$

The Prony time constants λ^l are set equal to the inverse of the time decay spanning the master curve history of the material (e.g., 0.1, 0.01, 0.001, etc.), and ΔK^l_{xx} are Prony series coefficients to be solved for numerically. The transverse curvature equation (5.3.2) can, therefore, be rewritten as

$$\Delta K_{xx}(t) = \Delta K^o_{xx} - H(t-t_o)\left(\Delta K^o_{xx} - \sum_{l=1}^{n} \Delta K^l_{xx} e^{-\lambda^l (t-t_o)}\right) \tag{5.3.8}$$

In order to solve the system of equations further the known relaxation flexure, $D(t)$, defined by the Prony series equation (1.3.8c) with $D^g = D^e + \sum_{m=1}^{n} D^m$ is inserted into the general form of the transverse moment equation (5.3.6b) to obtain for $t > t_o$

$$\begin{aligned} M_{xx}(t) = {} & \left(D^e_{xz} + \sum_{m=1}^{n} D^m_{xz} e^{-\alpha^m t}\right)\Delta K^o_{zz} - \left(D^e_{xz} + \sum_{m=1}^{n} D^m_{xz} e^{-\alpha^m (t-t_o)}\right)\Delta K^o_{zz} \\ & + \left(D^e_{xx} + \sum_{m=1}^{n} D^m_{xx} e^{-\alpha^m t}\right)\Delta K^o_{xx} \\ & - \left(D^e_{xx} + \sum_{m=1}^{n} D^m_{xx} e^{-\alpha^m (t-t_o)}\right)\left(\Delta K^o_{xx} - \sum_{l=1}^{n} \Delta K^l_{xx}\right) \\ & - \int_{t_o}^{t} \left(D^e_{xx} + \sum_{m=1}^{n} D^m_{xx} e^{-\alpha^m (t-\tau)}\right) \frac{d}{d\tau}\left(\Delta K^o_{xx} - \sum_{l=1}^{n} \Delta K^l_{xx} e^{-\lambda^l (\tau - t_o)}\right) d\tau \end{aligned} \tag{5.3.9}$$

The integral in equation (5.3.9) can be reduced further by differentiating the unknown curvature function.

$$\int_{t_o}^{t} \left(D^e_{xx} + \sum_{m=1}^{n} D^m_{xx} e^{-\alpha^m (t-\tau)}\right)\left(\sum_{l=1}^{n} \Delta K^l_{xx} \lambda^l e^{-\lambda^l (\tau - t_o)}\right) d\tau \tag{5.3.10}$$

The integral can then be separated into two parts.

$$D^e_{xx} \sum_{l=1}^{n} \Delta K^l_{xx} \lambda^l \int_{t_o}^{t} e^{-\lambda^l (\tau - t_o)} d\tau = D^e_{xx} \sum_{l=1}^{n} \Delta K^l_{xx} \left(1 - e^{-\lambda^l (t-t_o)}\right) \tag{5.3.11}$$

$$\int_{t_o}^{t} \sum_{m=1}^{n} D^m_{xx} e^{-\alpha^m (t-\tau)} \sum_{l=1}^{n} \Delta K^l_{xx} \lambda^l e^{-\lambda^l (\tau - t_o)}\, d\tau$$

$$= \sum_{m=1}^{n} \sum_{l=1}^{n} \frac{D_{xx}^{m} \Delta K_{xx}^{l} \lambda^{l}}{\alpha^{m} - \lambda^{l}} \left(e^{-\lambda^{l}(t-t_o)} - e^{-\alpha^{m}(t-t_o)} \right) \tag{5.3.12}$$

Inserting equation (5.3.11) and (5.3.12) into equation (5.3.9) results in the expression of the transverse moment equation for $t > t_o$.

$$\begin{aligned} M_{xx}(t) = {} & \left(D_{xz}^{e} + \sum_{m=1}^{n} D_{xz}^{m} e^{-\alpha^{m} t}\right) \Delta K_{zz}^{o} - \left(D_{xz}^{e} + \sum_{m=1}^{n} D_{xz}^{m} e^{-\alpha^{m}(t-t_o)}\right) \Delta K_{zz}^{o} \\ & + \left(D_{xx}^{e} + \sum_{m=1}^{n} D_{xx}^{m} e^{-\alpha^{m} t}\right) \Delta K_{xx}^{o} \\ & - \left(D_{xx}^{e} + \sum_{m=1}^{n} D_{xx}^{m} e^{-\alpha^{m}(t-t_o)}\right) \left(\Delta K_{xx}^{o} - \sum_{l=1}^{n} \Delta K_{xx}^{l}\right) \\ & - D_{xx}^{e} \sum_{l=1}^{n} \Delta K_{xx}^{l} \left(1 - e^{-\lambda^{l}(t-t_o)}\right) \\ & - \sum_{m=1}^{n} \sum_{l=1}^{n} \frac{D_{xx}^{m} \Delta K_{xx}^{l} \lambda^{l}}{\alpha^{m} - \lambda^{l}} \left(e^{-\lambda^{l}(t-t_o)} - e^{-\alpha^{m}(t-t_o)} \right) = 0 \end{aligned} \tag{5.3.13}$$

The transverse recovery curvature is evaluated by solving numerically for the Prony series coefficients ΔK_{xx}^{l} in equation (5.3.7) that result in satisfying the transverse moment equation (5.3.13). The time scale in which the data is obtained is dependent on the duration of storage t_o of the STEM and the material's viscoelastic master curve time history. The Prony series curvature constants are solved using a numerical method and are unique solutions dependent on the applied biaxial curvature, material properties, and duration of storage. As a result, the solution for one set of conditions cannot be applied universally. Using the numerical solution for the recovery curvature $\Delta \overline{K}_{xx}(t)$ (equation (5.3.7)), the result for the axial moment can now be obtained. First, equation (5.3.6a) is rewritten using the Prony series form of the relaxation curvature (5.3.6) and bending stiffness material properties (1.3.8c) with $D^{g} = D^{e} + \sum_{m=1}^{n} D^{m}$, and for $t > t_o$ leads to

$$\begin{aligned} M_{zz}(t) = {} & \left(D_{zz}^{e} + \sum_{m=1}^{n} D_{zz}^{m} e^{-\alpha^{m} t}\right) \Delta K_{zz}^{o} - \left(D_{zz}^{e} + \sum_{m=1}^{n} D_{zz}^{m} e^{-\alpha^{m}(t-t_o)}\right) \Delta K_{zz}^{o} \\ & + \left(D_{zx}^{e} + \sum_{m=1}^{n} D_{zx}^{m} e^{-\alpha^{m} t}\right) \Delta K_{xx}^{o} \end{aligned}$$

$$-\left(D_{zx}^{e}+\sum_{m=1}^{n}D_{zx}^{m}e^{-\alpha^{m}(t-t_o)}\right)\left(\Delta K_{xx}^{o}-\sum_{l=1}^{n}\Delta K_{xx}^{l}\right)$$

$$-\int_{t_o}^{t}\left(D_{zx}^{e}+\sum_{m=1}^{n}D_{zx}^{m}e^{-\alpha^{m}(t-\tau)}\right)\frac{d}{d\tau}\left(\Delta K_{xx}^{o}-\sum_{l=1}^{n}\Delta K_{xx}^{l}e^{-\lambda^{l}(\tau-t_o)}\right)d\tau \tag{5.3.14}$$

The approach used for the transverse moment equation (5.3.9) is also applied to the axial moment equation (5.3.14), for $t > t_o$ resulting in

$$M_{zz}(t)=\left(D_{zz}^{e}+\sum_{m=1}^{n}D_{zz}^{m}e^{-\alpha^{m}t}\right)\Delta K_{zz}^{o}-\left(D_{zz}^{e}+\sum_{m=1}^{n}D_{zz}^{m}e^{-\alpha^{m}(t-t_o)}\right)\Delta K_{zz}^{o}$$

$$+\left(D_{zx}^{e}+\sum_{m=1}^{n}D_{zx}^{m}e^{-\alpha^{m}t}\right)\Delta K_{xx}^{o}$$

$$-\left(D_{zx}^{e}+\sum_{m=1}^{n}D_{zx}^{m}e^{-\alpha^{m}(t-t_o)}\right)\left(\Delta K_{xx}^{o}-\sum_{l=1}^{n}\Delta K_{xx}^{l}\right)$$

$$-D_{zx}^{e}\sum_{l=1}^{n}\Delta K_{xx}^{l}\left(1-e^{-\lambda^{l}(t-t_o)}\right)$$

$$-\sum_{m=1}^{n}\sum_{l=1}^{n}\frac{D_{zx}^{m}\Delta K_{xx}^{l}\lambda^{l}}{\alpha^{m}-\lambda^{l}}\left(e^{-\lambda^{l}(t-t_o)}-e^{-\alpha^{m}(t-t_o)}\right) \tag{5.3.15}$$

Based on the method and equations derived above, the viscoelastic response of an anisotropic STEM, when stored with biaxial curvature, can be fully defined using equation (5.3.1) for axial curvature, $\Delta K_{zz}(t)$, equation (5.3.8) for the transverse curvature, $\Delta K_{xx}(t)$, equation (5.3.15) for the axial moment, $M_{zz}(t)$, and equation (5.3.13) for the transverse moment, $M_{xx}(t)$.

The biaxial anisotropic viscoelastic system of equations (biaxial bend model) can be validated by reducing the system of equations developed above to match that of the one-dimension isotropic condition, with the moment and curvature in the axial direction equal to zero. With the use of the Prony series, the history of the curvature change is given by

$$\Delta K(t)=H(t)\Delta K^{o}-H(t-t_o)\left(\Delta K^{o}-\sum_{l=1}^{n}\Delta K^{l}e^{-\lambda^{l}(t-t_o)}\right) \tag{5.3.16}$$

where the Prony coefficients ΔK^{l} are unknown and solved numerically by satisfying the bending moment equation for $t > t_o$.

$$M(t) = \left(D^e + \sum_{m=1}^{n} D^m e^{-\alpha^m t}\right)\Delta K^o$$

$$-\left(D^e + \sum_{m=1}^{n} D^m e^{-\alpha^m (t-t_o)}\right)\left(\Delta K^o - \sum_{l=1}^{n} \Delta K^l\right)$$

$$-D^e \sum_{l=1}^{n} \Delta K^l \left(1 - e^{-\lambda^l (t-t_o)}\right)$$

$$-\sum_{m=1}^{n}\sum_{l=1}^{n} \frac{D^m \Delta K^l \lambda^l}{\alpha^m - \lambda^l}\left(e^{-\lambda^l (t-t_o)} - e^{-\alpha^m (t-t_o)}\right) = 0 \qquad (5.3.17)$$

The Prony coefficients for the unknown recovery curvature, defined by equation (5.3.16) for a one-dimensional beam in bending, are numerically solved by equating the bending moment (equation (5.3.17)) to zero for $t \geq t_o$. The results are compared to the one-dimensional beam bending and curvature solutions derived based on the literature [16], [18], [20], [49], equation (5.2.6) and (5.2.7d), respectively, providing a level of confidence for the numerical method's use in the more complex multiaxial case of a composite STEM in biaxial bending.

5.4 Results

The numerical method derived to predict the viscoelastic response of a STEM in biaxial bending is evaluated for a one-dimensional case using the neat resin relaxation flexure properties $D(t)$ and creep flexure properties $d(t)$ recorded using Prony series coefficients in Table 5.4.1 and Table 5.4.2, respectively. For the following predictions, a one-dimensional beam is initially subjected to a change in curvature $\Delta K^o = 0.0098$ mm^{-1} and then released at $t_o = 100{,}000{,}000\ sec$ ($\sim 3.17\ years$). The bending moment due to the initially imposed change in curvature relaxes until the curvature is released, at which point the bending moment reduces completely to zero. Using the inputs listed above, the one-dimensional bending curvature and moment equations (5.3.16) and (5.3.17), respectively, derived from the reduced form of the biaxial bending model are evaluated. The Prony series representing

the recovery curvature portion of equation (5.3.16) ($t > t_o$) is evaluated using a numerical solver to find the Prony coefficients that satisfy the moment equation (5.3.17) set equal to zero for $t > t_o$. The Prony coefficients are listed in Table 5.4.3 and are unique for the given material properties and imposed bending history listed above. The result for the bending moment and curvature histories of the one-dimensional form of the biaxial bending model are compared to the respective one-dimensional moment and curvature equations (5.2.6) and (5.2.7d) derived based on literature results [16], [18], [20], [49] which are evaluated using the same input parameters listed above. Figure 5.4.1 presents the solutions for the bending moment (a) and the bending curvature (b) histories for a one-dimensional beam evaluated by both methods. The numerical results from the reduced biaxial bend model are represented by a solid orange line and the one-dimensional results are represented by a dashed blue line.

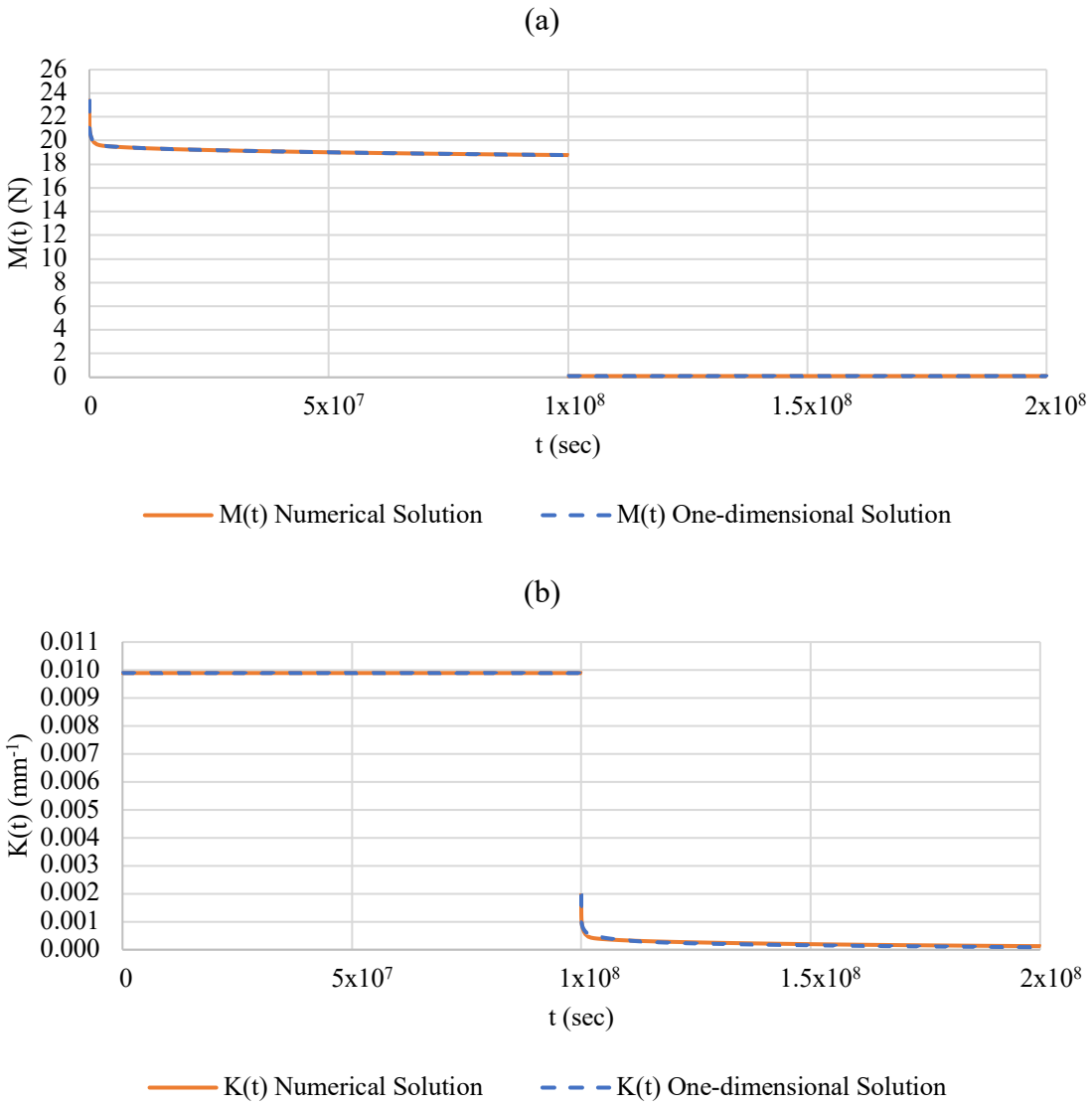

Figure 5.4.1: The histories of one-dimensional bending moment (a) and bending curvature (b) are shown for a one-dimensional beam in bending composed of a viscoelastic material. The relaxation and creep flexure properties represented by Prony series constants are given in Table 5.4.1 and Table 5.4.2, respectively. The dashed blue line is the solution from the one-dimensional beam bending equations developed in this chapter based on the solutions of the hereditary integrals found in the literature [16], [18], [20], [49]. *The orange solid line presents the numerical solution from the biaxial bend model developed in this chapter but reduced to one-dimensional bending.*

m	D^m (Nmm)	α^m (sec^{-1})
$\boldsymbol{e}$	1.60E+3	
1	2.47	1.60
2	5.74E-3	1.55E-1
3	1.15E+2	1.69E-2
4	1.01E-2	1.61E-3
5	8.47E+1	1.63E-4
6	5.87E+1	1.62E-5
7	1.20E+2	1.70E-6
8	2.12E+1	1.62E-7
9	6.67E+1	1.63E-8
10	9.20E+1	1.67E-9
11	7.27E+1	1.63E-10
12	6.45E+1	1.67E-11
13	6.11E+1	1.57E-12

Table 5.4.1 lists the Prony series coefficient representing the relaxation flexure properties $D(t)$ of the isotropic, one-dimensional, neat resin epoxy. The table lists the relaxation flexure properties starting with the equilibrium parameter D^e, followed by thirteen Prony series coefficients D^m and their respective time constants α^m where m = 1 through 13. The Prony coefficients have units of N-mm and the time constants have units of sec^{-1}.

m	d^m (Nmm^{-1})	β^m (sec^{-1})
$\boldsymbol{e}$	6.24E-4	
1	4.01E-7	1.61
2	4.89E-6	1.55E-1
3	9.12E-6	1.61E-2
4	1.15E-5	1.61E-3
5	1.38E-5	1.57E-4
6	1.62E-5	1.58E-5
7	1.69E-5	1.60E-6
8	1.65E-5	1.60E-7
9	1.86E-5	1.58E-8
10	2.23E-5	1.59E-9
11	2.47E-5	1.56E-10
12	2.41E-5	1.61E-11
13	2.16E-5	1.51E-12

Table 5.4.2 lists the Prony series coefficient representing the creep flexure properties $d(t)$ of the isotropic, one-dimensional, neat resin epoxy. The table lists the creep flexure properties starting with the equilibrium parameter d^e, followed by thirteen Prony series coefficients d^m and their respective time constants β^m where m = 1 through 13. The Prony coefficients have units of N-mm^{-1} and the time constants have units of sec^{-1}.

$\Delta K^o = 0.009884\ mm^{-1}$		$t_o = 1E8\ sec$
l	$\Delta K^l\ (mm^{-1})$	$\lambda^l\ (sec^{-1})$
1	6.53E-6	1.60
2	8.05E-7	1.55E-1
3	4.07E-4	1.69E-2
4	2.54E-8	1.61E-3
5	3.25E-4	1.63E-4
6	2.41E-4	1.62E-5
7	5.42E-4	1.70E-6
8	1.03E-4	1.62E-7
9	2.70E-4	1.63E-8
10	5.17E-5	1.67E-9
11	7.35E-6	1.63E-10
12	3.48E-8	1.67E-11
13	2.08E-5	1.57E-12

Table 5.4.3: The numerically predicted Prony series coefficients, ΔK^l and λ^l estimating the recovery response $\Delta K(t)$ defined in equation (5.3.16) are recorded for a neat resin, one-dimensional beam in bending. A series of thirteen coefficients are listed with l = 1 through 13. All curvature properties have units of mm^{-1} and the Prony series time coefficients have units of sec^{-1}.

The bending curvature and moment histories of composite STEMs with 3-ply and 4-ply laminate layups are evaluated using the biaxial bending model developed in this chapter for equivalent stowed and deployed conditions. The 3-ply and 4-ply laminate relaxation flexure properties predicted in Chapter 4 using the viscoelastic variant of classical laminate theory are recorded in Table 5.4.4 and Table 5.4.6, respectively, using the modeled coordinate STEM illustrated in Figure 5.3.1 which shows the z-axis in the axial direction along the deployed tube length and the y-axis in the transverse direction. At $t = 0$ a transverse curvature $\Delta K_{xx}^o = 0.009884$ mm^{-1} and an axial curvature $\Delta K_{zz}^o = 0.009843$ mm^{-1} are imposed to flatten (Figure 5.3.1 (b)) and then roll (Figure 5.3.1 (c)) the STEM into its stowed configuration. The imposed curvatures are held constant during which the resulting bending moments of the stowed STEM relax during $0 \leq t < t_o$. Equation (5.3.5a) and (5.3.5b) define the relaxation bending moments in the axial $M_{zz}(t)$ and transverse $M_{xx}(t)$ directions, respectively. At $t_o = 100{,}000{,}000 sec$ $(\sim 3.17\ years)$ the imposed biaxial curvatures are released, deploying the STEM. The axial curvature $\Delta K_{zz}(t)$ is forced to zero and the nonzero

transverse curvature $\Delta K_{xx}(t)$ of the deployed STEM results in a small axial moment $M_{zz}(t)$. As time progresses, $t > t_o$, both the axial moment (equation (5.3.15)) and transverse curvature (equation (5.3.8)) recover to zero as a result of the crosslinked polymer chains of the epoxy matrix slowly rearranging themselves back to their original chaotic, undeformed state. The unknown transverse curvature response in equation (5.3.8) is represented by a Prony series with coefficients for the 3-ply laminate and 4-ply laminate STEMs evaluated numerically by satisfying equation (5.3.13) which sets the transverse moment $M_{xx}(t)$ to zero for $t > t_o$. The Prony coefficients representing the 3-ply and 4-ply transverse curvature are recorded in Table 5.4.5 and Table 5.4.7, respectively. Figure 5.4.2 and Figure 5.4.4 representing the 3-ply and 4-ply laminates, respectively, contains four graphs illustrating the histories of the axial curvature (a), axial bending moments (b), transverse curvature (c), and transverse bending moments (d) predicted by the biaxial bend model of the STEM with material properties, and stowed and deformed configurations described above. Figure 5.4.3 and Figure 5.4.5 provide a magnified perspective of Figure 5.4.2 (b) and Figure 5.4.4 (b), respectively, showing in more detail the axial moment resulting from the deployed curvature of the STEM after prolonged storage.

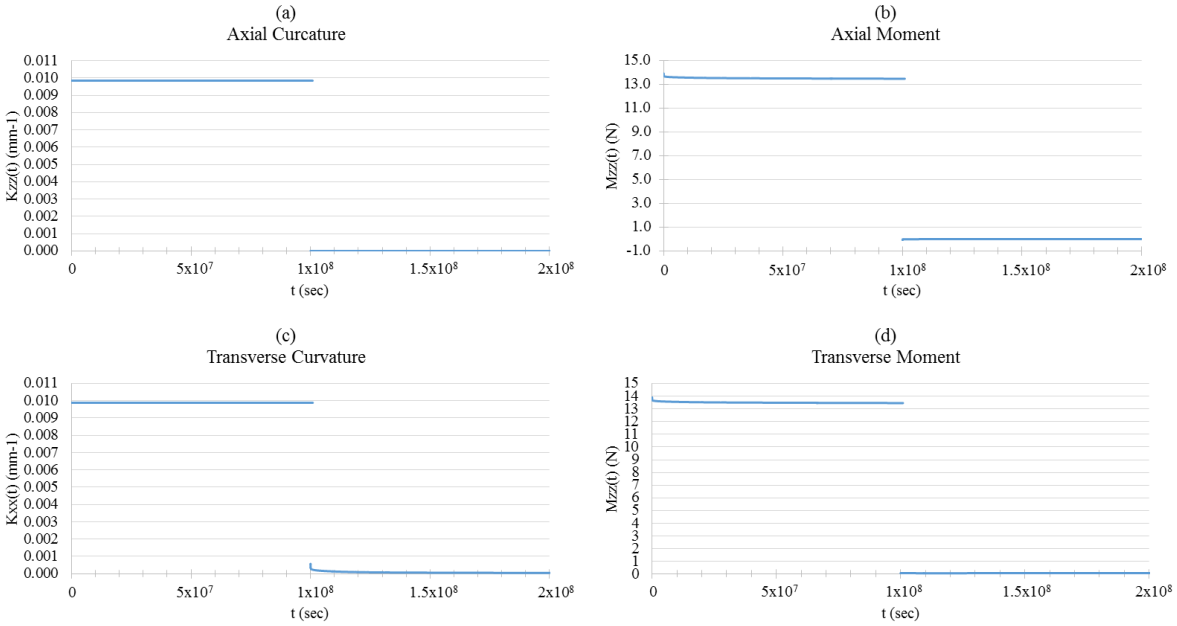

Figure 5.4.2: The bending curvature and moment histories obtained using the numerical method developed in Chapter 5 are graphed for a viscoelastic STEM in a state of biaxial bending. (a) illustrates the axial curvature, (b) the axial moment, (c) the transverse curvature, and (d) the transverse moment histories of a STEM composed of a 3-ply composite [45º PW/0º Uni/45º PW] with viscoelastic flexure properties recorded in Table 5.4.4. The STEM is subjected to biaxial bending during stowage $0 \leq t < t_o$*, then deployed at* $t_o = 100{,}000{,}000\ sec\ (\sim 3.17\ years)$*, and lastly allowed to recover to a zero-stress state over time* $t > t_o$*.*

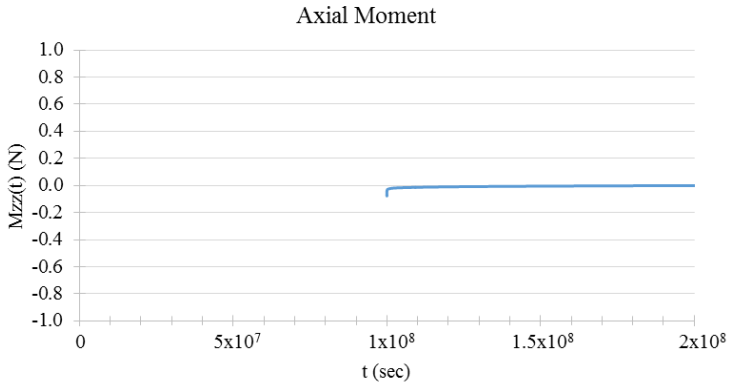

Figure 5.4.3: A magnified view of Figure 5.4.2 (b) depicts the axial moment in the 3-ply composite STEM due to a nonzero transverse curvature at the onset of deployment at $t = t_o$ *after prolonged stowage during* $0 \leq t < t_o$*. The viscoelastic properties of the 3-ply laminate used to form the STEM are modest, and as a result, the axial moment on deployment is small.*

m	D_{zz}^{m} (Nmm)	D_{zx}^{m} (Nmm)	D_{xx}^{m} (Nmm)	α^{m} (sec^{-1})
e	709.96	627.67	699.85	
1	0	9.07E-5	0	1
2	9.36E-7	0	0	1E-1
3	4.15	4.36E-3	4.06	1E-2
4	6.28	4.42E-3	6.32	1E-3
5	6.74	7.75E-3	6.70	1E-4
6	6.28	1.00E-7	6.36	1E-5
7	4.84	5.48E-2	4.80	1E-6
8	8.71	6.41E-1	9.02	1E-7
9	8.86	5.15E-1	8.99	1E-8
10	8.82	9.45E-2	8.34	1E-9
11	10.7	2.00E-1	10.7	1E-10
12	6.43	1.72E-1	6.64	1E-11
13	5.89E-6		0	1E-12

Table 5.4.4: The 3-ply composite [45º PW/0º Uni/45º PW] relaxation flexure properties recorded in Chapter 4. The Prony series coefficients are used to define the axial $D_{zz}(t)$, transverse/axial $D_{zx}(t)$, and transverse $D_{xx}(t)$ flexure properties in the curvature equations (5.3.1) and (5.3.8), and bending moment equations (5.3.13) and (5.3.15) developed in Chapter 5 for a STEM in a state of biaxial bending. The table lists the relaxation flexure Prony coefficients starting with the equilibrium parameters D_{ij}^{e} in which i, j = x or z followed by the Prony series coefficients D_{ij}^{m} where m = 1 through 13. The respective Prony series time constants α^{i} are also listed. The Prony coefficients have units of N-mm and the time constants have units of sec^{-1}.

$\Delta K_{zz}^{o} = 0.009843\ (mm^{-1})$		$t_o = 1E8$ sec
$\Delta K_{xx}^{o} = 0.009884\ (mm^{-1})$		
1	$\Delta K_{xx}^{l}\ (mm^{-1})$	$\lambda^{l}\ (sec^{-1})$
1	0	1
2	1.01E-8	1E-1
3	4.91E-5	1E-2
4	7.77E-5	1E-3
5	8.38E-5	1E-4
6	8.13E-5	1E-5
7	6.09E-5	1E-6
8	1.33E-4	1E-7
9	6.32E-5	1E-8
10	1.57E-5	1E-9
11	8.46E-6	1E-10
12	1.84E-9	1E-11
13	1.29E-6	1E-12

Table 5.4.5: The numerically predicted Prony series coefficients, ΔK_{xx}^{l} and λ^{l}, estimating the transverse recovery response $\Delta K_{xx}(t)$ defined in equation (5.3.8) are recorded for the 3-ply composite STEM in biaxial bending. The biaxial curvatures ΔK_{zz}^{o} and ΔK_{xx}^{o} are initially imposed at $t = 0$ on the 3-ply composite STEM and then released at $t_o = 100{,}000{,}000\ sec$. A series of thirteen Prony coefficients listed with l = 1 through 13 are used to define the transverse recovery curvature of the STEM. All curvature properties have units of mm^{-1}. Prony series time coefficients have units of sec^{-1}.

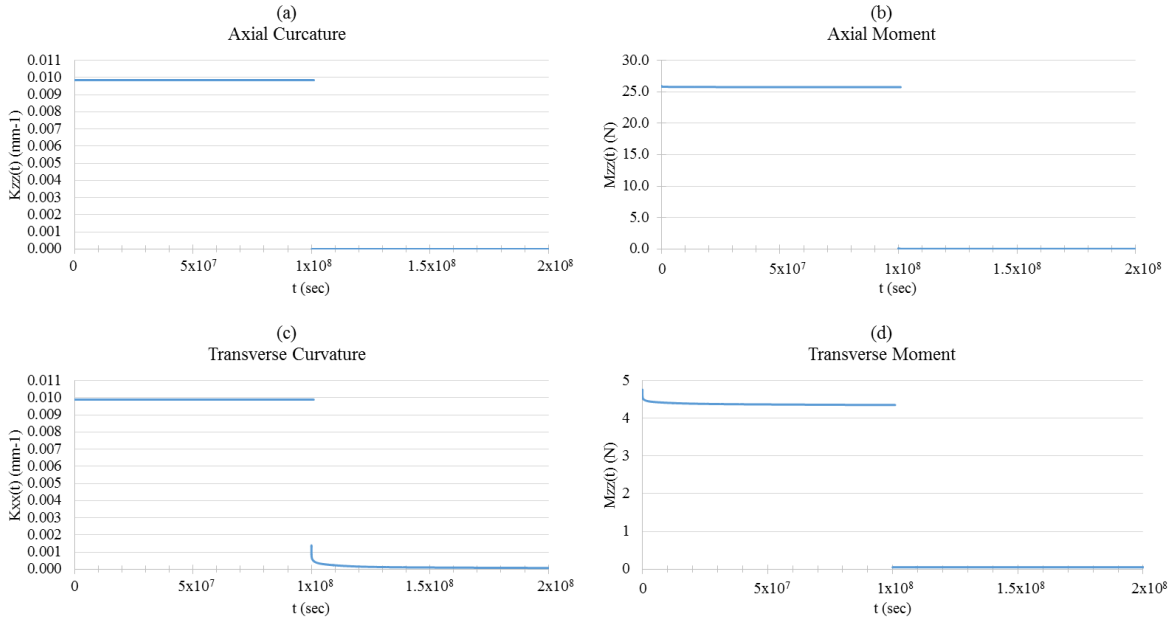

Figure 5.4.4: The bending curvature and moment histories obtained using the numerical method developed in Chapter 5 are graphed for a viscoelastic STEM in a state of biaxial bending. (b) the axial moment, (c) the transverse curvature, and (d) the transverse moment histories of a STEM composed of a 4-ply composite [0º Uni/45º PW/45º PW/0º Uni] with viscoelastic flexure properties recorded in Table (5.4.6). The STEM is subjected to biaxial bending during stowage $0 \leq t < t_o$*, then deployed at* $t_o = 100{,}000{,}000\ sec$ $(\sim 3.17\ years)$*, and lastly allowed to recover to a zero-stress state over time* $t > t_o$*.*

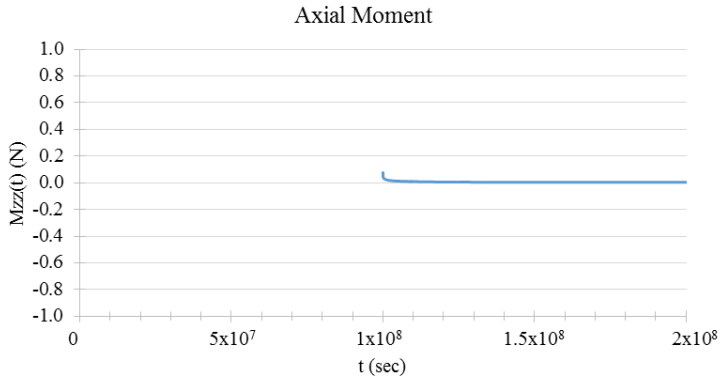

Figure 5.4.5: A magnified view of Figure 5.4.4 (b) depicts the axial moment in the 4-ply composite STEM due to a nonzero transverse curvature at the onset of deployment at $t = t_o$ *after prolonged stowage during* $0 \leq t < t_o$*. The viscoelastic properties of the 4-ply laminate used to form the STEM are modest, and as a result, the axial moment on deployment is small.*

m	$D^m_{zz}\ (Nmm)$	$D^m_{zx}\ (Nmm)$	$D^m_{xx}(Nmm)$	$\alpha^m\ (sec^{-1})$
e	2430.776	174.715	252.875	
1	0.000	0.170	0.692	1E-1
2	0.870	0.688	2.745	1E-2
3	1.446	1.027	4.276	1E-3
4	1.512	1.408	5.231	1E-4
5	1.389	1.505	5.285	1E-5
6	1.043	1.564	5.601	1E-6
7	1.999	1.442	5.853	1E-7
8	1.993	0.937	4.559	1E-8
9	1.969	0.335	2.946	1E-9
10	2.344	0.000	2.086	1E-10
11	1.420	0.030	1.134	1E-11
12	0.000	0.000	3.48E-06	1E-12

Table 5.4.6: The 4-ply composite [0º Uni/45º PW/45º PW/0º Uni] relaxation flexure properties recorded in Chapter 4. The Prony series coefficients are used to define the axial $D_{zz}(t)$, transverse/axial $D_{zx}(t)$, and transverse $D_{xx}(t)$ flexure properties in the curvature equations (5.3.1) and (5.3.8), and bending moment equations (5.3.13) and (5.3.15) developed in Chapter 5 for a STEM in a state of biaxial bending. The table lists the relaxation flexure Prony coefficients starting with the equilibrium parameters D^e_{ij} in which i, j = x or z followed by the Prony series coefficients D^m_{ij} where m = 1 through 13. The respective Prony series time constants α^i are also listed. The Prony coefficients have units of N-mm and the time constants have units of sec^{-1}.

$\Delta K^o_{zz} = 0.009843\ (mm^{-1})$		t_o = 1E8 sec
$\Delta K^o_{xx} = 0.009884\ (mm^{-1})$		
1	$\Delta K^l_{xx}\ (mm^{-1})$	$\lambda^l\ (sec^{-1})$
1	1.94E-10	1
2	2.58E-05	1E-1
3	1.04E-04	1E-2
4	1.64E-04	1E-3
5	2.14E-04	1E-4
6	2.26E-04	1E-5
7	2.50E-04	1E-6
8	2.69E-04	1E-7
9	9.99E-05	1E-8
10	2.20E-05	1E-9
11	1.19E-05	1E-10
12	5.29E-06	1E-11
13	1.42E-09	1E-12

Table 5.4.7: The numerically predicted Prony series coefficients, ΔK^l_{xx} and λ^l, estimating the transverse recovery response $\Delta K_{xx}(t)$ defined in equation (5.3.8) are recorded for the 4-ply composite STEM in biaxial bending. The biaxial curvatures ΔK^o_{zz} and ΔK^o_{xx} are initially imposed at $t = 0$ on the 4-ply composite STEM and then released at $t_o = 100{,}000{,}000\ sec$. A series of thirteen Prony coefficients listed with l = 1 through 13 are used to define the transverse recovery curvature of the STEM. All curvature properties have units of mm^{-1}. Prony series time coefficients have units of sec^{-1}.

5.5 Discussion

The analytical model developed in this chapter provides a tool for predicting the bending curvature and moment histories of a viscoelastic composite STEM deformed into a stowed and then a deployed configuration. The effects of material selection on the deployment performance of STEMs used for various applications (e.g., the deployment torque and deployed stiffness) can be easily evaluated using the method developed in this chapter for composites with differing ply orientation, stacking sequence, and laminae properties. In addition, the influence of a STEM's undeformed curvature shape (e.g., the radius of curvature of the undeformed STEM Figure 5.3.1 (a)), stowed duration and stowed configuration (Figure 5.3.1 (c)) on the deployment parameters can be assessed. Validation of the biaxial bend model in comparison with test data is not possible due to the non-availability of experimental results. As a consequence, the analytical model developed in this chapter and used to predict the biaxial bending of a STEM was simplified to model a one-dimensional beam in bending (equations (5.3.16) and (5.3.17)). A beam composed of neat resin epoxy, with properties collected from experimental data, was predicted using the simplified model. The bending moment and curvature results from the model are compared to the one-dimensional beam bending problems found in the literature [16], [18], [20], [49] that have been modified for use with laminate flexure notation (equation (5.2.6) and (5.2.7e)) and evaluated using the viscoelastic neat resin properties. The relaxation moment ($0 < t < t_o$) predicted by the models for a beam in bending due to a constant imposed curvature are illustrated in Figure 5.4.1 of the results section with the reduced biaxial model represented by a solid orange line and the one-dimensional results represented by a dashed blue line. The recovery curvature and moment response ($t > t_o$) predicted by the two methods are also

illustrated in Figure 5.4.1. It can be seen that there is very good agreement between the two sets of results for the one-dimensional beam bending problem, providing confidence in the reliability of the analytical solution developed in this chapter for a biaxial bent STEM composed of a viscoelastic composite.

To demonstrate the applicability of the biaxial bend model, the bending curvature and moment histories of two STEMs, one composed of a viscoelastic 3-ply laminate [45° PW/0° Uni/45° PW] and another composed of a viscoelastic 4-ply laminate [0° Uni /45° PW/45° PW/0° Uni], are predicted using the model. Both STEMs are stowed in a state of biaxial bending from $0 < t < t_o$ and then released at $t = t_o$ to deploy and then slowly recover as time progresses $t > t_o$. The numerically solved (a) axial curvature, (b) axial moment, (c) transverse curvature, and (d) transverse moment are presented in Figure 5.4.2 for the 3-ply composite STEM and in Figure 5.4.4 for the 4-ply composite STEM. Due to the viscoelastic properties of the laminates composing the STEMs, the model, as expected, predicts the relaxation of the axial and transverse moments due to the imposed biaxial bending curvatures required to stow the STEMs. At $t = t_o$ the imposed biaxial bending curvatures are released deploying the STEMs. The viscoelastic change in the composite STEMs as a result of prolonged stowage affects the STEMs' initial ($t = t_o$) deployed configuration. The transverse moments of the STEMs are equal to zero while the resulting transverse curvatures are nonzero. Due to the geometrical shape of the deployed STEM (nonzero transverse curvature), the axial curvature is forced to zero. The resulting axial moment predicted by the model is illustrated in Figure 5.4.2 (b) for the 3-ply composite STEM and in Figure 5.4.4 (b) for the 4-ply laminate. The results appear to be zero, contrary to the expected response. However, when this response is viewed in magnification as shown in Figure 5.4.3 for the 3-

ply composite STEM, a small, yet noticeably negative moment is observed which recovers to zero over time. The relaxation of the 3-ply composite STEM's modulus due to the stowed deformation reduces very little over the stowed duration (e.g., the stress relaxation is small during stowage). As a result, the moment required to force the axial curvature back to zero is small. A similar response is observed in Figure 5.4.5 illustrating the magnified axial moment response of the 4-ply laminate which shows a small positive moment recovery at the start of deployment $t = t_o$. The 4-ply axial flexure is essentially elastic as opposed to the slight viscoelastic response of the 3-ply laminate, which in turn produces a positive axial moment due to the curvature state of the deployed STEM. Materials that relax more due to the imposed stowed deformations will result in a greater deployed axial moment. The residual transverse curvature, however, is much more noticeable due to the viscoelastic properties of the 3-ply and 4-ply laminates. The reduced modulus due to relaxation of the material during stowage and the change in the deployed curvature can negatively affect the deployed stiffness of the STEM. As time progresses, both the axial moment and transverse curvature are predicted to recover to zero.

5.6 Conclusion

Hereditary integrals were adapted for classical laminate theory to provide an analytical tool that predicts the bending curvature and moment histories (e.g., deployment torque and deployed stiffness) of viscoelastic composite STEMs in a state of biaxial bending when stored and then deployed. The model and its results, reduced to represent a one-dimensional beam in bending, were compared to a one-dimensional bending solution developed in this chapter based on a problem found in the literature. The results match favorably to one

another, providing confidence in the bending moment and curvature histories predicted by the biaxial bend model for viscoelastic composite STEMs. Two STEMs, one composed of a 3-ply laminate [45^{o} PW/0^{o} Uni/45^{o} PW] and another composed of a 4-ply laminate [0^{o} Uni /45^{o} PW/45^{o} PW/0^{o} Uni] with measured viscoelastic properties predicted in Chapter 4, were evaluated using the biaxial bend model. The model predicted the expected bending curvature and moment histories of the STEMs stowed for a long duration before being deployed. The biaxial bend model provides a tool that can be used to aid in the design development of robust and reliable composite STEMs for the use in various deployment applications.

Chapter 6

Concluding Remarks

This dissertation had two objectives. The first was to observe the presence of viscoelasticity in composites and how various laminate layups, orientations, and stacking sequences influence their viscoelastic properties. The second was to develop a model to predict the viscoelastic behavior of STEMs used in structural applications, such as DSS' MEGA ROSA solar array, utilizing the insights learned about composite viscoelasticity from experimental data. These objectives were achieved.

The creep tests performed in Chapter 2 on a set of samples with varying compositions, e.g., ply orientation, ply type (unidirectional and/or plain weave laminae), and stacking sequence, with all having the same resin system allowed for a direct comparison of the measured creep properties of the various samples providing insight into how the introduction of elastic fibers and their placement affect the viscoelasticity of the neat resin matrix. The results of the tests performed in Chapter 2 show that the viscoelastic properties of the neat resin are mitigated by the placement of the elastic carbon fibers in the direction of loads. The presence of fibers reduces the degree laminae or laminates creep over their lifetime (glassy to equilibrium). However, the transient proportional response of the measured samples indicates

the viscoelastic behavior of the neat resin matrix of all the laminae and laminates tested is unchanged. The four-point-bending test validated the viscoelastic responses observed in the tensile creep tests and exemplified the influence that the ply stacking sequence has on thin shell composites viscoelastic properties. The creep properties recorded in Chapter 2 provide a good set of data for understanding the viscoelastic behavior of laminae and laminates, however further testing is required to measure the tensile shear properties and axial/transverse flexure properties of laminae and laminates. Creep tests measuring the influence of fiber volume fraction, which is well known in the literature to affect the elastic properties of composites, should also be explored. Lastly, the unique behavior observed by the plain weave laminate should be studied further. Tensile creep test measuring the plain weave laminates $0^o/90^o$ properties versus a laminate composed of unidirectional fiber $[0^o/90^o]_s$ would help characterize the influence of the assumed fiber tow elongation as a result of the weave pattern of the plain weave laminate straightening under load.

An analytical model, described in Chapter 5, was developed using hereditary integrals that are numerically solved to predict the viscoelastic behavior of composite storable tubular members with varying laminate composition. The 3-ply and 4-ply laminate creep and relaxation flexure properties measured and predicted in Chapters 2 and 4, respectively, are used to predict the relaxation moments and recovery curvatures of a STEM flattened and reversed rolled into a stowed position and then deployed. Due to the lack of available test data for the composite STEMs of interest and the expense of gathering experimental data, the multidimensional STEM model is validated by comparing the reduced one-dimensional version of the model to similar models published in the literature using the viscoelastic laminate properties recorded in Chapter 2 and 4 as inputs. The analytical model developed in

Chapter 5 provides a unique tool for adding in the design development of STEMs. A more complex FEA model is in development that predicts the non-uniform curvature transition zone of STEMs as they deploy from their stowed configuration.

In order to utilize the test data in the analytical STEM model, the measured tensile and flexure creep properties of the neat resin, unidirectional and plain weave laminae, and 3-ply and 4-ply laminates needed to be inverted to provide their corresponding relaxation response. Many viscoelastic inversion methods found in the literature suitable for inverting one-dimensional materials cannot be used for multidimensional materials, as discussed in Chapter 3. However, a numerical Laplace method was developed for inverting anisotropic multidimensional materials. This inversion method was applied to the lamina and laminate tensile creep data recorded in Chapter 2 to generate Prony series coefficients that modeled the relaxation master curves of the laminae and laminates tested. The numerical Laplace method is more robust than the other methods discussed in Chapter 3, producing inverted properties that are consistent with fundamental energy principles while more accurately estimating the Prony time constants of the inverted material. The creep flexure properties could not be inverted to acquire the relaxation flexure properties due to the lack of measured axial/transverse flexure data. Instead, relaxation flexure properties were successfully attained using a viscoelastic version of classical laminate theory, which used the inverted creep compliance properties (relaxation properties) from the unidirectional and the plain weave laminae as inputs. Relaxation tensile and flexure test on the laminae and laminates inverted would validate the relaxation properties predicted by both the numerical Laplace inversion method and the viscoelastic version of classical laminate theory.

References

[1] F. P. J. Rimrott, “Storable Tubular Extendible Member: A Unique Machine Element,” *Mach. Des.*, vol. 37, no. 28, pp. 156–165, 1965.

[2] J. D. F. George G. Herzl, William W. Walker, “Tubular Spacecraft Booms (Extendible, Reel Stored) [Monograph],” *NASA Sp. Veh. Des. Criteria (Guidance Control.*, vol. NASA SP-80, 1971.

[3] T. W. Murphey, S. Jeon, A. Biskner, and G. Sanford, “Deployable Booms and Antennas Using Bi-stable Tape-springs,” in *24th Annual AIAA/USU Conference on Small Satellites*, 2010.

[4] D. Campbell *et al.*, “Development of a Novel, Passively Deployed Roll-Out Solar Array,” in *IEEE Aerospace Conference*, 2006.

[5] J. N. Footdale and T. W. Murphey, “Mechanism Design and Testing of a Self-Deploying Structure Using Flexible Composite Tape Springs,” in *Proceedings of the 42nd Aerospace Mechanisms Symposium*, 2015.

[6] S. K. Jeon and T. W. Murphey, “Design and Analysis of A Meter-Class CubeSat Boom With A Motor-Less Deployment by Bi-Stable Tape Springs,” in *Collection of Technical Papers - AIAA/ASME/ASCE/AHS/ASC Structures, Structural Dynamics and Materials Conference*, 2011.

[7] “Roll-Out Solar Array Accomplishes Significant Spaceflight Milestone.” [Online]. Available: https://technology.grc.nasa.gov/featurestory/rosa-milestone. [Accessed: 08-Jun-2018].

[8] J. C. H. Yee and S. Pellegrino, “Folding of woven composite structures,” *Compos. Part A Appl. Sci. Manuf.*, vol. 36, no. 2, pp. 273–278, 2005.

[9] A. Brinkmeyer, S. Pellegrino, P. M. Weaver, and M. Santer, “Effects of Viscoelasticity on the Deployment of Bistable Tape Springs,” in *The 19th International Conference on Composite Materials*, 2013, pp. 1–11.

[10] A. Brinkmeyer, P. M. Weaver, and S. Pellegrino, “Effects of Long-Term Stowage on the Deployment of Bistable Tape Springs,” *ASME J. Appl. Mech.*, vol. 83, no. 1, 2015.

[11] H. D. Stenzenberger, “Thermosetting Matrix Systems and Their Influence for Carbon Fibre Reinforcement,” in *Carbon Fibres and Their Composites*, E. Fitzer, Ed. Berlin, Heidelberg: Springer Berlin Heidelberg, 1985, pp. 95–116.

[12] Y. T. Yeow, D. H. Morris, and H. F. Brinson, “Time-Temperature Behavior of Unidirectional Graphite/Epoxy Composite,” in *Composite Materials: Testing and Design (Fifth Conference)*, 1978, pp. 263–281.

[13] R. M. Jones, *Mechanics of Composite Materials*, Second. Philadelphia: Taylor and Francis, 1999.

[14] I. M. Daniel and O. Ishai, *Engineering Mechanics of Composite Materials*, Second. Oxford University Press, 2006.

[15] Michael Bak, “New FEA Tools Tackle Composite Challenges,” *Machine Design*, 2017. [Online]. Available: https://www.machinedesign.com/materials/new-fea-tools-tackle-composite-challenges. [Accessed: 05-Aug-2018].

[16] H. F. Brinson and L. C. Brinson, *Polymer Engineering Science and Viscoelasticity An Introduction*. Springer, 2008.

[17] I. M. Ward and J. Sweeney, *Mechanical Properties of Solid Polymers*, Third. Wiley, 2012.

[18] D. Gutierrez-Lemini, *Engineering Viscoelasticity*. Springer, 2014.

[19] D. G. Fesko and N. W. Tschoegl, “Time-Temperature Superposition In Thermorheologically Complex Materials,” *J. Polym. Sci. Part C Polym. Symp.*, vol. 35, no. 1, pp. 51–69, Mar. 2007.

[20] K. Kwok, “Mechanics of Viscoelastic Thin-Walled Structures,” California Institute of Technology, 2013.

[21] H. F. Brinson, D. H. Morris, W. I. Griffith, and D. Dillard, “The Viscoelastic Response of a Graphite/Epoxy Laminate,” in *Composite Structures*, I. H. Marshall, Ed. Springer Netherlands, 1981, pp. 285–300.

[22] M. Mobrem and D. S. Adams, “Deployment Analysis of the Lenticular Jointed Antennas Onboard the Mars Express Spacecraft,” *J. Spacecr. Rockets*, vol. 46, no. 2, pp. 394–402, Mar. 2009.

[23] H. F. Brinson and M. E. Tuttle, “Prediction of the Long-Term Creep Compliance of General Composite Laminates,” *Exp. Mech.*, vol. 26, no. 1, pp. 89–102, 1986.

[24] S. Ogihara and S. Moriwaki, “Tensile Creep Deformation in Unidirectional Carbon/Epoxy Laminates Under Off-axis Loading,” *J. Mater. Sci.*, vol. 39, no. 10, pp. 3465–3467, 2004.

[25] T. S. Gates, D. R. Veazie, and L. C. Brinson, “Creep and Physical Aging in a Polymeric Composite: Comparison of Tension and Compression,” *J. Compos. Mater.*, vol. 31, no. 24, pp. 2478–2505, 1997.

[26] E. J. Barbero, “Prediction of Long-term Creep of Composites from Doubly-shifted Polymer Creep Data,” *J. Compos. Mater.*, vol. 43, no. 19, pp. 2109–2124, 2009.

[27] S. Govindarajan, N. A. Langrana, and G. J. Weng, “An Experimental and Theoretical Study of Creep of a Graphite/Epoxy Woven Composite,” *Polym. Compos.*, vol. 17, no.

3, pp. 353–361, 1996.

[28] S. Deng, X. Li, and Y. J. Weitsman, “Time-Dependent Deformation of Stitched T300 Mat/Urethane 420 IMR Cross-Ply Composite Laminates,” *Mech. Time-Dependent Mater.*, vol. 7, no. 1, pp. 41–69, 2003.

[29] R. M. Guedes, A. T. Marques, and A. Cardon, “Creep/Creep-Recovery Response of Fibredux 920C-TS-5-42 Composite under Flexural Loading,” *Appl. Compos. Mater.*, vol. 6, no. 2, pp. 71–86, 1999.

[30] K. Kwok and S. Pellegrino, “Micromechanical Modeling of Deployment and Shape Recovery of Thin-walled Viscoelastic Composite Space Structures,” in *53rd AIAA/ASME/ASCE/AHS/ASC Structures, Structural Dynamics and Materials Conference*, 2012.

[31] W. Flügge, “Hereditary Integrals,” in *Viscoelasticity*, W. Flügge, Ed. Berlin, Heidelberg: Springer Berlin Heidelberg, 1975, pp. 34–45.

[32] T. M. Inc., “MATLAB R2014b.” Natick, Massachusetts, 2014.

[33] S. P. Zaoutsos, G. C. Papanicolaou, and A. H. Cardon, “On the Non-linear Viscoelastic Behaviour of Polymer-Matrix Composites,” *Compos. Sci. Technol.*, vol. 58, no. 6, pp. 883–889, 1998.

[34] D. S. Ivanov, S. V. Lomov, S. G. Ivanov, and I. Verpoest, “Stress Distribution in Outer and Inner Plies of Textile Laminates and Novel Boundary Conditions for Unit Cell Analysis,” *Compos. Part A Appl. Sci. Manuf.*, vol. 41, no. 4, pp. 571–580, 2010.

[35] A. Gupta and J. Raghavan, “Creep of Plain Weave Polymer Matrix Composites Under On-Axis and Off-Axis Loading,” *Compos. Part A Appl. Sci. Manuf.*, vol. 41, no. 9, pp. 1289–1300, Sep. 2010.

[36] R. A. Schapery, “Approximate Methods of Transform Inversion for Viscoelastic Stress Analysis,” in *Proceedings of the Fourth U.S. National Congress of Applied Mechanics*, 1962, vol. 2, pp. 1075–1085.

[37] R. A. Shapery, “Two Simple Approximate Methods of Laplace Transform Inversion for Viscoelastic Stress Analysis,” 1961.

[38] D. Gutierrez-Lemini, “Material Property Functions and Their Characterization,” in *Engineering Viscoelastcitiy*, Springer US, 2014, pp. 165–191.

[39] Z. Hashin, “Viscoelastic Fiber Reinforced Materials,” *AIAA*, vol. 4, no. 8, pp. 1411–1417, 1966.

[40] Z. V. I. Hashin, “Viscoelastic Behavior of Heterogeneous Media,” *J. Appl. Mech.*, vol. 32, no. 3, pp. 630–636, 1965.

[41] S. B. Sane and W. G. Knauss, “On Interconversion of Various Material Functions of PMMA,” *Mech. Time-Dependent Mater.*, vol. 5, pp. 325–343, 2001.

[42] H. H. Hilton, “Implications and Constraints of Time-Independent Poisson Ratios in Linear Isotropic and Anisotropic Viscoelasticity,” *J. Elast.*, vol. 63, pp. 221–251, 2001.

[43] H. H. Hilton and S. B. Dong, “An Analogy For Anisotropic, Nonhomogeneous, Linear Viscoelasticity Including Thermal Stresses,” *Dev. Mech.*, vol. 2, no. 2, pp. 58–73, 1963.

[44] R. A. Schapery, “Viscoelastic Behavior and Analysis of Composite Materials,” *Compos. Mater.*, vol. 2, pp. 85–168, 1974.

[45] R. A. Schapery, “Stress Analysis of Viscoelastic Composite Materials,” *J. Compos. Mater.*, vol. 1, pp. 228–267, 1967.

[46] R. A. Schapery and S. W. Park, “Methods of interconversion between linear viscoelastic material functions. Part I—A Numerical Method Based On Prony Series,” *Int. J. Solids Struct.*, vol. 36, pp. 1653–1675, 1999.

[47] M. E. Tuttle and H. F. Brinson, “Prediction of the Long-Term Creep Compliance of General Composite Laminates,” *Exp. Mech.*, vol. 26, pp. 89–102, 1986.

[48] K. Kwok and S. Pellegrino, “Viscoelastic Effects in Tape-Springs,” *52nd AIAA/ASME/ASCE/AHS/ASC Struct. Struct. Dyn. Mater. Conf.*, no. April, pp. 1–17, 2011.

[49] K. Kwok and S. Pellegrino, “Shape Recovery of Viscoelastic Deployable Structures,” in *50th AIAA/ASME/ASCE/AHS/ASC Structures, Structural Dynamics, and Materials Conference*, 2010, no. April.

[50] K. Kwok and S. Pellegrino, “Folding, Stowage, and Deployment of Viscoelastic Tape Springs,” *AIAA J.*, vol. 51, no. 8, pp. 1908–1918, 2013.

[51] H. F. Brinson and L. C. Brinson, “Elementary Viscoelastic Stress Analysis for Bars and Beams,” in *Polymer Engineering Science and Viscoelasticity*, Bostin, MA: Springer US, 2008, pp. 275–298.

[52] I. Viktorova, S. Alekseeva, L. K. Holden, M. A. Bates, and H. Maeser, “The Hereditary Approach to Time Dependent Modeling with Fractional Exponential Function,” *North Carolina J. Math. Stat.*, vol. 1, no. 0, pp. 58–62, 2015.

[53] M. E. Peterson and T. W. Murphey, “Large Deformation Bending of Thin Composite Tape Spring Laminates,” in *54th AIAA/ASME/ASCE/AHS/ASC Structures, Structural Dynamics, and Materials Conference*, 2013.

Appendix

The lamina and laminate relaxation and creep equations (1.3.8a) through (1.3.9d) are normalized by their respective material glassy properties

$$\frac{A_{ij}(t)}{A_{ij}^{g}} = 1 - \sum_{l=1}^{k} \frac{A_{ij}^{l}}{A_{ij}^{g}} \left(1 - e^{-\alpha_A^l t}\right) \tag{A.1a}$$

$$\frac{B_{ij}(t)}{B_{ij}^{g}} = 1 - \sum_{l=1}^{k} \frac{B_{ij}^{l}}{B_{ij}^{g}} \left(1 - e^{-\alpha_B^l t}\right) \tag{A.1b}$$

$$\frac{D_{ij}(t)}{D_{ij}^{g}} = 1 - \sum_{l=1}^{k} \frac{D_{ij}^{l}}{D_{ij}^{g}} \left(1 - e^{-\alpha_D^l t}\right) \tag{A.1c}$$

$$\frac{a_{ij}(t)}{a_{ij}^{g}} = 1 + \sum_{l=1}^{k} \frac{a_{ij}^{l}}{a_{ij}^{g}} \left(1 - e^{-\beta_a^l t}\right) \tag{A.2a}$$

$$\frac{b_{ij}(t)}{b_{ij}^{g}} = 1 + \sum_{l=1}^{k} \frac{b_{ij}^{l}}{b_{ij}^{g}} \left(1 - e^{-\beta_b^l t}\right) \tag{A.2b}$$

$$\frac{c_{ij}(t)}{c_{ij}^{g}} = 1 + \sum_{l=1}^{k} \frac{c_{ij}^{l}}{c_{ij}^{g}} \left(1 - e^{-\beta_c^l t}\right) \tag{A.2c}$$

$$\frac{d_{ij}(t)}{d_{ij}^{g}} = 1 + \sum_{l=1}^{k} \frac{d_{ij}^{l}}{d_{ij}^{g}} \left(1 - e^{-\beta_d^l t}\right) \tag{A.2d}$$

α_A^l, α_B^l, α_D^l, and β_a^l, β_b^l, β_c^l, β_d^l are the Prony time constants for the laminate relaxation modulus and creep compliance; A_{ij}^g, B_{ij}^g, D_{ij}^g, and a_{ij}^g, b_{ij}^g, c_{ij}^g, d_{ij}^g are the laminate relaxation modulus and creep compliance glassy response; A_{ij}^l, B_{ij}^l, C_{ij}^l, and a_{ij}^l, b_{ij}^l, c_{ij}^l, d_{ij}^l are the Prony constants for the laminate relaxation modulus and creep compliance.

The appendix contains a series of tables and graphs recording the neat resin, unidirectional, plain weave, 3-ply, and 4-ply laminate compliance and flexure properties measured by the tensile and four-point bend creep test described in Chapter 2. A Prony series which is fit to the measured creep data is presented in each of the figures. The tables record the Prony series constant for the respective measured samples. The time-temperature

superposition shift coefficients, e.g., activation energy and initial temperature, used to form the master curve for each sample are also recorded in the tables.

$T_o = 30^0C$	Neat Resin S_{xx}		Neat Resin S_{xy}	
$Ea\ (J/mol)$	1.76E+5		1.76E+5	
$S_{lm}^{g}\ (MPa^{-1})$	3.34E-4		-1.31E-4	
Prony Value	$S_{xx}^{i}\ (MPa)^{-1}$	$\beta_{xx}^{i}(s)^{-1}$	$S_{xy}^{i}(MPa)^{-1}$	$\beta_{xy}^{i}(s)^{-1}$
i = 1	1.18E-6	1.59	-5.93E-6	1.59E-1
2	2.11E-5	1.59E-2	-9.13E-6	1.59E-2
3	5.07E-6	1.59E-3	-3.22E-6	1.59E-3
4	1.03E-5	1.59E-4	-2.34E-6	1.59E-4
5	6.27E-6	1.59E-5	-2.77E-6	1.59E-5
6	2.76E-5	1.59E-6	-1.23E-5	1.59E-6
7	6.88E-6	1.59E-7	-2.83E-6	1.59E-7
8	1.03E-5	1.59E-8	-4.34E-6	1.59E-8
9	3.13E-5	1.59E-9	-1.92E-5	1.59E-9
10	1.12E-5	1.59E-10	-3.67E-6	1.59E-10
11	2.64E-5	1.59E-11	-3.85E-6	1.59E-11
12	2.77E-5	1.59E-12	-3.16E-5	1.59E-12
13	1.02E-4	1.59E-13	-1.48E-5	1.59E-13

Table A.11: Neat resin master curve Prony series constants and Arrhenius law activation energy from measured data.

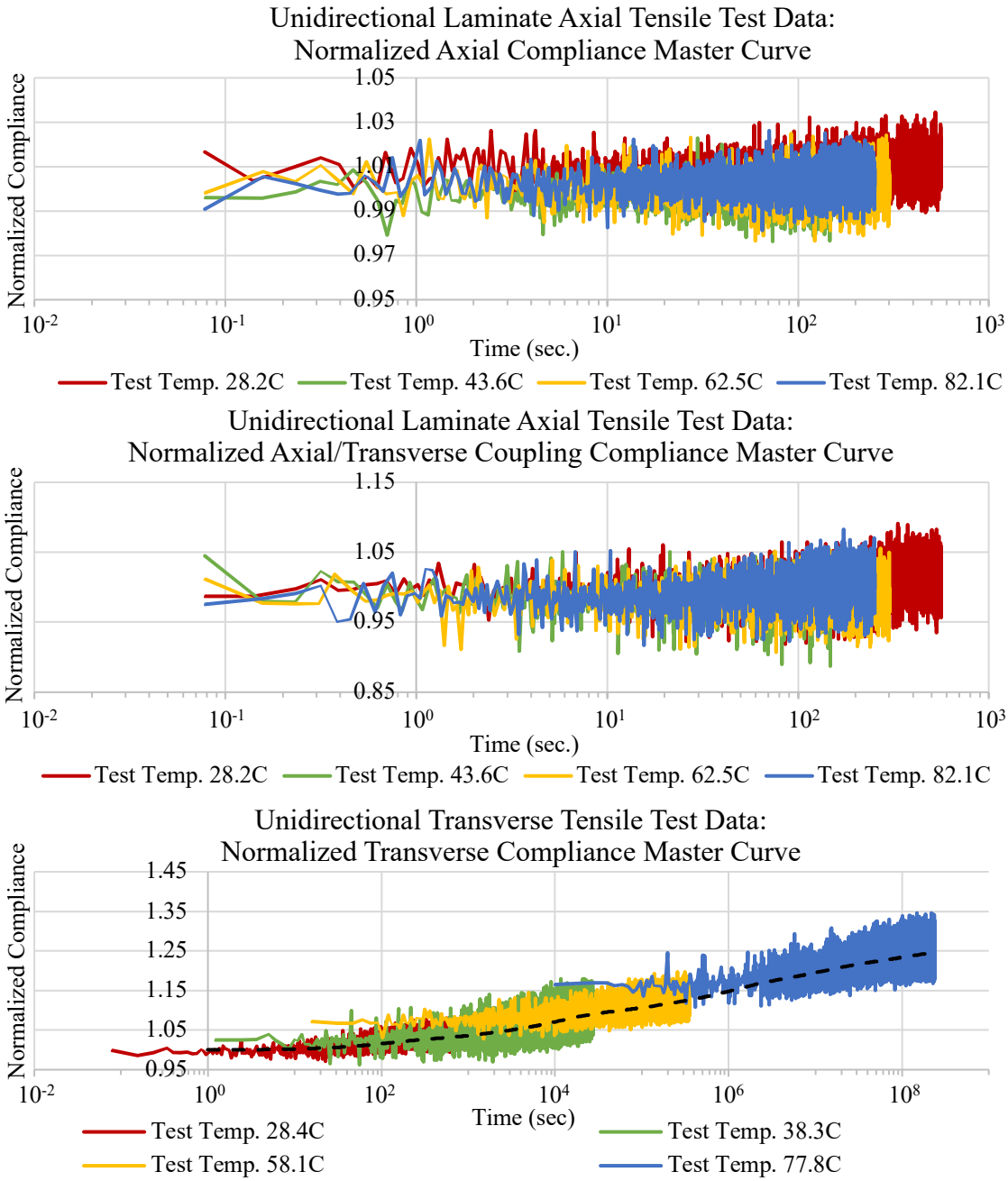

Figure A.9: The master curves for the unidirectional laminate axial compliance (top graph), axial/transverse coupling compliance (middle graph), and transverse compliance (bottom graph) obtained from tesnile test data. Tests are conducted at four different constant temperature tests for each material property. The axial and axial/transverse coupling compliance are elastic with a mean value that is constant in time. The transverse compliance is viscoelastic. A master curve is formed by shifting the data gathered at the four different temperatures on the time axis to create a creep compliance master curve. The creep compliance properties are normalized by the respective instantaneous (i.e., glassy) compliance of the initial creep test. A Prony series is fitted to the transverse creep compliance data representing the master curve.

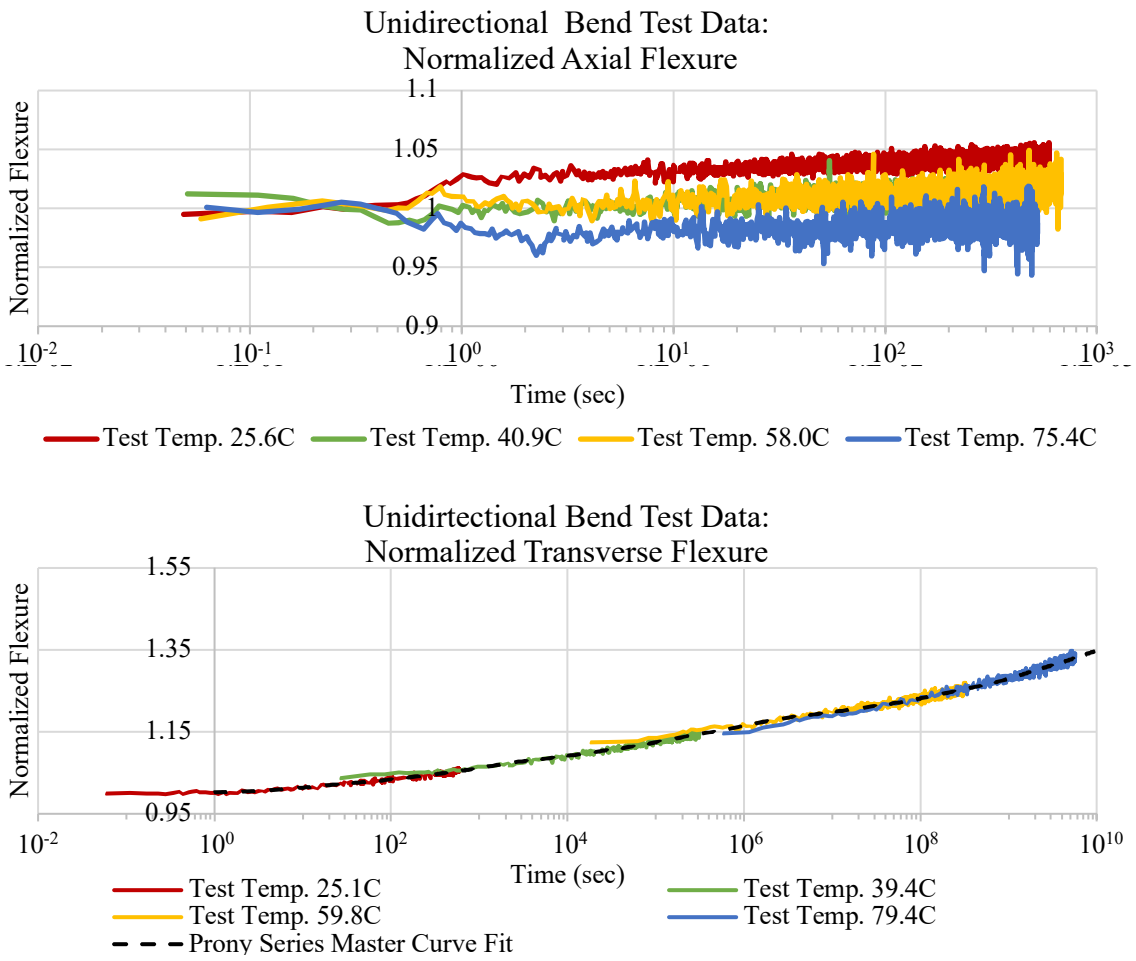

Figure A.10: The master curves for the unidirectional laminate axial flexure (top graph) and transverse flexure (bottom graph) obtained from four-point-bend test data. Four different constant temperature tests are conducted for each material property. The laminate behaves elastically in axial flexure. The transverse flexure response is viscoelastic. A master curve is formed by shifting the four temperature data sets along the time axis to create a creep flexure master curve. The creep flexure properties are normalized by the respective instantaneous (i.e., glassy) flexure of the initial creep test. A Prony series is fitted to the transverse creep flexure data representing the master curve.

$T_o = 30C$	Tensile Test Uni S_{xx}		Tensile Test Uni S_{xy}		Tensile Test Uni S_{yy}		Bend Test Uni d_{xx}		Bend Test Uni d_{yy}	
$E_a\ (J/mol)$	0		0		8.57E+04		0		1.13E+05	
$S^g_{lm}\ (MPa^{-1})$ or $d^g_{lm}\ (Nmm^{-1})$	7.95E-06		-2.86E-06		1.49E-04		4.39E-03		7.15E-02	
Prony Values	$S^i_{xx}\ (MPa^{-1})$	$\beta^i_{S_{xx}}\ (s^{-1})$	$S^i_{xy}\ (MPa^{-1})$	$\beta^i_{S_{xy}}\ (s^{-1})$	$S^i_{yy}\ (MPa^{-1})$	$\beta^i_{S_{yy}}\ (s^{-1})$	$d^i_{xx}\ (Nmm^{-1})$	$\beta^i_{d_{xx}}\ (s^{-1})$	$d^i_{yy}\ (Nmm^{-1})$	$\beta^i_{d_{yy}}\ (s^{-1})$
$i = 1$					1.00E-09	1.22E-01			1.29E-03	1.23E+00
2					3.28E-06	1.22E-02			1.37E-03	1.23E-01
3					2.10E-06	1.22E-03			2.45E-03	1.23E-02
4					7.55E-06	1.22E-04			1.78E-03	1.23E-03
5					3.30E-06	1.22E-05			2.59E-03	1.23E-04
6					8.06E-06	1.22E-06			3.26E-03	1.23E-05
7					6.55E-06	1.22E-07			1.77E-03	1.23E-06
8					6.25E-06	1.22E-08			2.54E-03	1.23E-07
9									3.64E-03	1.23E-08
10									6.69E-03	1.23E-09

Table A.12: The Prony time constants representing the creep compliance and flexure master curves of the unidirectional laminate. The table also records the Arrhenius law activation energies used to form the master curves from test data at varying constant temperatures.

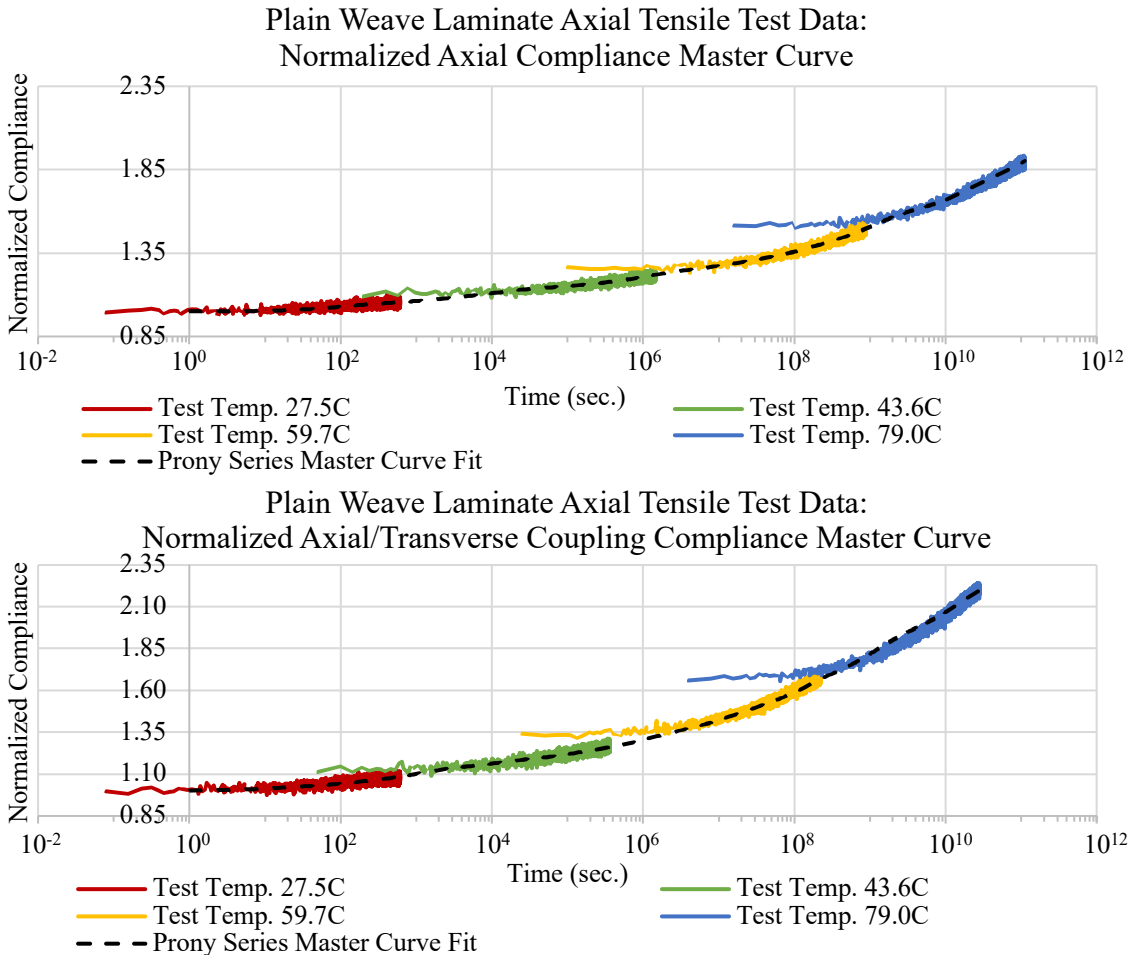

Figure A.11: The master curves for the plain weave laminate axial compliance (top graph) and axial/transverse coupling compliance (bottom graph) obtained by tensile test data. Tests at four different constant temperatures are conducted for each material property. The axial and axial/transverse coupling compliance are viscoelastic. The master curves of the respective properties are formed by shifting the four temperature data sets on the time axis. The creep compliance properties are normalized by the respective instantaneous (i.e., glassy) compliance of the initial creep test comprising the master curve. A Prony series is fitted to the creep compliance data representing the master curve axial and axial/transverse coupling.

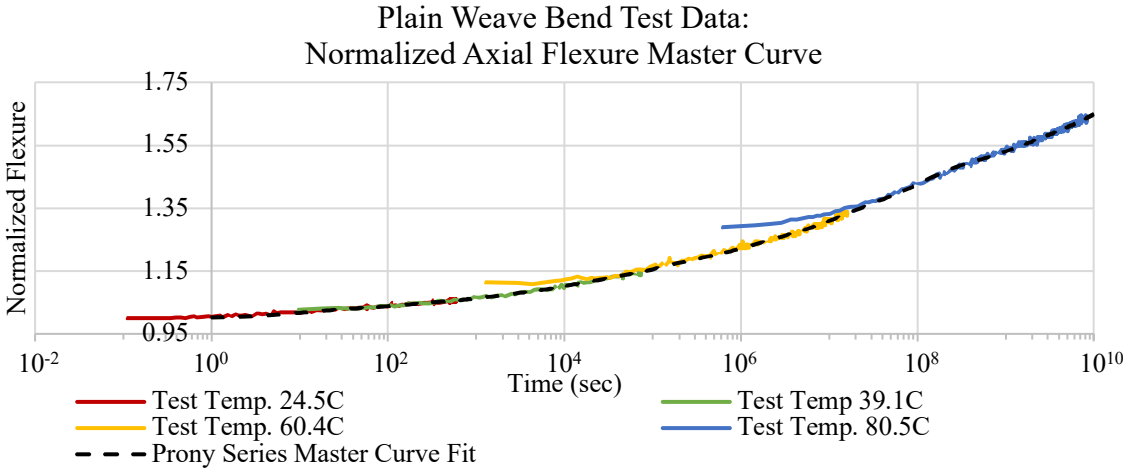

Figure A.12: The master curve for the plain weave laminate axial flexure obtained from four-point-bend test data. Four different constant temperature tests are conducted for each material property. The response in axial flexure is viscoelastic. The master curve of this property is formed by shifting the four temperature data sets along the time axis. The creep flexure property is normalized by the instantaneous (i.e., glassy) flexure of the initial thermal test. A Prony series is fitted to the creep flexure data to form the master curve for the axial property.

$T_o = 30C$	Tensile Test PW S_{xx}		Tensile Test PW S_{xy}		Bend Test PW d_{xx}		Bend Test PW d_{yy}	
$E_a\ (J/mol)$	1.40E+05		1.41E+05		1.09E+05		1.09E+05	
$S^g_{lm}\ (MPa^{-1})$ or $d^g_{lm}\ (Nmm^{-1})$	7.12E-05		-4.94E-05		8.45E-02		8.45E-02	
Prony Values	$S^i_{xx}\ (MPa^{-1})$	$\beta^i_{S_{xx}}\ (s^{-1})$	$S^i_{xy}\ (MPa^{-1})$	$\beta^i_{S_{xy}}\ (s^{-1})$	$d^i_{xx}\ (Nmm^{-1})$	$\beta^i_{d_{xx}}\ (s^{-1})$	$d^i_{yy}\ (Nmm^{-1})$	$\beta^i_{d_{yy}}\ (s^{-1})$
i = 1	2.82E-06	8.24E-02	-1.17E-06	8.24E-01	1.96E-03	6.32E-01	1.96E-03	6.32E-01
2	1.94E-06	8.24E-03	-1.18E-06	8.24E-02	1.63E-03	6.32E-02	1.63E-03	6.32E-02
3	4.40E-06	8.24E-04	-3.33E-06	8.24E-03	2.16E-03	6.32E-03	2.16E-03	6.32E-03
4	1.66E-06	8.24E-05	-2.69E-06	8.24E-04	3.60E-03	6.32E-04	3.60E-03	6.32E-04
5	5.46E-06	8.24E-06	-2.75E-06	8.24E-05	5.02E-03	6.32E-05	5.02E-03	6.32E-05
6	3.92E-06	8.24E-07	-6.74E-06	8.24E-06	5.49E-03	6.32E-06	5.49E-03	6.32E-06
7	6.16E-06	8.24E-08	-3.57E-06	8.24E-07	8.12E-03	6.32E-07	8.12E-03	6.32E-07
8	1.38E-05	8.24E-09	-1.13E-05	8.24E-08	1.15E-02	6.32E-08	1.15E-02	6.32E-08
9	8.09E-06	8.24E-10	-7.68E-06	8.24E-09	6.49E-03	6.32E-09	6.49E-03	6.32E-09
10	2.38E-05	8.24E-11	-1.44E-05	8.24E-10	1.27E-02	6.32E-10	1.27E-02	6.32E-10
11			-2.22E-05	8.24E-11	9.78E-03	6.32E-11	9.78E-03	6.32E-11

Table A.13: The Prony time constants representing the creep compliance and flexure master curves of the plain weave laminate. The table also records the Arrhenius law activation energies used to form the master curves from test data at varying constant temperatures.

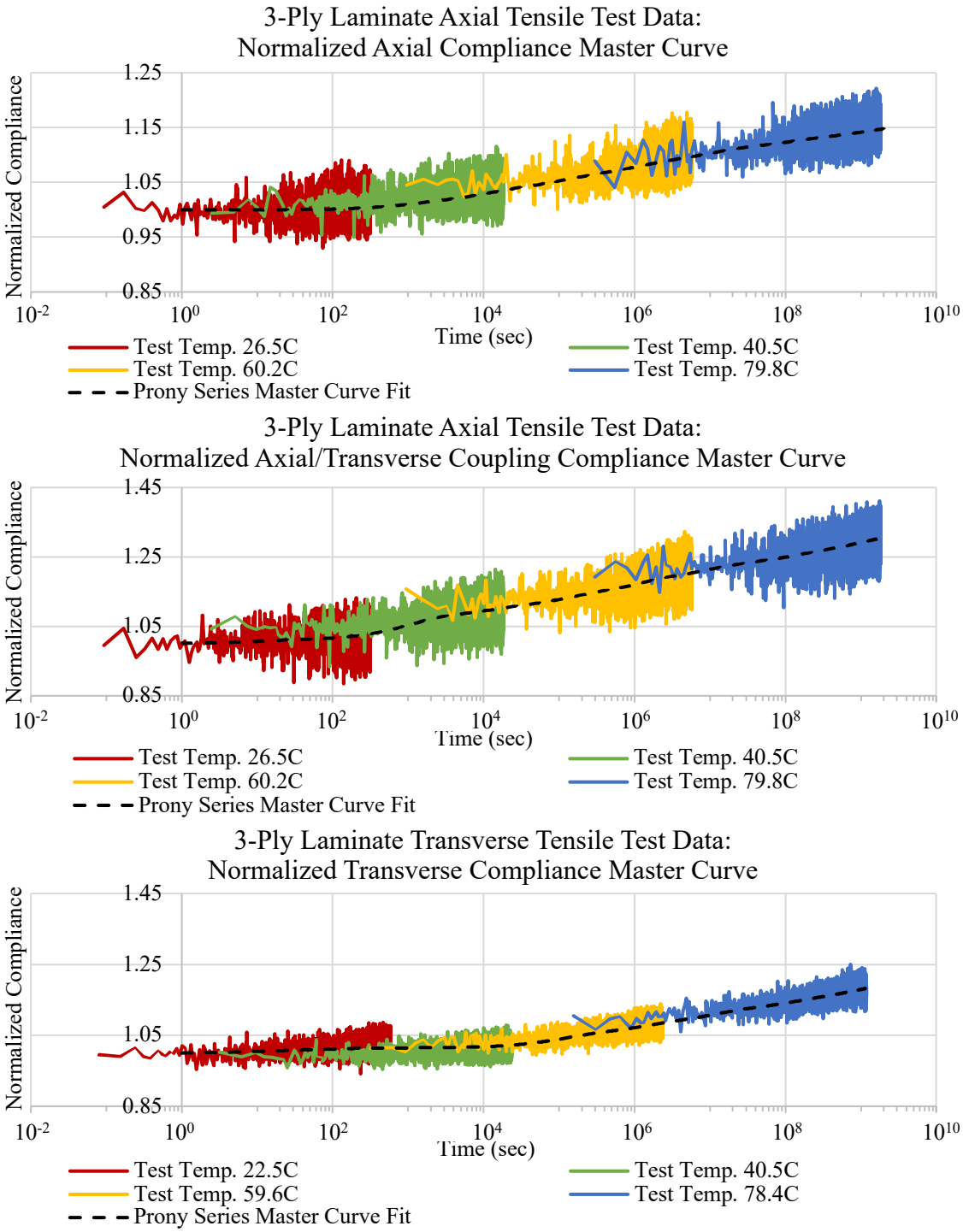

Figure A.13: The master curves for the 3-Ply laminate axial compliance (top graph), axial/transverse coupling compliance (middle graph), and transverse compliance (bottom graph) obtained from tensile test data. Tests at four different constant temperatures are conducted for each material property. The axial, axial/transverse coupling, and transverse compliance show some degree of viscoelasticity. The master curves of the respective properties are formed by shifting the four constant temperature data sets along the time axis. The creep compliance properties are normalized by the respective instantaneous (i.e., glassy) compliance of the initial creep test. A Prony series is fitted to the creep compliance data representing the master curve axial, axial/transverse coupling, and transverse properties.

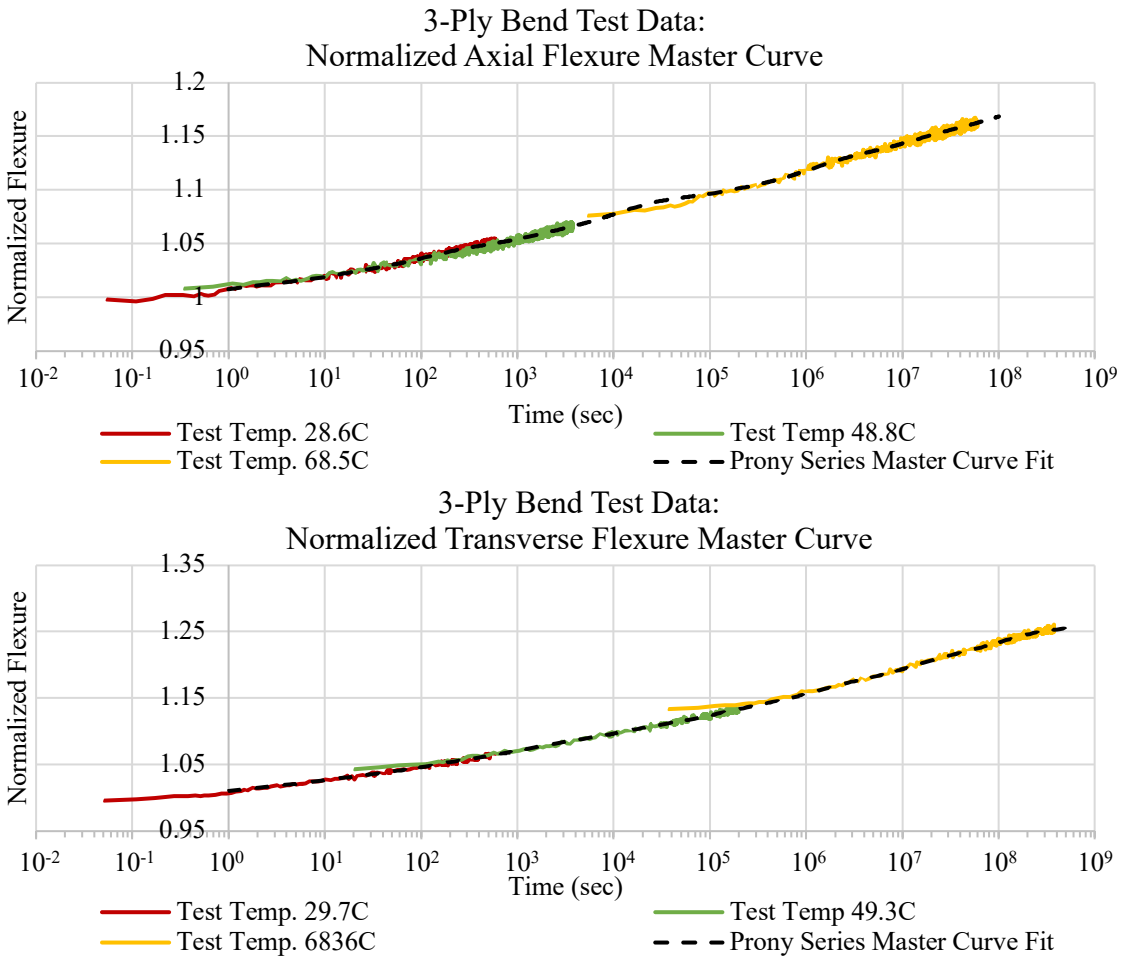

Figure A.14: The master curves for the 3-Ply laminate axial flexure (top graph) and transverse flexure (bottom graph) obtained from four-point-bend test data. Four constant temperature tests are conducted for each material property. The axial and transverse flexure properties are viscoelastic. A master curve is formed by shifting the data from the tests at the four different temperatures on the time axis to create a creep flexure master curve. The creep flexure properties are normalized by the respective instantaneous (i.e., glassy) flexure from the initial creep test. A Prony series is fitted to both the axial and transverse creep flexure data representing the master curve.

$T_o = 30C$	Tensile Test 3-ply S_{xx}		Tensile Test 3-ply S_{xy}		Tensile Test 3-ply S_{yy}		Bend Test 3-ply d_{xx}		Bend Test 3-ply d_{yy}	
$E_a\ (J/mol)$	1.08E+05		1.08E+05		9.61E+04		1.50E+05		8.75E+04	
$S^g_{lm}\ (MPa^{-1})$ or $d^g_{lm}\ (Nmm^{-1})$	2.82E-05		-2.01E-05		6.24E-05		3.82E+00		3.19E+00	
Prony Values	$S^i_{xx}\ (MPa^{-1})$	$\beta^i_{S_{xx}}\ (s^{-1})$	$S^i_{xy}\ (MPa^{-1})$	$\beta^i_{S_{xy}}\ (s^{-1})$	$S^i_{yy}\ (MPa^{-1})$	$\beta^i_{S_{yy}}\ (s^{-1})$	$d^i_{xx}\ (Nmm^{-1})$	$\beta^i_{d_{xx}}\ (s^{-1})$	$d^i_{yy}\ (Nmm^{-1})$	$\beta^i_{d_{yy}}\ (s^{-1})$
i = 1	3.35E-07	1.94E-03	-2.01E-07	1.94E-01	3.87E-07	4.33E-01	6.32E-02	2.29E+00	4.65E-02	1.19E+00
2	6.39E-07	1.94E-04	-1.28E-06	1.94E-03	5.10E-07	4.33E-02	3.63E-02	2.29E-01	6.30E-02	1.19E-01
3	6.87E-07	1.94E-05	-5.25E-07	1.94E-04	2.15E-06	4.33E-05	1.20E-01	2.29E-03	7.24E-02	1.19E-02
4	7.29E-07	1.94E-06	-7.15E-07	1.94E-05	1.88E-06	4.33E-06	7.70E-02	2.29E-04	8.25E-02	1.19E-03
5	7.29E-07	1.94E-07	-9.80E-07	1.94E-06	2.43E-06	4.33E-07	9.01E-02	2.29E-05	1.44E-01	1.19E-04
6	4.72E-07	1.94E-08	-8.27E-07	1.94E-07	1.80E-06	4.33E-08	9.29E-02	2.29E-06	1.26E-01	1.19E-05
7	5.98E-07	1.94E-09	-5.82E-07	1.94E-08	3.23E-06	4.33E-09	5.97E-02	2.29E-07	1.19E-01	1.19E-06
8	3.45E-07	1.94E-10	-1.19E-06	1.94E-09			6.14E-02	2.29E-08	7.64E-02	1.19E-07
9							1.42E-01	2.29E-09	1.12E-01	1.19E-08
10							6.56E-02	2.29E-10		
11							8.46E-02	2.29E-11		
12							1.99E-01	2.29E-12		

Table A.14: The Prony time constant representing the creep compliance and flexure master curves of the 3-ply laminate. The table also records the Arrhenius law activation energies used to form the master curves from test data at varying constant temperatures.

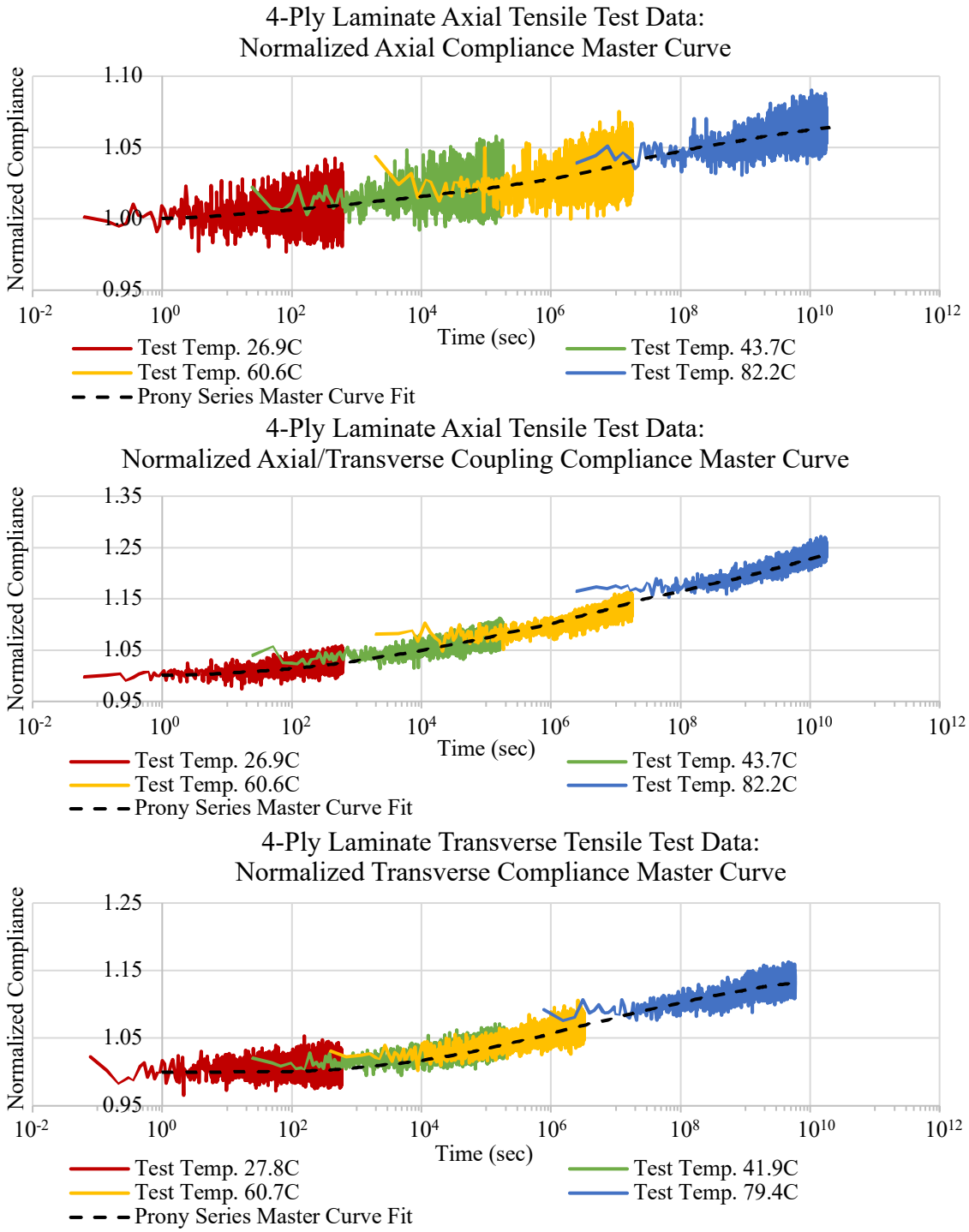

Figure A.15: The master curves for the 4-Ply laminate axial compliance (top graph), axial/transverse coupling compliance (middle graph), and transverse compliance (bottom graph) obtained from tensile test data. Tests are conducted at four different constant temperatures for each material property. The axial, axial/transverse coupling, and transverse compliance show some degree of viscoelasticity. The master curves of the respective properties are formed by shifting the four constant temperature data sets along the time axis. The creep compliance properties are normalized by the respective instantaneous (i.e., glassy) compliance of the initial creep test. A Prony series is fitted to the creep compliance data representing the master curve axial, axial/transverse coupling, and transverse properties.

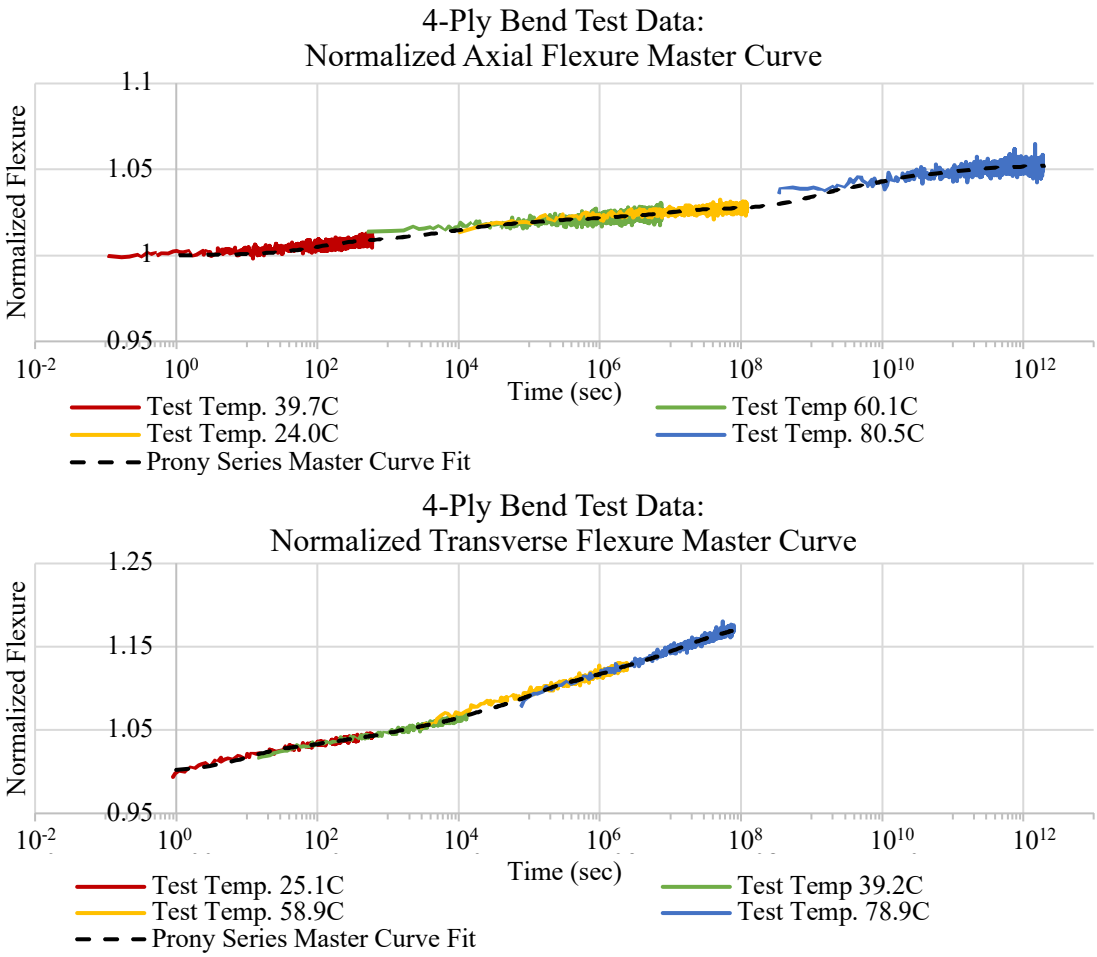

Figure A.16: The master curves for the 4-ply laminate axial flexure (top graph) and transverse flexure (bottom graph) obtained from four-point-bend test data. Four constant temperature tests are conducted for each material property. The axial and transverse flexure is viscoelastic. A master curve is formed by shifting the four temperature data sets along the time axis to create a creep flexure master curve. The creep flexure properties are nominalized by the respective instantaneous (i.e., glassy) flexure of the initial creep test. A Prony series is fitted to both the axial and transverse creep flexure data representing the master curve.

$T_o = 30C$	Inverted 4-ply S_{xx}		Inverted 4-ply S_{xy}		Inverted 4-ply S_{yy}		Inverted 4-ply d_{xx}		Inverted 4-ply d_{yy}	
$E_a\ (J/mol)$	1.19E+5		1.19E+5		1.12E+5		7.79E+4		8.45E+4	
$S_{lm}^g\ (MPa^{-1})$ or $d_{lm}^g\ (Nmm^{-1})$	1.68E-5		-1.09E-5		5.07E-5		4.16E-1		3.74	
Prony Value	$S_{xx}^i\ (MPa^{-1})$	$\beta_{S_{xx}}^i\ (s^{-1})$	$S_{xy}^i\ (MPa^{-1})$	$\beta_{S_{xy}}^i\ (s^{-1})$	$S_{yy}^i\ (MPa^{-1})$	$\beta_{S_{yy}}^i\ (s^{-1})$	$d_{xx}^i\ (Nmm^{-1})$	$\beta_{d_{xx}}^i\ (s^{-1})$	$d_{yy}^i\ (Nmm^{-1})$	$\beta_{d_{yy}}^i\ (s^{-1})$
i = 1	5.72E-8	2.64E-1	-7.00E-8	2.64E-1	3.96E-7	2.40E-3	1.31E-5	1.00E-1	9.40E-2	3.20E-1
2	6.17E-8	2.64E-2	-9.60E-8	2.64E-2	5.72E-7	2.40E-4	2.97E-3	1.00E-2	3.84E-2	3.20E-2
3	7.94E-8	2.64E-3	-1.99E-7	2.64E-3	1.01E-6	2.40E-5	1.25E-3	1.00E-3	5.25E-2	3.20E-3
4	8.49E-8	2.64E-4	-2.30E-7	2.64E-4	1.21E-6	2.40E-6	2.75E-3	1.00E-4	7.03E-2	3.20E-4
5	9.56E-8	2.64E-5	-2.89E-7	2.64E-5	1.21E-6	2.40E-7	1.40E-3	1.00E-5	1.20E-1	3.20E-5
6	1.06E-7	2.64E-6	-2.97E-7	2.64E-6	1.08E-6	2.40E-8	7.31E-4	1.00E-6	7.93E-2	3.20E-6
7	1.99E-7	2.64E-7	-4.00E-7	2.64E-7	9.87E-7	2.40E-9	1.94E-3	1.00E-7	1.14E-1	3.20E-7
8	1.49E-7	2.64E-8	-3.00E-7	2.64E-8	4.31E-7	2.40E-10	9.52E-7	1.00E-8	1.18E-1	3.20E-8
9	1.30E-7	2.64E-9	-3.00E-7	2.64E-9			4.38E-3	1.00E-9	1.54E-2	3.20E-9
10	1.30E-7	2.64E-10	-5.00E-7	2.64E-10			3.54E-3	1.00E-10		
11							1.89E-3	1.00E-11		
12							9.52E-4	1.00E-12		

Table A.15: The Prony time constant representing the creep compliance and flexure master curves of the 4-ply laminate. The table also records the Arrhenius law activation energies used to form the master curves from test data at varying constant temperatures.

Table A.16 to Table A.20 record the relaxation stiffness properties predicted using the numerical Laplace inversion method developed in Chapter 3 to invert the measured creep compliance properties of the neat resin, unidirectional, plain weave, 3-ply, and 4-ply laminates discussed in Chapter 2. The tables also record the relaxation flexure stiffness predicted using viscoelastic classical laminate theory (CLT) described in Chapter 4 in which the relaxation stiffness of the unidirectional and plain weave lamina inverted from test data are used as inputs.

$T_o = 30C$	Inverted NR Q_{xx}		Inverted NR Q_{xy}	
$Q_{lm}^{g}(MPa)$	3.54E+3		1.38E+3	
Prony Value	$Q_{xx}^{i}(MPa)$	$\alpha_{xx}^{i}\ (s^{-1})$	$Q_{xy}^{i}(MPa)$	$\alpha_{xy}^{i}\ (s^{-1})$
i = 1	3.71	1.60	9.49E-5	1.62E-3
2	8.61E-3	1.55E-1	4.02E+1	1.65E-4
3	1.73E+2	1.69E-2	9.85E+1	1.62E-5
4	1.51E-2	1.61E-3	2.58E+1	1.71E-6
5	1.27E+2	1.63E-4	9.61E-3	1.62E-7
6	8.81E+1	1.62E-5	6.57E+1	1.63E-8
7	1.80E+2	1.70E-6	4.65E-3	1.73E-9
8	3.18E+1	1.62E-7	8.96E+1	1.64E-10
9	1.00E+2	1.63E-8		
10	1.38E+2	1.67E-9		
11	1.09E+2	1.63E-10		
12	9.67E+1	1.67E-11		
13	9.17E+1	1.57E-12		

Table A.16: The neat resin Prony series constants representing the relaxation stiffness master curve properties inverted from measured creep compliance data using the Laplace numerical inversion method developed in Chapter 3.

$T_o = 30^oC$	Inverted Uni Q_{xx}		Inverted Uni Q_{xy}		Inverted Uni Q_{yy}		Inverted Uni D_{xx}		Inverted Uni D_{xy}		Inverted Uni D_{yy}	
$Q^g_{lm}\ (MPa)$ or $D^g_{lm}\ (Nmm)$	1.27E+5		2.44E+3		6.77E+3		2.08E+5		4.00E+3		1.11E+4	
Prony Value	$Q^i_{xx}(MPa)$	$\alpha^i_{xx}(s^{-1})$	$Q^i_{xy}(MPa)$	$\alpha^i_{xy}(s^{-1})$	$Q^i_{yy}\ (MPa)$	$\alpha^i_{yy}(s^{-1})$	$D^i_{xx}(Nmm)$	$\alpha^i_{xx}(s^{-1})$	$D^i_{xy}(Nmm)$	$\alpha^i_{xy}(s^{-1})$	$D^i_{yy}(Nmm)$	$\alpha^i_{yy}(s^{-1})$
i = 1	4.46E-1	1.2 E-1	3.55E-11	1.22E-1	3.87E-10	1.22E-1	3.95E-6	1.0E-5	1.65	1.0	1.55E+1	1.0E-1
2	1.28E+1	1.24E-2	5.29E+1	1.24E-2	1.48E+2	1.24E-2	7.73E-6	1.0E-6	1.48E+1	1.0E-1	2.33E+2	1.0E-2
3	2.33E+1	1.23E-3	3.32E+1	1.23E-3	9.15E+1	1.23E-3	9.81E-6	1.0E-7	5.62E+1	1.0E-2	1.93E+2	1.0E-3
4	2.40E+1	1.28E-4	1.10E+2	1.28E-4	3.08E+2	1.28E-4	7.24E-6	1.0E-8	9.62E+1	1.0E-3	4.72E+2	1.0E-4
5	1.34E+1	1.24E-5	4.86E+1	1.24E-5	1.25E+2	1.24E-5	3.29E-6	1.0E-9	1.25E+2	1.0E-4	2.29E+2	1.0E-5
6	5.58E+1	1.28E-6	9.74E+1	1.28E-6	2.87E+2	1.28E-6	1.30E-7	1.0E-10	1.32E+2	1.0E-5	4.68E+2	1.0E-6
7	1.35E-4	1.26E-7	8.30E+1	1.26E-7	2.13E+2	1.26E-7	2.69E-7	1.0E-11	1.47E+2	1.0E-6	3.53E+2	1.0E-7
8	3.29E+1	1.26E-8	6.46E+1	1.26E-8	1.88E+2	1.26E-8			1.34E+2	1.0E-7	2.67E+2	1.0E-8
9									7.76E+1	1.0E-8	7.13E-4	1.0E-9
10									1.40E+1	1.0E-9		
11									1.60E-6	1.0E-10		
12									1.23E-6	1.0E-11		
13									8.96E-7	1.0E-12		

Table A.17: The unidirectional lamina Prony series constants representing the relaxation stiffness master curve properties inverted from measured creep compliance data using the Laplace numerical inversion method developed in Chapter 3. The table also records the relaxation flexure stiffness Prony series constants predicted using viscoelastic classical laminate theory (CLT) with the unidirectional lamina inverted relaxation stiffness as an input.

$T_o = 30^oC$	Inverted PW Q_{xx}		Inverted PW Q_{xy}		Inverted PW D_{xx}		Inverted PW D_{xy}	
$Q^g_{lm}\ (MPa)$ or $D^g_{lm}\ (Nmm)$	4.41E+4		3.60E+4		3.76E+4		3.07E+4	
Prony Value	$Q^i_{xx}(MPa)$	$\alpha^i_{xx}(s^{-1})$	$Q^i_{xy}(MPa)$	$\alpha^i_{xy}(s^{-1})$	$D^i_{xx}(Nmm)$	$\alpha^i_{xx}(s^{-1})$	$D^i_{xy}(Nmm)$	$\alpha^i_{xy}(s^{-1})$
i = 1	5.77E+2	2.58E-3	1.24E+1	2.61E-7	1.28	1.00E-1	2.88E-6	1.00E-5
2	1.25E+2	2.38E-4	5.84E+1	2.75E-8	1.70E+2	1.00E-2	1.10E+1	1.00E-6
3	5.87E+2	2.81E-5	2.38E+1	2.90E-11	3.44E+2	1.00E-3	2.08E+1	1.00E-7
4	1.89E+2	2.23E-6			2.83E+2	1.00E-4	2.00E+1	1.00E-8
5	3.14E+2	2.56E-7			4.26E+2	1.00E-5	1.09E+1	1.00E-9
6	8.01E+2	3.39E-8			4.95E+1	1.00E-6	9.92	1.00E-10
7	2.90E+2	1.94E-9			6.41E+2	1.00E-7	7.91	1.00E-11
8	5.29E+2	2.31E-10			3.98E+2	1.00E-8	1.54E-4	1.00E-12
9	6.99E+2	2.93E-11			2.64E+2	1.00E-9		
10					6.83E+2	1.00E-10		
11					2.42E+2	1.00E-11		

Table A.18 : The plain weave lamina Prony series constants representing the relaxation stiffness master curve properties inverted from measured creep compliance data using the Laplace numerical inversion method developed in Chapter 3. The table also records the relaxation flexure stiffness Prony series constants predicted using viscoelastic classical laminate theory (CLT) with the plain weave lamina inverted relaxation stiffness as an input.

$T_o = 30^oC$	Inverted 3-ply Q_{xx}		Inverted 3-ply Q_{xy}		Inverted 3-ply Q_{yy}		Inverted 3-ply D_{xx}		Inverted 3-ply D_{xy}		Inverted 3-ply D_{yy}	
$Q^g_{lm}\ (MPa)$ or $D^g_{lm}\ (Nmm)$	4.60E+4		1.48E+4		2.08E+4		7.82E+2		6.29E+2		7.72E+2	
Prony Value	$Q^i_{xx}(MPa)$	$\alpha^i_{xx}(s^{-1})$	$Q^i_{xy}(MPa)$	$\alpha^i_{xy}(s^{-1})$	$Q^i_{yy}\ (MPa)$	$\alpha^i_{yy}(s^{-1})$	$D^i_{xx}(Nmm)$	$\alpha^i_{xx}(s^{-1})$	$D^i_{xy}(Nmm)$	$\alpha^i_{xy}(s^{-1})$	$D^i_{yy}(Nmm)$	$\alpha^i_{yy}(s^{-1})$
i = 1	1.40E+3	1.91E-5	5.76E+2	1.98E-5	3.18E+2	4.37E-2	9.36E-7	1.0E-1	9.07E-5	1.0	4.06	1.0E-2
2	6.94E+2	1.90E-7			5.48E+2	4.49E-6	4.15	1.0E-2	4.36E-3	1.0E-2	6.32	1.0E-3
3	4.47E+2	1.88E-9			6.74E+2	4.47E-8	6.28	1.0E-3	4.42E-3	1.0E-3	6.70	1.0E-4
4					4.30E+2	4.59E-9	6.74	1.0E-4	7.75E-3	1.0E-4	6.36	1.0E-5
5							6.28	1.0E-5	1.00E-7	1.0E-5	4.80	1.0E-6
6							4.84	1.0E-6	5.48E-2	1.0E-6	9.02	1.0E-7
7							8.71	1.0E-7	6.41E-1	1.0E-7	8.99	1.0E-8
8							8.86	1.0E-8	5.15E-1	1.0E-8	8.34	1.0E-9
9							8.82	1.0E-9	9.45E-2	1.0E-9	1.07E+1	1.0E-10
10							1.07E+1	1.0E-10	2.00E-1	1.0E-10	6.64	1.0E-11
11							6.43	1.0E-11	1.72E-1	1.0E-11		
12							5.89E-6	1.0E-12				

Table A.19: The 3-ply laminate Prony series constants representing the relaxation stiffness master curve properties inverted from measured creep compliance data using the Laplace numerical inversion method developed in Chapter 3. The table also records the relaxation flexure stiffness Prony series constants predicted using viscoelastic classical laminate theory (CLT) with the unidirectional lamina and plain weave lamina inverted relaxation stiffness as inputs.

$T_o = 30^oC$	Inverted 4-ply Q_{xx}		Inverted 4-ply Q_{xy}		Inverted 4-ply Q_{yy}		Inverted 4-ply D_{xx}		Inverted 4-ply D_{xy}		Inverted 4-ply D_{yy}	
$Q^g_{lm}\ (MPa)$ or $D^g_{lm}\ (Nmm)$	6.92E+4		1.49E+4		2.29E+4		2.45E+3		1.84E+2		2.93E+2	
Prony Value	$Q^i_{xx}(MPa)$	$\alpha^i_{xx}(s^{-1})$	$Q^i_{xy}(MPa)$	$\alpha^i_{xy}(s^{-1})$	$Q^i_{yy}\ (MPa)$	$\alpha^i_{yy}(s^{-1})$	$D^i_{xx}(Nmm)$	$\alpha^i_{xx}(s^{-1})$	$D^i_{xy}(Nmm)$	$\alpha^i_{xy}(s^{-1})$	$D^i_{yy}(Nmm)$	$\alpha^i_{yy}(s^{-1})$
i = 1	4.54E-4	2.65E-1	1.13E-3	2.64E-1	1.16E+1	2.40E-2	8.70E-1	1.0E-2	1.70E-1	1.0E-1	6.92E-1	1.0E-1
2	1.43E-4	2.64E-2	1.41E+2	2.64E-2	1.54E-3	2.67E-3	1.45	1.0E-3	6.88E-1	1.0E-2	2.74	1.0E-2
3	5.80E+2	2.42E-3	1.28E+2	2.62E-3	5.83E-4	2.66E-4	1.51	1.0E-4	1.03	1.0E-3	4.28	1.0E-3
4	1.66E-5	2.43E-4	4.58E+2	2.61E-6	8.48E+2	2.67E-5	1.39	1.0E-5	1.41	1.0E-4	5.23	1.0E-4
5	2.70E-4	2.46E-5	4.47E+2	2.58E-10	3.53E-4	2.67E-6	1.04	1.0E-6	1.51	1.0E-5	5.28	1.0E-5
6	1.12E-3	2.47E-6			9.11E+2	2.67E-8	2.00	1.0E-7	1.56	1.0E-6	5.60	1.0E-6
7	3.83E-4	2.47E-7			3.32E-4	2.68E-10	1.99	1.0E-8	1.44	1.0E-7	5.85	1.0E-7
8	5.55E+2	2.46E-8					1.97	1.0E-9	9.37E-1	1.0E-8	4.56	1.0E-8
9	1.00E-6	2.45E-9					2.34	1.0E-10	3.35E-1	1.0E-9	2.95	1.0E-9
10							1.42	1.0E-11	3.04E-2	1.0E-11	2.09	1.0E-10
11							2.81E-5	1.0E-12			1.13	1.0E-11
12											3.48E-6	1.0E-12

Table A.20 : The 4-ply laminate Prony series constants representing the relaxation stiffness master curve properties inverted from measured creep compliance data using the Laplace numerical inversion method developed in Chapter 3. The table also records the relaxation flexure stiffness Prony series constants predicted using viscoelastic classical laminate theory (CLT) with the unidirectional lamina and plain weave lamina inverted relaxation stiffness as inputs.